



Concordia
UNIVERSITY

TN-EMC-98-01

March 31, 1998

Final Report

**A RESEARCH STUDY ON ELECTROMAGNETIC
FIELDS PRODUCED BY PORTABLE TRANSCEIVERS**

Dr. C.W. Trueman

Dr. S.J. Kubina

**FACULTY OF
ENGINEERING
AND COMPUTER
SCIENCE**

TK
6553
T787
1998
#01

IC

EMC LABORATORY

DEPARTMENT OF ELECTRICAL AND COMPUTER ENGINEERING

7141 Sherbrooke St. West, L-AD-532
Montreal, Quebec, Canada H4B 1R6

Tic
6553
T787
1998
#1
c.a
S-Gen

TN-EMC-98-01

March 31, 1998

Final Report

**A RESEARCH STUDY ON ELECTROMAGNETIC
FIELDS PRODUCED BY PORTABLE TRANSCEIVERS**

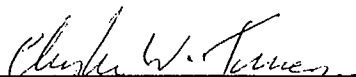
Dr. C.W. Trueman

Dr. S.J. Kubina

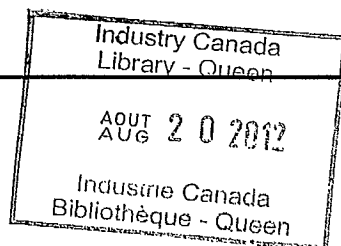
~~CRC LIBRARY
-01- 11 2000
BIBLIOTHEQUE~~



Dr. S.J. Kubina, Eng.



Dr. C.W. Trueman, Eng.



Prepared For:

Communications Research Centre

Public Works and Government Services Canada Contract
PWGSC/CRC U6800-7-0726/001/ST

Table of Contents

A Research Study on Electromagnetic Fields Produced by Portable Transceivers

	Page
Table of Contents	i
1. Introduction	1
1.1 Project Objectives	1
1.2 Review of Previous Work.....	2
1.2.1 Computation of the Far Fields	2
1.2.2 Computation of the Near Fields	3
1.2.3 Measurement of the Near Fields	4
1.2.4 Measurement of the Far Fields	4
1.2.5 Measurement of the Brain-Liquid Parameters	5
1.2.6 Creation of Cell Models of Handsets and Heads	5
1.2.7 Anatomical Model of the Head.....	6
1.2.8 Summary	6
1.3 The Portable Radio Handset	6
1.4 Orientation of the Handset Relative to the Head	6
1.5 Issues Studied in this Report.....	7
1.6 Overview of the Work	7
2. Radiation Patterns of the Vertical Handset	12
2.1 FDTD Model of the Handset	12
2.2 The Perfectly-Matched Layer Absorbing Boundary Condition.....	12
2.2.1 Designing the PML	14
2.3 The Isotropic Reference Level.....	15
2.4 The Principal Plane Patterns of the Handset.....	16
2.5 Comparison of the Principal Plane Patterns by NEC and by FDTD	17
2.6 Radiation Pattern Dependence on the Cell Size	18
2.7 Conclusion	19
3. Measured Radiation Patterns of the Vertical Handset	27
3.1 The Portable Radio Handset	27
3.2 The Measurement Setup	27
3.3 Pattern Dependence on Range	28
3.4 Scaling the Measurements	29

3.5	Comparison of the Measured and Computed Patterns.....	30
3.6	Comparison of the 2.205 mm Cell Computation with the Measurement	31
3.7	Conclusion	32
4.	Radiation Patterns of the Handset and Box Head	44
4.1	The FDTD Model of the Handset and Box Head	44
4.2	The Radiation Patterns of the Handset and Box Head.....	44
4.3	Changes in the Handset Patterns due to the Box Head.....	45
4.4	The Box Head Mounting Jig.....	46
	4.4.1 Measured Radiation Patterns Including the Bolts.....	47
	4.4.2 Effect of the Bolts in the Computed Radiation Patterns	48
4.5	Comparison of the Computed and Measured Radiation Patterns	49
4.6	Conclusion	50
5.	Radiation Patterns of the Handset and Sphere Head	66
5.1	FDTD Model of the Handset and Sphere Head	66
5.2	The Radiation Patterns of the Handset and the Sphere Head	67
5.3	Changes in the Handset Patterns due to the Sphere Head	67
5.4	Comparison with the Measured Radiation Patterns	68
5.5	Conclusion	70
6.	Radiation Patterns of the Tilted Handset	79
6.1	Far Field Coordinate Transformation For Use With FDTD	79
	6.1.1 Angle Transformation.....	80
	6.1.2 Spherical Field Components in Global Coordinates.....	81
	6.1.3 Procedure for Computing the Radiation Patterns with FDTDANT.....	82
6.2	Radiation Patterns of the Tilted Handset	82
6.3	Validation Against the Wire-Grid Patterns.....	84
6.4	The Tilted Handset Near the Sphere Head	84
6.5	Tilted Handset and Sphere Head vs. Tilted Handset Alone.....	86
6.6	Conclusion	87
7.	An Anatomical Head Model.....	101
7.1	The Electrical Parameters of Biological Materials	102
7.2	The Digitized Anatomical Sections	103
7.3	Assembling an FDTD Cell Model	104
7.4	The Anatomical Head Cell Model	105
7.5	Radiation Patterns of the Handset near the Anatomical Head Model	106
7.6	Conclusion	108
8.	The Head Phantom	116
8.1	The Head Phantom.....	116

8.1.1	MRI Scans.....	116
8.1.2	CT Scans.....	117
8.1.3	Identifying Tissue Types.....	118
8.2	Identifying Tissues in the CT Scan Cross-Sections.....	118
8.2.1	The Bone Tissue.....	119
8.2.2	The Muscle Tissue.....	119
8.2.3	The Skin Tissue.....	120
8.2.4	Discussion.....	120
8.3	Conclusion.....	121
9.	Conclusions and Recommendations.....	130
9.1	Summary and Conclusions.....	130
9.1.1	Handset and Head Radiation Patterns.....	130
9.1.2	Validation.....	131
9.1.3	Phantom Head Cell Model.....	131
9.2	Recommendations for Further Work.....	131
9.2.1	Modern Handset Design.....	131
9.2.2	Development of a Cell Model of the Phantom.....	132
9.2.3	Development of a Precise Anatomical Head Model.....	132
9.2.4	Far Fields of the Handset with the Head.....	132
9.2.4.1	Principal Plane Measurements with the Head Phantom.....	132
9.2.4.2	Calibration of the Pattern Measurements.....	133
9.2.4.3	Validation of the Computer Models.....	134
9.2.4.4	Investigation of the Handset and Head Radiation Patterns.....	134
9.2.4.5	Assessment of Adequate Coverage.....	134
9.2.5	Near Field Measurements.....	135
9.2.5.1	Simple Head Models.....	136
9.2.5.2	With the Head Phantom.....	136
9.2.5.3	Discussion.....	137
9.2.6	Computational Issues.....	137
9.3	Conclusion.....	137
	References.....	139
	Appendix 1 – Reference [27], “Comparison of the Performance of the PML and the Liao Absorbing Boundary Formulation,” Vall-Ilossera, Trueman.....	143
	Appendix 2 – Reference [28], “Validation of FDTD-Computed Handset Patterns by Measurement,” Trueman, Kubina, Roy, Lauber, Vall-Ilossera.....	152
	Appendix 3 – Reference [29], Permittivity and conductivity data for the materials making up the head phantom.....	159

Chapter 1

Introduction

This is the Final Report in Contract Number U68000-7-0726/001/ST. It reports work completed in the period April 1, 1997 to March 31, 1998. The current project carries on the work of previous projects[1,2,3,4], and prepares for the next phase of the project.

1.1 Project Objectives

The user of a portable radio such as a cellular telephone holds the handset in the hand with the earpiece against the ear, and speaks into the mouthpiece. The handset is typically held at about 60 degrees to the vertical, and must provide satisfactory communication with the base station, in the presence of the head, hand, of the body, and of nearby surfaces such as the ground. In assessing whether a given handset and antenna will be satisfactory in use requires a knowledge of the field strengths in E_θ and E_ϕ over the whole radiation sphere. Are there angular regions where the field strength in both polarizations falls below the minimum acceptable value? How does the base station receive the signal? Does the base station receive only circular polarization, or can it receive the two linear components independently of one another? How do the handset patterns change as the handset is held in different positions against the head, at different angles to the vertical, and with the hand in various positions? Is satisfactory coverage achieved over a variety of typical handset positions? An objective of this project is to investigate the radiated fields of a handset, including the effect of the head and hand. In broad terms, all possible handset designs and antenna designs are of interest in the project.

The handset must not cause interference with other equipment nearby. Thus, are the near fields of the handset so large as to cause a nearby computer to crash. Interference with equipment is a particularly egregious problem in hospital environments, where the malfunction of a heart monitor or an electronic pump controlling a drug administered intravenously may be life-threatening[5]. A portable radio such as a walkie-talkie can cause such equipment to behave unpredictably. A detailed knowledge of the near fields of portable radio handsets, again in typical positions relative to the head and hand, can be helpful in assessing risks, and perhaps in setting standards to ensure electromagnetic compatibility with other equipment. Such standards need to specify the permissible levels of near field from the portable radio and also the required immunity for the victim equipment.

The major objective of this project is to study the near fields and the far fields of portable radio handsets such as cellular telephones. Both the fields of the handset in isolation and of the handset near the operator's head and hand are to be determined. The

fields of the handset held in various positions against the head are of interest, including the presence of the hand. Various designs of handsets and handset antennas are of interest to this project.

The fields are to be found both by measurement and by computation. Hence an objective is to measure the fields as accurately as possible, both in the near field and in the far field. Another objective is to compute the fields as accurately as possible. In this project the finite-difference time-domain method, or "FDTD", has been selected, because it is extensively used by other researchers and in industry.

A major objective of the project is the validation of the computations by comparison with the measured data, both for radiation patterns and for near fields. This verifies that similar computations done by others by the same methods provide realistic results. Thus we can judge the degree to which computations alone can be used to assess the radiation patterns and near fields of a given handset design, and be used as the basis for the development of handset designs.

Many other researchers are investigating this problem. The state-of-the-art was summarized in a short course entitled "Personal Communications Antennas: Modern Design and Analysis Techniques Including Human Interaction" presented by Rahmat-Samii and Jensen[6], that was part of the IEEE Antennas and Propagation Symposium in Montreal in July, 1997. The course provided an overview of techniques for computational modeling of antennas and dielectric structures. Modeling of the human head was discussed. Cellular telephone handsets and their antennas were extensively examined, including new innovative antenna designs. The changes in the antenna patterns and input impedance due to the head were studied, mainly by examining data computed using the finite-difference time-domain(FDTD) method[7,8,9].

1.2 Review of Previous Work

The major objective is the study of the near fields and of the far fields of the radio handset. The work of this project can be divided into the computational segment on the one hand and the measurement segment on the other. In each case, finding the near field and finding the far field present somewhat different challenges.

1.2.1 Computation of the Far Fields

Ref. [2] proposed the study of a portable radio handset very similar to that shown in Fig. 1.1[10]. In Ref. [2] an FDTD code designed for plane-wave scattering was modified to solve antenna problems and to create maps of the near field, and was called FDTDANT. The program uses the Liao second-order absorbing boundary condition[11,12]. Ref. [2] used a time-domain near-zone to far-zone transformation to find the radiated fields of the handset in the FDTD computation, which proved very hungry for both computer memory and computational time. Hence Ref. [2] recommended that a frequency-domain near-zone to far-zone transformation be added to FDTDANT.

In Ref. [2] the computations with the FDTDANT code for the far field of the handset are validated against computations by a completely different method. A wire-grid model of the handset is solved with the Numerical Electromagnetics Code(NEC)[13,14,15,16] to obtain the far fields of the handset. The two computations

are compared on the basis of equal radiated power. The far fields E_θ and E_ϕ of the handset are computed over the surface of the radiation sphere, and then the power flow density is integrated over the sphere to find the radiated power. Both the FDTD computation and the NEC computation in Ref. [2] are scaled to 700 mW radiated power. Very good agreement between the FDTD and the NEC computation is shown in Ref. [2]. The study is repeated in this report as a validation of the far fields of the handset computed with FDTD using the “perfectly-matched layer” absorbing boundary condition[17,18,19].

Ref. [3] examines the far fields of the handset in free space with the antenna oriented vertically. Three different antennas are compared: the quarter-wave monopole; the half-wave monopole fed at the base; and the half-wave monopole fed at the center. The fields of each antenna are reported over the whole radiation sphere. It was found that the quarter-wave monopole and the half-wave center-fed monopole radiate very similar fields.

Ref. [4] presented a new version of the FDTDANT code that implements the near-to-far zone transformation in the sinusoidal steady state. The new FDTDANT code was run to compute the principal plane patterns for the portable radio handset and the results compared with the wire-grid computation as a validation of the new code. Also, the commercial FDTD code called XFDTD[20] was used to solve the same problem and finds identical results to the FDTDANT code. The near-to-far zone transformation is used extensively in the present report.

Ref. [3] used wire-grid modeling to study the far fields of the handset operated over a perfectly-conducting ground plane. The handset patterns for the handset oriented vertically, and also tilted at 30 degrees to the vertical, were examined. Also, the patterns were computed with the three antennas discussed above.

1.2.2 Computation of the Near Fields

In Ref. [2], the near field component E_z of the portable radio handset was computed by FDTD in planes close to the surfaces of the handset. The fields were computed in the same planes using the wire-grid model of the handset, and compared with the FDTD result, with excellent agreement. The field strengths were compared on the basis of equal radiated power in Ref. [2]. It was found that the near field is very strong near the tip of the antenna, near the base of the antenna at the top of the handset case, and near the bottom of the handset case.

Ref. [3] proposed simplified models of the head for study. The box model of the head or “box head” consists of a thin-walled plexiglas box filled with “brain liquid”, which is a mixture of deionized water, sugar and salt[21] having the electrical properties of brain matter at 850 MHz. The box geometry can be represented quite accurately with FDTD cells. The “sphere head” is a thin-walled plexiglas sphere, also filled with brain liquid. The sphere geometry is less well represented in FDTD because the curved surface of the sphere must be modeled with a “staircase” of cubical FDTD cells.

Ref. [3] reported extensive computations of the near fields of the handset, the handset and the box head, and the handset and the sphere head. In each case contour maps of E_z were made in xz planes adjacent to the handset, yz planes in front of the head,

and xz planes on the opposite side of the head from the handset. The fields were graphed for a 1 volt sinusoidal generator applied at the base of the antenna. Ref. [3] contains extensive comparisons with measured fields, discussed below.

Ref. [4] revisited the problem of computing maps of the near field with FDTDANT, and upgraded the software setup of Ref. [3]. The objective is to compare computations and measurements in planes at the same location in three-dimensional space, and normalized to the same RMS field strength over a reference plane. For the computation, field maps are computed at planes of cell faces in the FDTD model; an interpolation step is required to find the field strength at the location of the measurement plane, generally between two planes of cell faces. Scaling of the measured and computed fields to the same level is done in Refs. [3] and [4] based on the RMS field strength over one of the near field planes. The measured near fields are scaled to the same RMS level as the computed fields. The software tools to perform these steps were upgraded, to prepare for new measurements with an improved probe and the battery-operated handset.

1.2.3 Measurement of the Near Fields

Ref. [3] reports extensive but preliminary measurements of the near fields of the handset alone, the handset and box head, and the handset and sphere head. The measured vertical component of the field was compared with the computation in each case. There was generally good correspondence between the measured and the computed near fields, but there were also some significant differences, as follows.

This set of measurements is regarded as preliminary because compromises were made in the measurement setup that reduce the reliability of the measured data. The handset was fed from an external oscillator with a cable. This led to a distortion of the near field that was clearly seen in the contour maps, especially in the case of the box head. It was recommended that future measurements use a handset with a battery-operated oscillator. A new handset has been built as described below.

Also, the probe used in Ref. [3] was intended for wideband measurements in an EMC context, not for point measurements of the near field. The probe tended to average the fields over a region of significant size, leading to rounded peaks compared to the computation. It was recommended that a more suitable probe be purchased. Consequently, a three-axis probe specifically made for point measurement of the electric field strength was purchased from Schmid and Partner Engineering AG[22,23], and will be used for new measurements of the near field.

1.2.4 Measurement of the Far Fields

Ref. [3] recommended that the far fields be measured over the full radiation sphere, so that the power flow through the radiation sphere could be used to find the radiated power. Then computations and measurements could be compared on the basis of equal radiated power. Ref. [4] described an initial attempt to measure the far fields over the full radiation sphere. The measurement setup included metallic gears and shafts located quite close to the handset. The handset far fields were significantly affected. Also, the geometry of the measurement setup leads to a poor correspondence between the measured "horizontal" and "vertical" components of the field, and the desired E_θ and E_ϕ .

components in spherical coordinates. To find the spherical components, both the magnitude and the *phase* of the horizontal and vertical components must be measured.

This report presents a measurement of the far field principal plane patterns of the handset and shows excellent agreement with the computations. The far fields of the handset and box head, and of the handset and sphere head are measured, and are in good agreement with the computations. Such agreement requires a good knowledge of the permittivity and conductivity of the brain-equivalent liquid used to fill the head models.

1.2.5 Measurement of the Brain-Liquid Parameters

The head models in Ref. [3] were filled with a mixture of salt, sugar and distilled water according to the formula given in Ref. [21]. However, there was no way to verify that the permittivity and conductivity so obtained were actually the desired values of $\epsilon_r=41$ and $\sigma=1.3$ S/m. It was noted later that de-ionized water should be used rather than distilled water, to have good control over the conductivity. The computations in Ref. [3] used the intended values of $\epsilon_r=41$ and $\sigma=1.3$ S/m rather than the actual values of the mixture, which were unknown. Hence some of the differences between the measurements and computations of the near field may be due to erroneous electrical parameters in the computer model. This is especially true for the field strengths on the far side of the head from the radio handset, which agreed less well with the measurements than elsewhere.

Ref. [4] described an attempt to measure the electrical parameters of the brain liquid mixture using a probe of the type described in Ref. [24]. Errors were found in the equations in Ref. [6]. The conductivity and permittivity values extracted from the initial measurements described in Ref. [4] do not correspond well to the expected values. The results are critically dependent on the measurement of reflection coefficients very near unity.

A probe and measurement system commercially available from Hewlett-Packard(HP)[25] was purchased and used at CRC to measure the electrical parameters of the brain liquid mixture. The HP system includes analysis software. Measured values of permittivity and conductivity with this system are close to those expected using the recipe for brain liquid given in Ref. [21]. The values of the electrical parameters of the brain liquid used in this report were obtained by measurement with the HP probe system.

1.2.6 Creation of Cell Models of Handsets and Heads

Ref. [4] deals with the problem of creating cell models efficiently for the handset and box head or the handset and sphere head. It is intended that the cell model be the best approximation to the true geometry that is possible using solid cubical cells of a given size. In Ref. [3], cell models were hand crafted, which is tedious and error-prone. Ref. [4] describes a program called MKPHONE, which allows good models to be created rapidly and automatically, given the relative position of the handset and the box head or sphere head. In the present work, the MKPHONE function has been incorporated into a program called EDITCEL, which allows the user to examine and modify the cell model via a mouse-driven user interface.

1.2.7 Anatomical Model of the Head

To study the radiation patterns and near fields of a handset near a head, a realistic computer model of a human head is required, based on anatomical data. In Ref. [2], sections of a human head made at approximately 1 cm spacing were "digitized" onto a grid of 3.3 mm cells. The result is a set of 28 computer files each containing a map of one section, with the material of each 3.3 mm cell identified as one of 30 different tissues. The cross-sections were used to assemble a cell model of the head for computation. However, the cell size of this model proved to be too coarse for the model to be useful at 850 MHz. The present report uses this anatomical data set to create a new cell model with a 2.2 mm cell size. However, the roughly 1 cm spacing of the anatomical cross-sections is too large to create a precise cell model using 2.2 mm cells.

1.2.8 Summary

The work in this project to-date has examined the near fields and far fields of the simple portable radio of Fig. 1.1. The radio has been oriented with the antenna vertical. The far fields of the handset in free space have been computed by FDTD and by wire-grid modeling. Three types of antennas on the handset have been studied by computation. The handset patterns over a highly-conducting ground plane have been examined.

The vertical component of the near field of the handset in free space, and of the handset near the box head and near the sphere head have been computed and measured. The field was studied adjacent to the handset, in front of the head, and on the opposite side of the head from the handset.

1.3 The Portable Radio Handset

The handset used for the present study is an aluminum box of approximately the size and proportions of a cellular telephone in 1994, as shown in Fig. 1.1. The handset has a quarter-wave monopole on the top near one corner. For the present work, a new measurement model of the handset was made[26], that is similar but not identical to that used in previous work[3,4]. The new handset includes an internal, battery-operated oscillator at 850 MHz, and so does not have an external feed cable used in previous measurements[3]. The batteries can operate the oscillator for about 1 hour. The oscillator delivers about 100 mW at 850 MHz. Fig. 1.2 shows the dimensions of the new handset[26]. The previous case measured 5.30 by 1.76 by 16.76 cm; the new case measures 5.35 by 1.74 by 16.77 cm. The previous monopole was 8.80 cm in length; the new is 8.82 cm long. Although these are slight differences, they were taken into account in the work reported here.

1.4 Orientation of the Handset Relative to the Head

In this report the operator of the portable radio faces in the $+x$ direction, and holds the radio set in the right hand, with the antenna towards the rear of the handset. This is a change in the orientation compared to previous work, where the handset was held in the operator's left hand. Fig. 1.3 shows the orientation of the portable radio handset relative to the xyz coordinate axes. The antenna is positioned along the z -axis or "vertical" axis, with the base of the antenna at the origin, and the antenna on the $-x$ side of the handset

case. When the handset is operated near a model of the head it is held in the operator's right hand and so the head must be positioned in the +y half space in the xyz coordinate system, facing in the +x direction.

1.5 Issues Studied in this Report

In previous work, the computations of the handset radiation patterns with FDTD had been validated by comparison with computations using a wire-grid model. The wire-grid modeling method is unable to represent dielectric objects such as the head. This report presents a validation of the FDTD computations against measured far fields. The far fields are examined for the handset in isolation, and for the handset near the box head, and near the sphere head.

The simplified models of the human head that have been used to-date in this project have been intended to provide a good validation of the FDTD computations. The box head and the sphere head are both relatively simple to represent in terms of FDTD cubical cells. The geometrical errors of the cell model compared to the true geometry are clear. The box geometry can be represented with excellent fidelity in terms of cubes of dielectric, whereas the sphere's curved surface must be approximated with a "staircase" of cells. One objective of the present project is to verify, by comparison with measurements, that the far fields of the handset and sphere, computed with FDTD for the staircased approximation of the sphere, are in good agreement with the measured far fields. It may be possible to judge the modeling error introduced by "staircasing" by comparing the agreement of the computations for the box head and for the sphere head with the measurements.

More realistic head representations are part of the current project. One model is the "anatomical" head, derived from anatomical cross-sections of a human head. Another is the "head phantom", which is a model of a simplified but realistic head to be used in measurements of the far fields and near fields of a handset operating near a head. FDTD requires that the curved surfaces of a realistic model of a human head be "staircased", like the sphere. The staircasing approximation is expected to introduce the same degree of modeling error in the fields of the handset and realistic head, as in the fields of the handset and sphere head.

1.6 Overview of the Work

The work in this Final Report divides into several topic areas.

The FDTD code that is used for the computations was upgraded by adding the "perfectly-matched layer" absorbing boundary condition[17], and the new code was used in all the computations. Ref. [27], reproduced as Appendix 1, compares the performance of the PML absorbing boundary with the Liao second-order absorbing boundary used in previous work[11,12], and concludes that the PML should be used for day to day computations.

A new measurement model of the handset, Fig. 1.1, was built, with a self-contained, battery-operated RF source[26]. This eliminates the feed cable that was used in the measurements in previous reports[3]. This report contains extensive comparisons with the principal plane radiation patterns of the handset in isolation, and of the handset with the box head and with the sphere head. The measurements were done by the

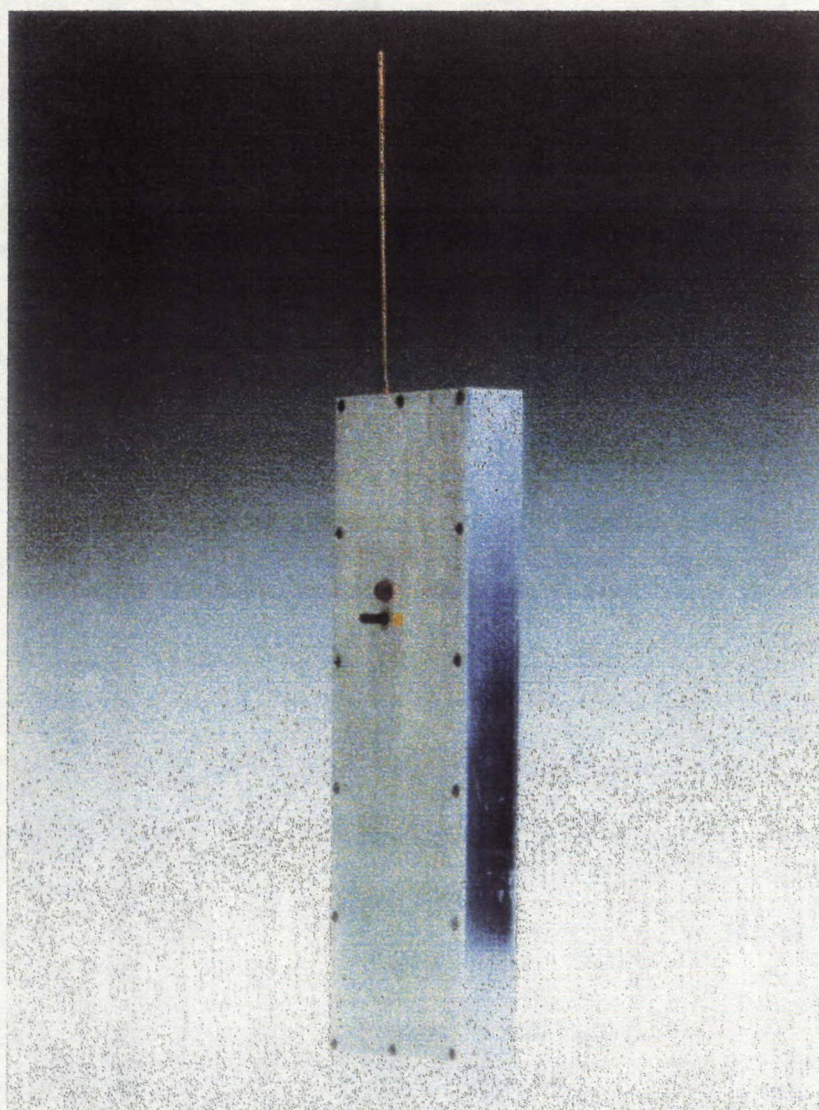
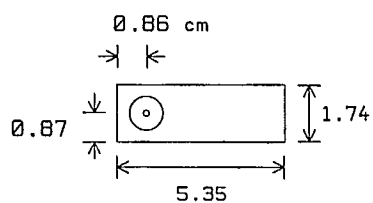
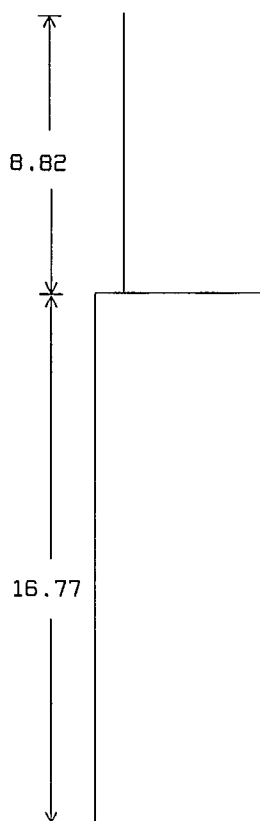


Fig. 1.1 The portable radio handset used in this study[10].

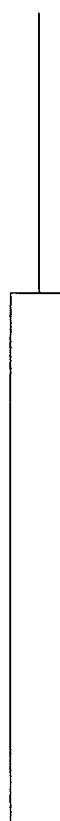


HANDDIM.LAB

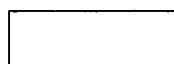
(a) top



(b) front



(c) right side



(d) bottom

Fig. 1.2 The dimensions of the portable radio handset.

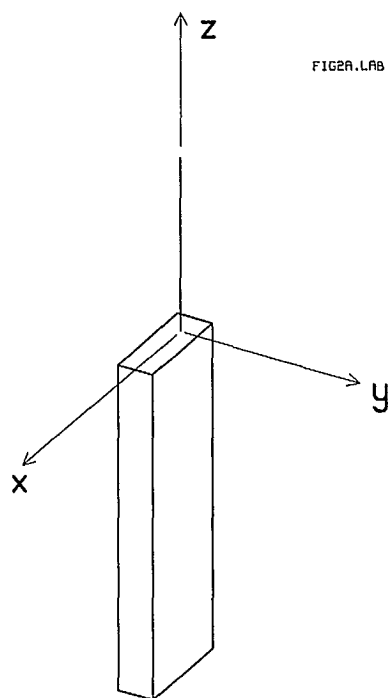


Fig. 1.3 The portable radio handset in the standard orientation in the coordinate system.

Chapter 2

Radiation Patterns of the Vertical Handset

This chapter examines the radiation patterns of the handset in free space with the antenna oriented vertically, as shown in Fig. 1.1. The patterns of the handset computed by FDTD and by wire-grid modelling and are compared. The sensitivity of the patterns to the cell size is investigated.

2.1 FDTD Model of the Handset

Previous computations using a cell model of the handset were done with a cell size of 8.82 mm[3,4]. The handset case was modelled with 6 by 2 by 19 cells, and the antenna 10 cells in length. In this chapter, cell sizes of 8.82, 4.41 and 2.205 mm are studied.

With 4.41 mm cells, the handset is modelled with 12 by 4 by 38 cells, and the antenna with 20 cells. The case dimensions are thus represented as 5.292 by 1.764 by 16.758 cm, slightly different from those of Fig. 1.1 of 5.35 by 1.74 by 16.77 cm. The antenna is 8.82 cm in length in the cell model, in agreement with Fig. 1.1. The maximum frequency at which the cells in this model are smaller than one-tenth of the wavelength is 6800 MHz, very much larger than our operating frequency of 850 MHz.

With a cell size of 2.205 mm, the handset is modelled with 24 by 8 by 76 cells and the antenna by 40 cell edges. The case is thus approximated as 5.292 by 1.764 by 16.758 cm as above, and the antenna as 8.82 cm in length. The bandwidth of the cell model with no dielectrics other than free space is 13,605 GHz.

The following section discusses the absorbing boundary condition used to terminate the cell space, which differs from that reported in previous work. Then a reference level for comparing radiation patterns is defined and the method of its computation is discussed. Then the radiation patterns of the handset are presented.

2.2 The Perfectly-Matched Layer Absorbing Boundary Condition

The “finite difference time domain”(FDTD) method divides space into “cells” of size Δx by Δy by Δz . A volume of space of N_x by N_y by N_z cells is solved and must contain the handset model and the head model, surrounded by a layer of N_w cells of free space, called “whitespace” in this report. In FDTD time is divided into steps of length Δt , and within the cell space the three vector components of the electric field and the three components of the magnetic field associated with each cell are found at each time step using the Yee FDTD algorithm[7]. With a sinusoidal generator that gradually turns on, the FDTD algorithm is run for N_{steps} time steps, or a total time of $N_{steps}\Delta t$, sufficiently long for the field in all the cells of the cell space to reach the sinusoidal

steady state. Some details of the FDTD method have been presented in a previous report[2] and a full description can be found in textbooks such as [8] or [9].

The outer boundary of the cell space is treated differently from the interior. The electric field components on the outer boundary are updated at each time step such that the boundary absorbs all energy incident upon it. The electric fields on the outer surfaces of the cell space are updated with an "absorbing boundary condition"(ABC) algorithm such that, ideally, they absorb all the energy incident upon them. All ABC formulations are somewhat imperfect, having non-zero reflection. Early FDTD codes used a first-order ABC, leading to high reflections[9]. FDTD became practical for routine computation with the advent of the second-order ABC due to Mur[30] having a reflection coefficient of the order of 20 dB or better, dependent upon the angle of incidence. The Liao second-order ABC[11,12] offers lower reflection coefficients than does the Mur formulation. Recently a new absorbing boundary formulation called the "perfectly-matched layer"(PML) absorbing boundary condition[17,18,19] has achieved a substantial reduction in reflections compared to the Liao formulation.

Previous work in this project [1,2,3,4] has used the Liao ABC formulation in the FDTDANT program. The FDTD cell model surfaces need to be separated from the outer boundary by a sufficient number of cells of whitespace that interactions with the rather imperfect absorbing boundary are minimized. Typically 15 to 20 cells of whitespace are needed with the Liao formulation. Thus with a handset model of 12 by 4 by 48 cells, including the antenna, and 15 cells of whitespace, a space size of 42 by 34 by 78 cells or 111,384 cells is required. The computation time for finding the fields within the cell space rises linearly with the number of cells and so reducing the cell count reduces the computation time.

The FDTD model was analyzed in this report using a new version of the FDTDANT program[3,4] called FDTD PML that incorporates the "perfectly-matched layer" absorbing boundary condition[17]. The PML allows the user to control the reflection from the boundary, at the cost of increased storage requirements and longer CPU times for the same FDTD space size. The PML formulation uses special equations to update the field components in a layer of N_{PML} cells coating the inner surface of the cell space. Thus the space size is now the size of the handset and head model, plus twice the whitespace size plus twice the PML thickness. Since the PML offers lower reflections than does the Liao boundary, far fewer whitespace cells are needed to separate the surfaces of the handset and antenna from the inner surface of the PML to reduce interactions between the model and the absorbing boundary. Typically four cells of whitespace are sufficient, with a six cell PML. Thus the space size required for the handset problem would be 32 by 24 by 68 cells or 52,224 cells, less than half of that needed using the Liao boundary. But the CPU time required to update the cells within the absorbing boundary is much larger than that required for the cells within the cell space so it is not clear that a significant advantage is achieved.

Appendix 1[27] investigates the tradeoff of computation time and memory requirements using the Liao boundary and using the PML, for two scattering problems, namely a conducting rod, and a dielectric cube. The measured radar cross-section is compared with that computed with FDTD using the Liao ABC and the PML, for various thicknesses of whitespace, and for various thicknesses of the PML layer. The memory

and letting θ range from zero to 360 degrees. Fig. 2.3 shows that the $\phi = 0$ elevation pattern has broad lobes in E_θ pointing downward. At $\theta = 116$ degrees the field strength is 4.29 dB, and at 232 degrees the field strength is 3.50 dB. There are smaller lobes pointing upward, at 33 degrees with a field strength of -6.52 dB, and 315 degrees at -3.75 dB. There is a sharp minimum at 61 degrees with a field strength of -22.58 dB. Because of the symmetry of the handset about the xz plane in Fig. 1.2 we do not expect any cross-polarized field. However, the FDTD computation is not exact. The cross-polarized field, E_ϕ , has a roughly circular pattern with a maximum level of -66.5 dB, below the range of the dB scale in Fig. 2.3.

The elevation pattern for $\phi = 90$ degrees is symmetric about the vertical axis. It also has broad lobes directed downward, at 120 and 240 degrees, of field strength 3.98 dB. There are smaller lobes directed upward at 40 and 320 degrees of field strength -6.19 dB. The cross-polarized field, E_ϕ has a level of about -10.7 dB and is almost circular in its radiation pattern.

The radiation patterns of Fig. 2.3 are very close to those of Ref. [2], except for the 180 degree change in the orientation of the handset.

2.5 Comparison of the Principal Plane Patterns by NEC and by FDTD

Two "validations" of the FDTD computations will be presented in this report. Chapter 3 will compare the radiation patterns computed with FDTD with measured patterns. This section compares the radiation patterns of the handset in free space computed by wire-grid modeling with those computed by FDTD.

The wire-grid modeling method was reviewed in detail in Ref. [2]. The handset patterns were computed by wire-grid modeling and by FDTD and compared with good agreement. A new wire-grid model was prepared for the present work. The new model represents the dimensions of the new handset, Fig. 1.1, slightly different from the old one. Also, in this report the handset's antenna is located on the $-x$ side of the case, Fig. 1.2, and so the handset is rotated 180 degrees about the z -axis compared to previous work[1,2,3,4]. The patterns of the new wire-grid model of the handset were computed using version 4[16] of the Numerical Electromagnetics Code"(NEC)[13,14,15].

Fig. 2.4 compares the handset principal plane patterns computed with FDTD/PML for the 12 by 4 by 38 cell model with 4.41 mm cells with the patterns computed with NEC. The agreement is very good, with only small differences between the two sets of data. In E_θ in the azimuth pattern, in the forward or $\phi = 0$ direction the field strength is 1.23 dB in the wire-grid model and 1.18 dB in the FDTD computation. In the backward or $\phi = 180$ direction, the wire-grid model's field strength is -5.37 dB, and the FDTD model, -5.47 dB. In the cross-polarization or E_ϕ component, the maximum field strength is -11.01 dB in the NEC calculation and -11.20 dB in the FDTD computation.

In the $\phi = 0$ pattern, the lobe at 31 degrees has field strength -6.75 dB in the wire-grid computation and -6.52 dB in the FDTD computation. The lobe at 115 degrees has field strength 4.29 dB in both computations. The lobe at 232 degrees has field 3.50 dB in both computations. The sharp, narrow minimum falls at 60 degrees in the NEC computation, with field strength -23.33 dB, and at 61 degrees in the FDTD computation

with a field of -22.58 dB. The cross-polarized field should be zero in this pattern, due to symmetry about the xz plane. The cross-polarization is lower than -40 dB hence does not appear in Fig. 2.4. Fig. 2.5 shows the $\phi = 0$ pattern on a scale from about -166 to $+6$ dB, and shows that the E_ϕ component has a maximum value of -149 dB in the wire-grid computation, which is essentially defines the noise level the wire-grid code. The FDTD computation shows a cross-polarized field strength of -66.5 dB, which we will take as the noise level for the FDTD code.

The $\phi = 90$ pattern is very similar in the NEC and the FDTD computation. The lobe at 39 degrees is -6.47 dB in the wire-grid computation and -6.19 dB in the FDTD calculation. The wire-grid computation has a minimum at 67 degrees of -16.56 dB field strength, corresponding to the minimum at 68 degrees and -17.29 dB in the FDTD model. The lobe at 120 degrees is 3.97 dB in both computations. The cross-polarized field agrees well between the two computations. The maximum value is -10.54 dB in the wire-grid computation and -10.70 in the FDTD calculation.

Ref. [2] reported a comparison of the principal plane patterns of a wire-grid model of the handset with an FDTD model using a cell size of 8.82 mm or 6 by 2 by 19 cells for the case and 10 cells for the antenna. The agreement was good; generally comparable to that reported above. But the minima in the $\phi = 0$ pattern at 75 degrees was considerably too deep in the FDTD computation, and the minima in the azimuth pattern at 70 and 290 degrees were much deeper than in the wire-grid computation in Ref. [2]. Evidently, reducing the cell size to 4.41 mm improves the agreement with NEC. It is tempting to conclude that a further reduction in cell size would lead to further improvement in the agreement. The patterns computed with FDTD using three different cell sizes are compared in the following.

2.6 Radiation Pattern Dependence on the Cell Size

In the FDTD method the cell size must be smaller than one-tenth wavelength at the frequency of operation. At 850 MHz, the wavelength is 35.29 cm and so cells of 3.529 cm are the largest that can be used. In previous reports[1,2,3,4] the cell size was 8.82 mm, or 4 times smaller than the minimum. In the foregoing, the handset was modelled with 4.41 mm cells, with good agreement with the measurement. This section compares the radiation pattern for $\phi = 0$ with 8.82 mm cells, with 4.41 mm cells, and with 2.205 mm cells. Ideally we would like the radiation patterns of the handset to be independent of the cell size used in the FDTD model. If not independent of cell size, then at least we would like the field at any point to "converge" to a constant value as the cell size is decreased. It will be shown that the radiation patterns do change with cell size, particularly in the minima, but do not appear to "converge" as desired.

Fig. 2.6(a) shows the azimuth pattern with cell sizes 8.82, 4.41 and 2.205 mm. The radiation patterns for all three cell sizes are scaled to have the same radiated power, corresponding to an isotropic level of 0 dB. In the E_θ polarization, the field at zero degrees is 1.004 dB with 8.82 mm cells, 1.183 dB with 4.41 mm cells, and 1.274 dB with 2.205 mm cells. At 180 degrees, the field is -6.225 dB with 8.82 mm cells, -5.469 dB with 4.41 mm cells and -5.226 dB with 2.205 mm cells. In the cross-polarized field, E_ϕ ,

the field in the maximum at 90 degrees is -11.04 dB with 8.82 mm cells, -11.20 dB with 4.41 mm cells, and -11.14 dB with 2.205 mm cells.

Fig. 2.6(b) shows the elevation pattern for $\phi = 0$ degrees with 8.82, 4.41 and 2.205 mm cells. The large lobes in E_θ at 117 and 232 degrees are almost independent of the cell size. The smaller lobes at 32 and 313 degrees decrease systematically with the cell size. The minima change dramatically with cell size. With 8.82 mm cells there is a maximum at 33 degrees, -5.72 dB. With 4.41 mm cells, the maximum is at 32 degrees, -6.52 dB. With 2.205 mm cells, at 32 degrees, -6.74 dB. There is a maximum at 314 degrees, -3.36 dB with 8.82 mm cells, which is found at 314 degrees, -3.75 dB with 4.41 mm cells, and 315 degrees, -4.15 dB with 2.205 mm cells.

The minima in the pattern are quite sensitive to cell size. There is a minimum at 62 degrees, -18.18 dB with 8.82 mm cells, at 61 degrees, -21.58 dB with 4.41 mm cells and 60 degrees, -19.23 dB with 2.205 mm cells. There is a big change in the depth of the minimum with each change in cell size, but the changes in depth are not in the same direction stepping from 8.82 to 4.41 mm cells and stepping from 4.41 to 2.205 mm cells. There is a minimum at 281 degrees, -17.84 dB with 8.82 mm cells, at 282 degrees, -14.88 dB with 4.41 mm cells, and at 283 degrees, -16.44 dB with 2.205 mm cells. Again the direction of the change is different for the two steps in cell size.

Fig 2.6(c) shows the elevation pattern for $\phi = 90$ degrees. The maxima in E_θ at 120 and 240 degrees are little changed by changing the cell size. The smaller maxima near 40 and 320 degrees are greatly affected. The field with 8.82 mm cells has a maximum at 41 degrees of -5.536 dB, which changes to 40 degrees, -6.913 dB with 4.41 mm cells and 39 degrees, -6.609 dB with 2.205 mm cells. The minimum with 8.82 mm cells falls at 69 degrees, -20.48 dB, with 4.41 mm cells at 68 degrees, -17.29 dB and with 2.205 mm cells at 67 degrees, -19.91 dB. Thus the minima are particularly sensitive to cell size.

This section has demonstrated that the FDTD-computed radiation patterns are sensitive to the cell size. The major lobes in the radiation patterns do not change greatly with cell size. But the minima are particularly sensitive. Thus we should not expect to achieve good agreement between the minima in the computations and those in the measurement.

2.7 Conclusion

This chapter has presented the radiation patterns of the handset computed with FDTD, oriented vertically in the coordinate system. The vertical handset has a roughly circular azimuth pattern in the principal or E_θ polarization, with about 7 dB variation from maximum to minimum. The cross-polarized or E_ϕ component is a figure-eight pattern about 12 dB below the maximum value of E_θ . The elevation patterns have their major lobes directed towards the ground. The handset is not normally operated in a vertical orientation, and a later chapter of this report explores the handset patterns when the handset is tilted.

Good agreement was shown in this chapter between the radiation patterns computed with a 4.41 mm cell size and those computed with using a wire-grid model of the handset. However, it was found that the radiation patterns computed with FDTD

change when the cell size is changed. Although the main lobes are reasonably independent of cell size, the minor lobes and particularly the minima are sensitive to the cell size. Thus in comparing the computed patterns with the measured data in the following chapter, we should not expect precise agreement in the minima of the radiation patterns.

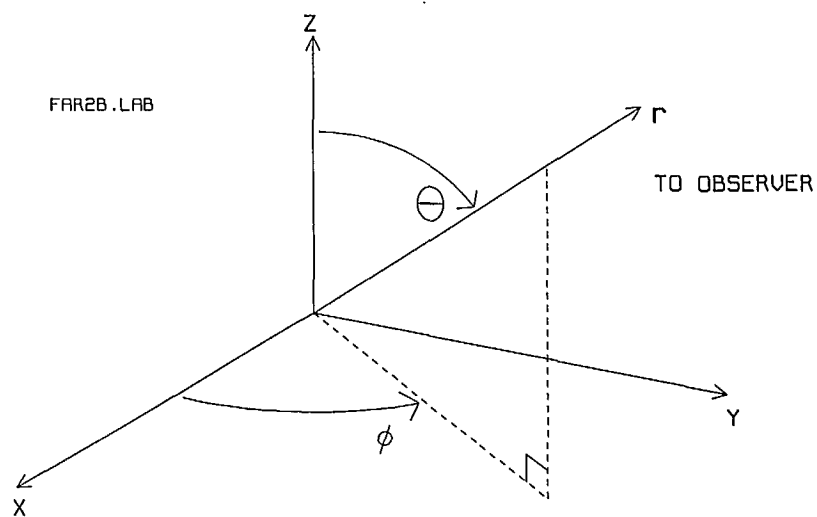


Fig. 2.1 Definition of the angles θ and ϕ in spherical coordinates.

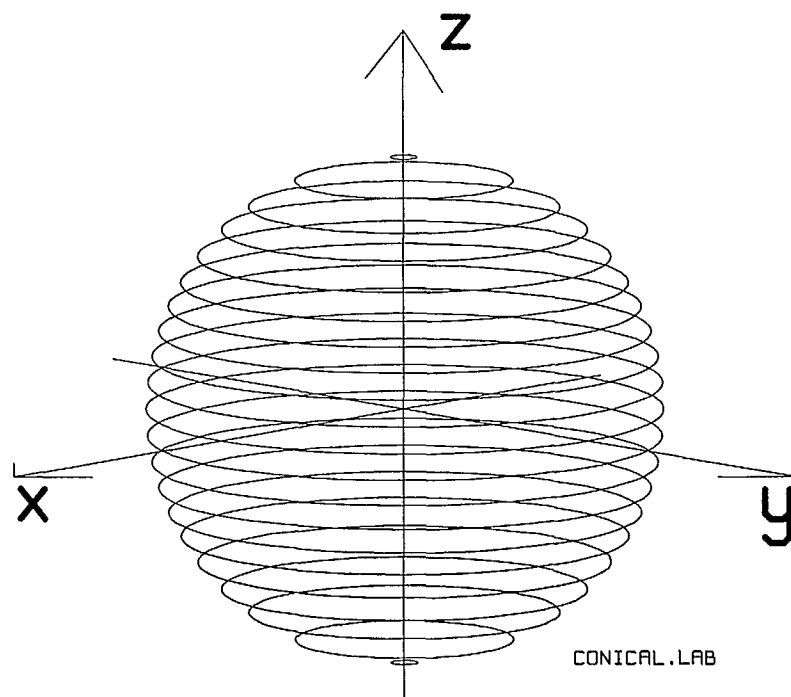


Fig. 2.2 The angles of the set of conical cut radiation patterns covering the surface of the radiation sphere.

Handset Alone
850 MHz
FDTD with the PHL

RADIATED FIELD
FREQUENCY = 850.00 MHz
DECIBEL SCALE
CONICAL CUT
 $\Theta = 90$

FOTO
—□— E-THETA
—○— E-PHI
— ISOTROPIC
LEVEL

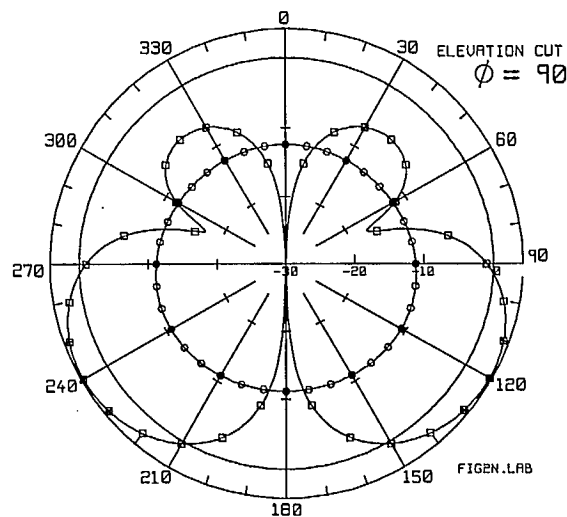
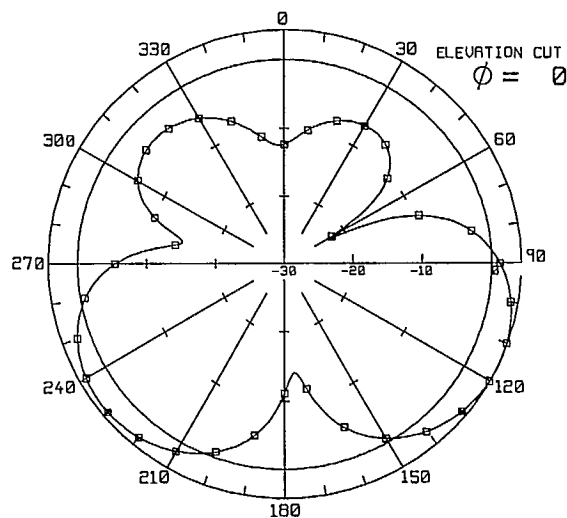
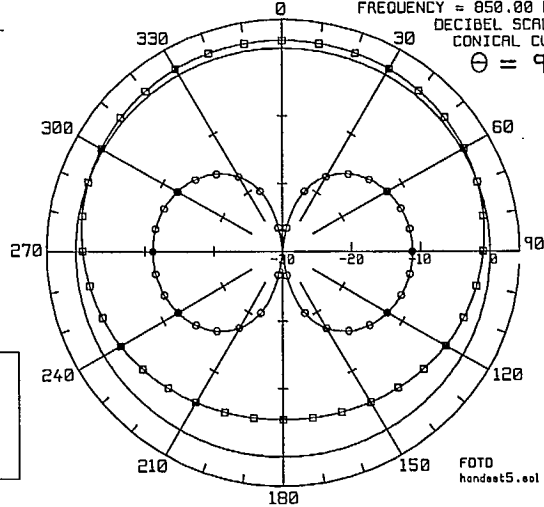
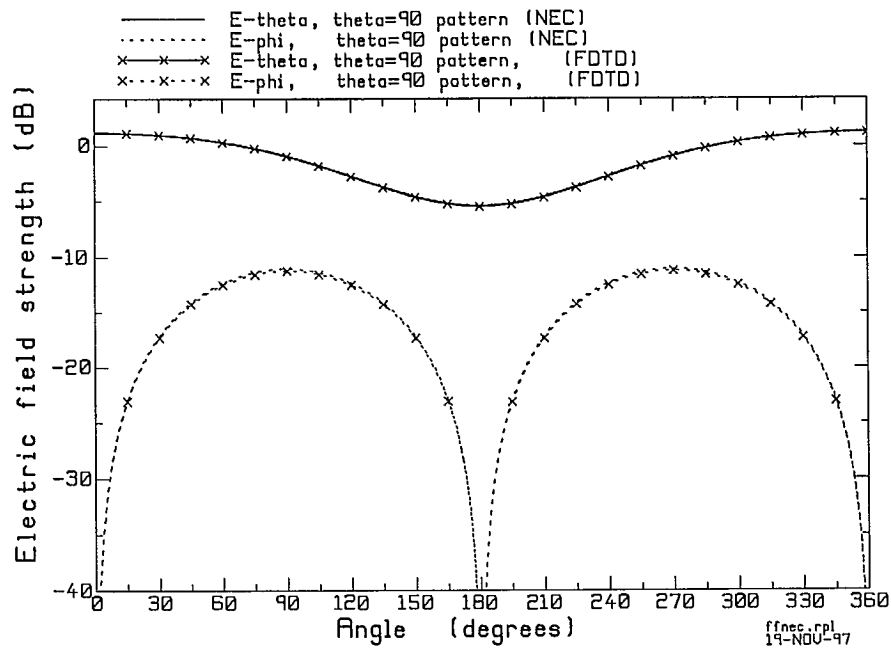


Fig. 2.3 The principal plane patterns of the radio handset computed with FDTD, using a cell size of 4.41 mm.



(a) Azimuth pattern.

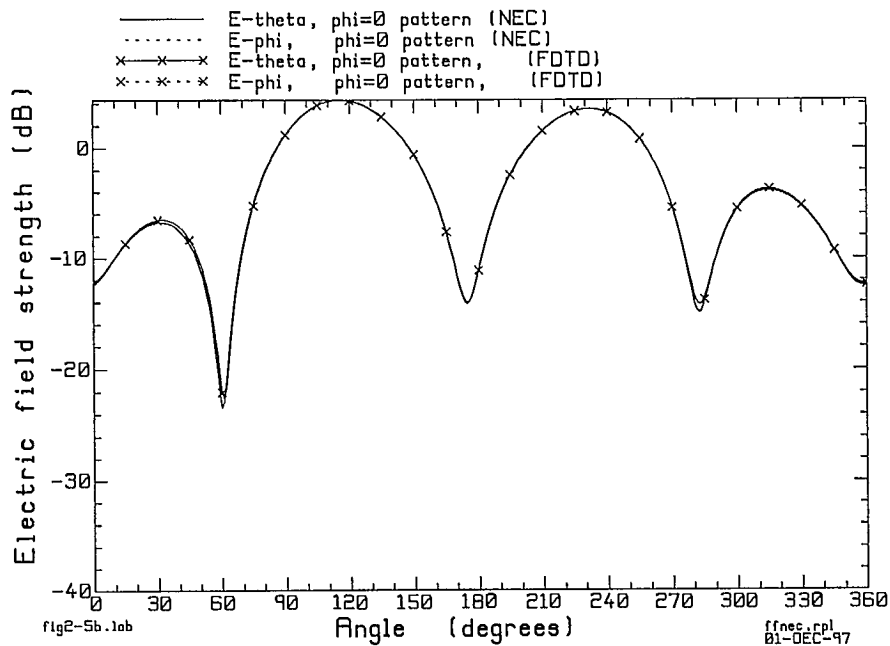
(b) Elevation pattern for $\phi = 0$ degrees.

Fig. 2.4 Comparison of the radiation patterns of the handset in free space computed with FDTD and computed with a wire-grid model using NEC.

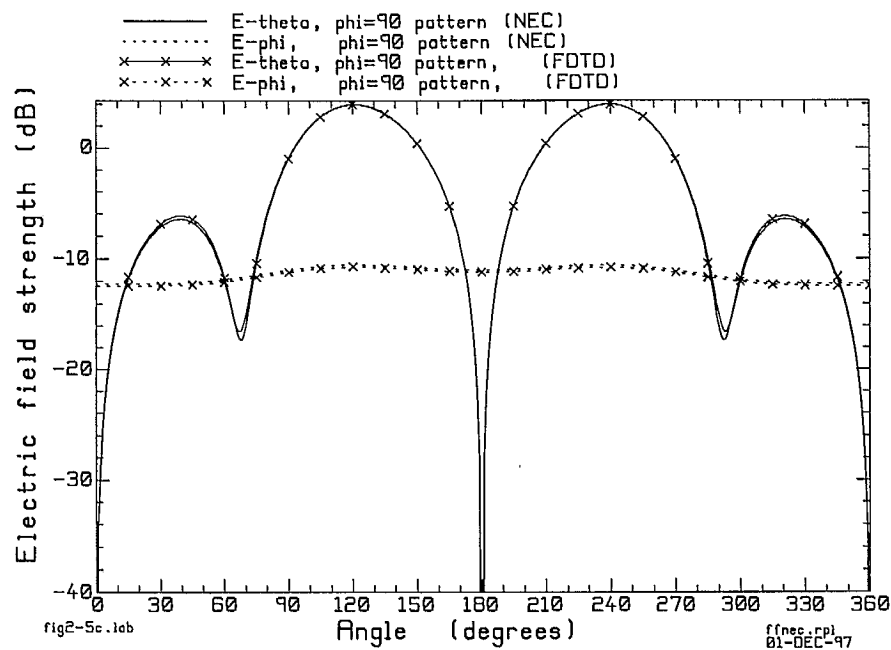
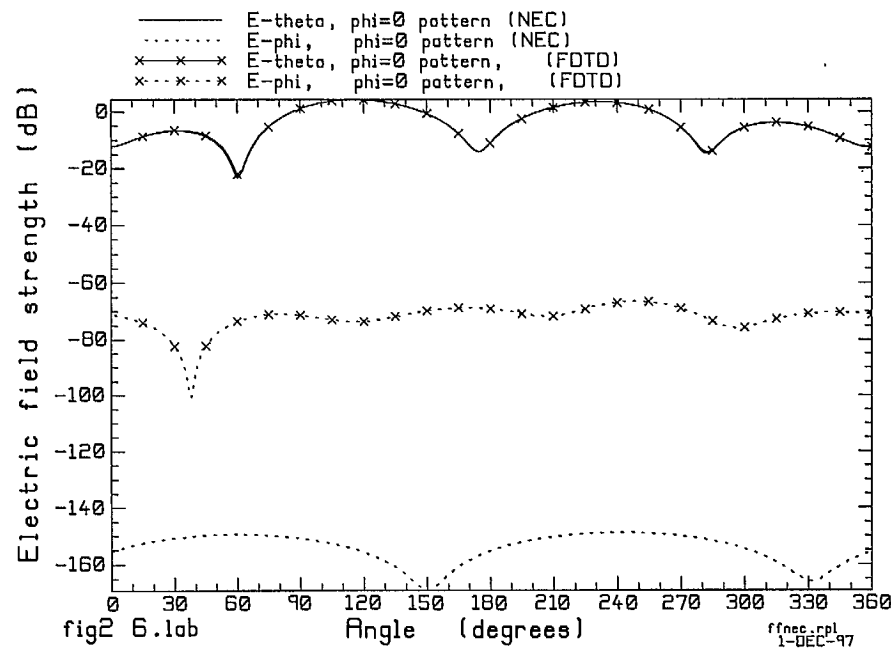
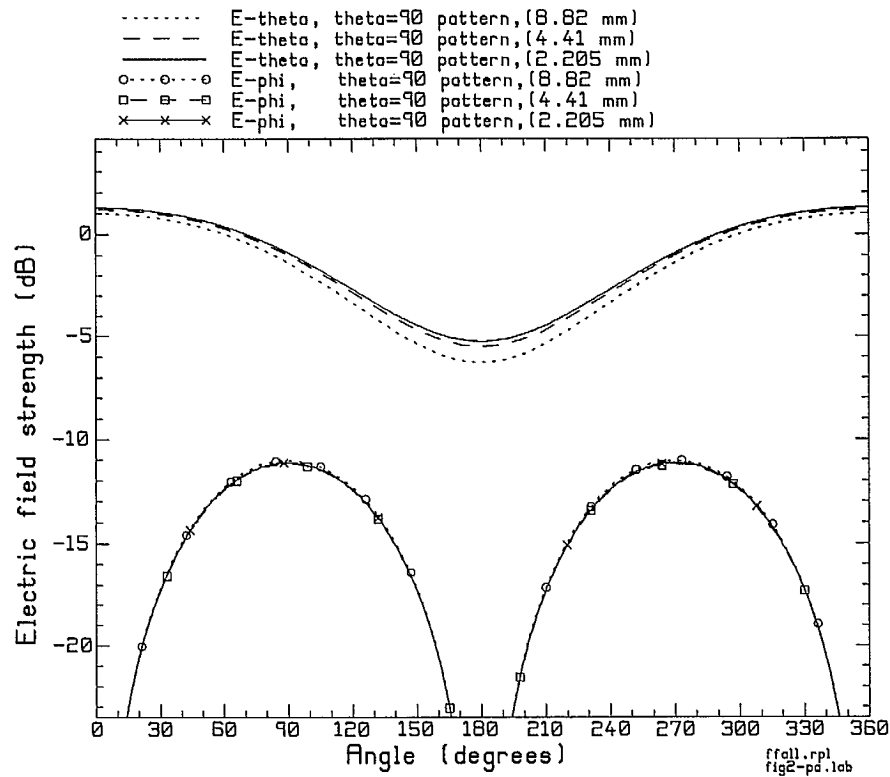
(c) Elevation pattern for $\phi = 90$ degrees.

Fig. 2.4 (continued) Comparison of the radiation patterns of the handset in free space computed with FDTD and computed with a wire-grid model using NEC.

Fig. 2.5 The elevation pattern for $\phi = 0$ showing the level of the cross-polarized field component.



(a) Azimuth pattern.

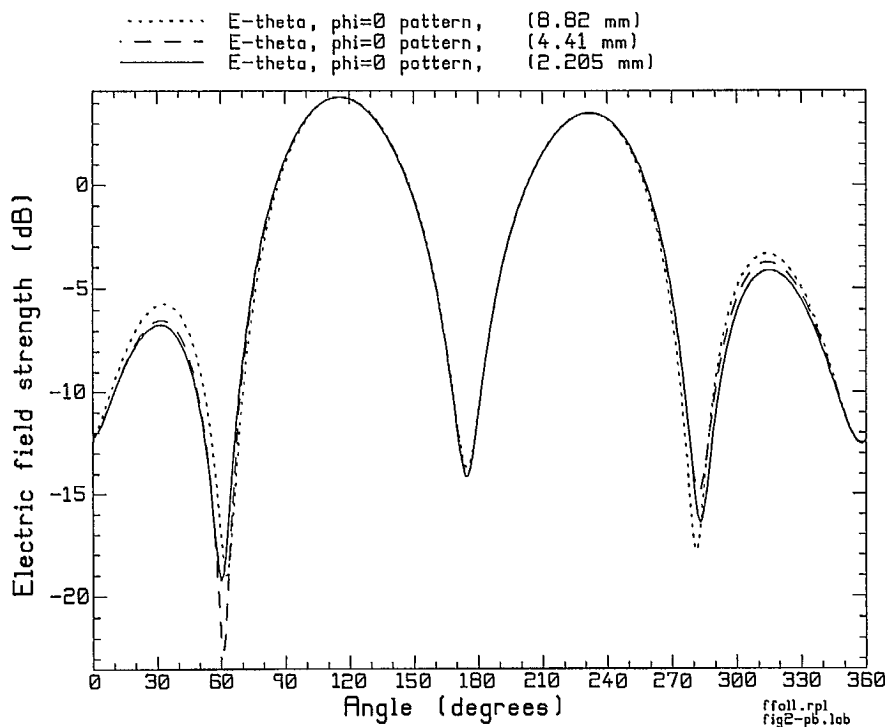
(b) Elevation pattern for $\phi = 0$ degrees.

Fig. 2.6 The FDTD-computed principal plane patterns with three different cell sizes.

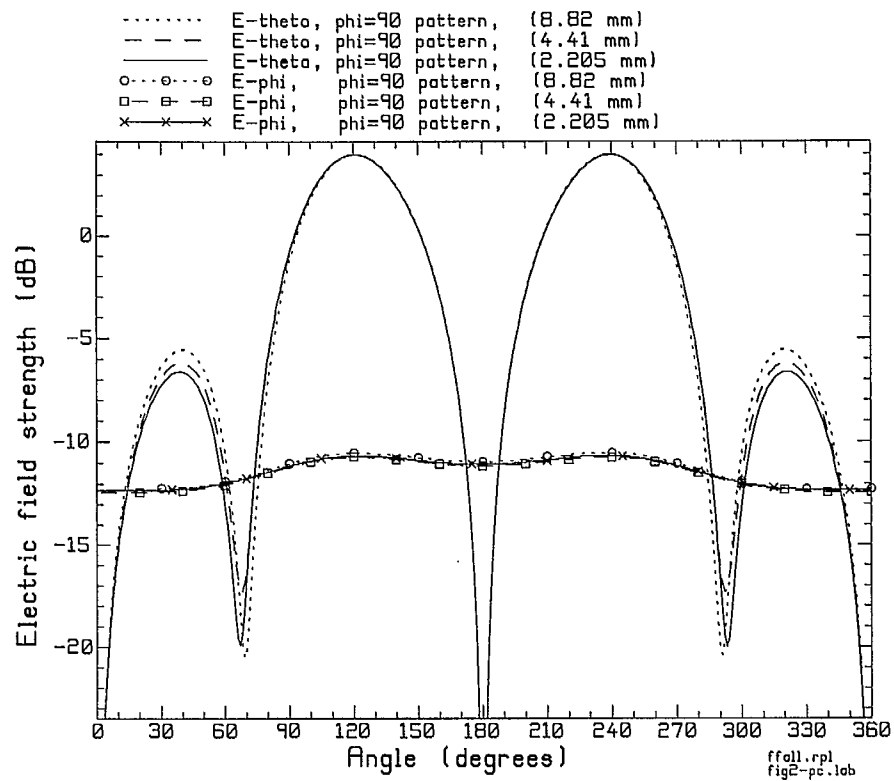
(c) Elevation pattern for $\phi = 90$ degrees.

Fig. 2.6 (continued) The FDTD-computed principal plane patterns with three different cell sizes.

Chapter 3

Measured Radiation Patterns of the Vertical Handset

This chapter presents the measurements of the radiation patterns of the handset in free space with the antenna oriented vertically. The anechoic chamber and instrumentation used at CRC[10] for the measurement are briefly described. Then the patterns of the handset computed by FDTD in the previous chapter are compared with measurements.

3.1 The Portable Radio Handset

The measured results reported in this chapter use a new portable radio handset that is similar but not identical to that used in previous work[3,4]. The new handset includes an internal, battery-operated oscillator and so does not have an external feed cable. Fig. 1.1 shows the dimensions of the new handset[26]. The previous case measured 5.30 by 1.76 by 16.76 cm; the new case measures 5.35 by 1.74 by 16.77 cm. The previous monopole was 8.80 cm in length; the new is 8.82 cm long.

In this report the operator of the portable radio faces in the $+x$ direction, and holds the radio set in the right hand, with the antenna towards the rear of the handset. Fig. 1.2 shows the portable radio handset relative to the xyz coordinate axes. The antenna is positioned along the z -axis or "vertical" axis, with the base of the antenna at the origin, and the antenna on the $-x$ side of the handset case. In later chapters, measured handset patterns including a head model are presented. In the presence of a head model, the head must be located in the $+y$ half space in the xyz coordinate system so that the handset is held in the operator's right hand.

3.2 The Measurement Setup

The radiation patterns of the handset presented in this report were measured at the David Florida Laboratory (DFL) under the supervision of CRC's Dr. Jasmin Roy[10]. The radiation patterns were measured in a 6x6x6 meter anechoic chamber, as shown in Fig. 3.1. One wall of the chamber is open to the outdoors and is sealed from weather with styrofoam. There is a rotator at the center of the chamber. The handset model is mounted atop a styrofoam column on the rotator, as shown in Fig. 3.2. The wall at right in Fig. 3.2 is the styrofoam wall. The handset contains a battery-operated oscillator at 850 MHz. An open-ended waveguide was mounted near the base of the rotator column, as in Fig. 3.3, to sample the field to provide a reference signal to phase-lock a network analyzer. The horizontal and vertical components of the field were measured by the dual-polarized ridged waveguide horn shown in Fig. 3.4, mounted about 330 cm from the handset in one wall of the chamber, as shown in Fig. 3.1. The position of the handset was aligned as accurately as possible using a laser beam as a reference. Simple styrofoam mounting jigs hold the handset securely during the measurement. Fig. 3.2 show the

handset held vertically for the measurement of the azimuth pattern. Fig. 3.5 shows the handset held with the broad face of the case in a horizontal plane, for the measurement of the xz plane or $\phi = 0$ degrees elevation pattern. Fig. 3.6 shows the handset held with the broad face in a vertical plane, for rotation in the yz plane, for measurement of the $\phi = 90$ degree elevation. These mounting jigs partially enclose the handset in styrofoam. In the computations the styrofoam has not been included.

Considerable care was taken to optimize the quality of the measured data. Unwanted reflections in the anechoic chamber were identified and reduced with absorber. However, the absorber in the chamber is designed for best performance above 1.5 GHz. The relatively short range from the handset to the horns incurs errors approaching one degree in the angle from the various parts of the handset case to the horn, compared to the true "far field" angle. These errors will primarily affect the measured patterns in the minima. The effect on the xz plane pattern is investigated with the NEC program in the next section.

The limitations of the absorber in the anechoic chamber and the short range from the handset to the measurement horn may account for some of the differences between the measured data and the computation.

3.3 Pattern Dependence on Range

The measurements of the radiation patterns are done with the horn at a range of 330 cm from the center of rotation of the handset. Is this far enough for a true "far field" measurement? The minimum distance is often taken to be

$$R > \frac{2D^2}{\lambda} \quad \dots(3.1)$$

where D^2 is the antenna aperture. Taking $D \approx 25.6$ cm, the largest dimension of the handset, at 850 MHz, the range must be greater than 37.1 cm., so by this criterion the distance to the horns of 330 cm is clearly far enough from the antenna. However, the minima in the pattern are sometimes formed by the cancellation of radiation from various parts of the antenna and handset. The depth of the minima are critically dependent on the relative phasing of the radiation arriving at the observer from various parts of the structure. The phasing is in turn dependent on the relative distance from the parts of the handset to the observer or measurement horn, and these relative distances change slightly with increasing range. This section uses the NEC model of the handset to compare the radiation patterns at the "near field" distance of 330 cm with those in the true "far field".

The wire-grid model of the handset was presented in the last chapter. It was shown that the radiation patterns of the wire-grid model solved with the NEC program are very similar to those of the FDTD model with 4.41 mm cells. The NEC program includes the ability to compute the fields at any distance from the handset, correctly accounting for the relative distances of various parts of the handset to the observer, and also for the near-field terms in computing the field of each part of the structure.

We can simulate the measurement setup in computation with the NEC program. Thus, the observer is put at a distance of 330 cm from the handset, and the near field is

calculated at one-degree increments on a circle in the xz plane. The NEC code returns the x , y , and z components of the electric field calculated using the actual distance from the various wires making up the wire-grid model of the handset to the observer. From the rectangular components, we can calculate the E_θ spherical field component. Fig. 3.7 compares the resulting near-field pattern at 330 cm with the true far-field $\phi = 0$ radiation pattern. The main lobes of the pattern are almost identical. The maximum in the far field pattern at 116 degrees, 4.29 dB is found in the near field pattern at 116 degrees, 4.37 dB, a small difference of 0.08 dB. The maximum in the far field pattern at 232 degrees, 3.49 dB falls at 231 degrees, 3.54 dB in the near field pattern, a very small difference. The minor lobes are more strongly affected. The maximum at 31 degrees, -6.75 dB in the far field falls at 32 degrees, -6.62 dB in the near field. The maximum at 315 degrees, -3.90 dB in the far field falls at 315 degrees, -4.18 dB in the near field, a difference of 0.28 dB.

The minima are very strongly affected by the closeness of the observer. The minimum at 60 degrees, -23.33 dB in the far field falls at 61 degrees, -19.43 dB in the near field, a difference of 3.9 dB. The minimum at 283 degrees, -14.21 dB in the far field falls at 282 degrees, -15.46 dB in the near field, a difference of 1.25 dB.

The conclusion from Fig. 3.7 is that we should be wary of comparing the depth of the minima in the measurement with that in the computation when the measurement horn is only 330 cm from the handset. Differences of as much as 3.9 dB were found. But the main lobes in the pattern are reliable to within about 0.1 dB, and the minor lobes to 0.3 dB.

3.4 Scaling the Measurements

The radiated power from the actual handset is not known, hence the isotropic level of the measurement cannot be evaluated. Consequently, a method of scaling the measured field strengths to approximately the same radiated power as the computed fields is required, and is presented in this section.

The three principal plane patterns are measured. To scale the measured field strengths to approximately the same level as the computed fields, the RMS field strength will be estimated using the data from all three principal plane patterns. Given field strength data $E_\theta(\phi)$ and $E_\phi(\phi)$ for one radiation pattern, we can calculate the RMS field strength as

$$E = \sqrt{\frac{1}{2} \left(\frac{1}{2\pi} \int_0^{2\pi} E_\theta^2 d\phi + \frac{1}{2\pi} \int_0^{2\pi} E_\phi^2 d\phi \right)} \quad \dots(3.2)$$

The RMS field is calculated for the measured azimuth pattern, E_1 , and for the two measured elevation patterns, E_2 and E_3 , and an overall RMS field strength estimate is computed as

$$E_{RMS,m} = \sqrt{(E_1^2 + E_2^2 + E_3^2)} \quad \dots(3.3)$$

The corresponding RMS field strength is found from the three principal plane patterns from the computation, $E_{RMS,c}$, and then the measured fields are multiplied by the scale factor $E_{RMS,c}/E_{RMS,m}$. Then both the measured and computed field strengths are reported in dB relative to the isotropic level field strength of the computation, which is zero dB.

3.5 Comparison of the Measured and Computed Patterns

This section compares the measured principal plane patterns with the patterns computed with FDTD with a cell size of 4.41 mm.

Fig. 3.8(a) compares the measured and the computed azimuth patterns. The scaling makes the level of the principal or E_θ polarization almost identical for the measured and the computed data. The measured field strength in the maximum at zero degrees is 0.76 dB, whereas the computed field strength is 1.183 dB. In the minimum at 180 degrees, the measured field is -6.00 dB and the computed, -5.47 dB. Thus the agreement in the principal polarization is about one-half a decibel. The cross-polarized field, E_ϕ , is generally in good agreement between the measurement and the computation

both in pattern shape and in level relative to the principal polarization. However, there are differences in detail between the measurement and the computation. The measured pattern tends to fall below the computation between 0 and 270 degrees, except in the deep minimum. Then the measured field is above the computed field between 270 and 360 degrees. It is very difficult to measure the cross-polarized component accurately and the agreement shown here is quite satisfactory for our purposes. The measured field at the maximum at 270 degrees is -11.39 dB, and in the computation the field is -11.20 dB. The overall level of the measurement and computation are reasonably in agreement.

Fig. 3.8(b) shows the elevation pattern in the $\phi=0$ or xz plane. The measurement and the computation agree very well in the E_θ polarization. The position and breadth of each of the four lobes is well matched. The lobe at 115 degrees, 4.77 dB falls at 115 degrees, 4.29 dB in the computation. The lobe at 332 degrees, 3.50 dB coincides between the measurement and the computation. The maximum at 316 degrees, -4.01 dB in the measurement falls at 315 degrees, -3.75 dB in the computation.

Comparing the depth of the minima between the measurement and the computation is less meaningful, both because the computed minima change when the cell size is changed, and because the measured minima are affected by the short range to the measurement horn. The minimum at 60 degrees, -22.04 dB in the measurement falls at 61 degrees, -22.58 dB in the computation. The measured minimum at 174 degrees, -14.44 dB is found at 175 degrees, -14.05 dB. The minimum at 284 degrees, -13.34 dB in the measurement is found at 283 degrees, -14.88 dB in the computation. The minimum at 358 degrees, -14.04 dB in the measurement is found at 358 degrees, -12.54 dB in the computation. In spite of our misgivings, the minima are in reasonable agreement, with differences of about 1.5 dB.

Due to symmetry, the cross-polarized field should be zero in the elevation pattern for $\phi = 0$ in Fig. 3.8(b). The measured cross-polarized field has a maximum level of -21.2 dB. The styrofoam cradle used to hold the handset introduces asymmetry into the

problem, which may raise the level of the cross-polarized field. This could be investigated by including the styrofoam mount in the FDTD model. In the computation, the maximum cross-polarized field strength is -66.5 dB, which is off-scale in Fig. 3.8(b).

Fig. 3.8(c) shows the elevation pattern for $\phi = 90$ degrees, which is the yz plane. Again, the main features of both polarizations are in reasonable agreement, including the relative level of the E_ϕ to the E_θ field strength. The lobe at 38 degrees has a level of -6.8 dB in the measurement, and is found at 40 degrees, -6.19 dB in the computation. The lobe at 119 degrees, 4.05 dB in the measurement is found at 120 degrees, 3.98 dB in the computation. The cross-polarized field has generally the same level, though the measured field strengths tend to sag below the computation. The maximum measured cross-polarized field is -10.3 dB, and the computed maximum field is -10.7 dB.

The comparison of measured and computed principal plane patterns in Fig. 3.8 shows generally good agreement. The principal polarization, E_θ , in the computation shows all the lobes and minima found in the measurement, with excellent correspondence of the shapes of these features throughout. The cross-polarized field component, E_ϕ , agrees well in level relative to the principal component in the azimuth pattern and in the elevation pattern for $\phi = 90$ degrees. The main differences between the measured and computed patterns are in the minima in the E_θ polarization in the two elevation patterns. The minima were shown to be dependent upon the range between the turntable and the receive horn in the anechoic chamber. It is shown below that the minima in the computed patterns are quite sensitive to the cell size. Also, the presence of the styrofoam in the measurement, not included in the computation, may affect the minima, the symmetry of the pattern, and the level and shape of the cross-polarized field.

3.6 Comparison of the 2.205 mm Cell Computation with the Measurement

To analyze the handset near the head models later in this report, the handset will be modeled using 2.205 mm cells. In the last chapter, the radiation patterns of the handset were compared using 8.82, 4.41 and 2.205 mm cells. This section compares the FDTD radiation patterns computed using the 2.205 mm cell size with the measured radiation patterns.

Fig. 3.9(a) compares the FDTD-computed azimuth pattern using 2.205 mm cells with the measured pattern. The measured field in the forward direction is 0.76 dB and the computed, 1.27 dB. The measured field in the backward direction is -6.00 dB, and the computed, -5.26 dB. The cross-polarized field has the same overall level in the measurement and the computation. The elevation pattern for $\phi = 0$ degrees is shown in Fig. 3.9(b). The measured pattern has a maximum at 32 degrees, 6.51 dB, corresponding to the computed peak at 32 degrees, -6.74 dB. There is a measured lobe at 115 degrees, 4.77 dB, corresponding to the computed lobe at 115 degrees, 4.30 dB. The lobe at 232 degrees has value 3.50 dB in the measurement and 3.53 dB in the computation. The measured lobe at 316 degrees, -4.01 dB falls at 315 degrees, -4.15 dB. Thus the agreement in the maxima is within about 0.5 dB. The measured cross-polarized field has a maximum value of -21.22 dB in the computation, and is much lower in the

computation at -65.75 dB. Due to symmetry the cross-polarized field should be zero volts/metre.

Fig. 3.9(c) shows the elevation pattern for $\phi = 90$ degrees. The lobe at 120 degrees, 3.97 dB in the computation is symmetric with the lobe at 240 degrees. In the measurement, these lobes fall at 119 degrees, 4.05 dB and 239 degrees, 4.42 dB. The lobes at 39 degrees, -6.61 dB and 321 degrees, -6.64 dB are an almost-symmetric pair in the computation, and correspond to lobes at 38 degrees, -6.80 dB and 321 degrees, -6.24 dB in the measurement. The cross-polarized field corresponds quite well in overall level between the measurement and the computation.

3.7 Conclusion

This chapter has demonstrated accuracy of the FDTD computation of the radiation patterns of the handset. The computed patterns were compared with measurements of the handset radiation patterns. The measured and computed radiation patterns are generally in good agreement. Features such as main lobes, minor lobes and the level of the cross-polarized field correspond very well. However the agreement in the minima of the radiation patterns is not as good as might be desired. It was shown that the depth of the minima is dependent on the range from the handset to the horn antenna, and that 330 cm is not far enough for true "far field". Also, because the minima in the computation are quite dependent on the cell size, comparing the measured and computed minima is not useful.

The following chapters examine the radiation patterns of the vertical handset in the presence of simple models of the head.

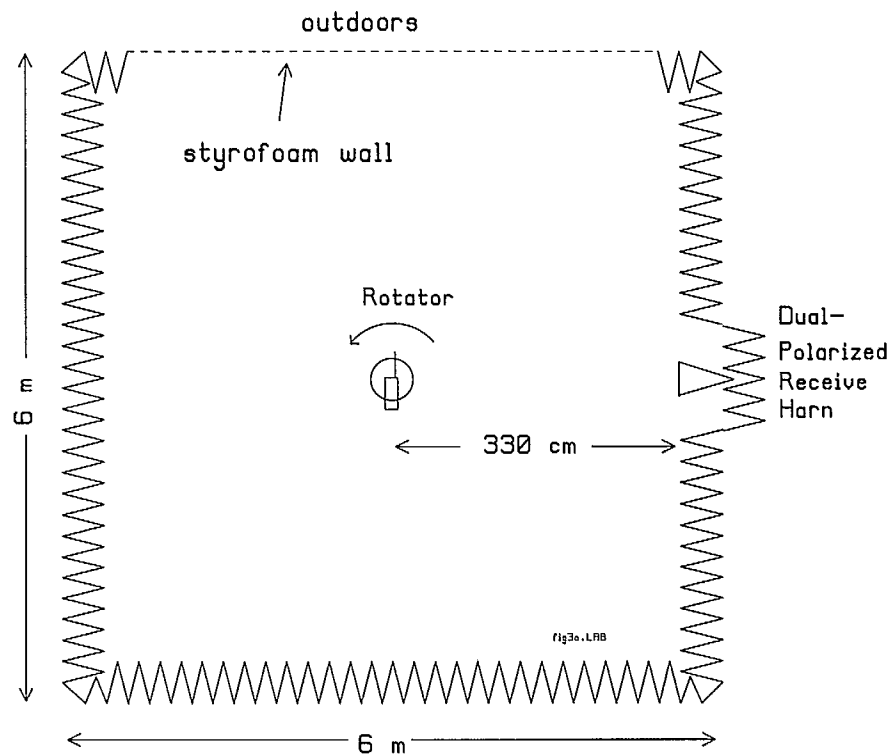


Fig. 3.1 Schematic of the anechoic chamber used to measure the handset patterns.

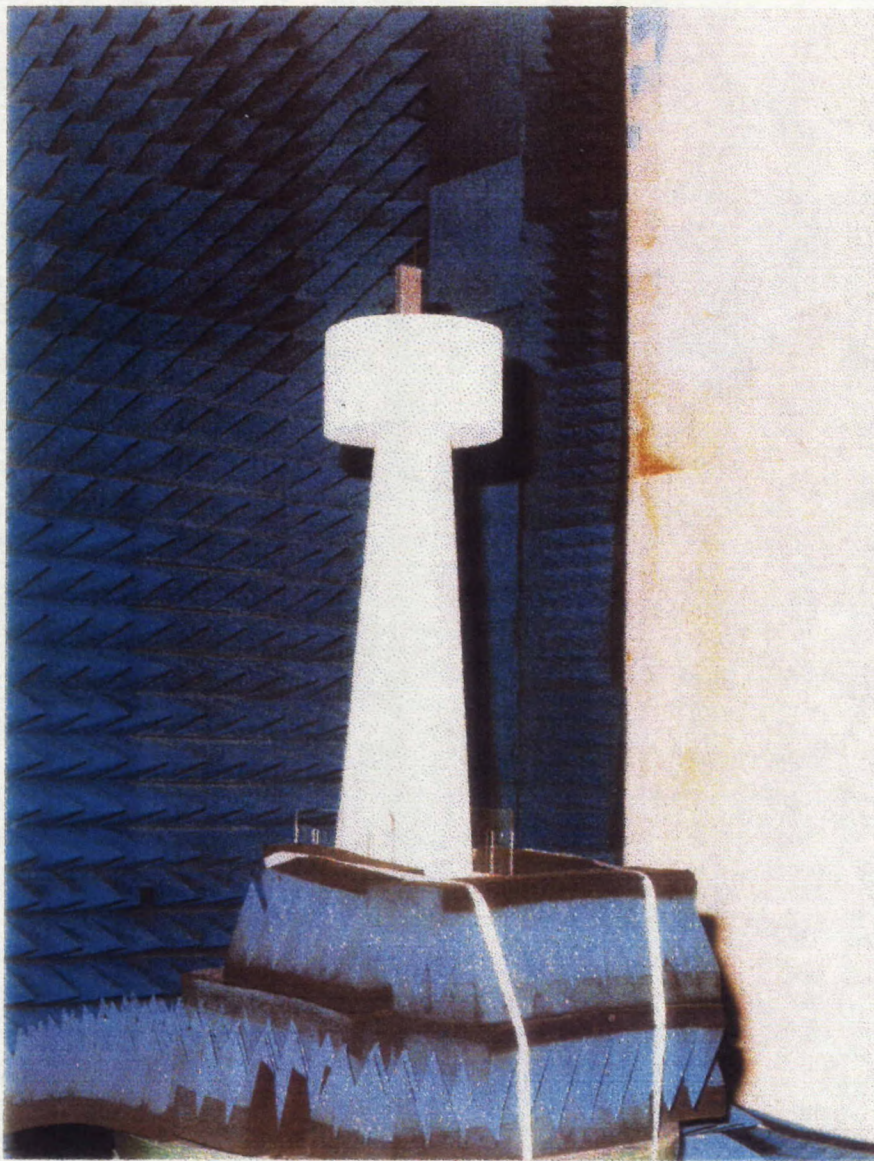


Fig. 3.2 The handset atop the rotator column in the anechoic chamber[10], oriented for the measurement of the azimuth pattern.

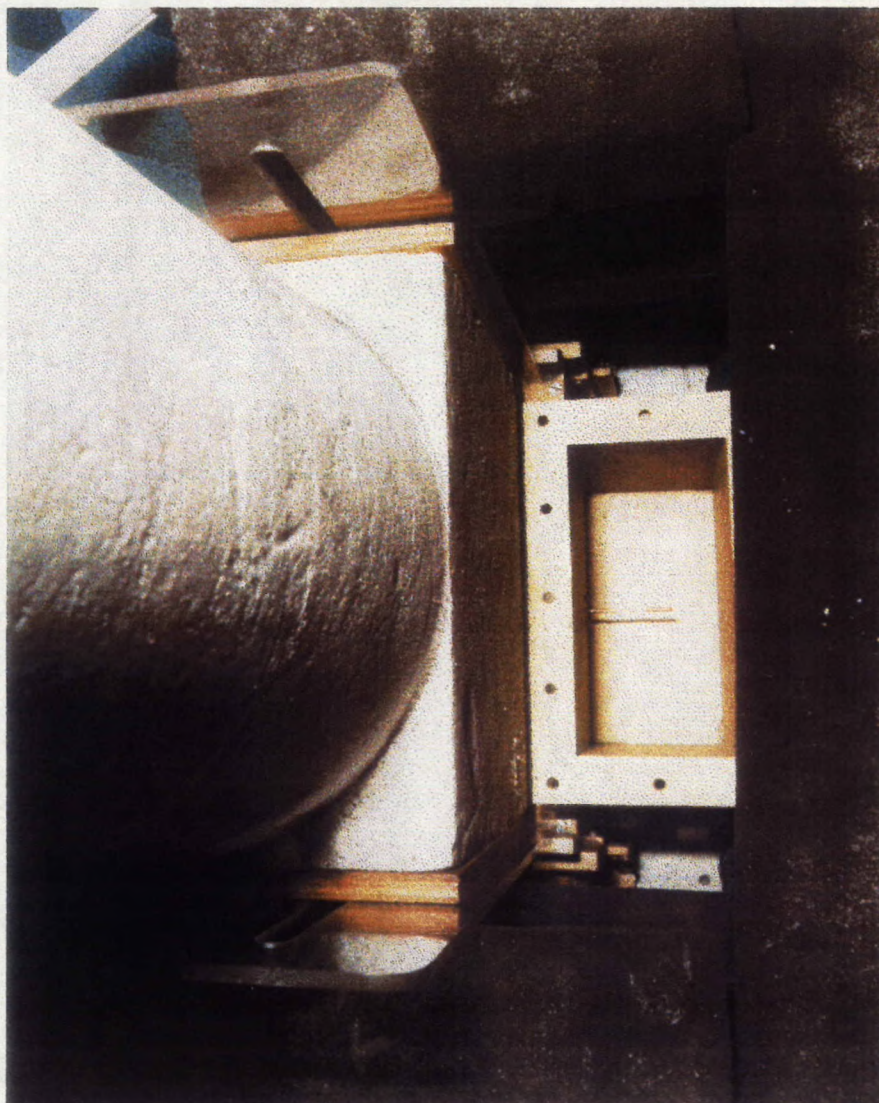


Fig. 3.3 An open-ended waveguide at the base of the rotator column is used to obtain a reference signal to phase-lock the network analyzer[10].

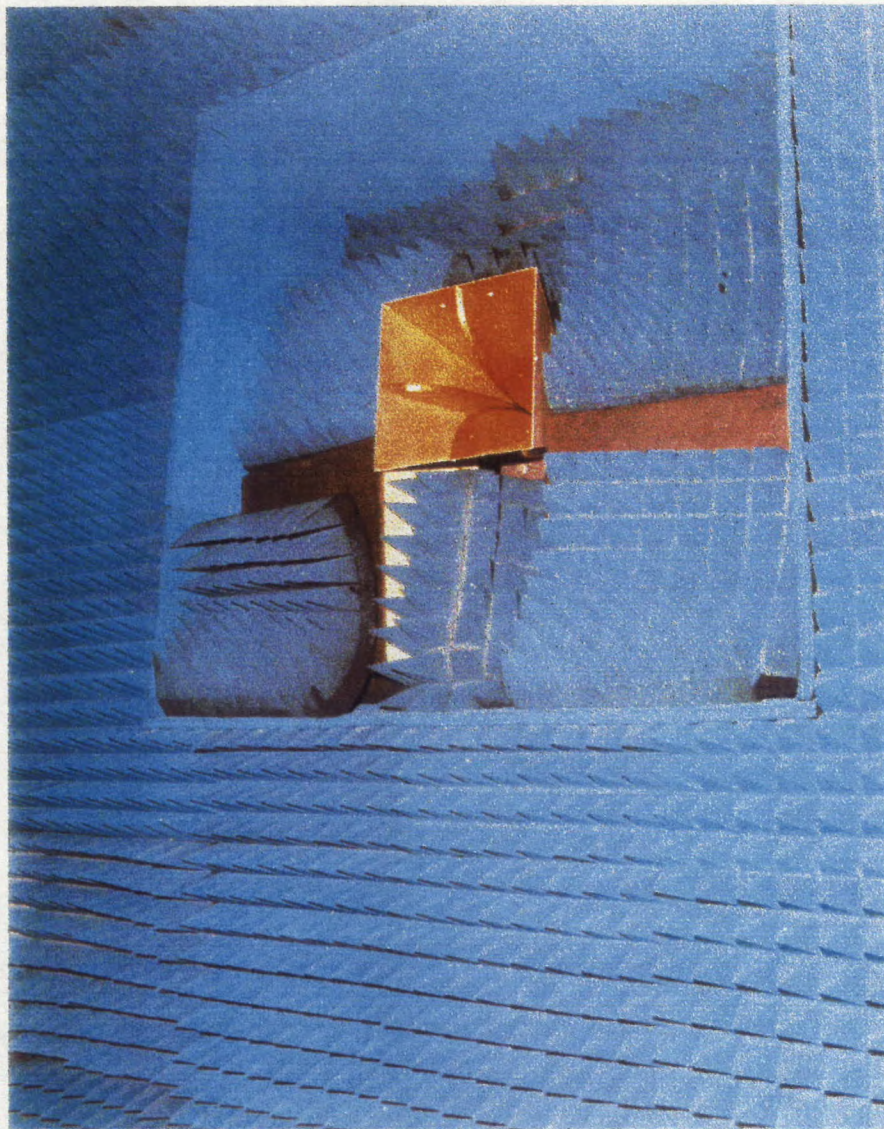


Fig. 3.4 A dual-polarized ridged-waveguide horn measures the horizontal and vertical components of the field radiated by the handset[10].

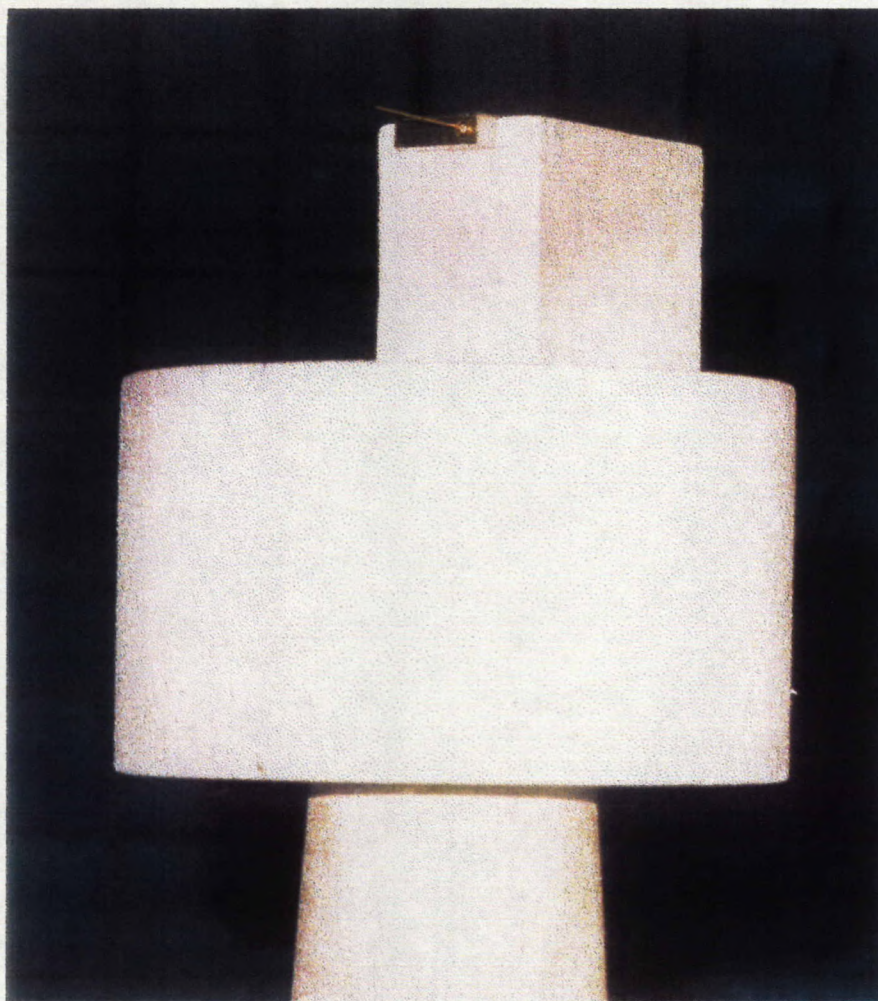


Fig. 3.5 The handset positioned in a styrofoam holder for the measurement of the elevation pattern for $\phi = 0$ [10].

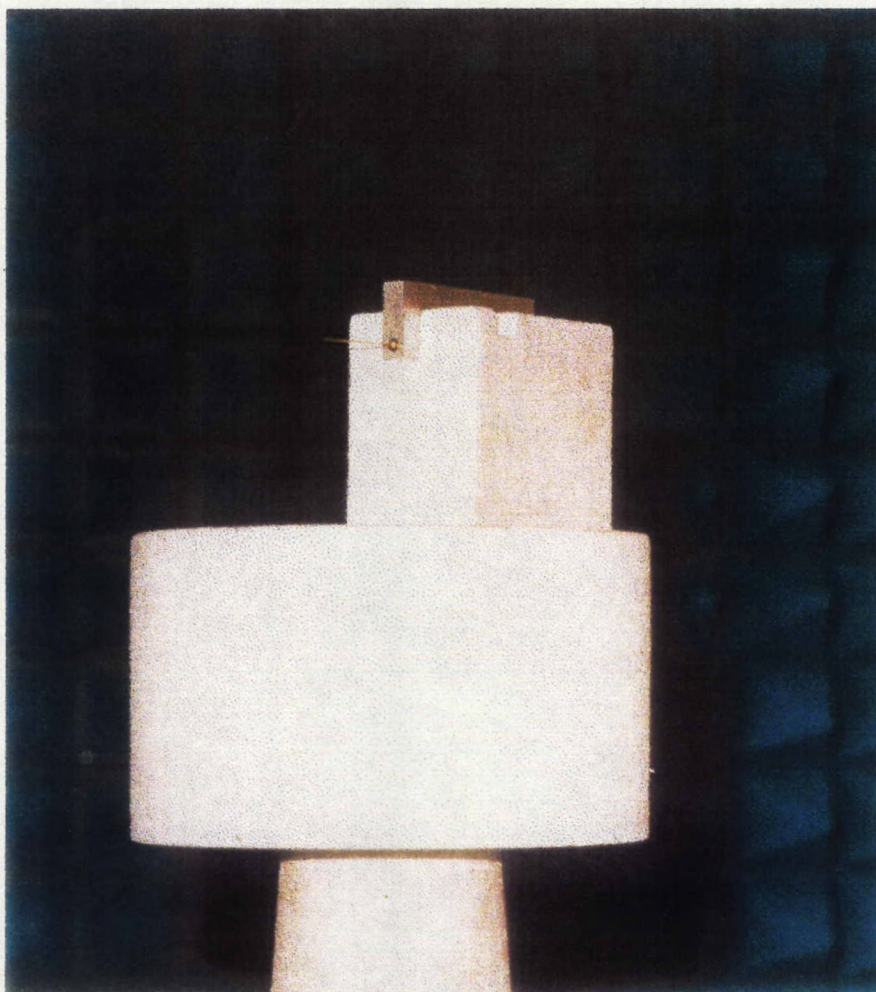


Fig. 3.6 The handset positioned in a styrofoam holder for the measurement of the elevation pattern for $\phi = 90$ [10].

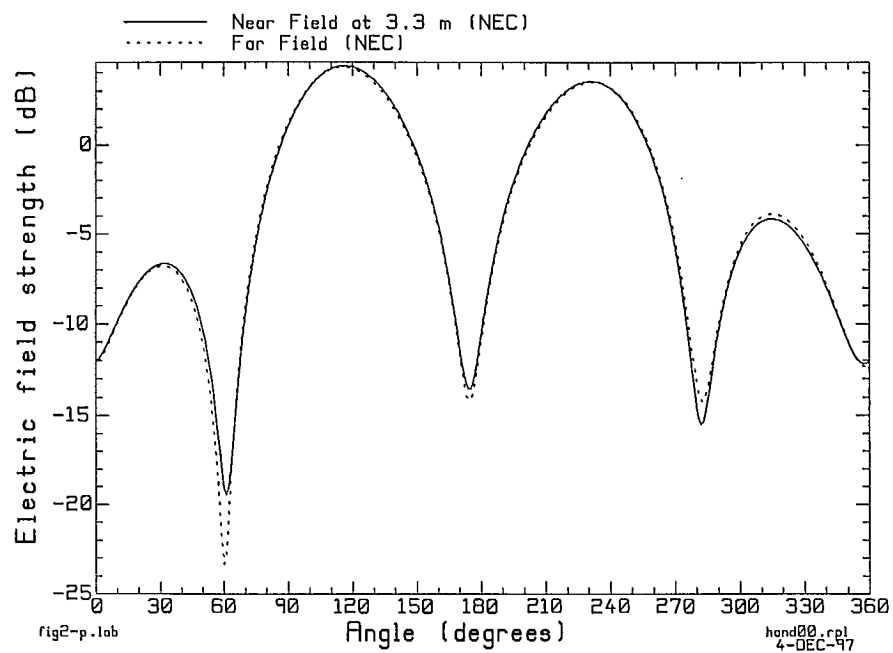
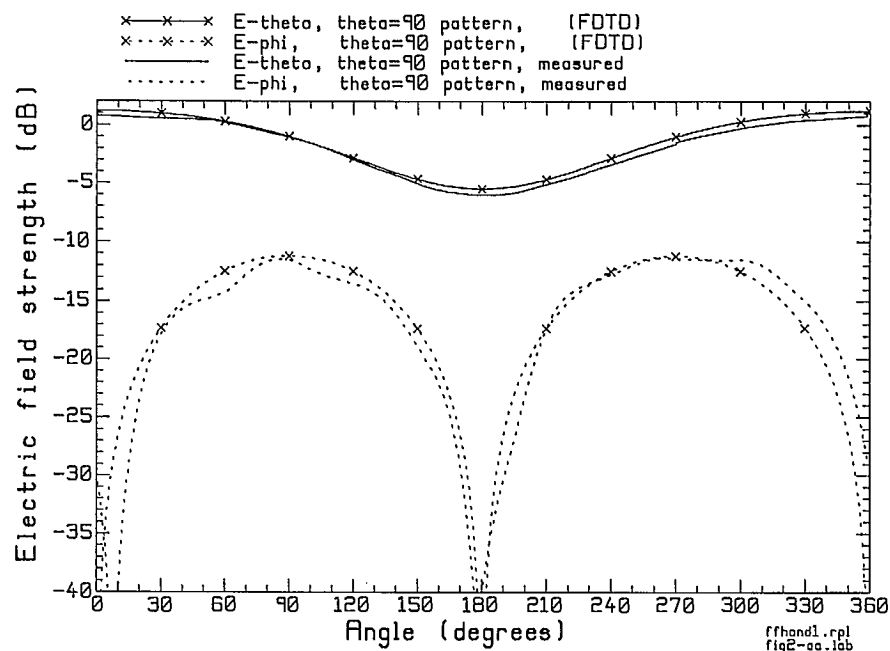


Fig. 3.7 Comparison of the true “far field” elevation pattern for $\phi = 0$ degrees with that at a range of 330 cm, both computed using the NEC program.



(a) Azimuth pattern.

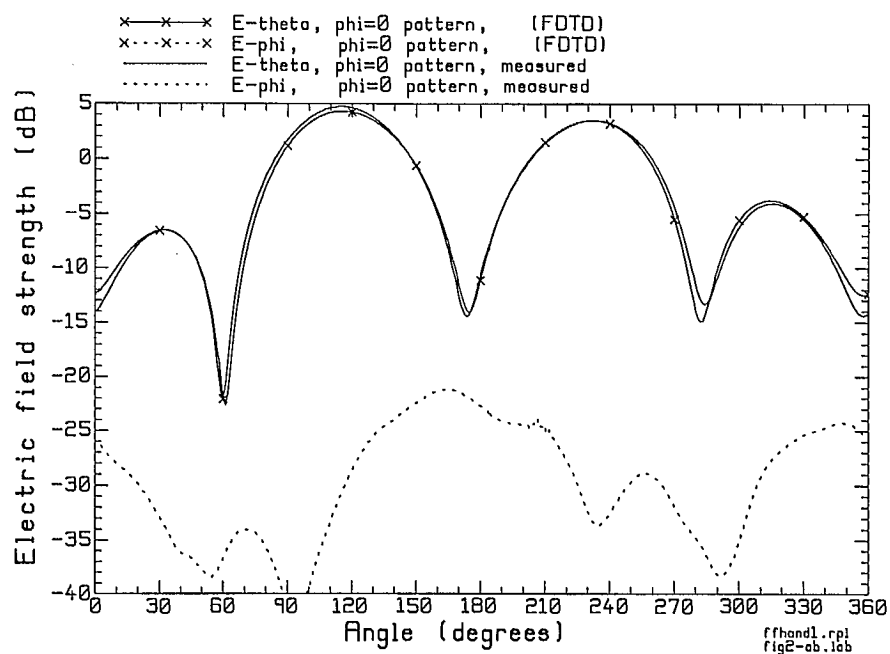
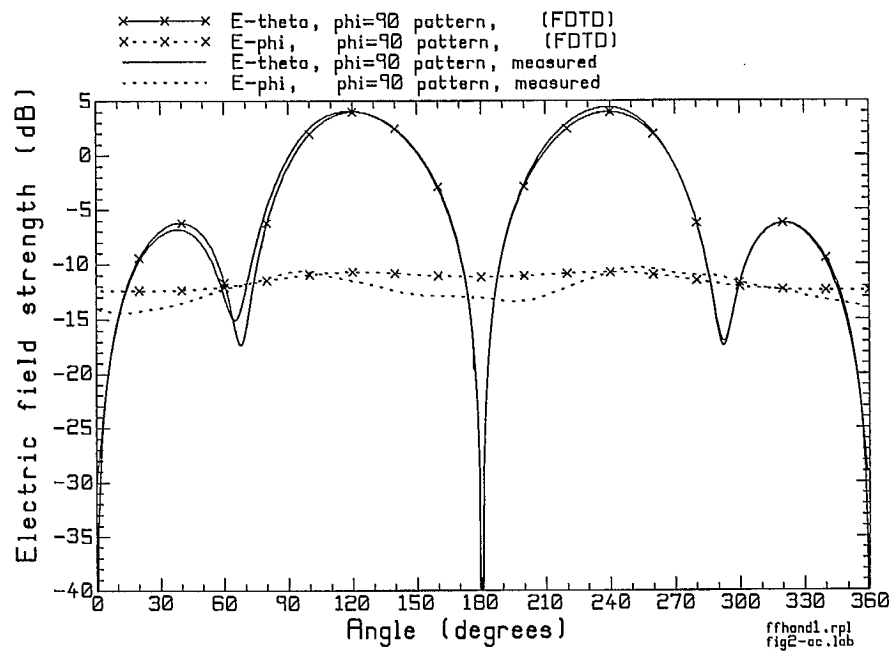
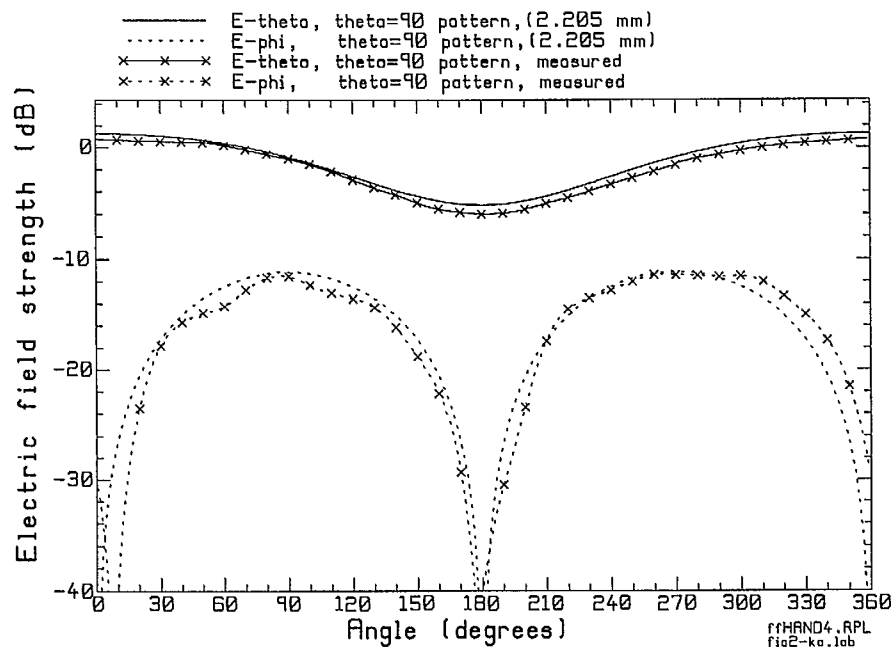
(b) Elevation pattern for $\phi = 0^\circ$.

Fig. 3.8 Comparison of the measured radiation patterns of the handset in free space with patterns computed with FDTD with a cell size of 4.41 mm.



(c) Elevation pattern for $\phi = 90$ degrees.

Fig. 3.8 (continued) Comparison of the measured radiation patterns of the handset in free space with patterns computed with FDTD with a cell size of 4.41 mm.



(a) Azimuth pattern.

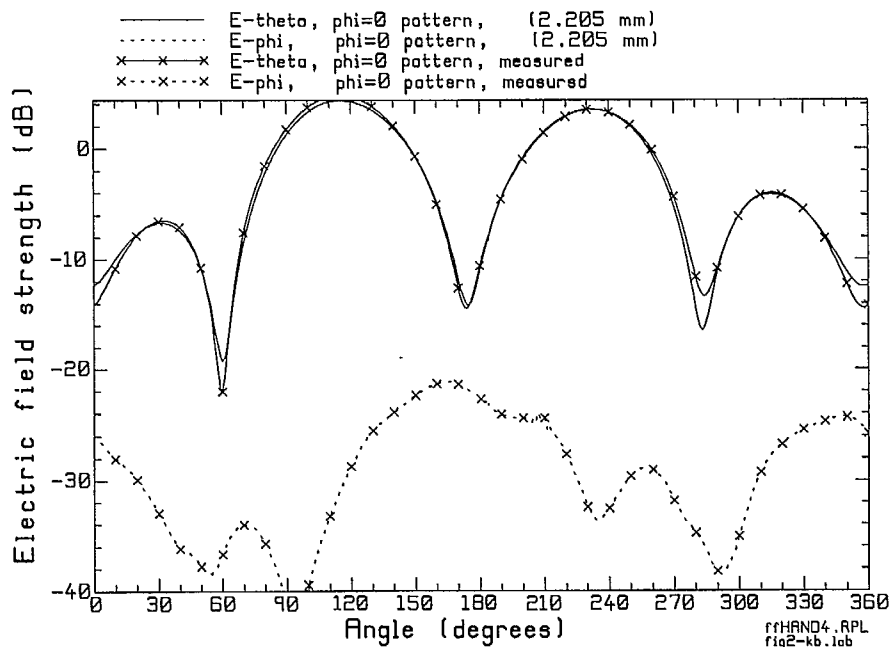
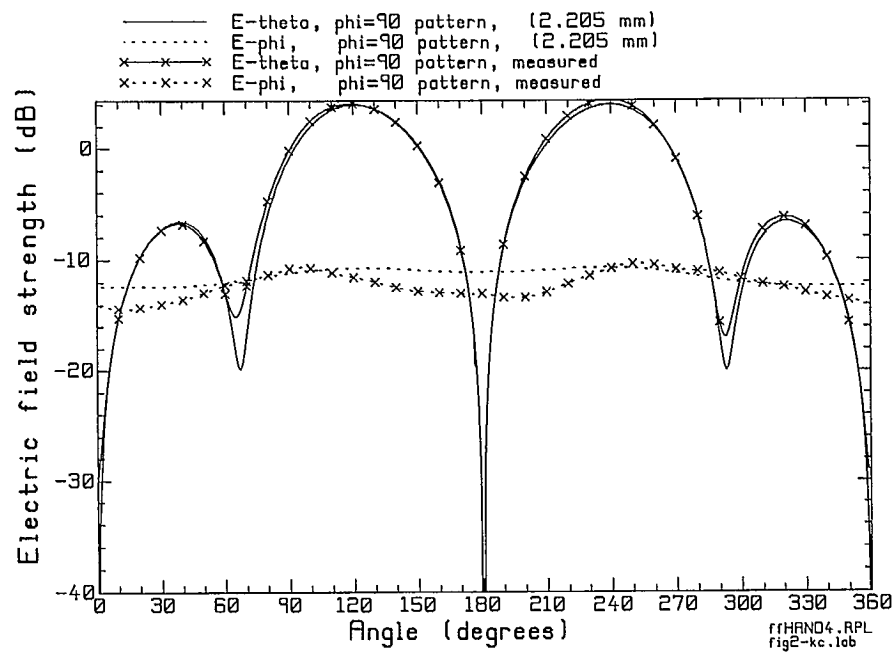
(b) Elevation pattern for $\phi = 0$ degrees.

Fig. 3.9 Comparison of the measured radiation patterns of the handset with the FDTD computation with 2.205 mm cell size.



(c) Elevation pattern for $\phi = 90$ degrees.

Fig. 3.9 (continued) Comparison of the measured radiation patterns of the handset with the FDTD computation with 2.205 mm cell size.

Chapter 4

Radiation Patterns of the Handset and Box Head

The “box head” of Fig. 4.1 is a plexiglas box measuring 17.07 by 13.89 by 21.06 cm, with a wall thickness of 0.51 cm. The cavity inside the box is filled with mixture of water, sugar and salt which has the electrical properties of the brain[3,21]. This chapter presents the radiation patterns of the portable radio handset operating near the box model of the head. The computed patterns are compared with measurements.

4.1 The FDTD Model of the Handset and Box Head

Fig. 4.2 shows the handset and box head schematically. Note that the bottom of the handset aligns with the bottom of the box head. The dimension shown in Fig. 4.2 give the true size of the box head and the relative position of the handset to the box head read from the mechanical drawings[32]. To derive the FDTD model, a “make file” was created[4] giving the true locations of the handset box, wire antenna, plexiglas walls of the box head, and brain liquid cavity. The “MKPHONE” program of Ref. [4] was revised extensively and incorporated into program “EDITCEL”. The new EDITCEL program reads the “make” file, derives the cell model, then lets the user view and edit the cell model, layer by layer. The computations presented in this section use a cell size of 4.41 mm. Thus to derive a cell model from the dimensions of Fig. 4.2, the plexiglas wall of the box head, which has an actual thickness of 5.1 mm, is approximated with one cell thickness of 4.41 mm. The size of the box head is rounded to the nearest cell, and is 39 by 32 by 48 cells overall, or 17.20 by 14.11 by 21.17 cm compared to the actual size of 17.07 by 13.89 by 21.06 cm. The position of the box relative to the handset is rounded to the nearest cell to derive the cell model. Thus neither the size of the box nor the position of the box precisely correspond to the measurement model.

The FDTD space size is 59 by 58 by 78 cells. The space is terminated with a PML boundary 6 cells thick, with parabolic evolution of the conductivity and a surface reflection coefficient of 60 dB. Four cells of whitespace separate the surfaces of the model from the inner surface of the cell space. The model was run for 4096 time steps to ensure that the solution has reached steady state.

The relative permittivity and conductivity of the brain liquid are 40.42 and 1.064 S/m, respectively. These values correspond to the brain liquid used in the measurement reported later in the chapter, and were measured at CRC[33]. For the plexiglas, the relative permittivity was 3.45 and the conductivity 0.005. The following sections discuss the radiation patterns of the handset near the box head and compare them with the patterns of the handset alone.

4.2 The Radiation Patterns of the Handset and Box Head

Fig. 4.3 shows the radiation patterns of the handset operating near the box head, computed using the FDTD model with 4.41 mm cells described above. The fiberglass bolts were not included in the computation. In the azimuth pattern the user faces in the

+x or $\phi = 0$ degree direction. The user's left hand is at 90 degrees, and his right hand at 270 degrees. We are seeing the pattern "from below" in Fig. 4.3. The azimuth pattern shows that the principal or E_θ polarization has a roughly circular radiation pattern. The field strength is larger in the region from 180 through 270 to 360 degrees, where the head lies behind the handset, than in the region from 0 through 90 to 270 degrees, where the head lies between the handset and the observer. The maximum field of 2.3 dB falls at 302 degrees where the handset lies between the head and the observer. The minimum of -7.6 dB falls at 126 degrees, where the handset lies behind the head as seen from the position of the observer. The cross-polarized field, E_ϕ , has a minimum near 90 degrees, where the head is between the handset and the observer. Also the cross-polarized field is comparable to the principal polarization near 30 degrees, and larger than the principal polarization near 135 degrees. In the region of the pattern where the head is behind the handset, from 180 to 360 degrees, the cross-polarized field is about 10 dB below the principal polarization.

In the elevation pattern for $\phi = 0$ degrees, the head is beside the handset, never behind it or in front of it. In this pattern the E_θ and E_ϕ polarizations are roughly equal in level, and the patterns are roughly symmetric about the 0 degree direction. The E_θ polarization has a minimum above the handset, and a deep minimum directly below. The E_ϕ polarization has a roughly circular pattern.

In the elevation pattern for $\phi = 90$ degrees, the handset lies behind the head from 0 through 90 to 180 degrees, and in front of the head for 180 through 270 to 360 degrees. The field strength in E_θ is largest at 245 degrees at 5.5 dB. The field strength when the observer is behind the head has lobes of -1.4 dB at 49 degrees and -0.7 dB at 112 dB. The deepest minima fall at 146 degrees, -13.3 dB and 293 degrees, -10.9 dB. The cross-polarized field, E_ϕ , is generally much smaller than E_θ in this pattern, having a maximum value of -10 dB at 129 degrees.

4.3 Changes in the Handset Patterns due to the Box Head

Fig. 4.4 compares the radiation patterns of the handset in free space to those of the handset operating near the box head. The basis for the comparison is that of equal radiated power. Thus, the fields E_θ and E_ϕ are computed for the set of conical cut radiation patterns of Fig. 2.2, and the radiated power is evaluated using Eqn. 2.1 for both the handset in free space and the handset operating near the box head. The isotropic level is computed using Eqn. 2.2 for each set of patterns, and then all field strengths are divided by the isotropic level field strength and converted to dB. Hence both sets of patterns correspond to the same radiated power. Since the box head consists of lossy dielectric material, it absorbs some power and so the input power to the handset operating near the box head is larger than for the handset alone, such that the radiated power is the same in both cases.

The azimuth pattern for E_θ in Fig. 4.4(a) is roughly circular for the handset alone, with a field of 1.2 dB in front of the operator at zero degrees and -5.5 dB behind, at 180 degrees. With the box head, the field strength is larger on the operator's right, at 270

degrees, where the handset lies between the head and the observer, than on the operator's left, 90 degrees, where the handset is blocked by the head. Thus the field at 302 degrees is 2.3 dB, falling to -7.6 dB at 127 degrees. The cross-polarized field is larger in the presence of the head, with a maximum of -4.3 dB, than for the handset alone, where the maximum is -11.2 dB.

The elevation pattern for $\phi = 0$ degrees is shown in part (b). For the handset alone, the E_θ polarization has major lobes directed downward, of field strength 4.3 dB at 116 degrees and 3.5 dB at 233 degrees. There are minor lobes directed upwards, of -6.5 dB at 33 degrees and -3.8 dB at 315 degrees. These lobes are separated by sharp minima, of depth -22.6 dB at 61 degrees and -14.9 dB at 282 degrees. In the presence of the box head, the sharp minima are filled in, and the size of the downward directed lobes shrinks. Thus at the maximum at 116 degrees the field is 1.8 dB and at the maximum at 239 degrees, 2.4 dB. The field strength at 33 degrees is increased to -4.2 dB and rises to a maximum of -3.0 dB at 49 degrees. The sharp minimum at 61 degrees is completely filled, such that the field at 61 degrees is -3.5 dB. The minimum at 282 degrees is also filled with a field of -5.9 dB. Hence the elevation pattern is much more circular in the presence of the box head. The cross-polarized field in this pattern had a maximum of -66.5 dB in the FDTD computation with 4.41 mm cells for the handset alone, and is theoretically zero due to symmetry. When the head is introduced, the cross-polarized field has a roughly circular radiation pattern, with a maximum of 1.68 dB at 166 degrees and a minimum of -7.4 dB at 94 degrees.

In the $\phi = 90$ elevation pattern, Fig. 4.4(c), the handset lies behind the box for the directions from 0 to 180 degrees, and the field strength in E_θ is strongly affected. For the handset alone there is a lobe of -6.2 dB at 39 degrees, with a minimum of -17.3 dB at 68 degrees and a large lobe of 4.0 dB at 121 degrees. These features change to a broad lobe of maximum value -1.4 dB at 50 degrees, followed by a shallow minimum of -7.5 dB at 82 degrees, and another lobe of -0.8 dB at 114 degrees. The head introduces a minimum of -13.3 dB at 146 degrees.

The box lies behind the head from 180 through 270 to 360 degrees, and the general shape of the radiation pattern is not greatly changed. The broad lobe of 4.0 dB at 241 degrees increases to 5.5 dB at 245 degrees. The minimum of -17.3 dB at 292 degrees is filled in to become -10.9 dB at 293 degrees. The lobe of -6.2 dB at 321 degrees changes to -2.2 dB at 326 degrees. Thus the field is generally increased when the head lies behind the handset. The cross polarized field, E_ϕ , has roughly the same strength from 0 to 150 degrees. The head introduces a minimum in E_ϕ at 194 degrees of -26.8 dB.

In summary, the box head tends to increase the field strength in the principal polarization when the head lies behind the handset, and reduce it when the head blocks the line of sight to the observer.

4.4 The Box Head Mounting Jig

A major objective of this work is the validation of the radiation patterns computed by FDTD against measured patterns. To analyze the handset and box head by computation, the relative position of the handset to the head must be well known. Then a

computer model can be derived that is a good approximation of the measurement conditions.

The handset and box head are held in a well-known position relative to one another by mounting them in a jig. Fig. 4.5 shows the jig without the box head, and with the handset fitted into its slot in the side of the jig. Fig. 4.9 is a similar view of the jig with the box head inside. The jig consists of a styrofoam bottom piece and top piece, with the box head sandwiched between the two. The assembly is held together by four fiberglass bolts, with plexiglas washers and fiberglass nuts at each end.

The nuts and bolts represent a considerable quantity of dielectric material located quite close to the handset and box head. CRC was concerned that the bolts would affect the radiation patterns. This section examines the changes to the handset radiation patterns that come about when the fiberglass bolts are introduced near the handset, with no model of the head. Both measurements and computations will be examined.

4.4.1 Measured Radiation Patterns Including the Bolts

By comparing the measured radiation patterns of the handset from the last chapter with the measured radiation patterns of the handset in the empty jig, as in Fig. 4.5, we can assess the effect of the four fiberglass bolts. Fig. 4.6 compares the measured principal plane patterns of the handset in the simple mounting jigs of Figs. 3.3, 3.5 and 3.6, with the principal plane patterns with the handset in the box head jig. The elastic bands seen in the photo of Fig. 4.5 were not included in the measurement. To scale the measured patterns for comparison, the RMS field strength for each set of measured patterns was computed according to Eqn. 3.3, and then the fields for each set were scaled to have the same RMS level as the computed patterns for the handset alone.

Fig. 4.6(a) shows that the azimuth plane pattern is less symmetric in E_θ in the measurement with the mounting jig and bolts than without. The cross-polarized field E_ϕ is slightly lower in level in the measurement with the jig.

In the $\phi = 0$ elevation pattern, Fig. 4.6(b), the main lobes are slightly higher for the handset alone than for the handset with the jig. The lobe at 115 degrees, 4.8 dB with no bolts falls at 115 degrees, 4.2 dB with the bolts. The lobe at 232 degrees, 3.5 dB with no bolts falls at 232 degrees, 2.9 dB with bolts. The minor lobes change as well. The lobe at 32 degrees, -6.5 dB with no bolts falls at 30 degrees, -6.1 dB with the bolts. The lobe at 316 degrees, -4.0 dB with no bolts falls at 314 degrees, -4.6 dB with the bolts. The minima change considerably. The sharp minimum at 60 degrees, -22.0 dB with no bolts falls at 60 degrees, -18.8 dB with bolts. The minimum at 174 degrees, -14.4 dB with no bolts falls 175 degrees, -16.1 dB with the bolts. The minimum at 284 degrees, -13.3 dB with no bolts falls at 283 degrees, -17.0 dB with bolts. That at 358 degrees, -14.4 dB with no bolts falls at 353 degrees, -11.6 dB with bolts. This is a significant shift in the angular position of the minimum. The cross-polarized field in Fig. 4.6(b) changes considerably in shape when the bolts are introduced. The maximum cross-polarized field is at 164 degrees, -21.2 dB with no bolts, and is found at 243 degrees, -23.1 dB with the bolts.

In the $\phi = 90$ pattern of Fig. 4.6(c), the measurement of E_θ with the bolts is less symmetric about 180 degrees than is the measurement with no bolts. The main lobe at

119 degrees, 4.1 dB with no bolts falls at 120 degrees 4.5 dB with the bolts. The symmetric lobe at 239 degrees, 4.4 dB with no bolts falls at 240 degrees, 3.4 dB with the bolts. The minor lobe with no bolts at 38 degrees, -6.8 dB should be symmetric with that at 320 degrees, -6.2 dB. With bolts, the corresponding minor lobes are at 42 degrees, -6.9 dB and 321 degrees, -6.5 dB. The minimum with no bolts at 65 degrees, -15.1 dB should be symmetric with the minimum at 293 degrees, -16.9 dB. With the bolts, the minimum at 67 degrees, -17.8 dB should be symmetric with that at 294 degrees, -14.9 dB. The deviation in these minima from the expected symmetry is no worse with the bolts than without. The cross-polarized field is higher through much of the pattern with the bolts. The maximum increase is about 3 dB.

In summary the bolts introduce changes in the lobes in the principal polarization of 0.4 to 1 dB, with 0.6 dB a typical change.

4.4.2 Effect of the Bolts in the Computed Radiation Patterns

Fig. 4.7 shows a computational model of the handset, the four fiberglass bolts, and the plexiglas washers and nuts, using a cell size of 8.82 mm. The length of the fiberglass bolts, and their position relative to the handset were determined from mechanical drawings of the jig[32]. This yielded a length of 303 mm and a diameter of 13 mm for the bolts. The nuts are 16 mm thick, and are hexagonal, with a maximum diameter of 12.9 mm. Fig. 4.7 shows that 303 mm bolts are almost flush with the ends of the nuts, unlike the photo of the jig in Fig. 4.5. The mechanical drawings of the bolts were in error in giving the length as 303 mm; the actual length is 316 mm. This error was noted but the present computations use 303 mm bolts.

With 8.82 mm cells, the “staircased” model of the bolts in Fig. 4.7 is very crude. To model the four fiberglass bolts more accurately, the FDTD cell size was reduced to 2.205 mm. The hexagonal nuts were approximated with cylinders, which were then staircased with FDTD cells. The styrofoam blocks of the jig in Fig. 4.5 were not included in the computer model.

Using 2.205 mm cells, the cell space with 303 mm bolts is 140 by 140 by 157 cells. The perfectly-matched layer absorbing boundary condition was used, with a thickness of 6 layers, a surface reflection coefficient of 60 dB, and parabolic evolution of the conductivity. There are four cells of free space separating the surfaces of the FDTD model from the inner surface of the PML.

The electrical parameters of fiberglass were approximated with the values given in Ref. [34] for 3 GHz, of $\epsilon_r = 3.99$ and loss tangent $\tan \phi = 0.0241$. The plexiglas washer was represented with relative permittivity $\epsilon_r = 3.4$, and no loss[35]. This value is high compared to that given in Moreno for “acrylic resins”.

Fig. 4.8 compares the computed radiation patterns of the handset isolated in free space to those of the handset with the nuts and bolts. The patterns are compared on the basis of equal *radiated* power. Since bolts are slightly lossy, the input power is slightly higher with the bolts to account for power dissipated in the bolts.

The azimuth pattern in Fig. 4.8(a) is almost unchanged by the bolts. The minimum in E_θ at 180 degrees, -5.2 dB with no bolts shifts to 185 degrees, -4.9 dB with the bolts. The nuts-and-bolts make the model unsymmetric about the xz plane and so the azimuth pattern is no longer perfectly symmetric about 180 degrees.

The elevation pattern for $\phi = 0$ in Fig. 4.8(b) is little changed in the maxima. The nut and bolt assemblies affect the field strength in the minima. The field at 60 degrees is -26.9 dB with no bolts, and is -19.2 dB with the nuts-and-bolts. This is a 7.7 dB change. The field at 283 degrees is -13.6 dB with no bolts, and increases to -16.4 dB with the bolts. The cross-polarized field, which is off-scale in Fig. 4.5(b), has a maximum of -65.8 dB with no nuts and bolts, whereas due to symmetry it should be zero. When the nuts and bolts are introduced, the cross-polarized field rises to a maximum of -46.9 dB, roughly a 20 dB increase. The bolts do couple energy into the cross-polarized field.

The elevation pattern for $\phi = 90$ in Fig. 4.5(c) is also not much changed in the maxima. The minimum at 67 degrees, -15.6 dB with no bolts falls to -19.9 dB with bolts. The minimum at 293 degrees, -15.3 dB with no bolts, which should be symmetric with that at 67 degrees, falls to -20.0 dB with bolts. The cross-polarized field is little changed by the presence of the bolts.

In conclusion, the fiberglass bolts mainly change the field strength in the minima in the computed radiation patterns. The bolts cause changes of 0.3 to 7.7 dB in the minima.

4.5 Comparison of the Computed and Measured Radiation Patterns

One objective of this report is the validation of FDTD computations of radiation patterns by comparison with measured patterns. In Chapter 3, the patterns of the handset in free space were compared with the measured radiation patterns. The handset is a metallic box, modeled as perfectly conducting in FDTD, and is expected to be solved to very good accuracy by the FDTD algorithm. The box head is more challenging for FDTD because it tests the method's ability to model lossy dielectric material. Also, the size and position of the head cannot be represented precisely with cubical FDTD cells. For the present FDTD model, the cell size was decreased from 4.41 mm in the foregoing, to 2.205 mm. This permits a reasonable "staircased" model of the fiberglass bolts, and the plexiglas nuts and washers. The FDTD model is similar to that discussed in Section 4.1.2 above, using a 140 by 140 by 157 cell FDTD space. The handset and box head model was re-derived for the new 2.205 mm cell size. The handset is 24 by 8 by 76 cells with an antenna 40 cell edges long. The plexiglas wall of the box head is now modeled as two cells thick. The overall dimensions of the box head is 78 by 63 by 95 cells, making the box in the FDTD model 17.20 by 13.89 by 20.95 cm. This is close to the actual dimensions of 17.07 by 13.89 by 21.06 cm. The fiberglass bolts and plexiglas nuts and washers were included in the computation. The bolts were 303 mm long. The styrofoam blocks of the holding jig were not included in the computation. The FDTD model was run for 4096 time steps, more than enough to reach steady state.

Fig. 4.10 compares the computed radiation patterns including the fiberglass nuts and bolts with the measurement of the handset in the jig of Fig. 4.9. In the azimuth pattern of Fig. 4.10(a), the computed field strength in both E_θ and E_ϕ match the measured field strengths quite well. The maximum measured E_θ is 3.0 dB at 297 degrees, and the maximum computed field is 2.4 at 304 degrees. The minimum measured E_θ is -7.3 dB at 119 degrees, compared to a computed field of -7.7 dB at 128 degrees.

The cross-polarized field E_ϕ has a maximum in the measured pattern of -4.1 dB at 129 degrees, compared to -4.4 dB at 128 degrees in the computation. The maximum at -5.1 dB, 35 degrees in the measurement falls at -5.0 dB, 34 degrees in the computation. The minimum at -14.9 dB, 244 degrees in the measurement falls at -16.2 dB, 245 degrees in the computation. For reasons previously discussed, comparisons of the depth of deep, sharp minima are not meaningful. The minimum at -29.9 dB, 80 degrees in the measurement corresponds to that at -24.9 dB, 81 degrees in the computation. The depth of such minima is sensitive to the range to the receive horns in the measurement and to the cell size in the computation.

The elevation pattern for $\phi = 0$ degrees in Fig. 4.10(b) shows good agreement between the measurement and the computation. In E_θ , the main lobe in the measured pattern at 1.86 dB, 116 degrees agrees well with the computation of 1.93 dB, 116 degrees. The next largest lobe is 0.9 dB, 237 degrees in the measurement and 1.4 dB, 238 degrees in the computation. The measured lobe at 3.6 dB, 311 degrees corresponds to the computed lobe at 3.3 dB, 311 degrees. In the cross-polarization, E_ϕ , The maximum measured field strength is -2.7 dB, 168 degrees, compared to -1.6 dB, 169 degrees in the computation.

The elevation pattern for $\phi = 90$ degrees in Fig. 4.10(c) has the largest measured E_θ at 6.2 dB, 246 degrees compared to a computed field of 5.4 dB, 245 degrees. The minor lobe in the measurement at -0.6 dB, 48 degrees falls at -1.5 dB, 51 degrees in the computation. The lobe at -1.2 dB, 113 degrees in the measurement falls at -0.6 dB, 113 degrees in the computation. The maximum cross-polarized field is -10.9 dB, 125 degrees compared to -10.9 dB, 129 degrees in the measurement.

Fig. 4.10 demonstrates that very good agreement has been achieved between the computations and the measurements for the handset and box head. In the maxima, differences of less than 1 dB have been achieved in most cases.

4.6 Conclusion

This chapter has examined the radiation patterns of the handset oriented vertically, operated near a box representation of the head. The radiation patterns of the handset and head were compared with those of the handset alone. It was found that the field strengths in E_θ in the parts of the pattern where the head lies behind the handset tend to be bigger than those of the handset alone. But where the handset is behind the head, the field strengths tend to be smaller. Also, the head tends to fill in the sharp minima in the fields of the handset alone. The head tends to increase the cross-polarization substantially.

This chapter compared the computed radiation patterns for the handset and head with measured radiation patterns. The head is held in a mounting jig for measurement and the effect of the four fiberglass bolts on the handset patterns was examined. It was found that in the measured patterns, the bolts change the field strength in the main lobes by 0.4 to 1 dB. The handset with the four bolts was solved by computation and it was found that the bolts have little effect in the maxima, but cause changes in the minima of as much as 7.7 dB. The styrofoam blocks in the measurement jig were not included in the model.

The radiation patterns of the handset, boxhead and fiberglass bolts were found by FDTD using a smaller cell size than for the handset and box head, to permit a finer staircased model of the bolts. The computed radiation patterns were found to be in quite good agreement with the measurement. Differences of about 1 dB in the main lobes were found. The geometric errors incurred by modelling a rectangular box with FDTD cells are small. The size of the box must be rounded to the nearest whole cell size. The position of the box relative to the handset must also be rounded to the nearest whole cell. With 2.205 mm cells, the errors are at most half a cell or about 1.1 mm. The comparison of the computations and measurements show that the resulting FDTD model is a good representation of the true geometry.

A square model of the head is quite unrealistic. It was used because the FDTD method permits a good approximation of a rectangular box. The following chapter models the head as a sphere, which is much more realistic but is also less well approximated with a staircased model.

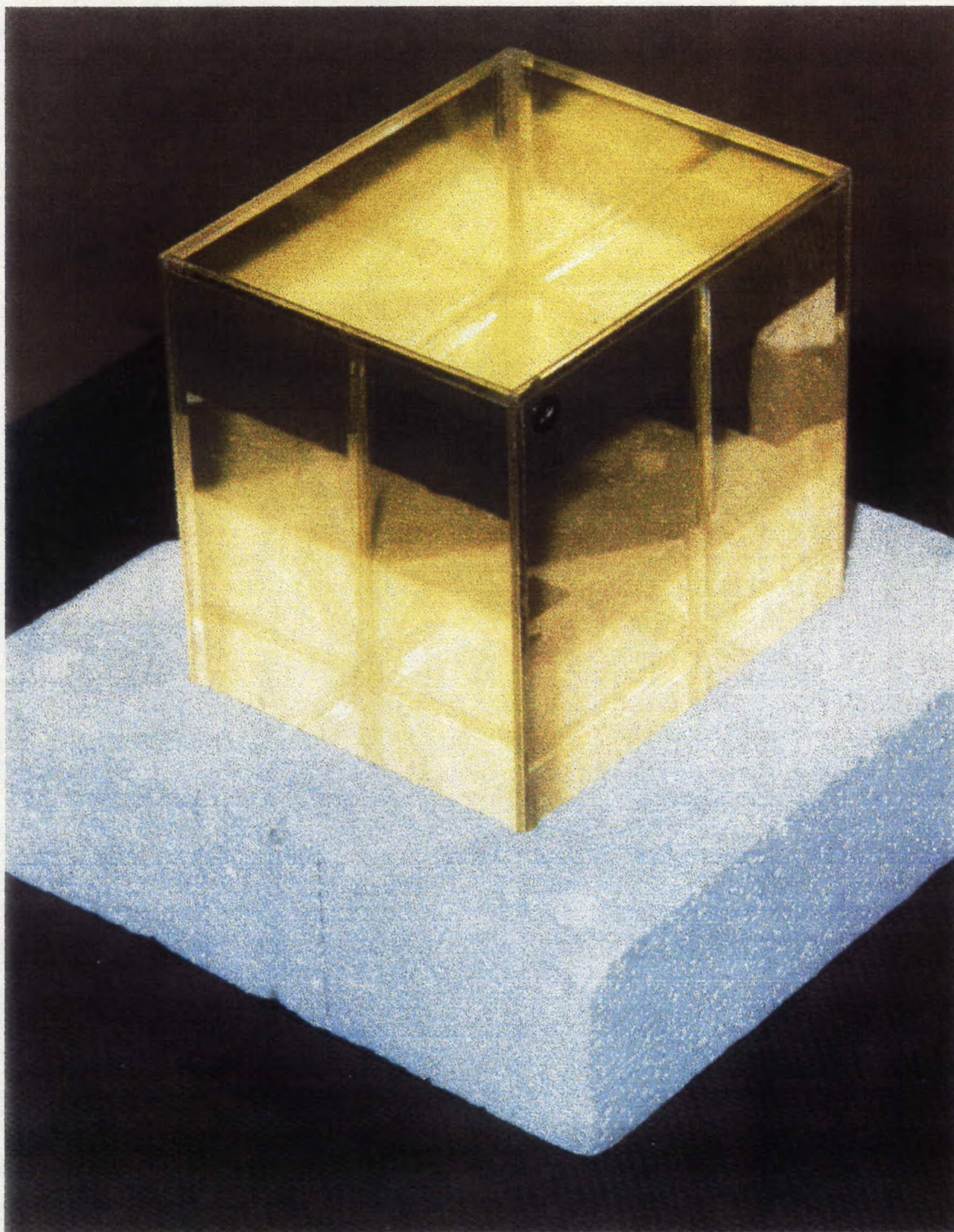


Fig. 4.1 The “box head” is a thin-walled plexiglass box filled with liquid having the electrical properties of brain matter at 850 MHz[10].

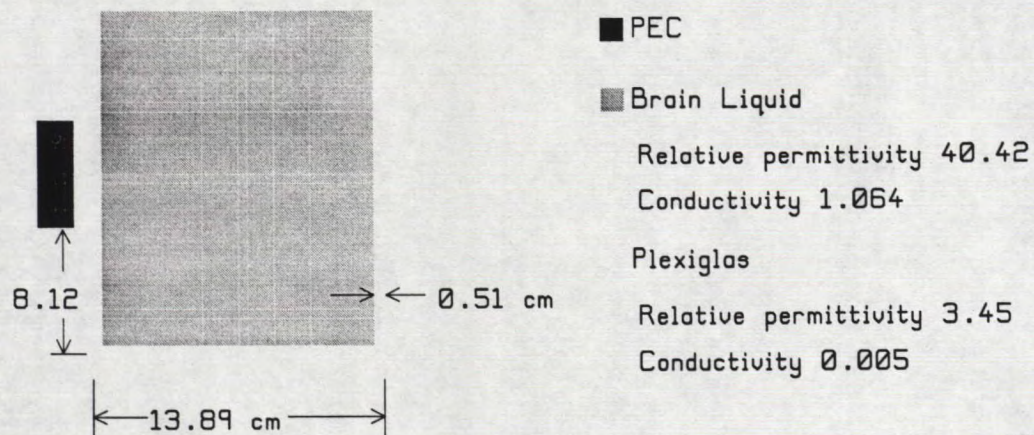


FIG4B.LAB

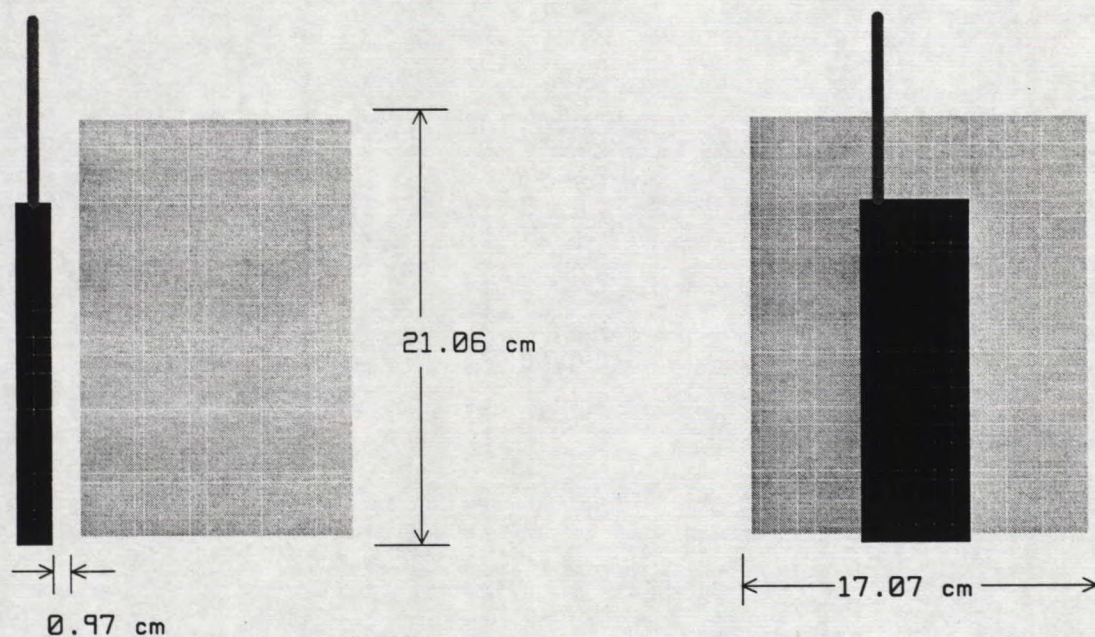


Fig. 4.2 The handset and box head, showing the relative position of the handset to the box head[10].

Handset and Box Head
FDTD Computation
4.41 mm cell size

RADIATED FIELD
FREQUENCY = 850.00 MHz
DECIBEL SCALE
CONICAL CUT
 $\Theta = 90^\circ$

FDTD
— E-THETA
— E-PHI
— ISOTROPIC LEVEL

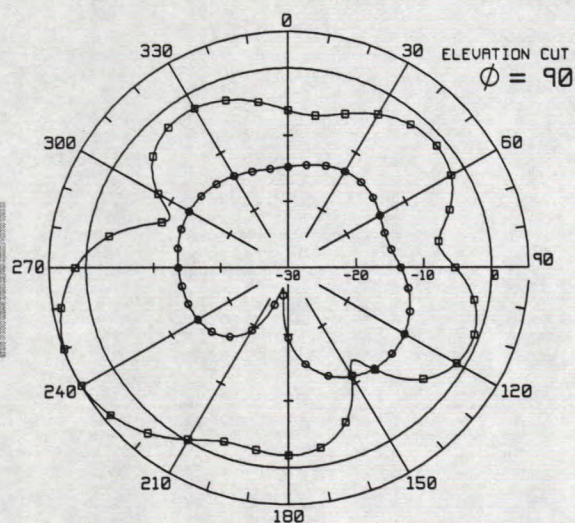
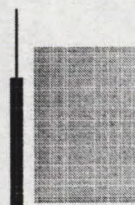
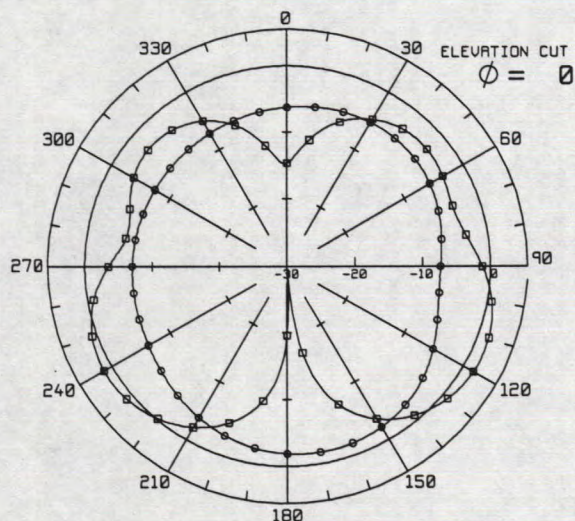
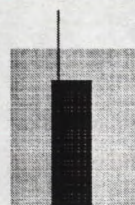
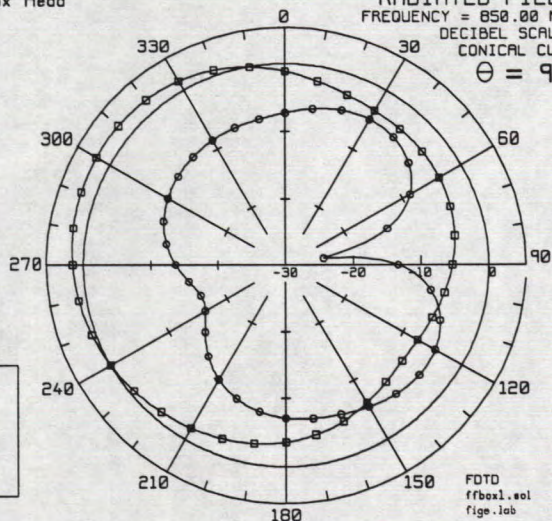
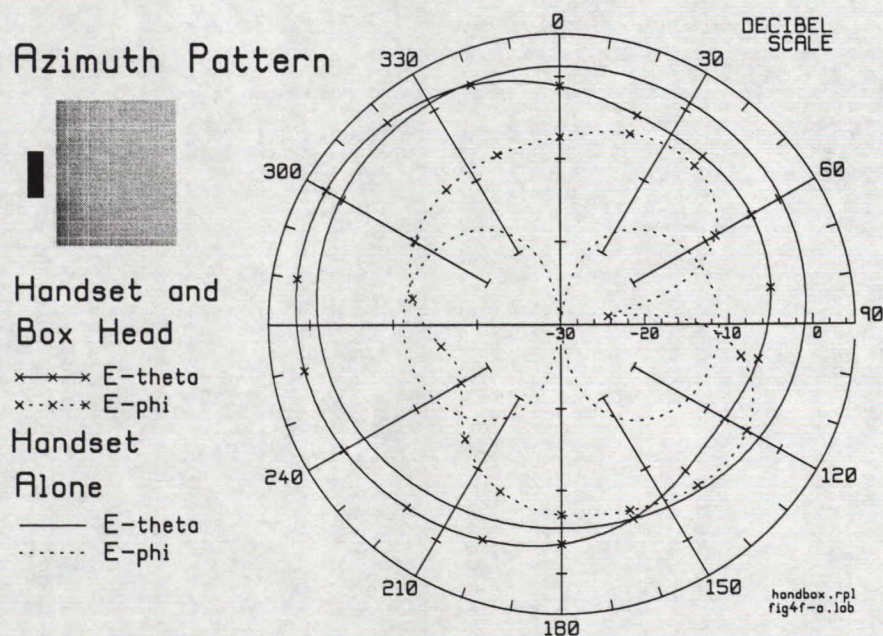


Fig. 4.3 The principal plane patterns of the handset and box head, computed with FDTD with a cell size of 4.41 mm.



(a) Azimuth pattern.

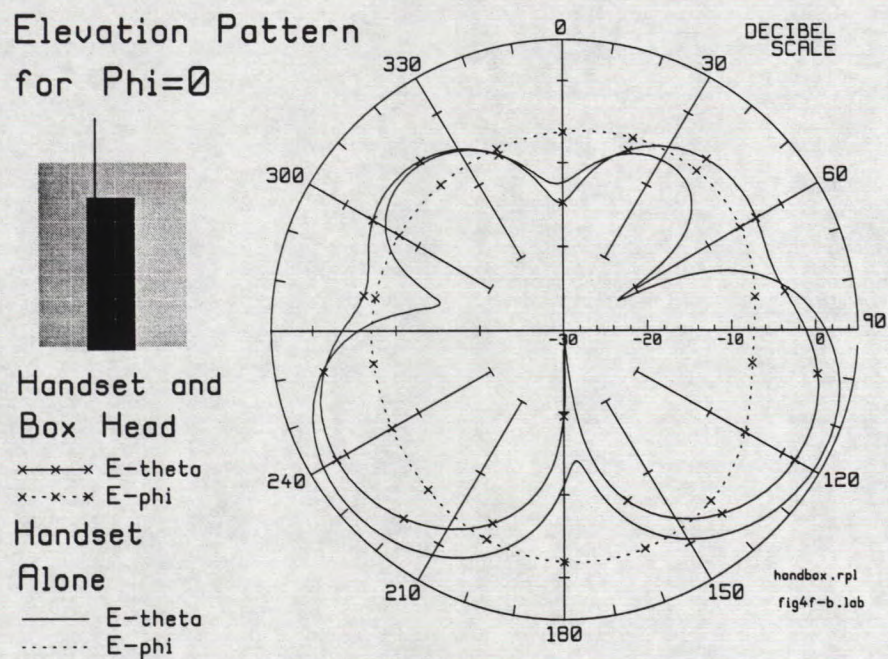
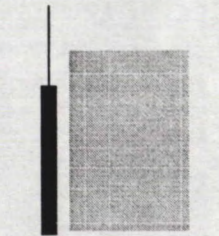
(b) Elevation pattern for $\phi = 0$ degrees.

Fig. 4.4 Effect of the box head on the radiation patterns of the handset.

Elevation Pattern for $\Phi=90$



Handset and
Box Head

x-x-x E-theta
x-x-x-x E-phi

Handset
Alone

— E-theta
..... E-phi

(c) Elevation pattern for $\phi = 90$ degrees.

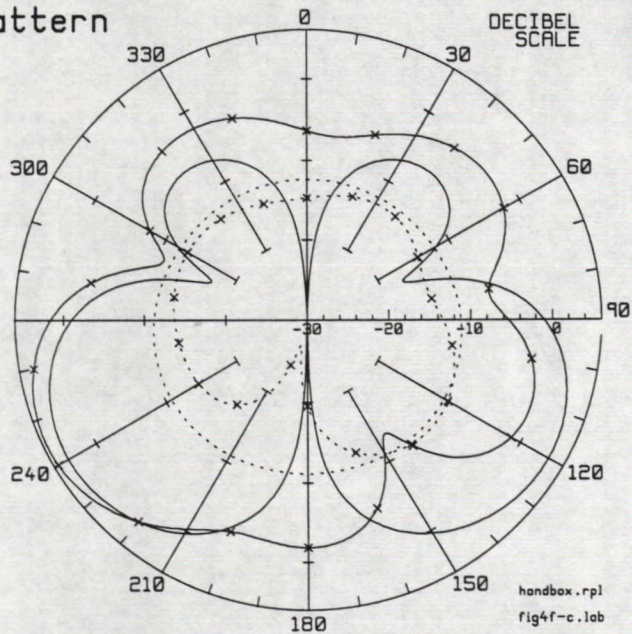


Fig. 4.4 (continued) Effect of the box head on the radiation patterns of the handset.

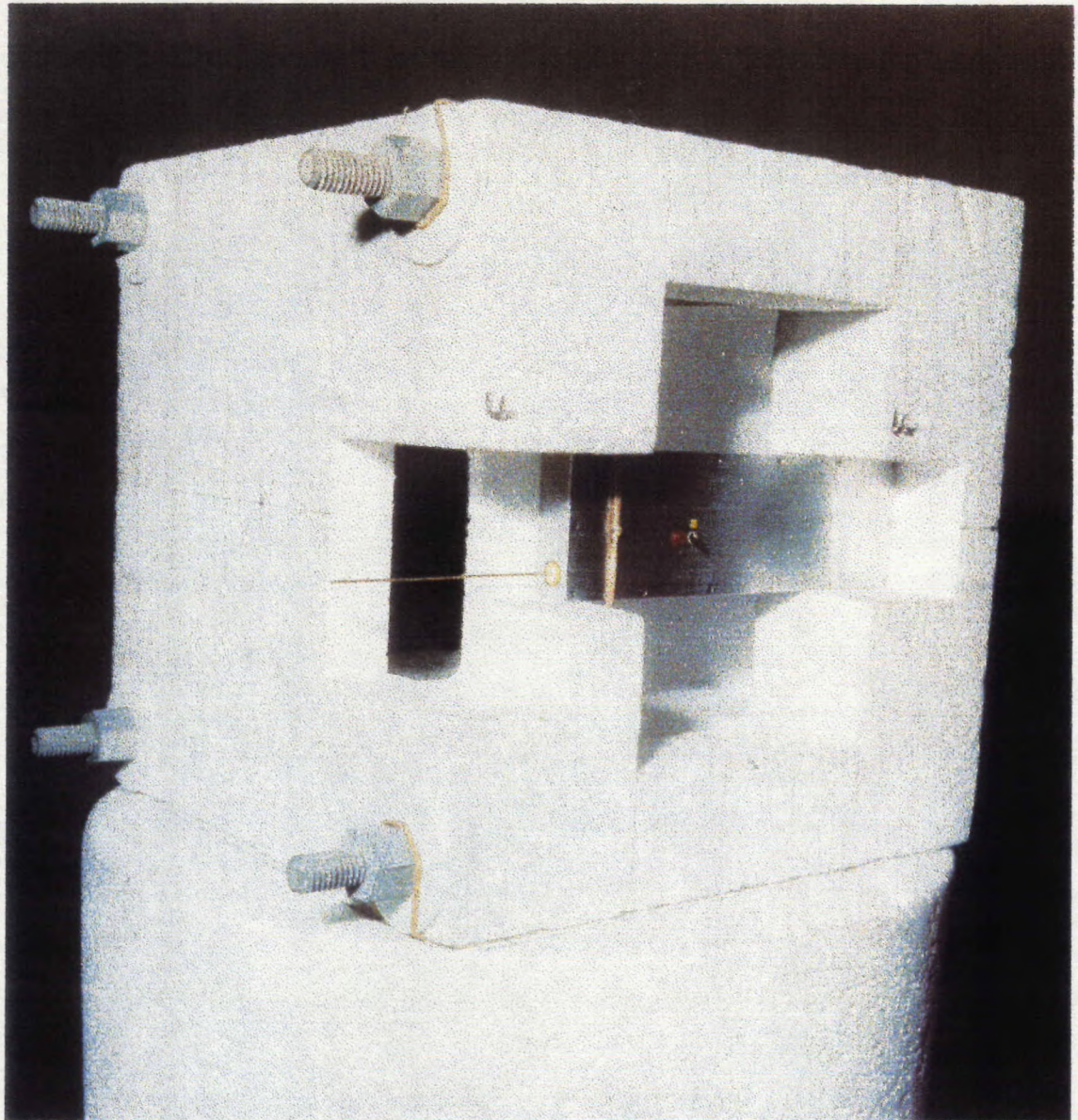


Fig. 4.5 The handset mounted in the jig which will hold the box head[10].

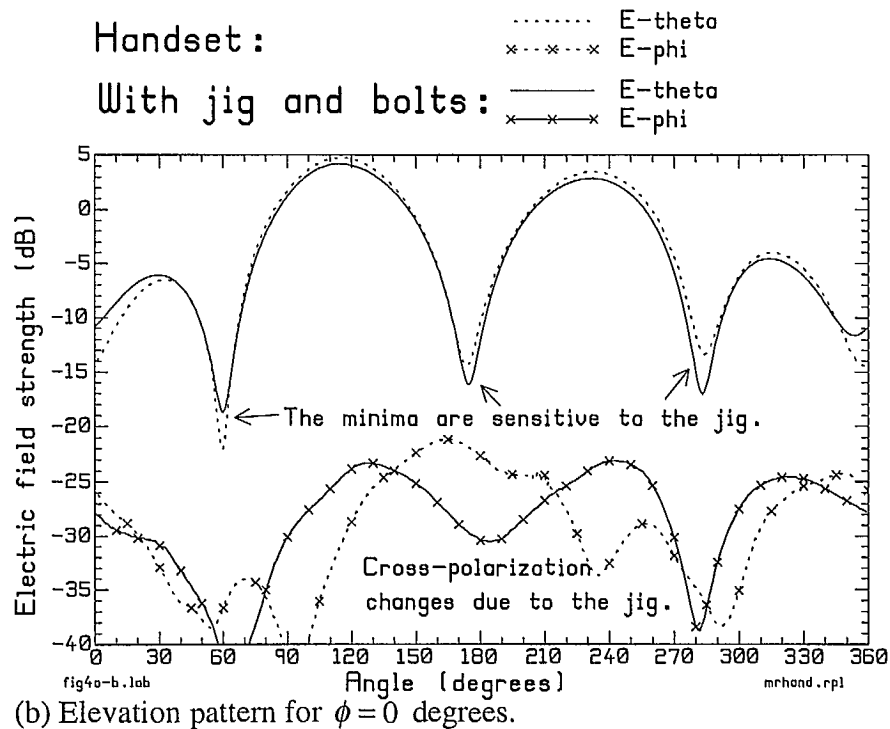
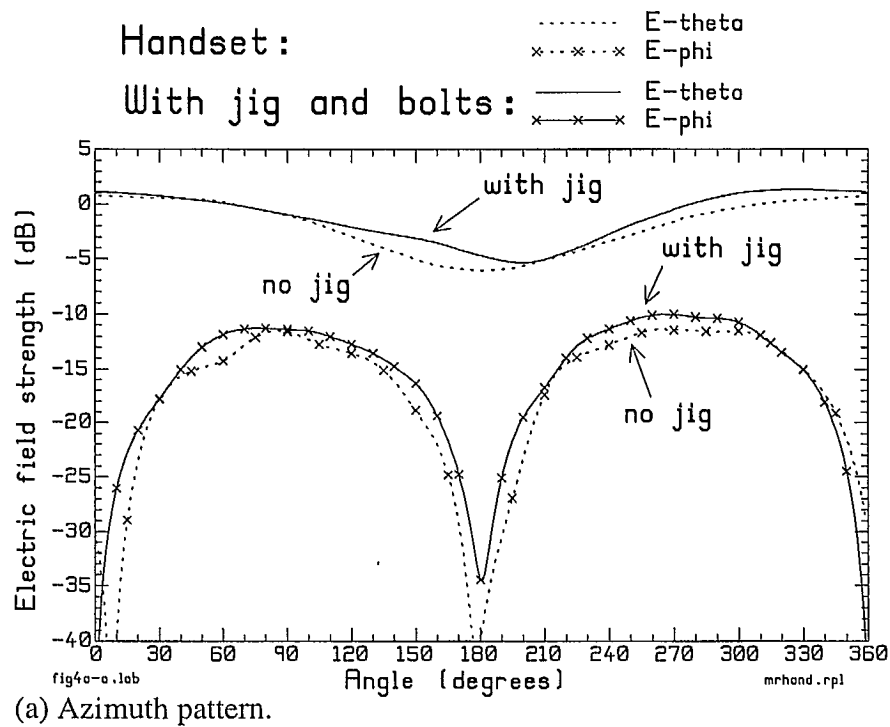


Fig. 4.6 Comparison of the measured radiation patterns of the handset alone and of the handset in the styrofoam jig including fiberglass nuts and bolts.

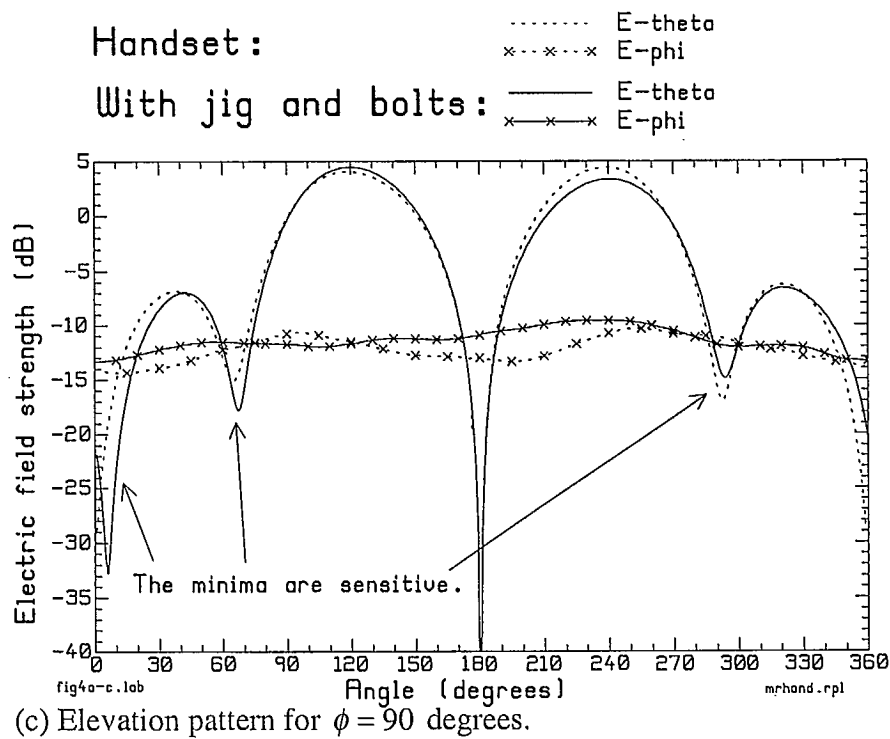


Fig. 4.6 (continued) Comparison of the measured radiation patterns of the handset alone and of the handset in the styrofoam jig including fiberglass nuts and bolts.

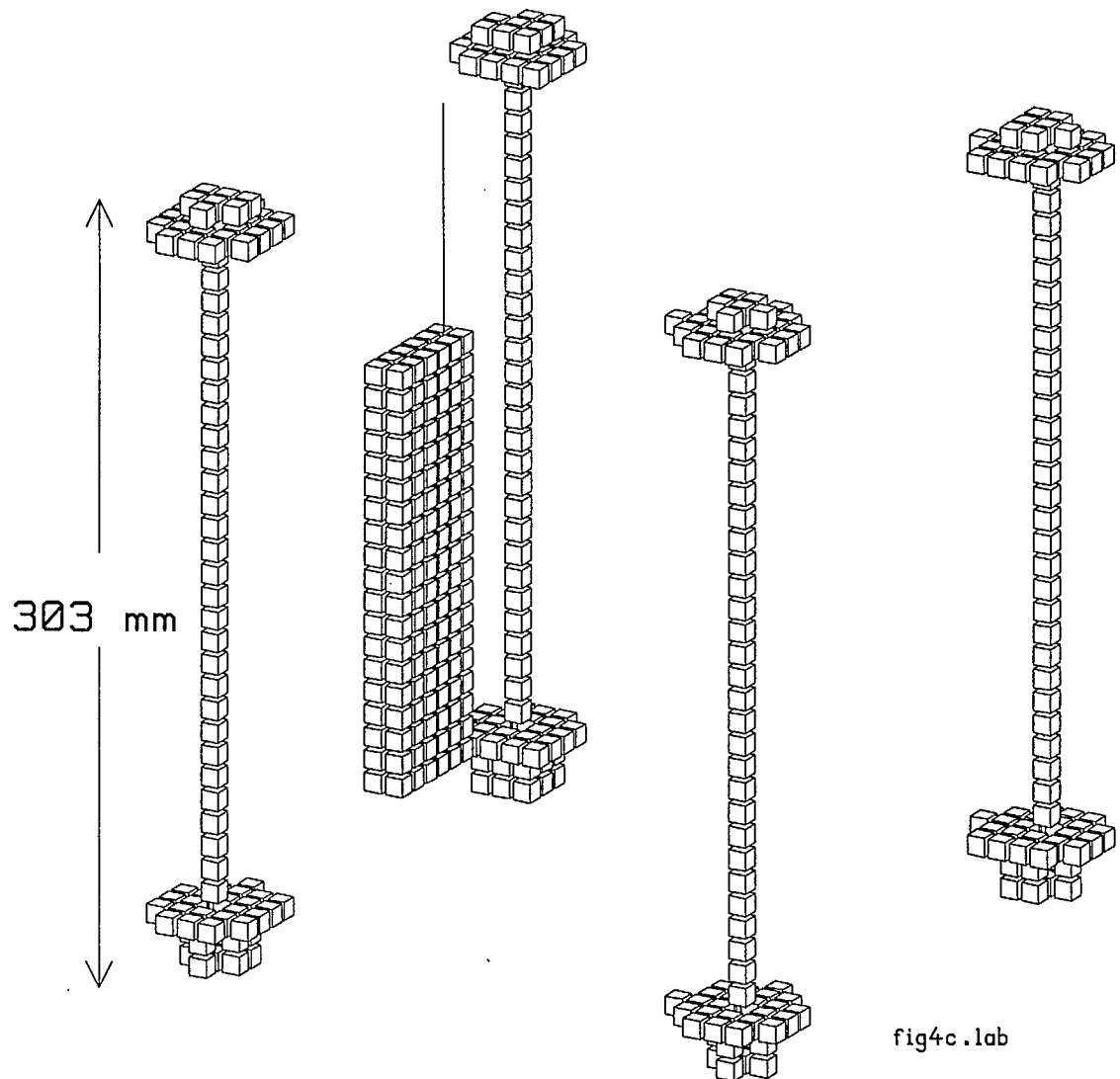


Fig. 4.7 The FDTD model of the handset and the four fiberglass bolts, with plexiglas nuts and washers, using a cell size of 8.82 mm.

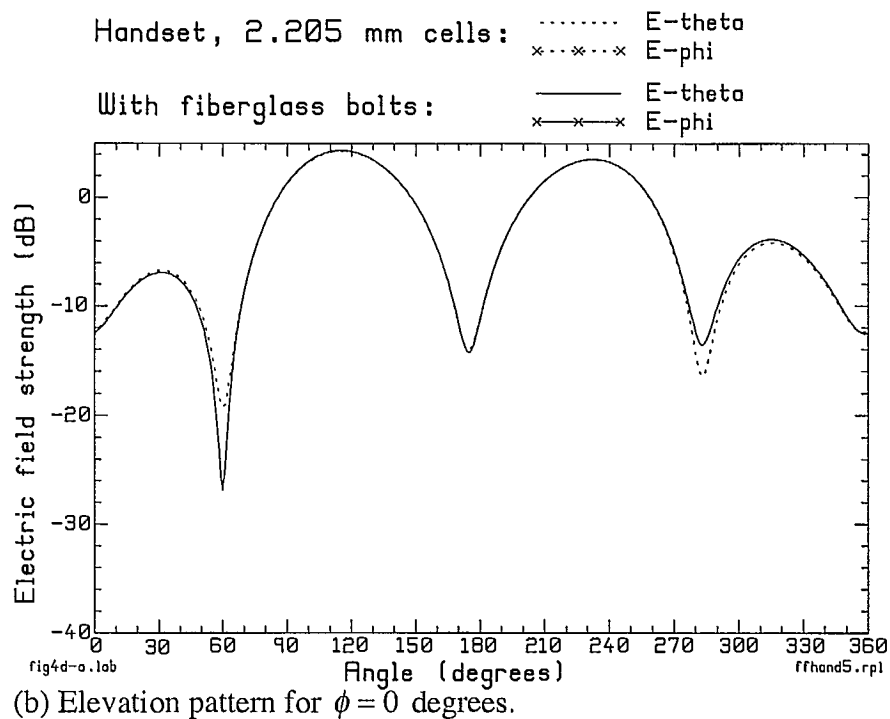
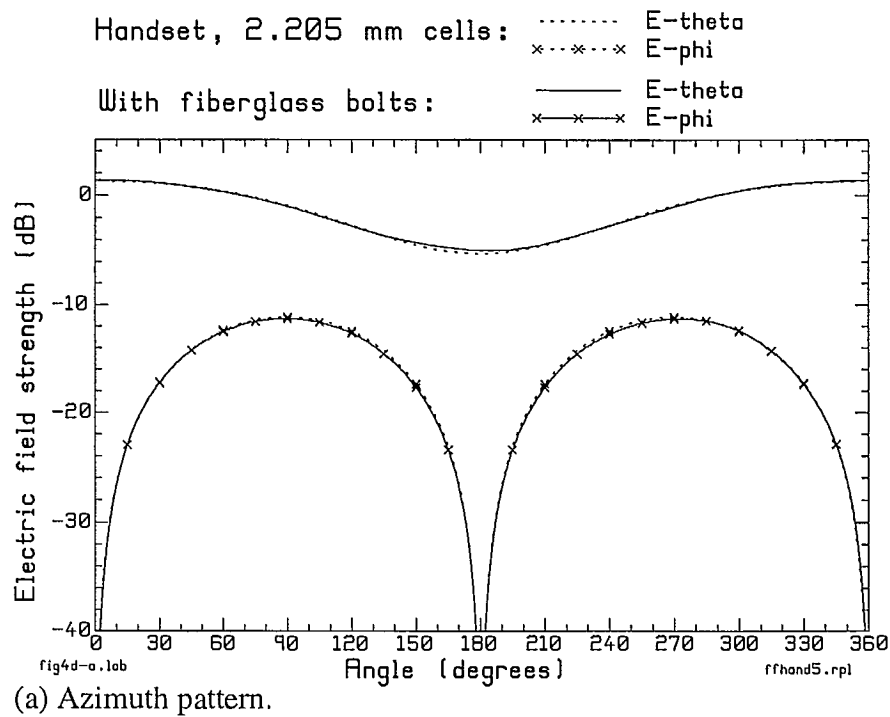


Fig. 4.8 Comparison of the computed radiation patterns of the handset alone and of the handset and the fiberglass nuts and bolts, using a cell size of 2.205 mm.

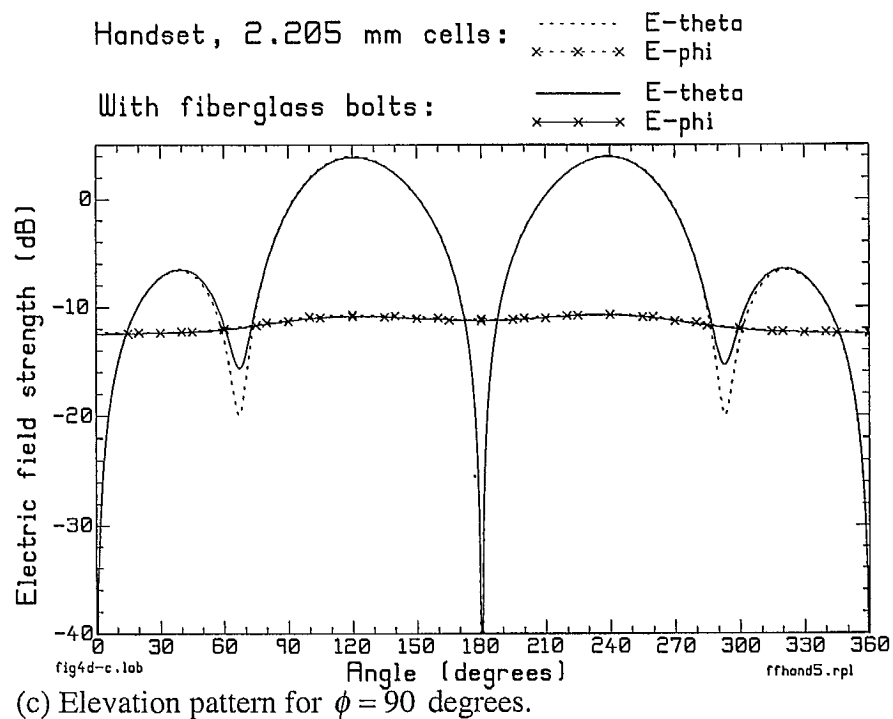


Fig. 4.8 (continued) Comparison of the computed radiation patterns of the handset alone and of the handset and the fiberglass nuts and bolts, using a cell size of 2.205 mm.

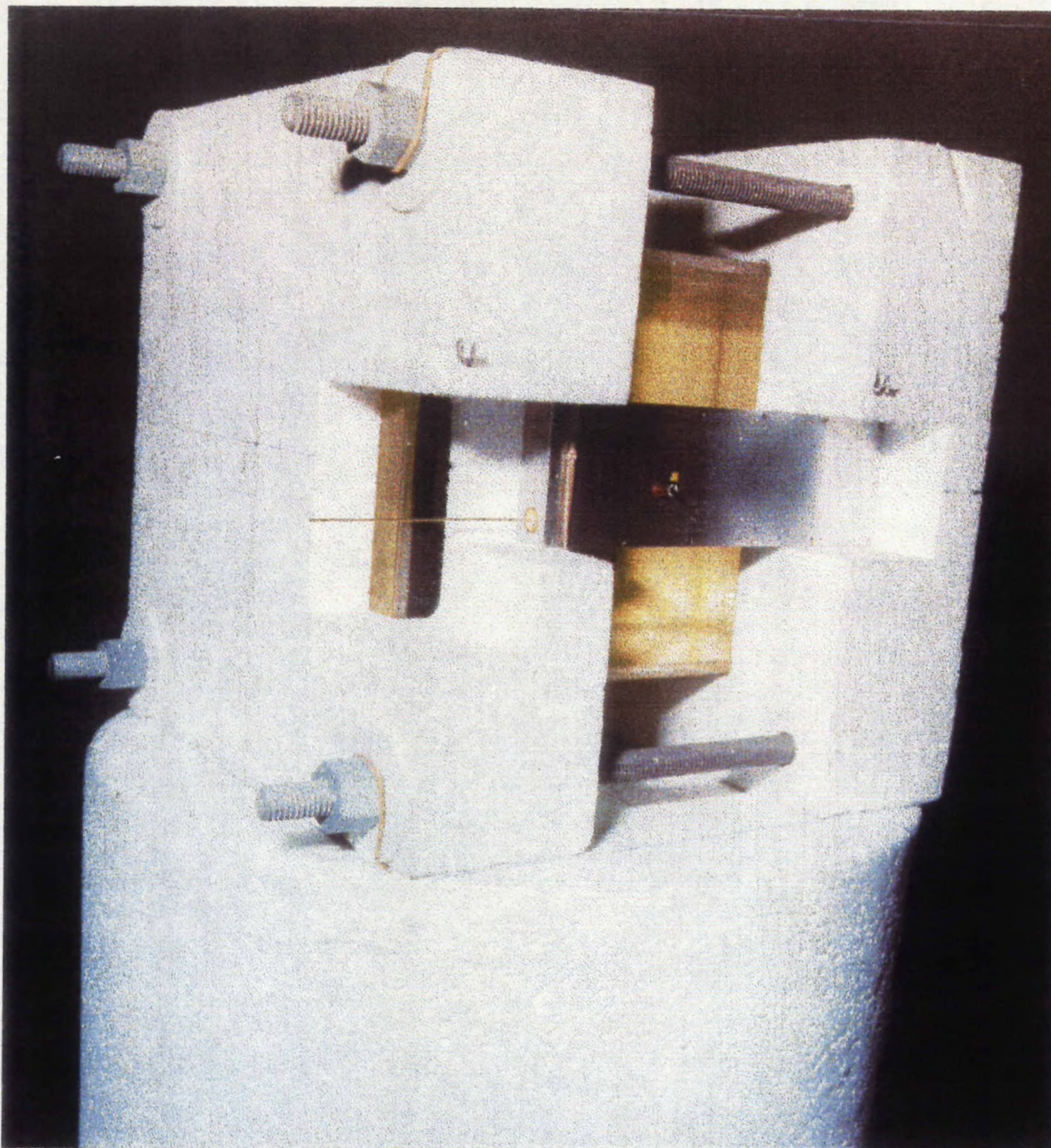
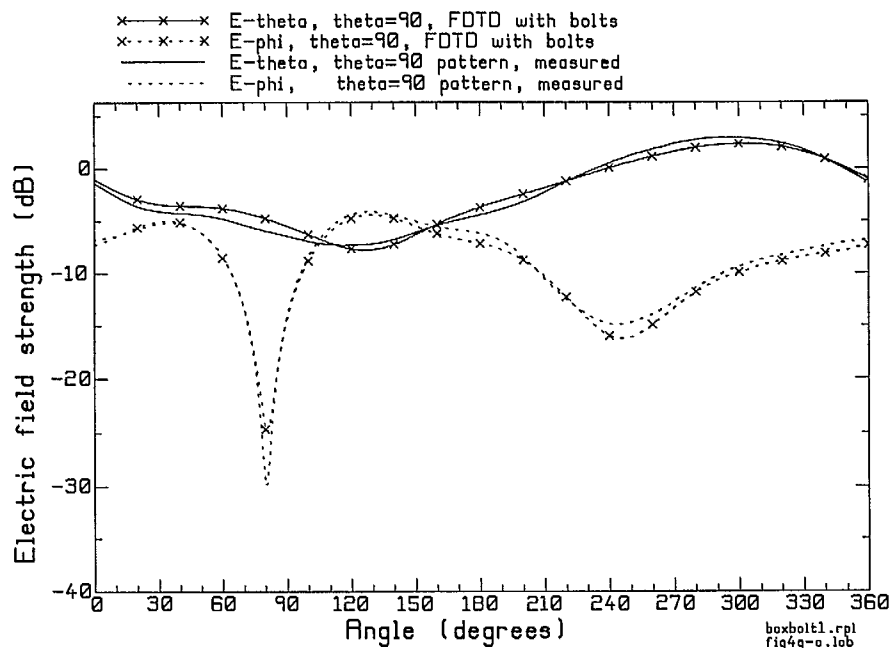


Fig. 4.9 The handset and box head in a jig which holds the handset in a well-known position relative to the box head[10].



(a) Azimuth pattern.

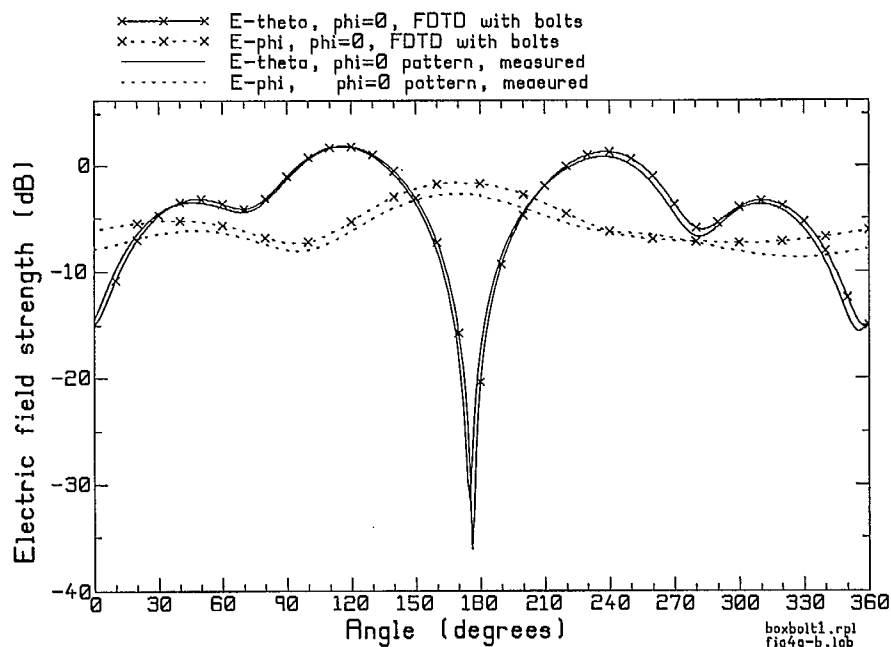
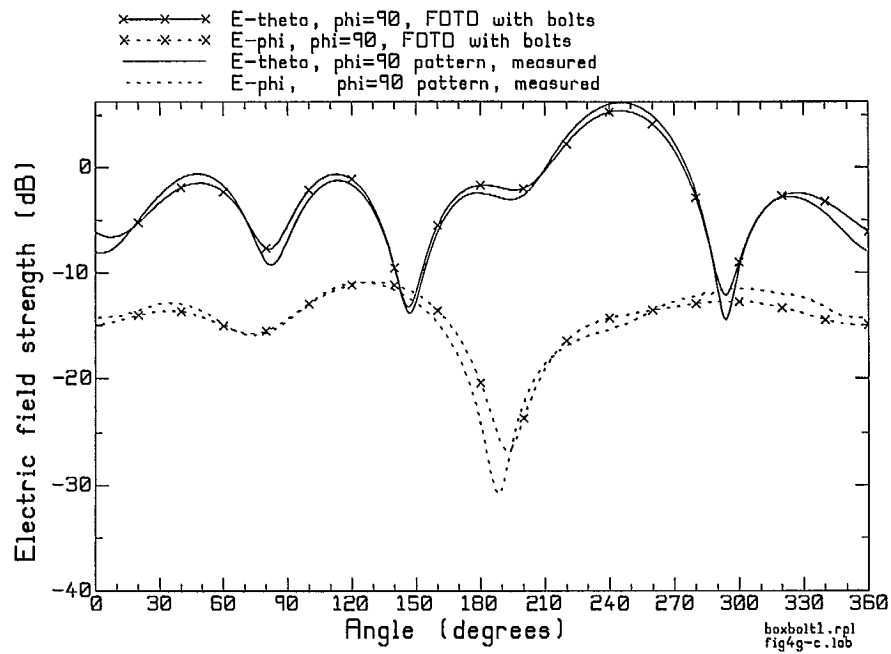
(b) Elevation pattern for $\phi = 0$ degrees.

Fig. 4.10 Comparison of the measured radiation patterns of the handset and box head with the computed patterns, including the fiberglass bolts.



(c) Elevation pattern for $\phi = 90$ degrees.

Fig. 4.10 (continued) Comparison of the measured radiation patterns of the handset and box head with the computed patterns, including the fiberglass bolts.

Chapter 5

Radiation Patterns of the Handset and Sphere Head

This chapter models the head as a sphere, as shown in Fig. 5.1. The sphere is a much more realistic approximation of the shape of the head than is a rectangular box. However, the curved surface of the sphere is less well approximated by a staircase of cubical FDTD cells than is the flat surface of the box. This chapter compares the computed radiation patterns for the handset and sphere head with those measured at CRC[10]. Since the representation of the geometry in the model is poorer for the sphere, we expect poorer agreement with the measured radiation patterns than was reported in the last chapter. The degree of agreement between the computations and measurements for the sphere may be representative of the errors incurred using FDTD to solve an anatomical model of the head.

The sphere head is a thin-walled plexiglas sphere filled with liquid simulating the permittivity and the conductivity of the brain[21]. The sphere is 20.68 cm in diameter with a wall thickness of 3.65 mm. Fig. 5.2 shows the actual position of the handset relative to the sphere, derived from the mechanical drawings[32]. The bottom of the handset is aligned with the bottom of the sphere. The handset is separated from the sphere by 9.3 mm, and is approximately centered on the sphere in a back-to-front sense.

5.1 FDTD Model of the Handset and Sphere Head

The sphere geometry is approximated in Fig. 5.2 with a staircase of 4.41 mm FDTD cells. The 3.65 mm plexiglas wall thickness is modeled with one FDTD cell. The sphere is 47 cells or 20.73 cm in diameter, compared to a true diameter of 20.68 cm. The surface of the sphere is staircased as shown in three cross-sections in Fig. 5.2. The cross-sections in the xy plane were edited by hand so that no cell filled with brain liquid has a common edge with any free-space cell; however in the xz and yz planes there are brain liquid cells "touching" free-space cells. The handset is two cells from the surface of the sphere, or 8.82 mm, compared to 9.3 mm in the true geometry. The fiberglass bolts and plexiglas nuts and washers are not included in the computation.

The liquid simulating the brain has a relative permittivity of 40.42 and a conductivity of 1.064 S/m, corresponding to the mixture used in the measurement[33]. The relative permittivity and conductivity of the plexiglas wall are 3.45 and 0.005 S/m, respectively.

The FDTD model uses a space size of 67 by 73 by 78 cells. The space is terminated with a PML 6 cells thick, having a surface reflection coefficient of 60 dB and parabolic progression of the conductivity. Four cells of free space separate the surfaces of the handset and sphere from the inner surface of the PML. The FDTD model was run for 4096 time steps, sufficient for the fields inside the head to reach steady state in response to a sinusoidal generator at 850 MHz.

5.2 The Radiation Patterns of the Handset and the Sphere Head

Fig. 5.3 shows the principal plane radiation patterns of the handset operating near the sphere head. Fig. 5.3(a) shows the azimuth pattern. As remarked in Chapter 4, we are looking from below. The user faces in the 0 degree direction, with his left hand at 90 degrees and his right hand at 270 degrees. The E_θ field strength is above the isotropic level from about 240 degrees to 360 degrees, where the head is behind the handset. The maximum field strength is 2.0 dB at 304 degrees. However, when the handset lies behind the head, from 0 to 180 degrees, the field is below the isotropic level and falls to a minimum of -14.2 dB at 142 degrees. The cross-polarization has a maximum of -2.3 dB at 130 degrees. The cross-polarized field is five to ten dB lower than the principal polarization when the head is behind the handset, but is comparable to the principal polarization when the handset is behind the head.

Fig. 5.3(b) shows the elevation pattern for $\phi = 0$. The E_θ polarization has main lobes directed towards the ground, of 2.00 dB at 114 degrees and 0.8 dB at 236 degrees. The minor lobes are directed upwards, of -4.9 dB at 38 degrees and 7.8 dB at 311 degrees. The E_ϕ polarization is very roughly circular in shape, with a maximum field strength of -3.6 dB at 39 degrees, and a minimum of -13.5 dB at 218 degrees.

The $\phi = 90$ elevation pattern is shown in Fig. 5.3(c). On the right side of the head, near 270 degrees, where the head lies behind the handset, there is a large lobe in the field strength directed towards the ground, at 5.8 dB and 243 degrees. There is a minimum of -14.6 dB at 292 degrees, and a small broad lobe of field -1.9 dB at 325 degrees. Where the handset lies behind the head, there is a lobe of -3.2 dB at 49 degrees, a minimum of -17.0 dB at 78 degrees, a larger lobe reaching 1.4 dB at 116 degrees, and a deep, sharp minimum of -24.4 dB at 155 degrees. The cross-polarized field has a maximum value of -10.7 dB at 122 degrees.

5.3 Changes in the Handset Patterns due to the Sphere Head

Fig. 5.4 compares the radiation patterns of the handset and sphere head with the patterns of the handset alone. The patterns are compared on the basis of equal radiated power. Due to power dissipation in the lossy materials of the head, the input power to the handset is larger for the handset and head problem.

Fig. 5.4(a) compares the azimuth patterns. The field strength in E_θ is generally larger on the operator's right side between 190 and 310 degrees, where the head lies behind the handset. For instance, at 270 degrees the field strength of the handset and head is 1.3 dB compared to -1.0 dB for the handset alone. Conversely, where the handset lies behind the head the field in E_θ is generally lower, from 0 to 180 degrees. Thus at 90 degrees, the handset-alone field is -1.0 dB and the handset and head field is -5.2 dB. The handset and head field strength has a minimum of -14.2 dB at 142 degrees. The cross-polarized field, E_ϕ , is generally much larger in the presence of the head. Thus for the

handset alone, the cross-polarized field has a maximum of -11.2 dB; for the handset and head the maximum is -2.3 dB.

In the elevation cut for $\phi = 0$ in Fig. 5.4(b), the pattern for E_θ is nearly the same shape for the handset alone as for the handset and head. The main difference is that in the presence of the head, the sharp minima at 61 degrees and 176 degrees are filled in. The large, downward-directed lobes for the handset alone at 4.3 dB, 117 degrees and 3.5 dB, 233 degrees are reduced in level to 2.0 dB at 114 degrees and 0.8 dB at 236 degrees. The minor lobe at -3.8 dB, 315 degrees is reduced to -7.8 dB, 311 degrees. With the head near the handset, there is a cross-polarized field, which has a maximum value of -3.6 dB at 37 degrees and a minimum of -13.5 dB at 219 degrees.

The $\phi = 90$ elevation pattern is similar in shape in E_θ for the handset alone and for the handset and sphere head. With the head behind the handset, the major lobe at 4.0 dB, 240 degrees is enhanced to 5.8 dB, 242 degrees. The minor lobe at -6.2 dB, 621 degrees rises to -1.9 dB at 326 degrees. With the handset behind the head, the field strengths are reduced over part of the pattern. Thus the lobe at 4.0 dB 121 degrees is reduced to 1.4 dB at 116 degrees. However the lobe for the handset alone at -6.2 dB, 39 degrees is increased to -3.3 dB at 50 degrees. The cross-polarized field in this pattern is not greatly different in maximum level for the handset alone and for the handset and head. In both cases the field is -10.7 dB at 124 degrees. However with the head there are minima in the cross-polarized field of -16.9 dB at 54 degrees and -20.0 dB at 188 degrees.

In summary the sphere head changes the handset's radiation patterns in a way that is quite similar to the box head. The handset and sphere head patterns more closely resemble the patterns of the handset alone than the handset and box head patterns, perhaps because the sphere curves away from the handset and puts much less dielectric material near the feed point of the antenna. In general, the E_θ polarization is enhanced when the head lies behind the handset and reduced when the head is between the handset and the observer.

5.4 Comparison with the Measured Radiation Patterns

A mounting jig was constructed for the sphere head, Fig. 5.5, which is very similar to that for the box head, discussed in the last chapter. The jig holds the handset in a well-known position relative to the sphere. The location is given in Fig. 5.2. The jig consists of a styrofoam bottom piece and top piece, which hold the sphere between them. The styrofoam pieces are held together by four fiberglass bolts, with eight plexiglas nuts and washers, as for the box head. The elastic band seen in Fig. 5.5 holds the handset in place when the jig is being handled, and was removed during the measurement.

Chapter 4 investigated the changes in the radiation pattern of the handset when the four fiberglass bolts were included in the computational model. The bolts had little effect on the radiation patterns, except in the minima. For the present purpose the bolts were not included in the computation. Thus in Fig. 5.6 the computed radiation patterns of the handset and sphere head, modeled with 4.41 mm cells, but with no bolts, are compared with the measured patterns.

Fig. 5.6(a) shows the measured and computed azimuth patterns. The maximum E_θ in the measured pattern is 2.9 dB at 300 degrees, compared to 2.0 dB at 303 degrees

in the computation. The measured pattern has its minimum field strength of -11.4 dB at 141 degrees, compared to -14.2 dB at 143 degrees in the computation. In the E_ϕ component, the measured field has a maximum at -3.3 dB, 134 degrees, compared to -2.3 dB, 132 degrees in the computation. The lobe at -4.4 dB, 33 degrees in the measurement is found at -3.1 dB, 35 degrees in the computation. The measured minimum at -12.6 dB, 278 degrees is found at -11.5 dB, 277 degrees in the computation. The deep minimum at -30.3 dB, 83 degrees in the measurement is found at -22.5 dB, 81 degrees in the computation. But we should be wary of comparing deep, sharp minima, which are affected by the range from the handset and head to the receive horn in the measurement, and by the cell size in the computation. Both measurement and computation are affected by the presence of the fiberglass bolts.

Fig. 5.6(b) shows the measured and computed elevation pattern for $\phi = 0$ degrees. The main lobes in the pattern in E_θ agree remarkably well. The lobe at 2.01 dB, 115 degrees in the measurement falls at 1.96 dB, 115 degrees in the computation. The lobe at 0.69 dB, 235 degrees in the measurement is found at 0.75 dB, 235 degrees in the computation. However the minima in this pattern agree less well. The minimum at -8.8 dB, 62 degrees in the measurement is found at -6.7 dB, 65 degrees in the computation. The minimum at -15.0 dB, 286 degrees in the measurement falls at -11.8 dB, 285 degrees in the computation. The cross-polarized field has much the same shape in the measurement and the computation, but the measured field strength is somewhat lower than the computed field throughout the pattern. The maximum measured field in E_ϕ is -4.4 dB at 38 degrees, compared to -3.6 dB at 39 degrees. The lowest measured field in E_ϕ is -18.6 dB at 216 degrees, much lower than the computed field of -13.5 dB at 219 degrees.

The elevation pattern for $\phi = 90$ degrees is shown in Fig. 5.6(c). In the principal polarization, E_θ , the largest lobe falls at 6.2 dB, 246 degrees in the measurement, corresponding to 5.8 dB, 243 degrees in the computation. The next largest lobe is 1.2 dB, 116 degrees in the measurement compared to 1.4 dB, 115 degrees in the computation. The minor lobe at -3.3 dB, 325 degrees in the measurement falls at -1.9 dB, 128 degrees in the computation and agrees less well with the measurement than do the main lobes. The cross-polarized field is generally smaller in the measurement than in the computation, except for the angles from 18 to 58 degrees. The maximum cross-polarized field is -11.4 dB at 124 degrees in the measurement, compared to -10.7 dB, 125 degrees in the computation.

In summary, the agreement between the measurement and the computation in Fig. 5.6 is quite good, especially in the maxima in the elevation patterns. The cross-polarized field for the sphere and box head is generally in better agreement between the computation and the measurement in Fig. 4.10 than is the cross-polarized field for the handset and sphere head in Fig. 5.6. This may be because of the poorer geometric fidelity of the staircased model of the sphere compared to the cell model of the box.

5.5 Conclusion

This chapter has examined the principal plane radiation patterns of the handset operated near the sphere head. The E_θ polarization is generally enhanced when the sphere is behind the handset, and generally reduced when the sphere lies between the handset and the observer. The presence of the sphere tends to fill in the deep minima in the handset-alone patterns. The sphere tends to raise the level of the cross-polarized field. The patterns of the handset and sphere are generally quite similar to those of the handset and box.

This chapter compared the computed radiation patterns of the handset and sphere with measured radiation patterns. The agreement is generally quite good. However, the degree of agreement between the computed and measured patterns for the sphere is not as good as that for the box, particularly in the cross-polarized field component.

Up to this point in this report, the radiation patterns of the handset oriented vertically have been studied. The handset is generally not held in a vertical position when using a cellular phone. The following chapter develops a method for computing the radiation patterns of the handset when it is held at some angle to the vertical, with or without a model of the head. Also, neither the sphere nor the box head are very like a real human head. Later in this report the development of an anatomically realistic model of the head is discussed.

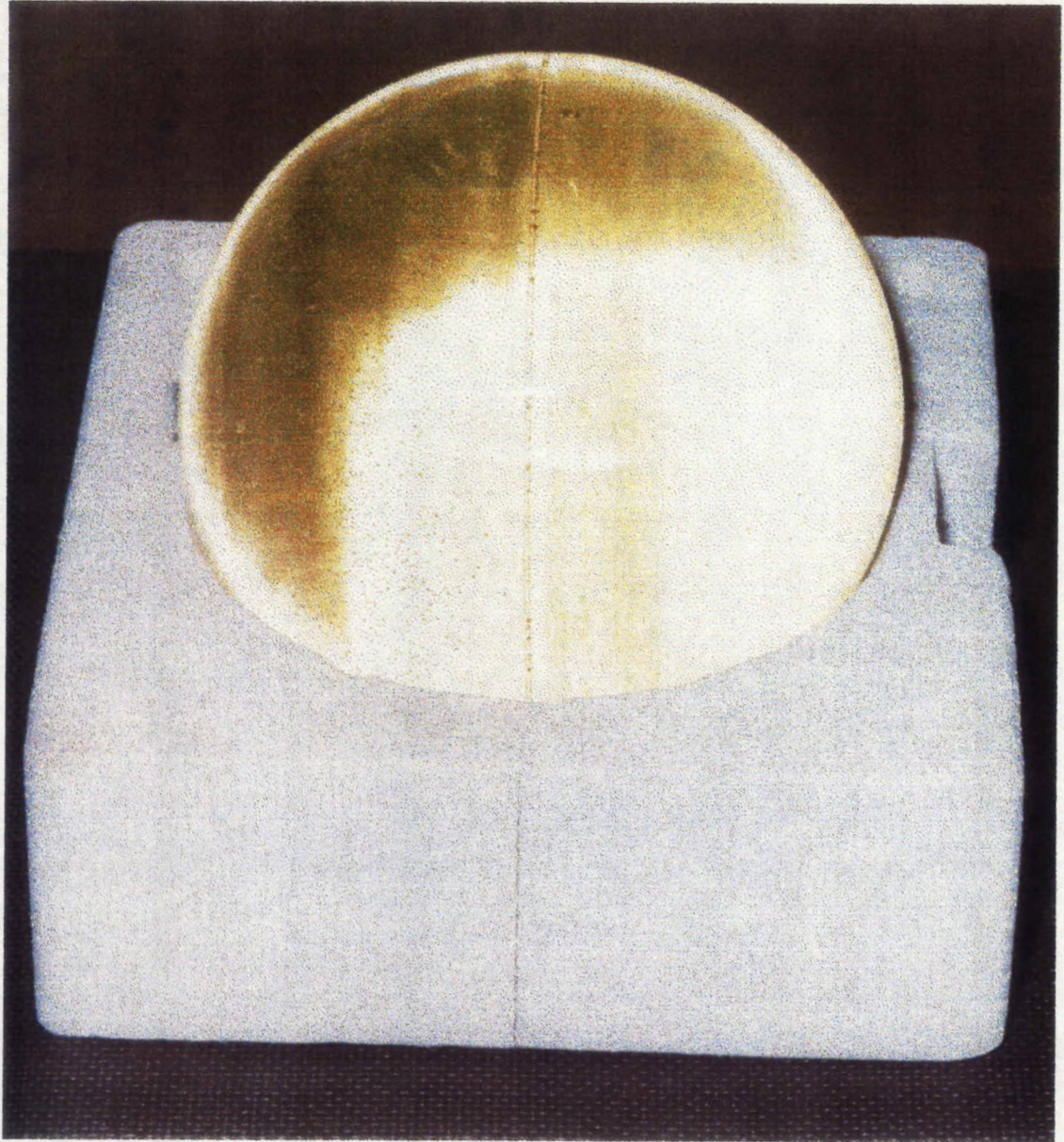


Fig. 5.1 The “sphere head” is a thin-walled plexiglass sphere filled with brain-equivalent liquid[10].

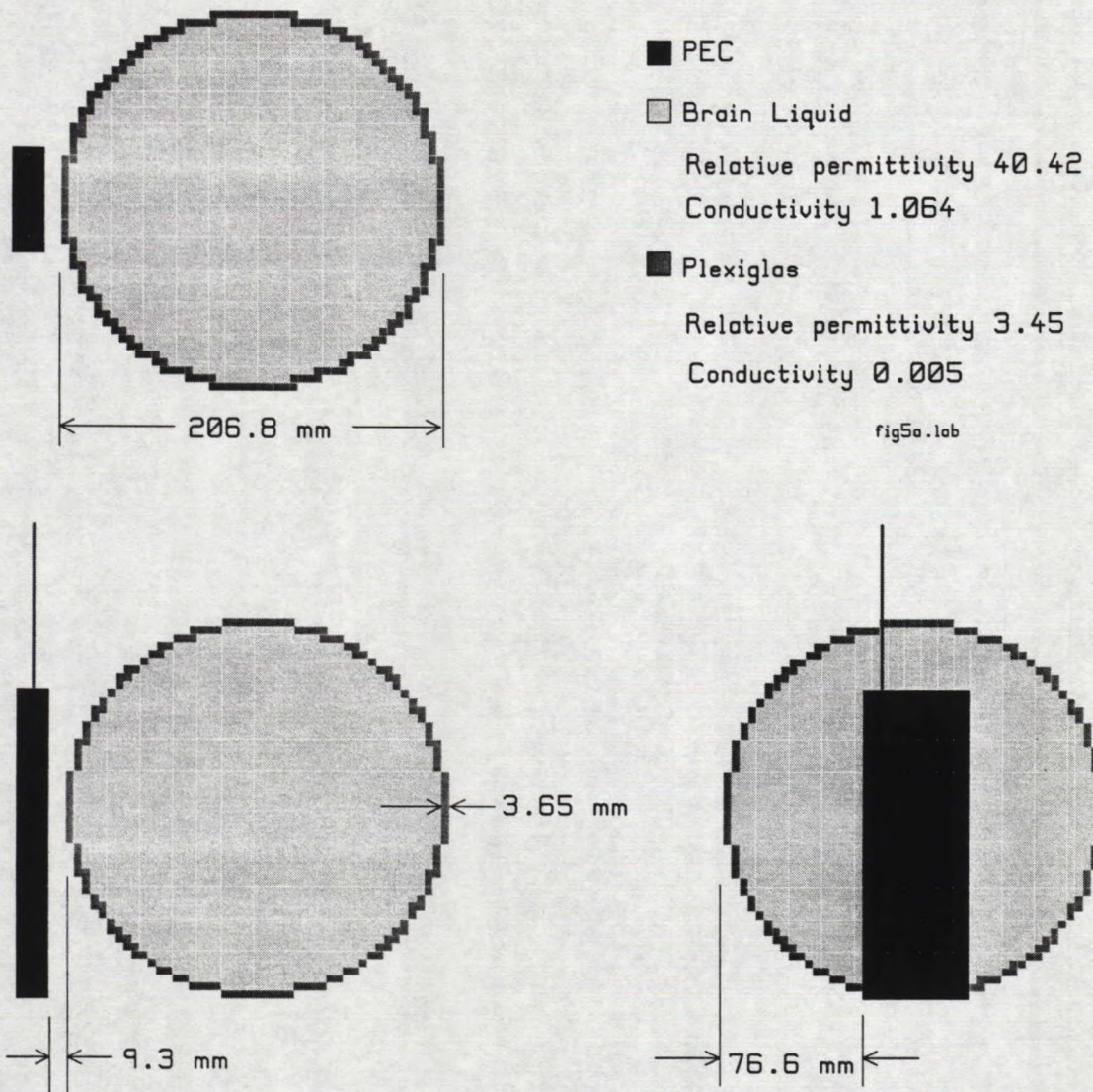


Fig. 5.2 The cell model of the handset and sphere head, showing the relative position of the handset to the sphere.

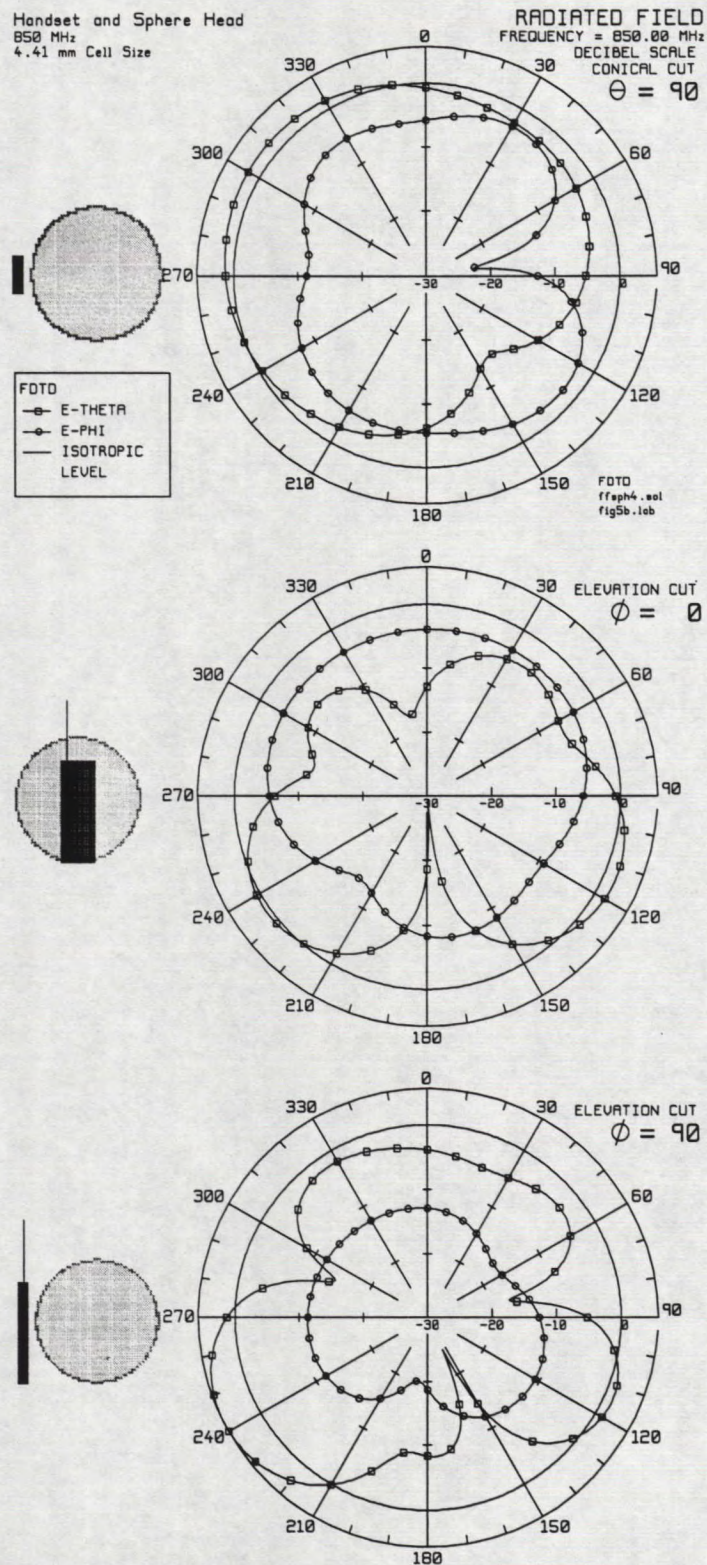
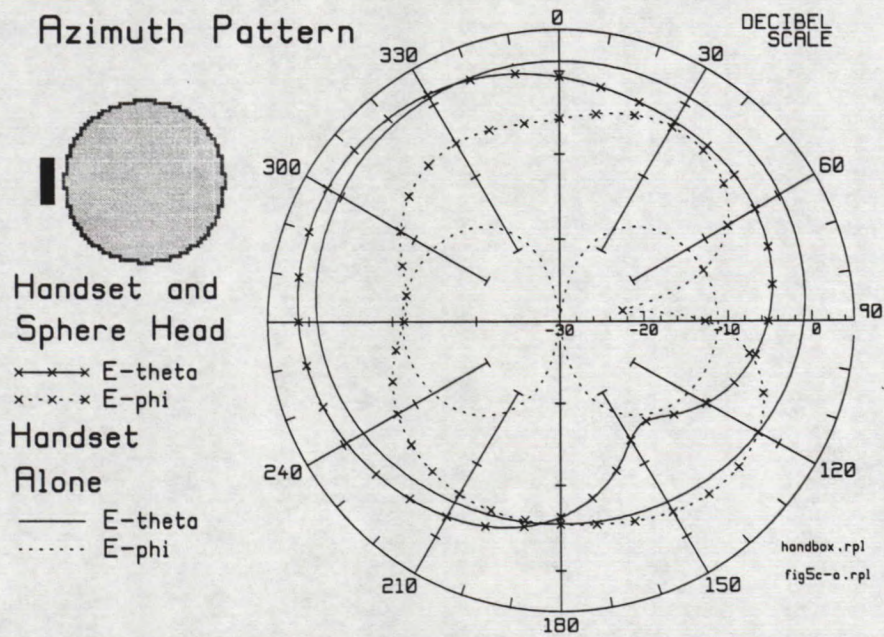


Fig. 5.3 The principal plane patterns of the handset and sphere head, computed with FDTD with a cell size of 4.41 mm.



(a) Azimuth pattern.

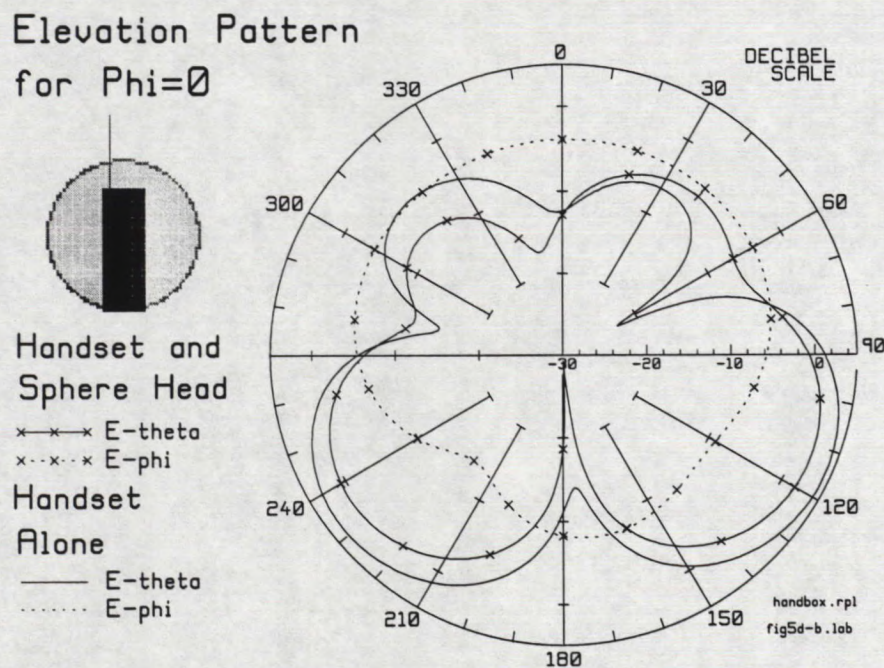
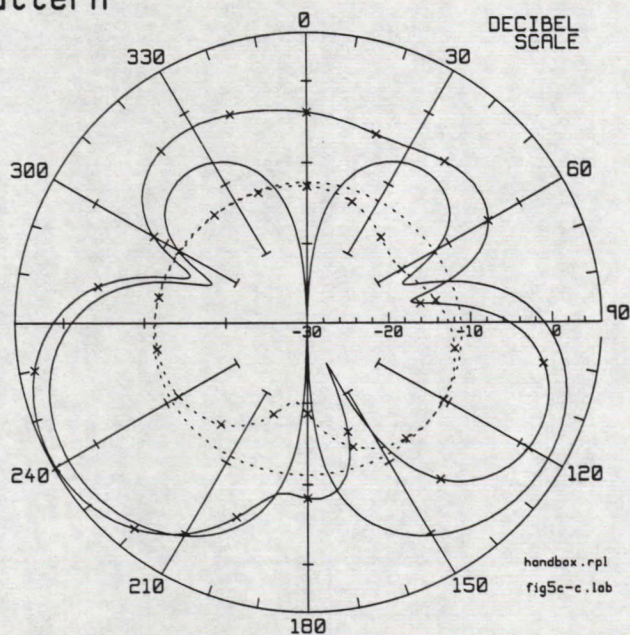
(b) Elevation pattern for $\phi = 0$ degrees.

Fig. 5.4 Effect of the sphere head on the radiation patterns of the handset.

Elevation Pattern for $\Phi=90^\circ$


 Handset and
 Sphere Head
 x-x-x E-theta
 x-x-x E-phi
 Handset
 Alone
 — E-theta
 E-phi



(c) Elevation pattern for $\phi = 90$ degrees.

Fig. 5.4 (continued) Effect of the sphere head on the radiation patterns of the handset.

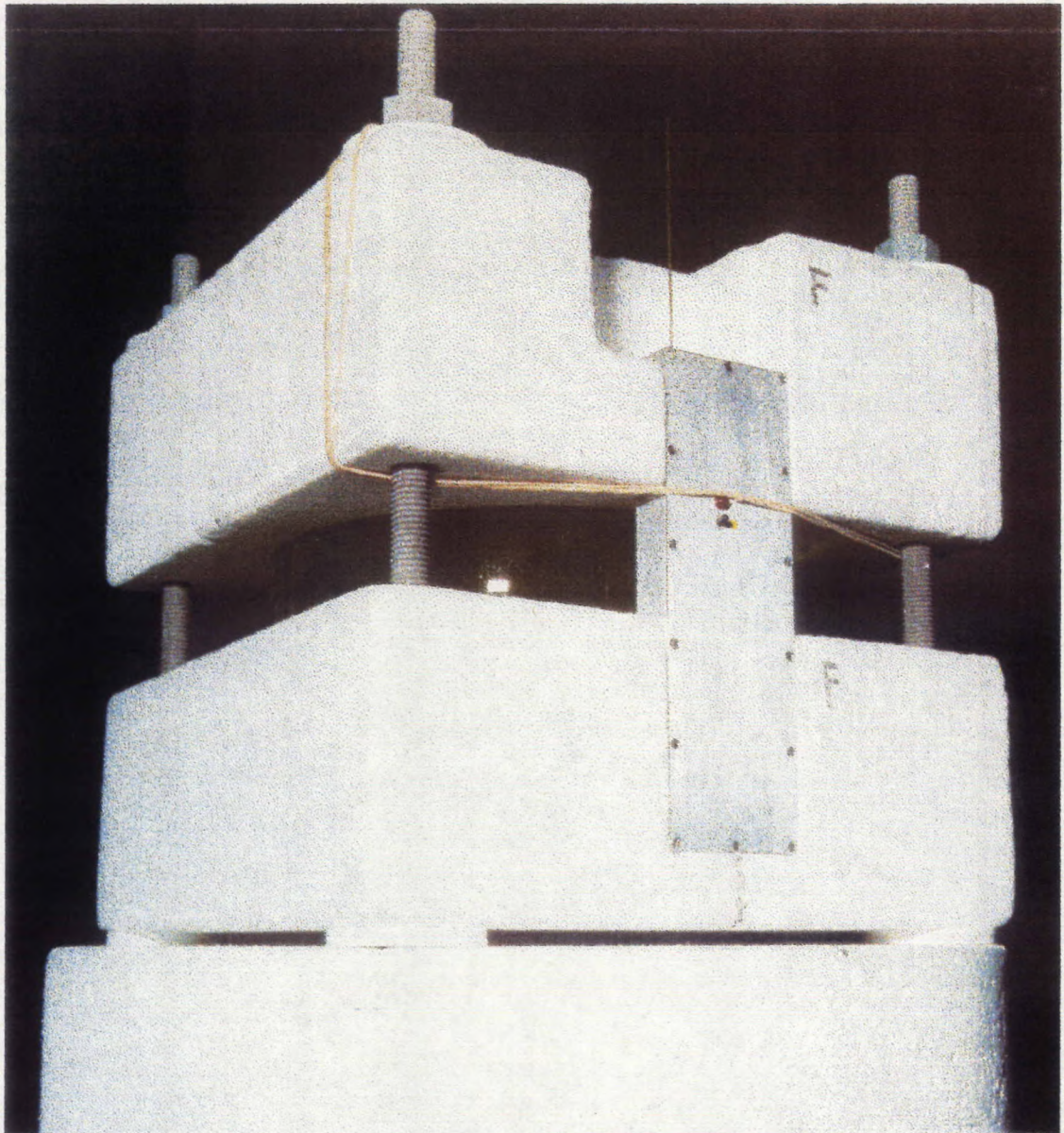


Fig. 5.5 The handset and sphere head in a jig which holds the handset in a well-known position relative to the sphere head[10].

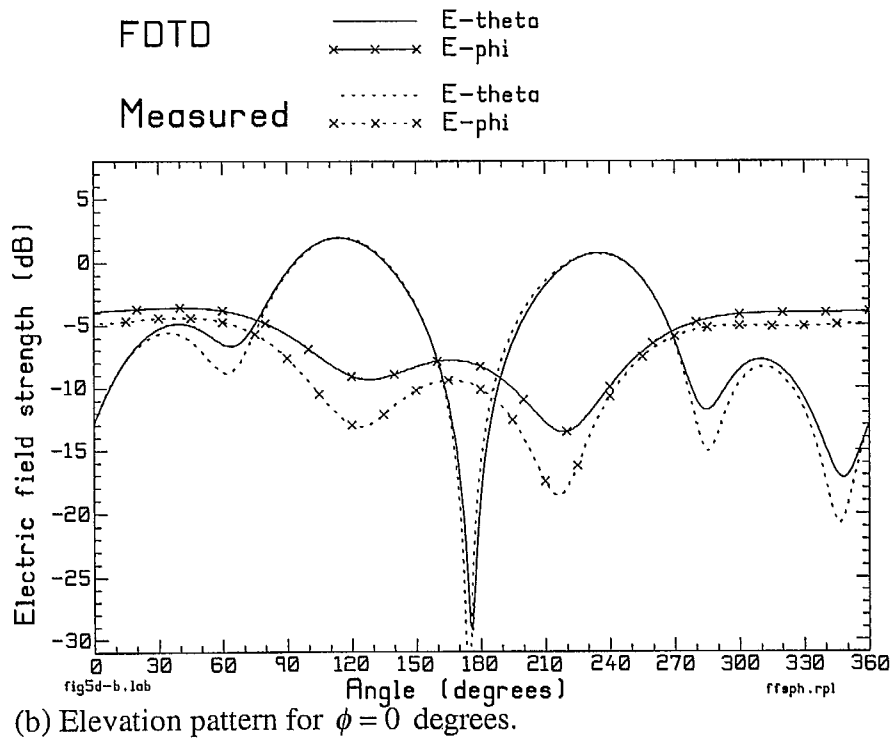
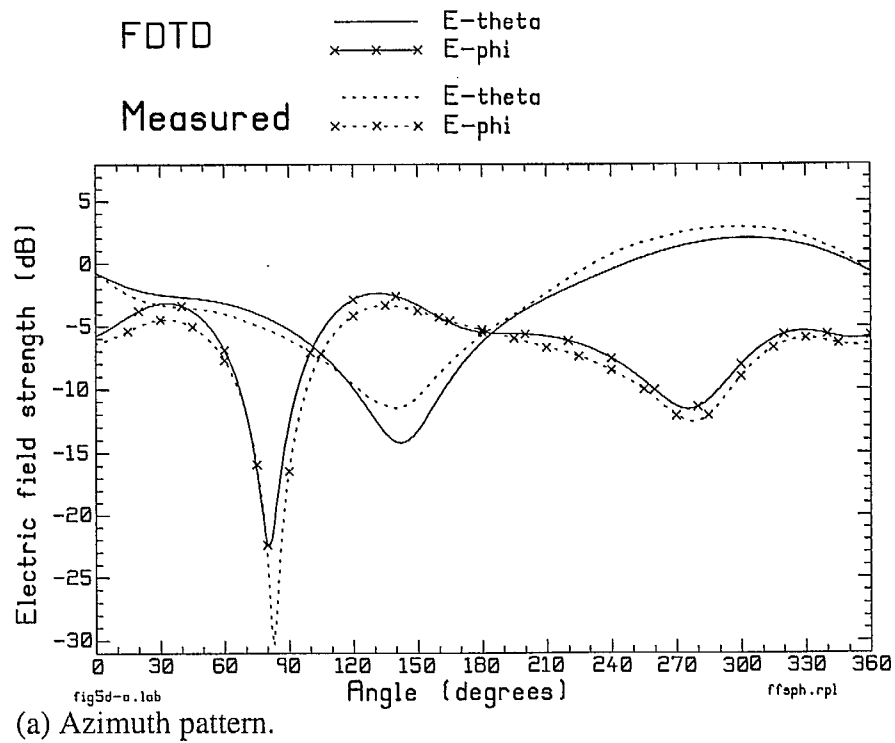


Fig. 5.6 Comparison of the measured radiation patterns of the handset and sphere head with the computed patterns, including the fiberglass bolts.

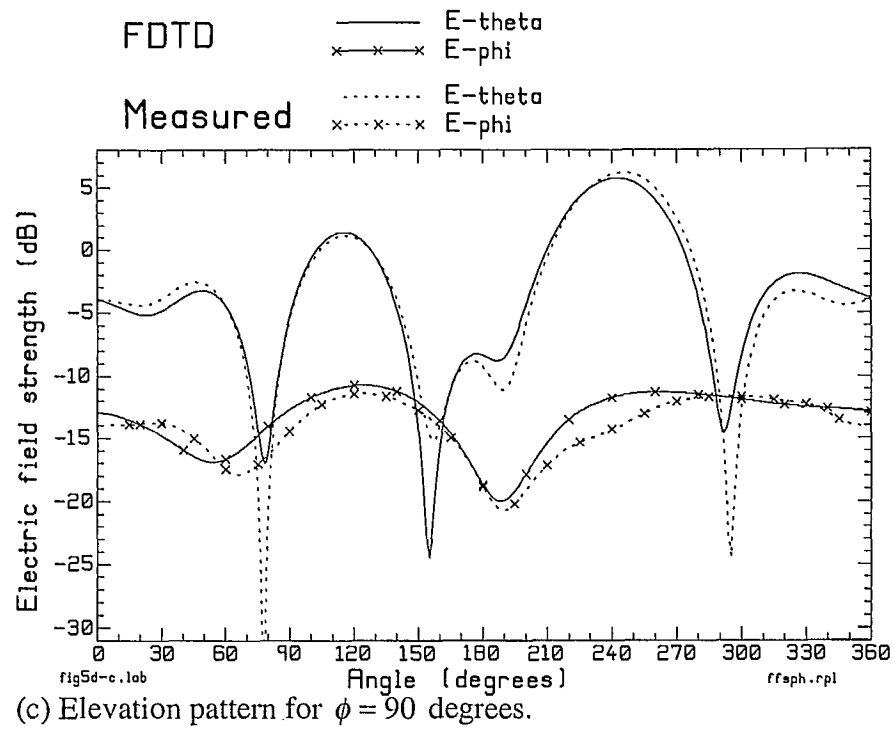


Fig. 5.6 (continued) Comparison of the measured radiation patterns of the handset and sphere head with the computed patterns, including the fiberglass bolts.

Chapter 6

Radiation Patterns of the Tilted Handset

The last four chapters have studied the radiation patterns of the handset held vertically, in isolation and near simple models of the head. But a person holding the handset typically tilts the antenna at about 60 degrees from the vertical, towards the back of the head. This chapter determines the patterns of the handset tilted 60 degrees and compares them to the patterns of the handset with its antenna vertical.

In FDTD it is desirable to keep the antenna oriented along the z -axis in the FDTD coordinate system. Then the handset can be modeled in FDTD without using a staircase of cells to represent the handset box. This chapter defines an angle transformation that permits the handset problem to be solved in a local, FDTD coordinate system with the antenna along the FDTD z -axis, and then the far fields to be transformed to a global coordinate system in which the handset is tilted to the vertical. The tilted handset's radiation patterns computed with FDTD are compared with those found by wire-grid modeling, to verify that the transformation has been implemented correctly. The angle transformation can be used to find the radiation patterns of the tilted handset near a model of the head.

6.1 Far Field Coordinate Transformation For Use With FDTD

The handset consists of a perfectly-conducting box and a monopole antenna parallel to a long edge of the box. The handset can be represented very accurately by an FDTD cell model when the handset box is oriented in the cell space with the surfaces of the handset parallel to the coordinate planes, as shown in Fig. 6.1. However, if we wish to tilt the handset with respect to the z axis as in Fig. 6.2, then some surfaces of the handset are not parallel to the coordinate planes and the handset has to be modeled as a staircase of FDTD cells. We do not want to incur the error associated with staircasing in modeling the handset. Hence to compute the radiation patterns of the tilted handset, we will solve the handset in a "local" or "FDTD" coordinate system with the antenna parallel to the local z axis, then transform the fields into a "global" coordinate system where the antenna is tilted relative to the z axis.

Fig. 6.2 shows the handset tilted at an angle of α to the z axis. The handset has been rotated about the y axis towards the x axis, through angle α . We will refer to the (x,y,z) coordinate system in Fig. 6.2 as the "global" coordinates. The handset is actually solved by FDTD in the "FDTD coordinate system" (x_f, y_f, z_f) , in which the y_f axis is parallel to the global y axis, but the x and z axis are at an angle of α to the global axes. If we wish to compute a radiation pattern in the global system, then for each point at global angles (θ, ϕ) , the corresponding point (θ_f, ϕ_f) is be found in the FDTD coordinate system. Then program FARZONE is run to find the spherical components of the far fields in the FDTD coordinate system, $(E_{\theta_f}, E_{\phi_f})$. Then the FDTD field components are

used to find the corresponding spherical components E_θ and E_ϕ in the global coordinate system.

6.1.1 Angle Transformation

Given spherical angles (θ, ϕ) in the global coordinate system, how do we find the corresponding angles (θ_f, ϕ_f) in the FDTD coordinate system? For a point at (R, θ, ϕ) in global coordinates, the rectangular global coordinates are

$$x = R \sin \theta \cos \phi$$

$$y = R \sin \theta \sin \phi$$

$$z = R \cos \theta$$

The point in the global system has position vector

$$\vec{p} = x\hat{x} + y\hat{y} + z\hat{z}$$

where \hat{x} , \hat{y} and \hat{z} are the unit vectors along the coordinate axes in the global system.

We need to express these unit vectors in terms of \hat{x}_f , \hat{y}_f and \hat{z}_f , the unit vectors along the coordinate axes in the FDTD coordinate system. From Fig. 6.2, the global y direction is the same as the FDTD y direction, so

$$\hat{y} = \hat{y}_f$$

The unit vectors along the x and z axes in the global system can be expressed in terms of the FDTD coordinate unit vectors as

$$\hat{x} = \cos \alpha \hat{x}_f - \sin \alpha \hat{z}_f$$

$$\hat{z} = \sin \alpha \hat{x}_f + \cos \alpha \hat{z}_f$$

Substituting, point \vec{p} is given in FDTD components by

$$\vec{p} = (x \cos \alpha + z \sin \alpha) \hat{x}_f + y \hat{y}_f + (-x \sin \alpha + z \cos \alpha) \hat{z}_f$$

hence the FDTD rectangular coordinates are

$$x_f = (x \cos \alpha + z \sin \alpha)$$

$$y_f = y$$

$$z_f = (-x \sin \alpha + z \cos \alpha)$$

Then the spherical angles in the FDTD system are found as

$$\phi_f = \tan^{-1}(y_f / x_f)$$

and

$$\theta_f = \tan^{-1}(\sqrt{x_f^2 + y_f^2} / z_f)$$

Thus given a set of spherical angles (θ_i, ϕ_j) corresponding to a radiation pattern in global coordinates, we can find the corresponding set of angles (θ_{fi}, ϕ_{fj}) in the FDTD coordinate system.

The next step is to run program FARZONE to find the spherical components of the field in the FDTD coordinate system, $(E_{\theta_f}, E_{\phi_f})$, at each far field point. The

following describes how to obtain the spherical components of the far field in global coordinates (E_θ, E_ϕ) are found from the field components in FDTD coordinates.

6.1.2 Spherical Field Components in Global Coordinates

Given the spherical components $(E_{\theta_f}, E_{\phi_f})$ of the far field at point (θ_f, ϕ_f) in the FDTD coordinate system, this section describes how the spherical components are found in the global coordinate system, (E_θ, E_ϕ) .

The far field in spherical components in the FDTD coordinate system is given by

$$\bar{E} = E_{\theta_f} \hat{\theta}_f + E_{\phi_f} \hat{\phi}_f$$

where $\hat{\theta}_f$ and $\hat{\phi}_f$ are the spherical unit vectors. We can express these spherical unit vectors in terms of the FDTD coordinate axis unit vectors as

$$\hat{\theta}_f = -\sin \theta_f \hat{z}_f + \cos \theta_f (\cos \phi_f \hat{x}_f + \sin \phi_f \hat{y}_f)$$

and

$$\hat{\phi}_f = -\sin \phi_f \hat{x}_f + \cos \phi_f \hat{y}_f$$

where θ_f and ϕ_f are the coordinate angles in the FDTD coordinate system. Hence the field in rectangular components in the FDTD system is given by

$$\begin{aligned} \bar{E} &= (E_{\theta_f} \cos \theta_f \cos \phi_f - E_{\phi_f} \sin \phi_f) \hat{x}_f \\ &\quad + (E_{\theta_f} \cos \theta_f \sin \phi_f + E_{\phi_f} \cos \phi_f) \hat{y}_f \\ &\quad - E_{\theta_f} \sin \theta_f \hat{z}_f \\ &= E_{xf} \hat{x}_f + E_{yf} \hat{y}_f + E_{zf} \hat{z}_f \end{aligned}$$

Then the rectangular components of the field in FDTD coordinates are

$$E_{xf} = E_{\theta_f} \cos \theta_f \cos \phi_f - E_{\phi_f} \sin \phi_f$$

$$E_{yf} = E_{\theta_f} \cos \theta_f \sin \phi_f + E_{\phi_f} \cos \phi_f$$

$$E_{zf} = -E_{\theta_f} \sin \theta_f$$

By substituting the FDTD unit vectors expressed in terms of the global unit vectors,

$$\hat{x}_f = \cos \alpha \hat{x} + \sin \alpha \hat{z}$$

$$\hat{y}_f = \hat{y}$$

and

$$\hat{z}_f = -\sin \alpha \hat{x} + \cos \alpha \hat{z}$$

we can find the rectangular components of the field in global coordinates as

$$E_x = E_{xf} \cos \alpha - E_{zf} \sin \alpha$$

$$E_y = E_{yf}$$

and

$$E_z = E_{xf} \sin \alpha + E_{zf} \cos \alpha$$

Then the rectangular components in the global coordinate system are used to find the spherical components in the global coordinate system using

$$E_{\theta} = E_x \cos \theta \sin \phi + E_y \cos \theta \sin \phi - E_z \sin \theta$$

and

$$E_{\phi} = -E_x \sin \phi + E_y \cos \phi$$

Thus our procedure is as follows. Given a desired far field point (θ, ϕ) in global coordinates, we find the corresponding point (θ_f, ϕ_f) in FDTD coordinates. Then FARZONE computes the spherical components of the far field in FDTD coordinates, $(E_{\theta_f}, E_{\phi_f})$. These are resolved first into rectangular components in FDTD coordinates, (E_{xf}, E_{yf}, E_{zf}) then into rectangular components in global coordinates, (E_x, E_y, E_z) . Finally the rectangular components are resolved into spherical components in global coordinates, (E_{θ}, E_{ϕ}) .

6.1.3 Procedure for Computing the Radiation Patterns with FDTDANT

Fig. 6.3 shows the processing steps used to compute the far field patterns of the handset when it is tilted with respect to the global vertical axis. A list of the desired radiation patterns in global coordinates is prepared, in a file called RPLIST.IN. A program called MAKERP evaluates the angle transform of Section 6.1.1 to find the spherical angles of each far field point in FDTD coordinates, in a file called RPLIST.OUT. The RP commands in this file are pasted into the FDTDANT input file for the handset, HANDSET.BLD, using a file editor. Then FDTDANT is run to obtain the intermediate file SSSNZFZ.DAT[4], and FARZONE is run to compute the far field in the FDTD coordinate system, to obtain the output "solution" file HANDSET.SOL. To change back to global coordinates, the program TOGGLOBAL is run. This program correlates the desired radiation patterns in the RPLIST.IN file with the computed fields in HANDSET.SOL. For each far field point, TOGGLOBAL evaluates the transformation of the FDTD spherical field components to the global spherical field components. TOGGLOBAL writes a new "solution" file called RPOUT.SOL giving the far fields in global coordinates. This file is often renamed to HANDSET.SOL.

In the following, the far field patterns of the handset tilted at 60 degrees to the vertical are examined. Then the patterns are compared against those computed by wire-grid modeling, as a check that the method has been implemented correctly.

6.2 Radiation Patterns of the Tilted Handset

A talker on a cellular telephone rarely holds the handset with the antenna oriented vertically. Normally the handset is tilted relative to the vertical axis such that earpiece rests against the ear and the mouthpiece is adjacent to the source of the sound. An angle of inclination of 60 degrees to the vertical[6] is typical in the use of handsets. In Fig. 6.4, the handset is rotated about the y axis toward the negative x axis, such that the antenna makes an angle of $\alpha = -60$ degrees to the positive z axis. This section presents the principal plane patterns of the handset in free space with the antenna inclined at 60 degrees to the vertical.

FDTD was used to compute the radiation patterns of the tilted handset with a cell size of 4.41 mm. The FDTD PML code was used with a 6-cell PML and 4 cells of

whitespace separating the surfaces of the handset from the inner surface of the PML. The surface reflection coefficient was set to 0.001, and parabolic evolution of the conductivity was used. The overall space size was 32 by 24 by 78 cells, and the solution was run for 2048 time steps. This the same setup for the FDTD analysis as was used in Chapter 2 of this report for the vertical handset.

When the handset is tilted at 60 degrees to the vertical, the antenna has a larger horizontal component than vertical component and we can reasonably expect it to radiate a larger horizontal or E_ϕ field component in the azimuth plane than vertical or E_θ component.

Fig. 6.5 compares the principal plane patterns of the tilted handset with those of the vertical handset. In the $\phi=0$ plane, Fig. 6.5(b), the radiation pattern is simply rotated by 60 degrees counterclockwise. Then the sharp minimum falls at 61 degrees becomes a sharp minimum at one degree. The major lobe at 4.3 dB, 116 degrees for the vertical handset was pointing towards the ground, and rotates to 56 degrees, pointing slightly upward. The major lobe that points downward at 3.5 dB, 233 degrees for the vertical handset points almost directly downward at 173 degrees. In the region of the radiation pattern "behind" the user, from 180 to 360 degrees, the tilted handset has two minor lobes in its pattern, one pointing upward at -6.5 dB, 332 degrees and the other downward at -3.8 dB, 254 degrees. There is a minimum in the radiation pattern of the tilted handset at -12.5 dB, 298 degrees, which is at a modest elevation angle above the ground directly behind the user.

In the azimuth plane, Fig. 6.5(a), the roughly omnidirectional pattern of the vertical handset becomes more directional. The field directly in front of the user drops from 1.2 dB for the vertical handset to -0.4 dB for the tilted handset. The field directly behind the user rises slightly from -5.5 dB to -5.1 dB for the tilted handset. There are broad minima at -10.5 dB, 111 degrees and 249 degrees. The cross-polarized field, E_ϕ , is much, much larger for the tilted handset than for the vertical handset. The maximum cross-polarized field for the vertical handset is -11.2 dB at 90 and 270 degrees; for the tilted handset there are lobes at 3.1 dB, 60 degrees and 300 degrees, where the cross-polarized field is larger than E_θ .

In the $\phi=90$ plane, the radiation patterns are also substantially changed. In E_θ the vertical handset has major lobes of 4.0 dB at 111 degrees and 239 degrees, minor lobes at -6.2 dB, 40 and 320 degrees, with sharp, deep minima at zero and 180 degrees. For the tilted handset, the field strength in E_θ is much smaller. There are lobes at -5.7 dB, 113 degrees and 247 degrees, separated by sharp, deep minima at zero and 180 degrees. The cross-polarized field is much, much larger for the tilted handset, with a maximum of 3.4 dB at 180 degrees, directly downward, and minima of -22.5 dB at 16 degrees and 344 degrees.

Tilting the handset leads to much larger radiation in the cross-polarized field than for the vertical handset. If the base station transmits and receives circular polarization, the energy radiated in the E_ϕ component is not wasted.

6.3 Validation Against the Wire-Grid Patterns

This section compares the far field patterns of the tilted handset computed with FDTD against those computed with wire-grid modeling. This provides a validation of the implementation of the coordinate transformation described in Section 6.1 above.

Fig. 6.6 compares the principal plane patterns of the tilted handset computed by FDTD with those computed by wire-grid modeling using the NEC program. The azimuth pattern in Fig. 6.6(a) shows excellent agreement between the two methods, with small differences as follows. In E_θ directly in front of the handset, the field strength in the wire-grid computation is -0.52 dB, and -0.45 dB in the FDTD computation. Directly behind the handset the field is -5.20 dB in the wire-grid computation and -5.07 dB using FDTD. In the minimum, the wire-grid calculation has field strength -10.1 dB at 111 degrees, at the FDTD computation, -10.5 dB at 110 degrees. In E_ϕ the major lobes are almost identical between the two computations. The minor lobe in the wire-grid calculation is -8.6 dB at 143 degrees, and is -8.3 dB at the same angle in the FDTD computation.

The $\phi=0$ pattern of Fig. 6.6(b) is very similar between the two computations. The main lobes are almost identical. The minor lobe in the wire-grid computation at -3.7 dB, 254 degrees falls at -3.6 dB in the FDTD computation. The minor lobe at -6.6 dB, 331 degrees in the wire-grid method falls at -6.4 dB, 332 degrees in FDTD. The minimum at -14.1 dB, 223 degrees in the NEC computation shows the largest difference from the FDTD computation, where the minimum falls at -14.7 dB. The maximum field strength in the cross-polarized field is -148 dB in the wire-grid computation but is only -67 dB in the FDTD calculation.

The elevation pattern for $\phi = 90$ degrees is shown in Fig. 6.6(c). The agreement in E_θ is excellent, with little difference in the peaks. There is some difference on the shoulder of the curves near 60 degrees and 300 degrees. The agreement in E_ϕ is also excellent.

This section has demonstrated that the radiation patterns of the tilted handset are almost the same whether computed by wire-grid modeling with the NEC program, or computed using FDTD and the coordinate transformation described in this chapter.

6.4 The Tilted Handset Near the Sphere Head

Chapter 5 examined the radiation patterns of the handset near the sphere head with the handset oriented vertically or parallel to the z -axis. In this section the radiation patterns of the handset and sphere head are examined, when the handset is tilted by 60 degrees towards the negative x axis, as shown in Fig. 6.7. The relative position of the handset to the sphere head is as shown in Fig. 5.2, except that the handset and head have been rotated about the y axis by 60 degrees towards the negative z axis. This configuration will provide an initial look at the radiation patterns of the handset held in a realistic position near a model of the head.

To compute the radiation patterns of the handset in the tilted position near the sphere head, the FDTD code is used to solve the handset and sphere problem with the cell model of the sphere described in Section 5.1, which has the handset antenna aligned

along the z axis. The cell size is 4.41 mm. FDTD MER creates the near- to far-zone data file SSSNZFZ.DAT, from which program FARZONE can compute at any far field point (θ, ϕ) . Program MAKERP is used to create RP cards for a set of (θ, ϕ) angle pairs corresponding to “conical cut” radiation patterns on the radiation sphere, with the handset tilted at 60 degrees to the “global” vertical axis. These RP cards are pasted into the “build” file for the handset and sphere and program FARZONE is run to compute the far fields. Then program TOGLOBAL assembles the radiation patterns from the individual E_θ and E_ϕ values at the desired (θ, ϕ) points, as described in Section 6.1.3 above.

Fig. 6.8 compares the radiation patterns of the vertical handset near the sphere head with those of the tilted handset near the sphere head. When the handset is tilted at 60 degrees to the vertical, then for angles near the azimuth plane the handset radiates more field in the horizontal or E_ϕ component than in the vertical or E_θ component.

The elevation pattern for $\phi = 0$ in Fig. 6.8(b) for the tilted handset is simply the vertical handset pattern rotated counterclockwise by 60 degrees. The sharp minimum in E_θ at 176 degrees is rotated back to 116 degrees. The tilted handset near the sphere head has a broad lobe in E_θ at 2.1 dB, 54 degrees, inclined upward and forward. The sharp minimum at 116 degrees points towards the ground. There is a broad, downward-directed lobe at 0.9 dB, 174 degrees. In the backward direction, there is a modest lobe inclined slightly downward at -7.7 dB, 250 degrees, and a minimum of -17.1 dB at 288 degrees, pointing slightly upward. There is a small, upward-directed lobe at -4.8 dB, 340 degrees. The cross-polarized field has a maximum of -3.5 dB at 341 degrees and a minimum of -13.4 dB at 159 degrees.

Recall that the user of our portable radio handset holds the handset in the right hand and faces in the $+x$ direction. Thus, the $+y$ axis at $\phi = 90$ degrees is on the operator's left and the $-y$ axis or $\phi = 270$ degrees is on the right. The azimuth pattern, Fig. 6.8(a), shows the largest fields in E_θ ahead of the operator, between 270 degrees (the operator's right hand) and 90 degrees, (the operator's left hand). The maximum field of -1 dB occurs at 307 degrees, to the operator's right, where the sphere lies behind the handset. There is a lobe at -2.5 dB at 35 degrees, to the operator's left. As we move behind the operator, there is a modest minimum of -13.0 dB at 98 degrees, and a lobe of -5.9 dB at 140 degrees. In the region of the pattern from about 180 to 270 degrees, the handset lies behind the head, and we see a broad minimum in the field strength in E_θ . The minimum field is -14.2 dB at 239 degrees. The cross-polarized field, E_ϕ , has much stronger peaks for the tilted handset than for the vertical handset. Thus, there is a peak of 0.6 dB at 66 degrees, and another of 4.9 dB at 297 degrees. Both these peaks are larger than the maximum field in the E_θ component and indeed the field strength in E_ϕ is larger than E_θ through most of the pattern.

Fig. 6.8(c) shows the elevation pattern for $\phi = 90$ degrees, in the “side to side” direction. The E_θ pattern for the tilted handset shows generally smaller field strengths than for the vertical handset, and conversely the field strength in E_ϕ for the tilted handset is generally much larger than for the vertical handset. The maximum in E_θ occurs at -

0.7 dB, 235 degrees, followed by -1.8 dB at 32 degrees. There are sharp minima in E_θ at 78 degrees and 298 degrees. The maximum field in E_ϕ is at 2.9 dB, 230 degrees. The E_ϕ pattern has a broad, deep minimum at -28.5 dB, 59 degrees.

It is of interest to note in Fig. 6.8(c) that where E_θ has a deep minimum, -28.2 dB, 298 degrees, then E_ϕ is much larger at -3.3 dB. Where E_ϕ has a deep minimum, -28.5 dB, 59 degrees, then E_θ is much larger at -5.4 dB. Thus there is useful signal in either E_θ or E_ϕ everywhere in the pattern. Conversely, the azimuth pattern Fig. 6.8(a) has nearly coincident minima in E_θ at -13.0 dB, 98 degrees and in E_ϕ at -11.4 dB, 102 degrees. Again, E_θ has a minimum at -14.2 dB, 239 degrees and E_ϕ at -11.4 dB, 250 degrees. In these directions, where both polarizations have field strengths more than 11 dB down from the isotropic level, there may not be adequate signal strength to communicate with a distant base station.

Fig. 6.8 shows that the patterns of the handset held in a tilted position near the head differ greatly than those of the handset held vertically against the head. The tilt of the handset profoundly changes the amount of field radiated into each polarization.

6.5 Tilted Handset and Sphere Head vs. Tilted Handset Alone

This section compares the radiation patterns of the tilted handset in free space to those of the tilted handset operated adjacent to the sphere head. The objective is to assess the effect of the sphere head on the patterns of the handset, when it is held in the tilted position.

Fig. 6.9(a) shows the azimuth pattern of the tilted handset alone compared to the tilted handset near the sphere. The radiation patterns for E_θ are quite similar. The field strength in E_θ for the handset near the sphere is smaller over most of the pattern than for the handset alone. The maximum E_θ for the handset alone is -0.4 dB, and is -1.0 dB for the handset and sphere. The minimum field for the handset alone is -10.4 dB. The handset and sphere has deeper minima, with a minimum field of -13.1 dB. The cross-polarized field, E_ϕ , is similar for the handset and sphere to that of the handset alone. The maximum field is 3.1 dB for the handset alone, and is 4.9 dB for the handset and sphere head. The cross-polarized field strength is larger over most of the pattern for the handset and sphere. The handset alone has deep minima in E_ϕ at 115, 180 and 245 degrees, but these are filled in when the sphere is introduced near the handset. The sharp, deep minimum at zero degrees in the handset-alone pattern is shifted to 26 degrees for the handset and sphere, but the minimum is still very deep.

Fig. 6.9(b) shows the elevation pattern for $\phi = 0$ degrees. The radiation pattern for E_θ is again quite similar for the handset alone and for the handset and sphere. The principal effect of the sphere is to fill in some of the minima in the handset alone patterns and to generally reduce the field strength in E_θ . The sharp, deep minimum at -22.4 dB, 1 degree for the handset alone is filled to become -6.6 dB, 3 degrees for the handset and sphere. Conversely the minimum at -13.9 dB, 115 degrees for the handset alone becomes

much deeper for the handset and sphere at, -29.1 dB, 116 degrees. The handset-alone minimum at -14.7 dB, 233 degrees becomes -11.7 dB, 225 degrees for the handset and sphere. The main lobe in the handset-alone pattern at 4.5 dB, 56 degrees is reduced to 2.1 dB, 55 degrees for the handset and sphere. The lobe at 3.7 dB, 171 degrees is reduced to 0.9 dB, 176 degrees, and that at -3.6 dB, 254 degrees is reduced by the sphere to -7.7 dB, 250 degrees. The handset alone has a low cross-polarized field, E_ϕ . The sphere introduces cross-polarized field, with a maximum of -3.8 dB and a minimum of -13.4 dB. The cross-polarized field is stronger than the principal polarization over the region from about 210 to about 20 degrees. This is the half of the radiation pattern where the radio handset lies behind the head.

Fig. 6.9(c) shows the elevation pattern for $\phi = 90$ degrees. The sphere changes the shape of the radiation pattern in E_θ quite considerably. The deep minima at zero and 180 degrees are gone. The handset and sphere pattern has a new sharp, deep minimum of -28.2 dB at 298 degrees. The Field strength in E_θ over much of the pattern is larger for the handset and sphere than for the handset alone. Thus the maximum field for the handset alone is -5.7 dB at 110 and 250 degrees, and for the handset and sphere head it is -0.7 dB at 235 degrees. The radiation pattern in E_ϕ does not differ greatly for the handset alone and for the handset and sphere head. The maximum field is 3.4 dB at 180 degrees for the handset alone, and is 2.9 dB at 229 degrees for the handset and sphere head. The handset-alone has a minimum field of -22.5 dB at 17 and 343 degrees. The handset and sphere head has a sharp, deep minimum of -28.5 dB at 58 degrees.

Thus overall the radiation patterns of the handset operating near the sphere head are not greatly different from the patterns of the handset alone. The sphere tends to reduce the field strength in the E_θ component and fill in deep minima. The field strength in E_ϕ is raised in value by the sphere, and again sharp, deep minima are filled. Hence the sphere couples more power into the E_ϕ component. However, the handset and sphere patterns do have some sharp, deep minima of their own.

6.6 Conclusion

This chapter presented a coordinate transformation permitting the radiation patterns of the handset to be computed accurately with FDTD when the handset is tilted away from the z axis by rotation around the y axis. The implementation of the transformation was validated by comparing the handset patterns computed with FDTD with those computed by wire-grid modeling using the NEC program.

The radiation patterns of the handset held at a "natural" angle for use were then examined. The patterns were computed with the handset tilted back, at 60 degrees to the vertical. The azimuth pattern in E_θ becomes more directional with modest minima introduced at 110 and 250 degrees. The cross-polarized field E_ϕ is much higher, with maxima of 3.1 dB compared to -0.5 dB for the principal polarization. The elevation pattern for $\phi = 0$ simply rotates by 60 degrees. This puts the minor lobes behind the user, leading to smaller radiation in the backward direction. The elevation pattern for

$\phi = 90$ degrees is less directional and has a much lower field strength in E_θ , and conversely, a much, much higher field strength in E_ϕ . Thus in the tilted position the handset introduces much more of its power into the cross-polarized field.

To assess the effect of a model of the head on the radiation patterns of the tilted handset, the sphere head was used. It was found that the patterns of the handset alone and of the handset and sphere head are generally similar. The head tends to couple more energy into the E_ϕ component at the expense of reduced field strengths in E_θ . The sharp minima in the handset-alone radiation patterns tend to be filled in, but the head introduces some new deep minima into the radiation patterns.

It was noted that in some radiation patterns, where E_θ has a deep minimum, then E_ϕ does not, and conversely where E_ϕ has a minimum, then E_θ does not. If the base station can use both polarizations, this will help to ensure satisfactory communications with the portable radio. But in some other radiation patterns, both E_θ and E_ϕ have nearly-coincident minima, and this may be a limiting factor in the range to the base station for satisfactory communications. A systematic assessment of the radiation patterns for a handset with a given antenna design operating at a specified tilt angle to a model of the head requires examining the radiation patterns over the whole radiation sphere, not just the principal plane patterns. A criterion for the minimum acceptable field strength is required. This could consist of individual minimum values for E_θ and for E_ϕ . Or, if the base station can transmit and receive both polarizations, then the criterion could specify a minimum value for a measure of the net field strength, such as $\sqrt{(|E_\theta|^2 + |E_\phi|^2)}$.

A "figure of merit" could be used to compare various antennas. For example, for aircraft antennas intended to radiate E_θ , the percentage of the total radiated power that is radiated as E_θ in the "useful" angular sector for communications, from $\theta = 60$ to 120 degrees, is sometimes used to compare various antenna design proposals.

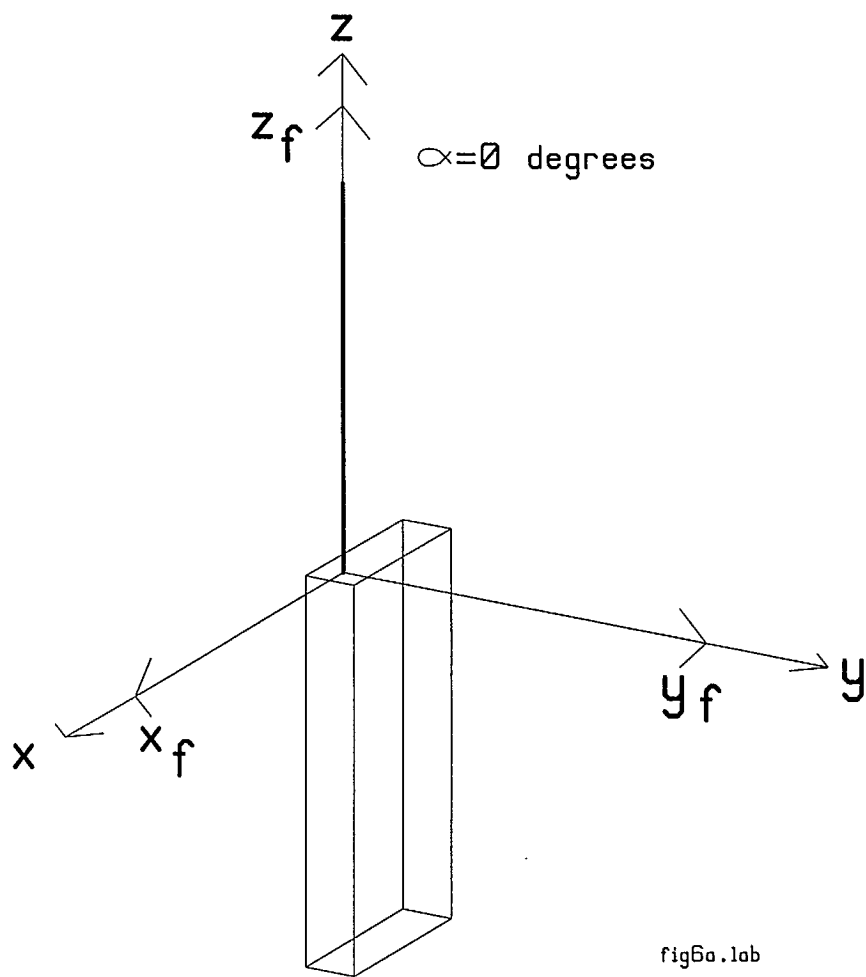


Fig. 6.1 The handset oriented with the antenna vertical.

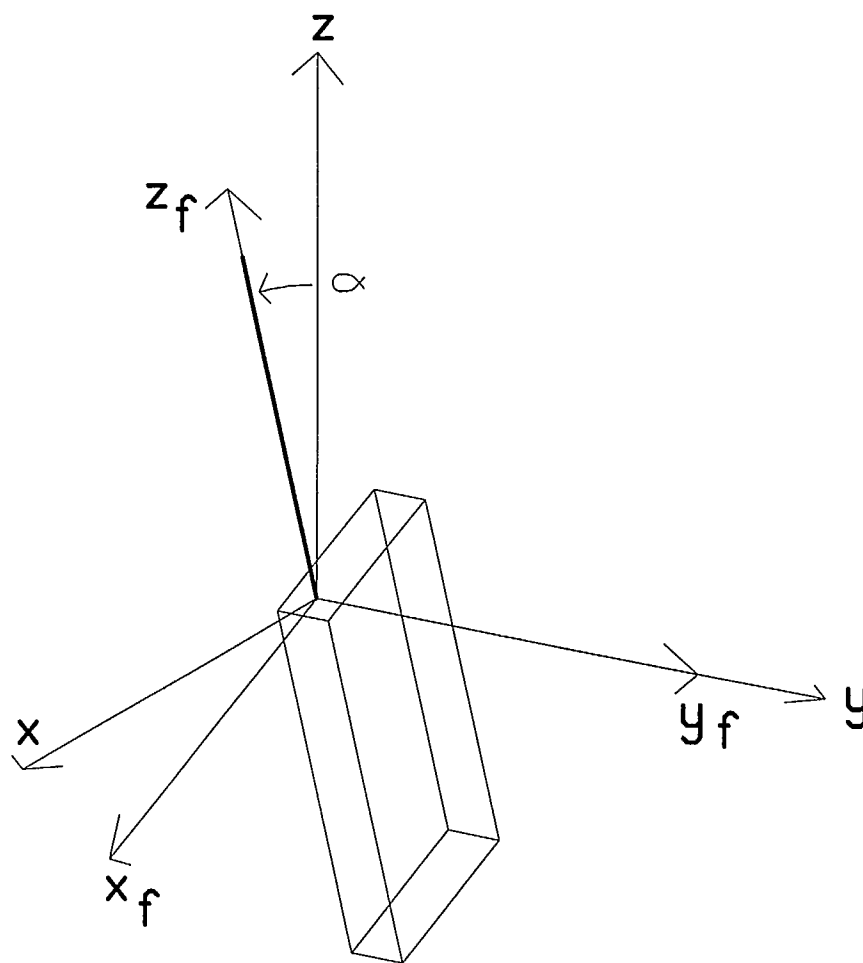


fig6c.lab

Fig. 6.2 The handset with the antenna tilted through angle α towards the x axis.

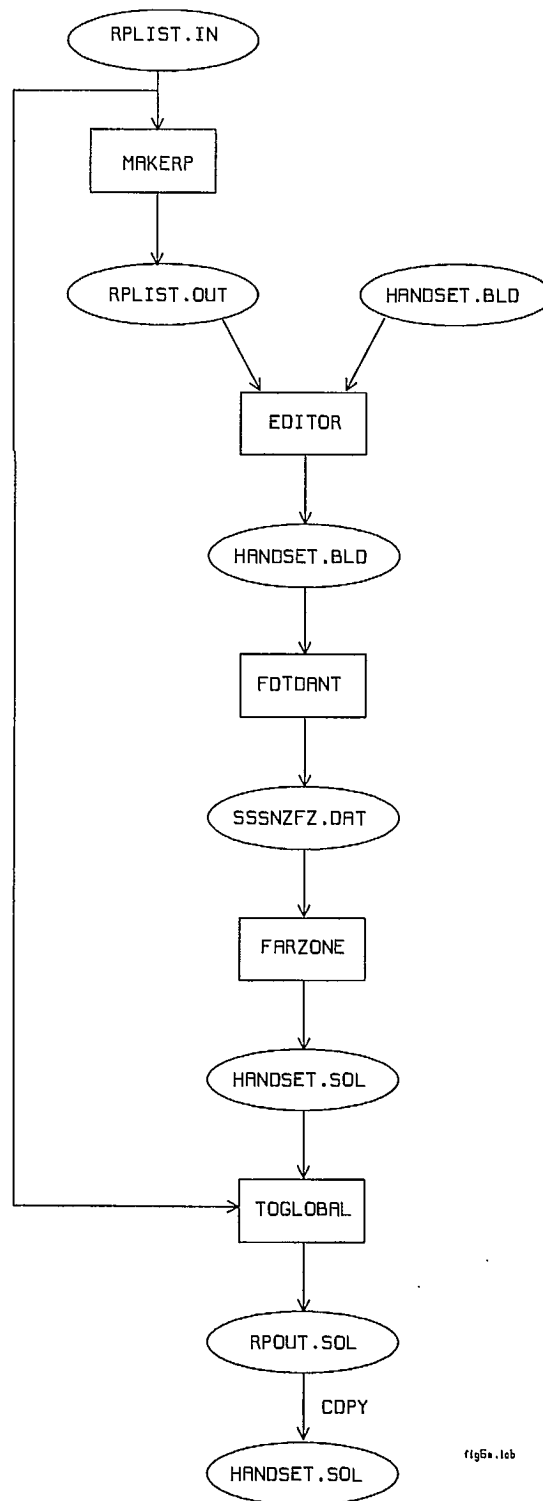


fig6a.1cb

Fig. 6.3 The processing steps used for computing the far field patterns of the handset tilted with respect to the vertical axis.

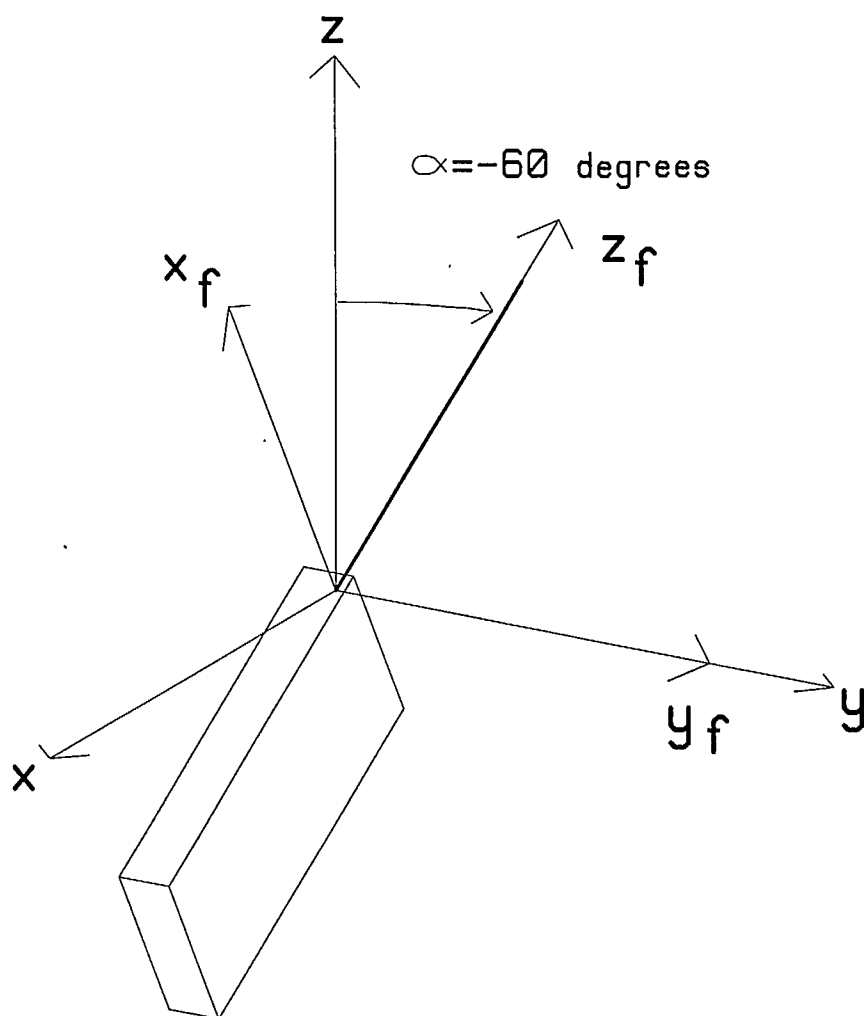


fig6b .lab

Fig. 6.4 The handset with the antenna tilted through angle $\alpha = -60$ degrees, hence tilted towards the negative x axis.

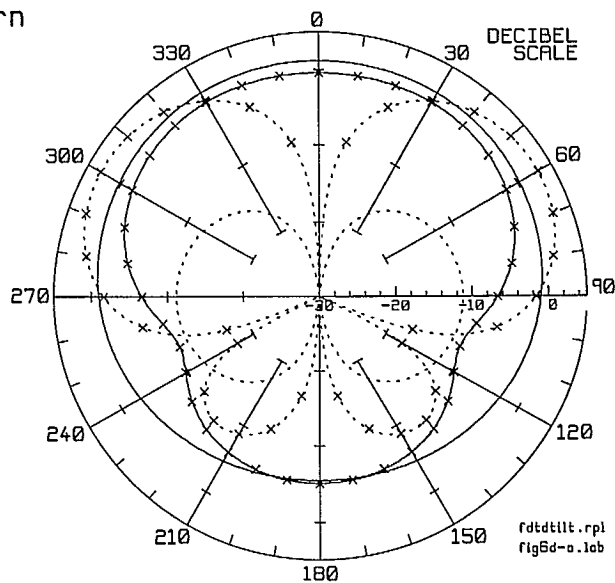
Azimuth Pattern

Tilted Handset

x—x—x E-theta
 x...x...x E-phi

Vertical Handset

— E-theta
 E-phi



(a) Azimuth pattern.

Phi=0 Elevation Pattern

Tilted Handset

x—x—x E-theta
 x...x...x E-phi

Vertical Handset

— E-theta
 E-phi

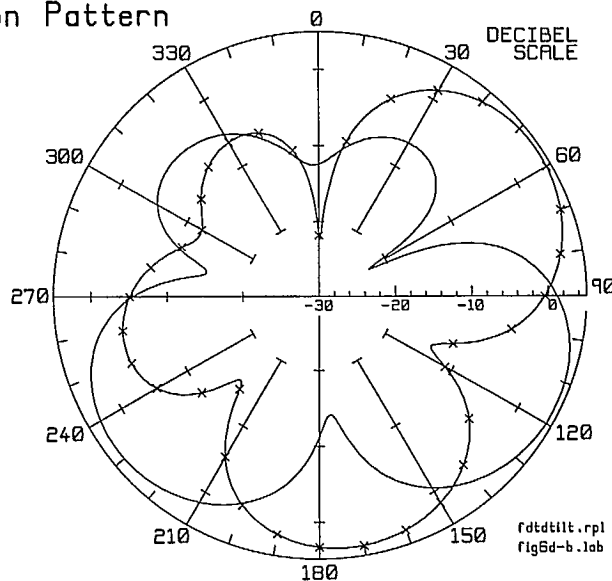
(b) Elevation pattern for $\phi = 0$ degrees.

Fig. 6.5 Radiation patterns of the tilted handset compared to those of the vertical handset.

Phi=90 Elevation Pattern

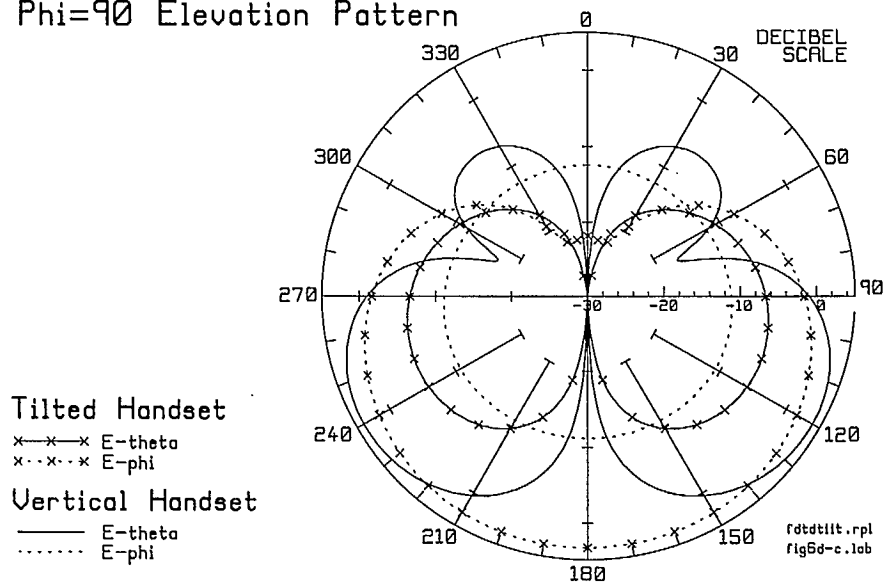
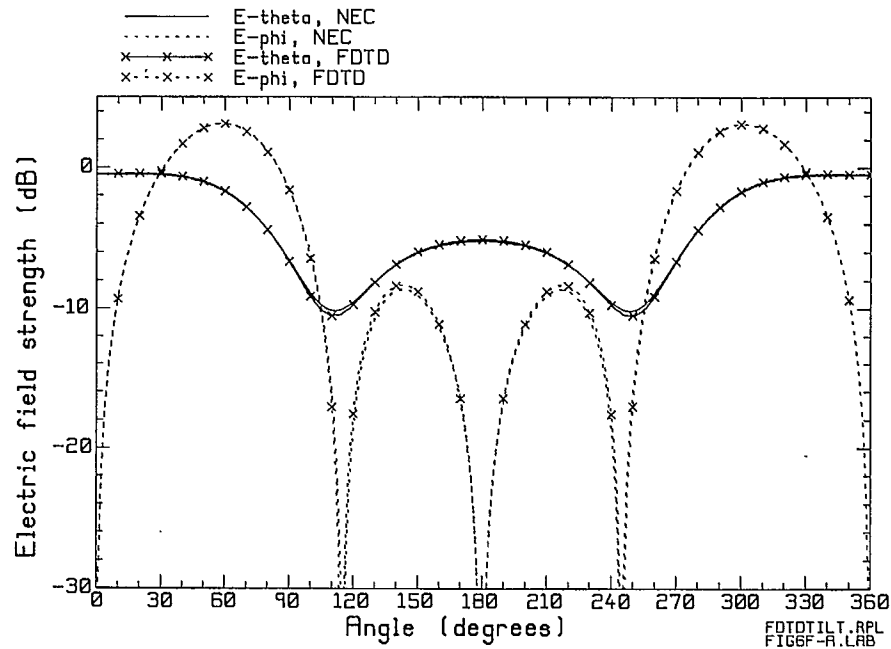
(c) Elevation pattern for $\phi = 90$ degrees.

Fig. 6.5 (continued) Radiation patterns of the tilted handset compared to those of the vertical handset.



(a) Azimuth pattern.

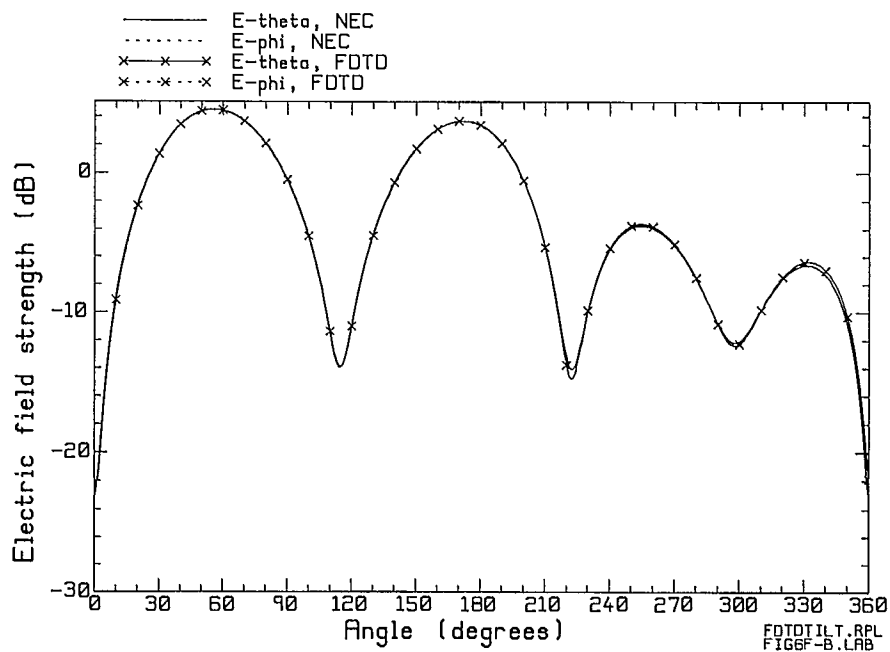
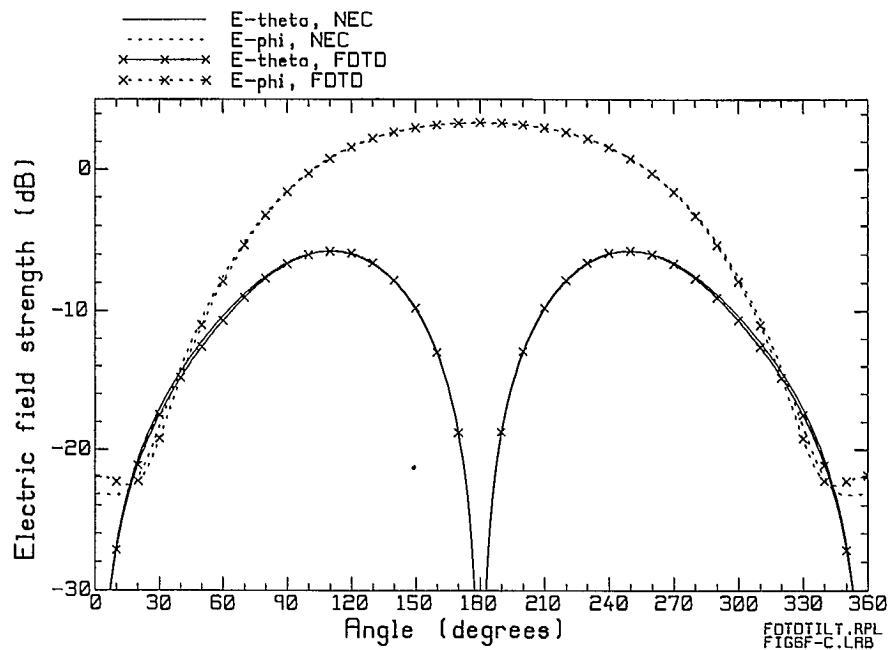
(b) Elevation pattern for $\phi = 0$ degrees.

Fig. 6.6 Comparison of the radiation patterns of the tilted handset computed with FDTD with those computed with NEC.



(c) Elevation pattern for $\phi = 90$ degrees.

Fig. 6.6 (continued) Comparison of the radiation patterns of the tilted handset computed with FDTD with those computed with NEC.

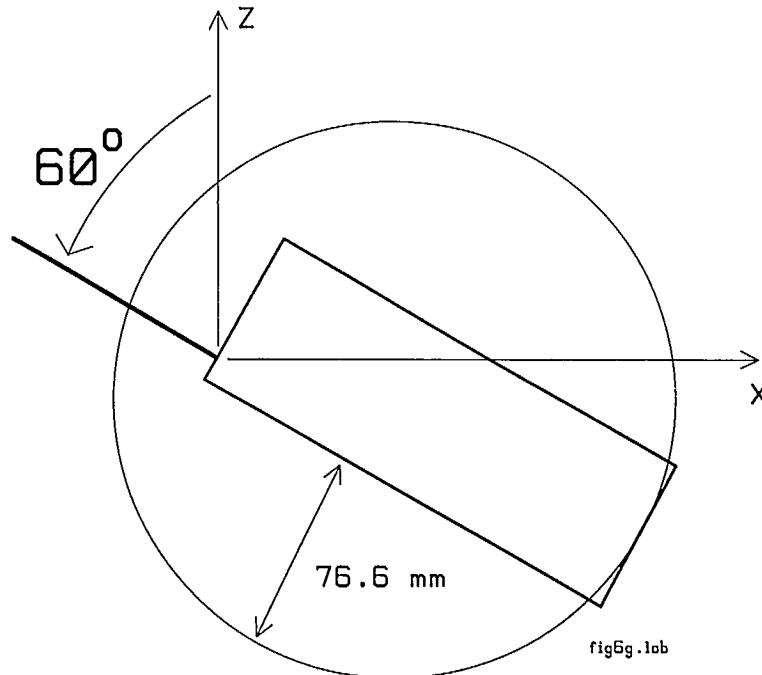


Fig. 6.7 The handset tilted at 60 degrees towards the $-x$ axis, near the sphere head.

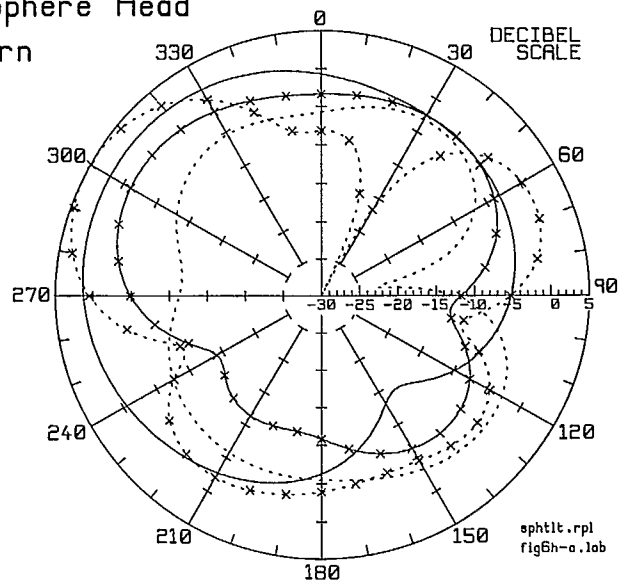
Handset and Sphere Head Azimuth Pattern

Tilted Handset

x-x-x E-theta
x-x-x E-phi

Vertical Handset

— E-theta
..... E-phi



(a) Azimuth pattern.

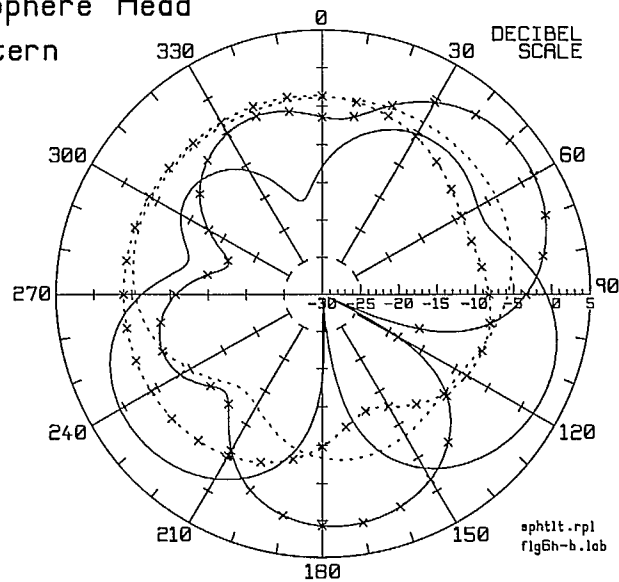
Handset and Sphere Head Elevation Pattern for $\phi = 0$

Tilted Handset

x-x-x E-theta
x-x-x E-phi

Vertical Handset

— E-theta
..... E-phi

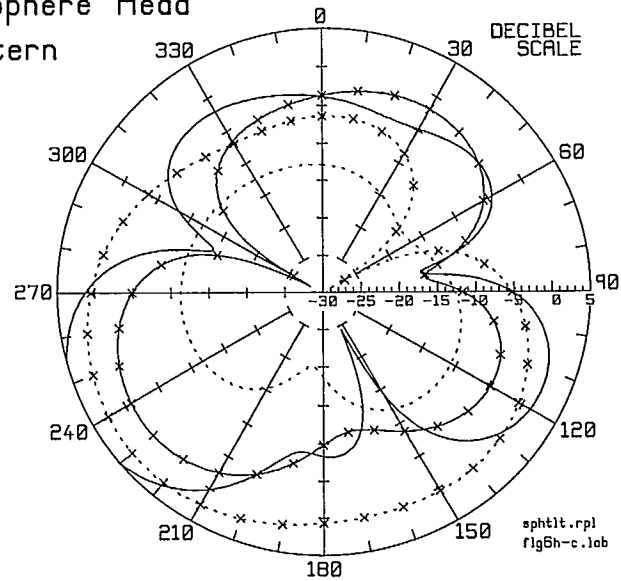


(b) Elevation pattern for $\phi = 0$ degrees.

Fig. 6.8 The radiation patterns of the vertical and tilted handset near the sphere head.

Handset and Sphere Head
Elevation Pattern
for $\phi=90$

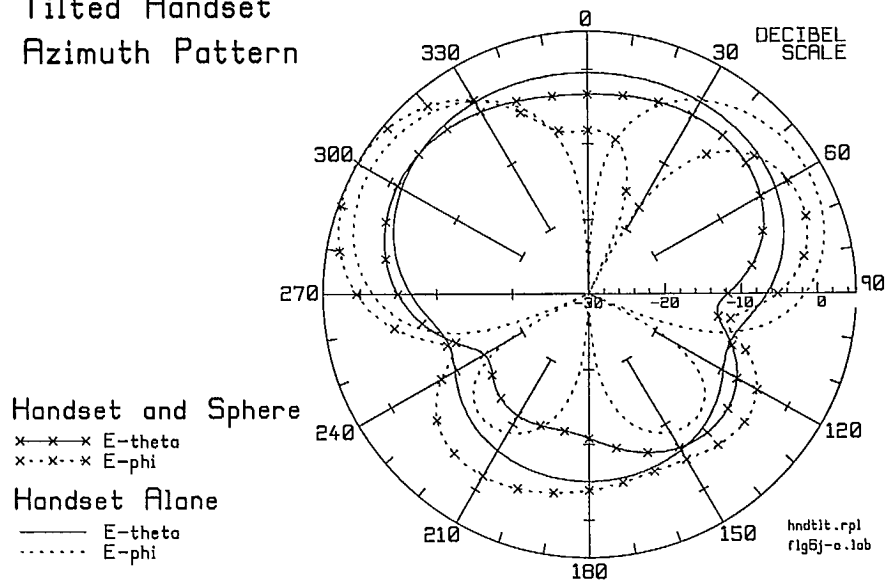
Tilted Handset
 x-x-x E-theta
 x...x...x E-phi
 Vertical Handset
 — E-theta
 E-phi



(c) Elevation pattern for $\phi = 90$ degrees.

Fig. 6.8 (continued) The radiation patterns of the vertical and tilted handset near the sphere head.

Tilted Handset Azimuth Pattern



(a) Azimuth pattern.

Tilted Handset Elevation Pattern for $\phi=0$

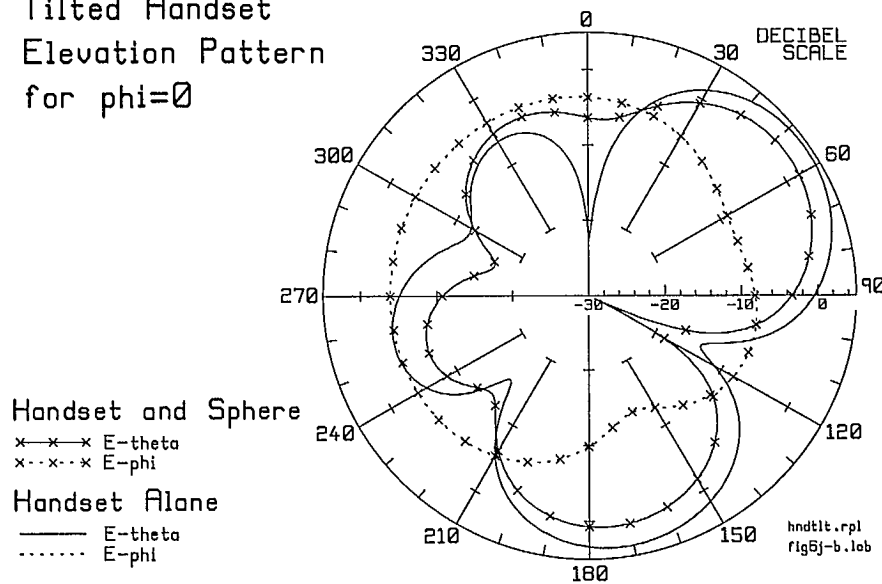
(b) Elevation pattern for $\phi = 0$ degrees.

Fig. 6.9 The radiation patterns of the tilted handset alone and of the tilted handset near the sphere head.

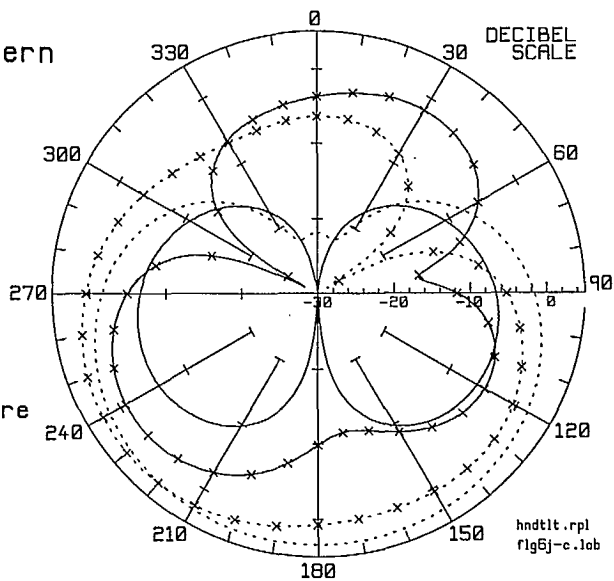
Tilted Handset
Elevation Pattern
for $\phi=90$

Handset and Sphere

x-x-x E-theta
x--x--x E-phi

Handset Alone

— E-theta
- - - E-phi



(c) Elevation pattern for $\phi = 90$ degrees.

Fig. 6.9 (continued) The radiation patterns of the tilted handset alone and of the tilted handset near the sphere head.

Chapter 7

An Anatomical Head Model

To examine the radiation patterns of a portable radio handset operating near a human head, an FDTD cell model of the head must be developed. This requires a detailed knowledge of the internal anatomy of the head. It is necessary to identify three-dimensional regions filled with various tissues, such as skin, muscle, bone and brain, and to describe them in a suitable form for analysis by the FDTD method. The head is coded as an FDTD model by specifying cell size, the size of the FDTD space, and the material type of each cell which is part of the head: skin, muscle, bone, and so forth. The number of tissue types that are used is limited by the available data on the permittivity and conductivity of human tissue. Older models in the literature use six tissues[36]. Newer models use as many as fifteen[37,38], with the material parameters listed in Table 7.1 for 900 MHz.

The maximum frequency at which the model can be used is determined by the requirement that the cell size be less than a tenth of a wavelength in the material with the shortest wavelength. The human tissues Table 7.1 have relatively high permittivities and are quite conductive. This leads to short wavelengths in tissue and so the cell size must be much smaller than that in free space to be valid at the same frequency. Further, the electrical parameters of human tissue are strongly frequency dependent, or “dispersive”. Dispersion can be modelled in FDTD[39,40,41,42] and codes have been developed to track the material properties of tissue over a wide bandwidth. Then the frequency dependence of the fields surrounding the head can be found efficiently using a Gaussian pulse excitation[8]. The FDTD code used here does not model dispersive materials. Thus the electrical properties of each tissue are specified at or near the frequency of interest, 850 MHz, and then the model is run with a sinusoidal generator at that frequency.

To develop a cell model of the head, cross-sections of the head are needed that display the internal structure. Ref. [43] was originally published in 1911 and presents a set of 19 sections of half of the head, roughly from the nose to the top of the skull, and 8 full sections from nose level to neck level. The sections were made by dissecting a male cadaver.. The sections are not made in parallel planes, but instead are inclined to one another, as shown in Fig. 7.1. The sections are well labeled with tissue types, in Latin. Ref. [44] presents a series of sections that are also well identified, but are not as complete a data set as those in the older textbook. More recently, cross-sectional information has become available on the world-wide web from the “Visible Human” project [45], which presents a great many cross-sections of a male cadaver. One set was made by magnetic resonance imaging(MRI) of the fresh cadaver; a second set consists of MRI scans of the frozen cadaver; and a third set is a series of photographs of the cross-section of the frozen cadaver at approximately 1 mm intervals. The photographs are available at the site of Ref. [45] including a viewer. There is a series of 250 photos of cross-sections of the head and neck at 1 mm intervals. However, the cross-sections are not labeled by tissue type

and some expertise would be required to “read” the cross-sections in detail to identify all the tissue types.

Ref. [2] presents initial work that was done in this project to develop a cell model of a head based on the set of 27 sections in Ref. [43]. Each section was “digitized” and each cell in each section was identified as one of 28 different biological materials. Two more simple sections were created from the drawing in Ref. [43] of the top of the head to give the head a more rounded appearance, resulting in a set of 29 sections. The problem of assembling the sections into a cell model is considerably complicated by the fact that the sections in the 1911 textbook are not in parallel planes, as shown in Fig. 7.1. Also, it is desired to create cell models of various cell sizes based on the digitized sections. The software developed in Ref. [2] did not lead to a satisfactory cell model.

This chapter re-examines the problem of assembling the 27 anatomical sections of Ref. [2] into an FDTD model of the head, with a suitably small cell size for analysis of the head at 850 MHz.

7.1 The Electrical Parameters of Biological Materials

Table 7.1 lists the materials that have been used in the anatomical model of the head described in this chapter. The table gives the relative permittivity and conductivity of each material from three reference sources, and then gives the value used in the present anatomical model. Hartsgrove et al.[21] give formulas for mixing water, sugar and salt to prepare liquids to simulate brain, muscle, and bone. Lazzi and Gandi[38] describe an anatomical model of the head for dosimetry studies at 835 MHz. Hombach et al.[37] describe an anatomical head used to study the fields and SAR in the head due to a dipole antenna, at 900 MHz. We note that the values given for the relative permittivity and conductivity of muscle are somewhat different. For bone, the relative permittivity in Ref. [B] is much lower than in Refs. [37] or [38]. The conductivity for the brain is higher in Ref. [21] than in [37] or [38], suggesting that the water, sugar and salt mixture recommended by Hartsgrove may be too conductive. It is interesting to note that Refs. [37] and [38] differ somewhat in the values of the parameters for bone, skin, and parotid gland. The values for other tissues are similar between the two references. Ref. [38] uses an average value for the electrical parameters of all brain tissue, whereas Ref. [37] has values for white matter, grey matter, and for other brain tissue under the generic name “average brain”. Ref. [38] identifies three types of glands, but uses the same value of the electrical parameters for all three. Ref. [38] only identifies one type of gland, but uses a much higher permittivity and conductivity than does Ref. [37]. Ref. [38] does not identify nerve tissue as distinct from brain tissue, whereas Ref. [37] provides different parameters for nerve.

Table 7.1
Electrical Properties of Biological Materials

Material	Ref. [21] 900 MHz		Ref. [38] 835 MHz		Ref. [37] 900 MHz		Used in this Report	
	ϵ_r	σ	ϵ_r	σ	ϵ_r	σ	ϵ_r	σ
Muscle	54.7	1.38	51.8	1.11	57.4	0.82	57.4	0.82
Bone, fat							20.9	0.33
Bone	7.4	0.16	17.4	0.25	20.9	0.33		
Fat			9.99	0.17	10.0	0.17		
Skin			35.4	0.63	40.7	0.65	40.7	0.65
Blood			55.5	1.86	55.0	1.86	55.0	1.86
Cartilage			40.7	0.82	41.9	0.83	41.9	0.73
Ligament							41.9	0.83
Eye							67.9	1.68
Eye humour			67.9	1.68	67.9	1.68		
Eye lens nucleus			36.6	0.51	36.6	0.51		
Eye lens outer					51.6	0.90		
Eye sclera			54.9	1.17	54.9	1.17		
Gland							45.3	0.92
Parotid Gland			45.3	0.92	70.0	1.90		
Pituitary Gland			45.3	0.92				
Pineal Gland			45.3	0.92				
Cerebral spinal fluid			78.1	1.97	79.1	2.14	79.1	2.14
Brain, white matter					34.5	0.59	34.5	0.59
Brain, grey matter					53.8	1.17	53.8	1.17
Brain, average	41.2	1.22	45.3	0.92	41.0	0.86	41.0	0.86
Nerve			33.4	0.60			33.4	0.60

7.2 The Digitized Anatomical Sections

During the 1994-95 contract period[2] the set of 27 sections of the brain in Ref. [43] were “digitized” to form the basis for an anatomical model of the head. The sections are well labeled with their tissue types, albeit in Latin. Each section was overlaid with a grid of squares, on a digitizing tablet. A mouse was used to classify the material type of each square into one of 28 different material types, using the labeling on the anatomical drawings as a guide. The size of each square was 2.5 mm. Since the anatomical drawings are at three-quarter scale, this corresponds to a 3.3 mm cell size at full scale. However, the sections are approximately 1 cm apart so the “voxel” size in the digitization is very roughly 0.33 by 0.33 by 1 cm

The set of 27 sections was supplemented by two more that were assembled from the drawing of the top of the head in Ref. [43] to form a set of 29 sections. Ref. [43] provides an elevation drawing of the head giving the location of each section, from which Fig. 7.1 was derived. This was used to tie together the set of 29 cross-sections, so the

center of each square on each cross-section could be assigned x, y, z coordinates in a global coordinate system.

To assemble a new FDTD cell model from the digitized sections, each section was aligned with the others to ensure that the set forms a coherent model of the head. Each section was surrounded by one cell of free-space as a border, which is convenient in assembling the sections into an FDTD cell model.

Considerable pain was taken to identify the tissue types in the digitized sections of Ref. [2], because they were not adequately labeled or documented. The original set of 28 tissue types was retained. These include bone, muscle, blood, eye, skin, cartilage, ligament, gland, nerve, CSF, and 15 different kinds of tissue within the brain. Of these, only white matter and grey matter have known electrical parameters, and the remaining must be assigned "average brain" parameters. Some nerve tissue is identified separately from brain tissue in the digitization. The digitized cross-sections do not differentiate between bone and fat, hence small regions in the model, which should be fat, have the same electrical parameters as bone. Correcting this shortcoming would require considerable manual labor. Another error in the 1994 digitization misinterpreted apparently-empty regions inside the skull as filled with air, when in fact they are filled with cerebral spinal fluid (CSF). This error was corrected in the set of digitized sections. The digitized sections do not distinguish the various kinds of gland tissue, hence all four of the gland tissues in Table 1 were assigned the same electrical parameters. Only one type of eye tissue was identified in the 1994 digitization. Table 7.1 gives the values used for the relative permittivity and conductivity of the tissues in the model described in this chapter. The values in Ref. [37] have been used for most of the tissues. However, for gland tissue and for nerve, the values from Ref. [38] were used.

7.3 Assembling an FDTD Cell Model

A new computer program called "MKHEAD" was written to assemble an FDTD cell model from the digitized anatomical sections. MKHEAD uses the 29 digitized anatomical cross-sections as input data, and creates a cell model of the anatomical head with a specified cell size. The user specifies the tilt angle of the head to the vertical. Thus with a tilt angle of zero degrees, the vertical axis of the head aligns with the vertical axis of the FDTD coordinate system. Since the antenna of the handset always aligns with the FDTD vertical axis, the major axis of the head is then parallel to the antenna. As the tilt angle is increased, the major axis of the head is rotated from $+z$ towards the $+x$ axis in the FDTD coordinate system. To derive a head to be used for computing radiation patterns with the handset held at 60 degrees to the vertical, in the FDTD coordinate system the antenna is vertical and the head is tipped 60 degrees towards the $+x$ axis. The software described in the last chapter is used in conjunction with FDTD PML and FARZONE to find radiation patterns as if the head were vertical and the handset tipped back 60 degrees.

The MKHEAD derives the material type for each cell in the FDTD cell space using the digitized anatomical sections as a guide. The program works as follows. For each cell in the FDTD cell space, the program search through all the cells on each of the 29 digitized cross-sections to find the closest cell on any cross-section. This must

account for the relative alignment of the cross-sections one to the other, and their tilt to the vertical axis of the head, illustrated in Fig. 7.1. Also, the user's desired tilt angle of the head to the vertical in the FDTD coordinate system must be accounted for. Each FDTD cell is assigned the material of the nearest cell in the set of 29 cross-sections. Although the search for the nearest cell was programmed efficiently, MKHEAD requires substantial computer time to execute. Provided the cell size is not much smaller than half the distance between the anatomical sections, the resulting cell model is quite reasonable. Thus this process works well for cells as small as 5 mm in size. For smaller cells, the FDTD cell model tends to be unsatisfactory and requires considerable hand-editing, to smoothly interpolate between the digitized anatomical cross-sections. As discussed below, a cell size of 2.205 mm is desirable. Hence models created with this anatomical data base and MKHEAD require a large investment of labor to clean up their internal structure. This is because the underlying data base of 29 cross sections simply is not sufficiently dense to create cell models with a 2 mm cell size. The correspondence of the resulting cell model to real head anatomy is also somewhat imprecise. The anatomical head created in this way must be regarded as a rough tool for evaluating gross changes in the radiation patterns of the handset, rather than the best possible anatomical model.

Note that it is necessary to derive an explicit FDTD cell model for each desired tilt angle of the handset to the head. Each cell model requires a substantial amount of manual optimization. Hence a cell model oriented vertically in the FDTD coordinate system was the only one actually created.

7.4 The Anatomical Head Cell Model

To be valid at 850 MHz, the cell size in the FDTD model must be smaller than one-tenth of the wavelength in the material, for the biological material having the shortest wavelength. The high relative permittivities and conductivities listed in Table 7.1 make a cell size of 0.441 cm too large at 850 MHz. The cell size was halved and the MKHEAD program was used to derive an anatomical model at 2.205 mm cell size. Table 7.2 lists the highest frequency at which a 2.205 mm cell of various biological materials can be used. Free-space cells are good to beyond 13 GHz. Many of the materials have limiting frequencies above 2000 MHz. As the relative permittivity of the material goes up, the limiting frequency tends to go down. Higher conductivity also reduces the limiting frequency. The eye, with a relative permittivity of 67.9 and a conductivity of 1.68 S/m imposes a severe limitation on the frequency range of the model. In evaluating the specific absorption rate(SAR) of power in the head, the eye is critical because the body's heat dissipation mechanisms are not as efficient for the eye as elsewhere. Cerebral spinal fluid(CSF) with a high relative permittivity of 79.1 and a high conductivity of 2.14 puts the most severe restriction on cell size, and limits the frequency range of the present model to 1509 MHz. There are many cells throughout the brain cavity of the present model that are filled with CSF.

A cell size of 0.2205 cm is much smaller than the vertical spacing of approximately 1 cm of the anatomical cross-sections of Fig. 7.1. As a result, the cell model assembled by MKHEAD tends to contain discontinuities as the program switches from using the material types of the anatomical section "below" the plane of FDTD cells being created, to using the section "above". The EDITCEL program was used to

manually smooth the internal structure of the head cross-sections to remove such abrupt transitions and to ensure the continuity of the skin and bone layers inside the head. Fig. 7.3 shows an xz plane through cell #60 of the anatomical head. Fig. 7.4 shows an xy plane through cell #84. The skin, bone, muscle and brain are clearly seen. The voids in Fig. 7.3 are sinus cavities. The tongue muscle is clearly seen. The overall size of the head is 76 by 60 by 80 cells, or 16.76 by 13.23 by 17.64 cm.

Table 7.2
Limiting Frequencies for Biological Materials with a Cell Size of 2.205 mm

Material	Relative Permittivity	Conductivity S/m	Limiting Frequency MHz
Free Space	1.00	0.	13598
Bone	20.90	0.33	2970
Nerve	33.40	0.60	2347
White Matter	34.50	0.59	2309
Skin	40.70	0.65	2126
Brain, average	41.00	0.86	2115
Cartilage	41.90	0.83	2092
Gland	45.30	0.92	2011
Grey Matter	53.80	1.17	1843
Blood	55.00	1.86	1808
Muscle	57.40	0.82	1789
Eye	67.90	1.68	1635
CSF	79.10	2.14	1509

In order to analyze the handset and anatomical head with the FDTD PML program, a cell space of 116 by 110 by 156 cells is required. This includes 6 cells for the PML, which used parabolic evolution of the conductivity and a surface reflection coefficient of 0.001. Four cells of whitespace separate the surfaces of the head and handset from the inner surface of the PML. This is the same design of the cell space that was used in earlier in this report. The cell model was run on a Pentium Pro computer with a 200 MHz processor and 256 Megabytes of memory.

The following compares the principal plane patterns of the vertical handset operating near the anatomical head to those of the handset near the sphere head.

7.5 Radiation Patterns of the Handset near the Anatomical Head Model

Fig. 7.5 shows the handset adjacent to the sphere head in part (a), and the handset near the anatomical head in part (b), drawn to the same scale. The handset was positioned with the top of the box adjacent to the ear, where a real portable radio would have its earpiece. The handset orientation is vertical, as shown in Fig. 7.3. This section

compares the radiation patterns of the vertical handset adjacent to the anatomical head with those of the handset near the sphere head.

Fig. 7.5 shows that the anatomical head is much smaller than the sphere head. The sphere is 20.68 cm in diameter, bigger than the back-to-front size of the head of 16.76 cm including the nose, or the side-to-side size of 13.23 cm including the ears. The head is 17.64 cm tall, and does not include much neck, as shown in Fig. 7.3. Additional anatomical cross-sections are available for the neck, but were not digitized.

Fig. 7.6 compares the radiation patterns of the handset and anatomical head with those of the handset and sphere head. Overall, the radiation patterns are quite similar, both for E_θ and E_ϕ , despite the difference in size of the head and the sphere. The azimuth pattern in Fig. 7.6(a) shows a broadly directional pattern for E_θ . The handset and sphere pattern has a maximum of 2.0 dB at 303 degrees, while the handset and head has a maximum of 0.7 dB at 294 degrees. The sphere pattern has a minimum of -14.2 dB at 142 degrees, while the head pattern is smallest at -10.4 dB at 160 degrees. In the E_ϕ component, the handset and sphere has a maximum of -2.3 dB at 132 degrees, compared to the handset and head, which has a maximum of -2.1 at 144 degrees. Both patterns have a sharp, deep minimum at 81 degrees, -22.5 dB for the handset and sphere and -22.8 dB for the handset and head. The patterns are somewhat different from 190 to 280 degrees, where the handset lies behind the head. The handset and sphere pattern has a minimum of -11.5 dB at 278 degrees. The handset and head has a much larger minimum of -16.7 dB at 252 degrees.

The elevation pattern for $\phi = 0$ is shown in Fig. 7.6(b). In E_θ , the handset and sphere pattern has main lobes at 2.0 dB, 114 degrees and 0.8 dB, 235 degrees. The handset and head pattern has main lobes at 2.2 dB, 116 degrees and 1.7 dB, 234 degrees. The handset and sphere pattern has minor lobes at -4.9 dB, 39 degrees, and -7.8 dB, 311 degrees. The handset and head has minor lobes at -3.5 dB, 40 degrees, and -2.5 dB, 314 degrees. The minor lobe near 310 degrees is quite different in level between the two head models. At this angle the handset lies in front of the head. The anatomical head causes less change in the handset-alone pattern than does the larger sphere head. The radiation pattern for the E_ϕ component is higher in level and less directional for the handset and anatomical head than for the handset and sphere head. The maximum field for the sphere is -3.6 dB at 39 degrees, compared to -2.2 dB at 53 degrees for the head. The smallest E_ϕ with the sphere head is -13.5 dB at 220 degrees, compared to -7.0 at 218 degrees with the anatomical head.

Fig. 7.6(c) shows the elevation pattern for $\phi = 90$ degrees. In E_θ , the main lobes in the handset and sphere pattern fall at 1.4 dB, 115 degrees and at 5.8 dB, 243 degrees. For the handset and head, the main lobes are 1.9 dB at 113 degrees and 4.5 dB at 245 degrees. There are minor lobes for the sphere at -3.3 dB, 50 degrees and -1.9 dB, 327 degrees. For the head, the minor lobes fall at -1.3 dB, 41 degrees and -1.4 dB, 332 degrees. The minima in the two patterns are also quite similar. The E_ϕ component is larger in this pattern for the handset and sphere, having a maximum value of -10.7 dB at 123 degrees. For the head, the maximum is -13.5 dB at 130 degrees. The minimum for

the handset and sphere is -20 dB at 188 degrees, and for the head is -18.6 dB at 195 degrees.

This section has compared the radiation patterns of the handset in the vertical position operated near the anatomical head with those of the handset and sphere head. In spite of the much larger size of the sphere compared to the anatomical head, the radiation patterns are very similar.

7.6 Conclusion

This chapter presented the derivation of an FDTD cell model of the head based on anatomical cross-sections. This set of cross-sections was digitized with a 2.5 mm cell size. Since the drawings in Ref. [43] are three-quarters size, the digitization actually corresponds to a 3.33 mm cell size. Also, the cross-sections in Ref. [43] are spaced roughly 1 cm apart. From this anatomical data, a cell model using a cell size of 2.205 mm was developed. This small cell size was chosen so that the dimensions of the handset can be accurately represented, and also that the cell size remains smaller than a tenth-wavelength for all the materials making up the head. A computer program called "MKHEAD" was written to derive the material type of each cell in the FDTD head model from the set of 29 anatomical cross-sections. The resulting cell model can be considered "coarse" in that the anatomical basis for the model is not on as fine a scale as the 2.205 mm cell size in the model. Also, the resulting head is rather small in overall size, only 16.8 cm back-to-front and 13.2 cm side-to-side. A larger head could be created by simply increasing the scale factor used in the MKHEAD program.

The anatomical head model was used in this chapter for an initial evaluation of the radiation patterns of the portable radio handset patterns when the handset is operated in the presence of a head. The handset was oriented vertically and the patterns of the handset and head were compared with the patterns of the handset and the sphere model of the head. The patterns with the anatomical head are very similar to those with the sphere head.

It is more realistic to operate the handset tilted at 60 degrees to the vertical axis. The MKHEAD program can be used to develop an anatomical head model that looks "down" at 60 degrees in the FDTD coordinate system, and so can be used to predict the radiation patterns of the handset tilted back 60 degrees when the head is vertical.

Overall, the present anatomical head model is considered coarse and it is recommended that a better anatomical model be developed based on the 250 cross-sections of a head available from the Visible Human project[45].

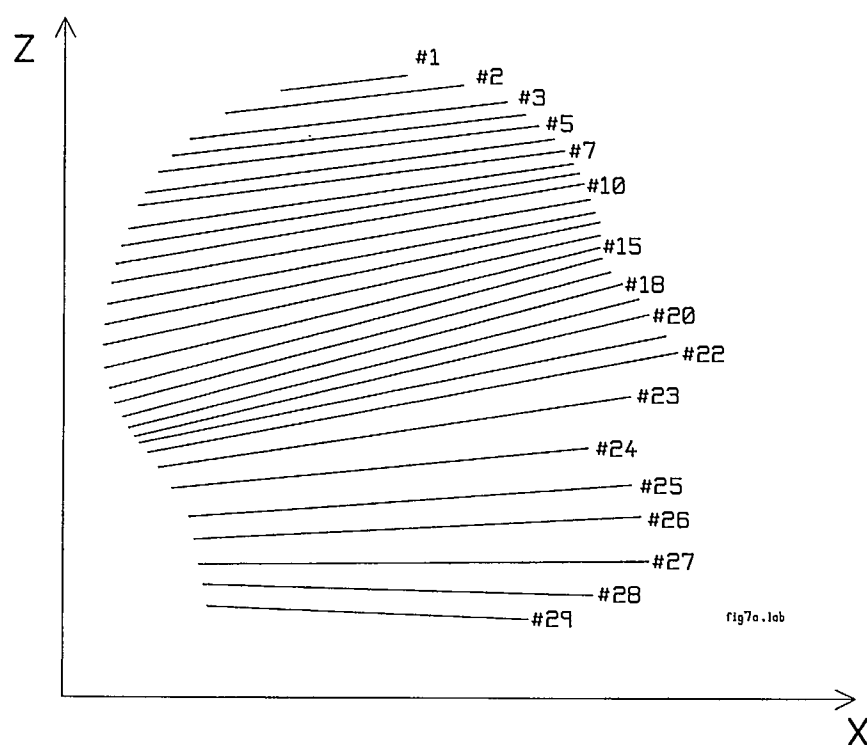


Fig. 7.1 The location of the cross-sections of the head in Ref. [43].

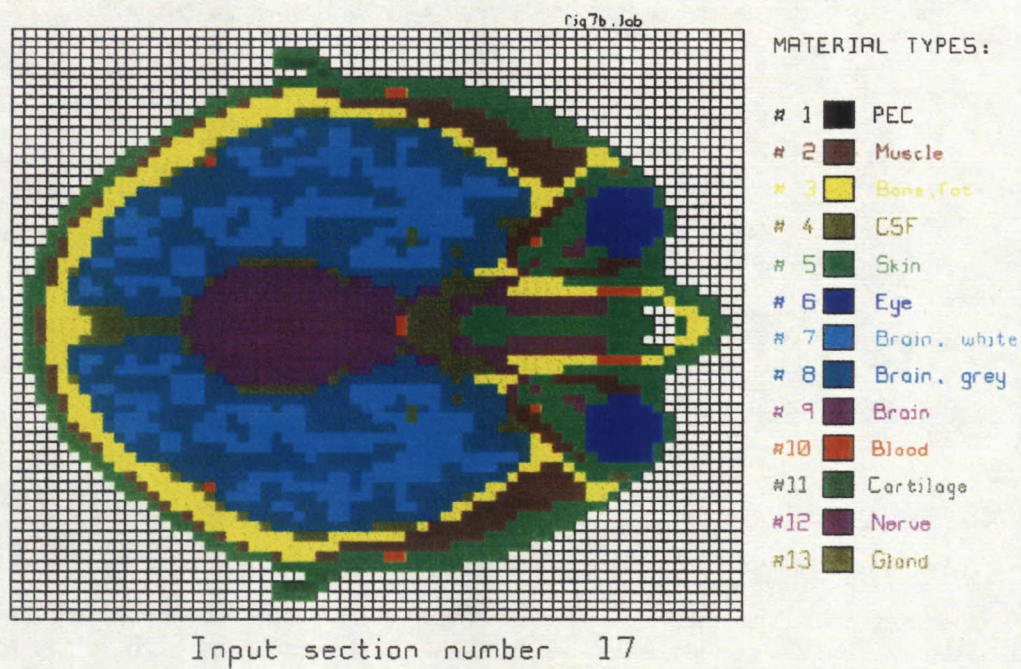


Fig. 7.2 Digitized anatomical cross-section number 17.

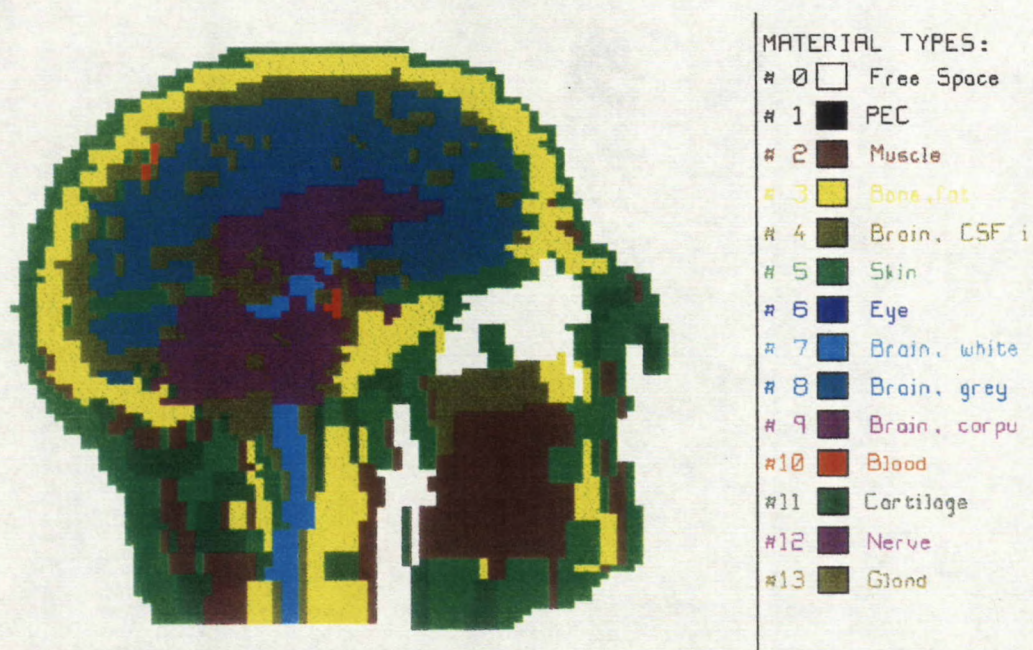


Fig. 7.3 A vertical or xz plane section at cell #60 through the cell model of the anatomical head.

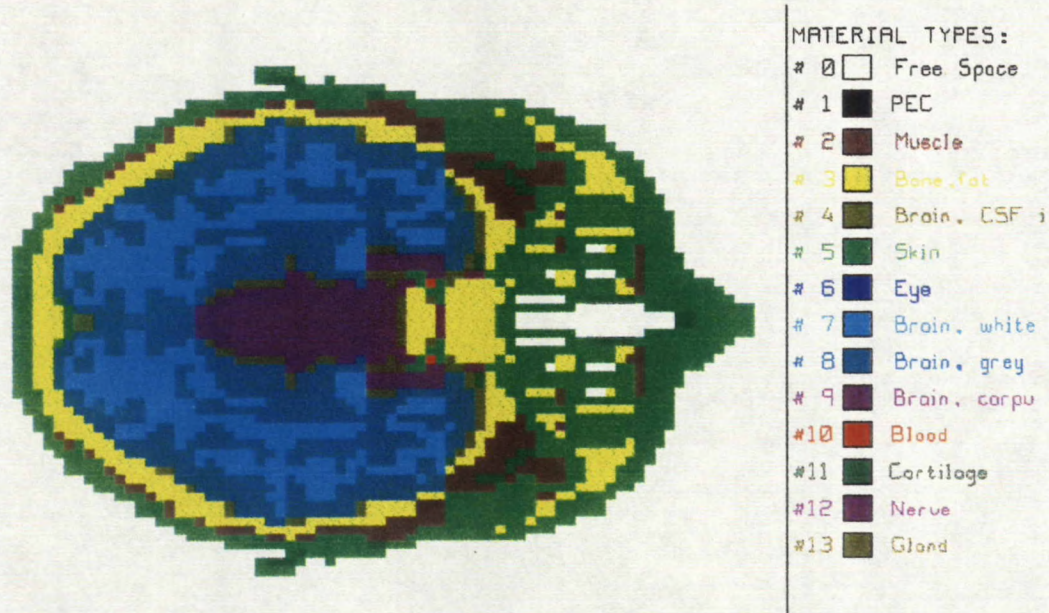
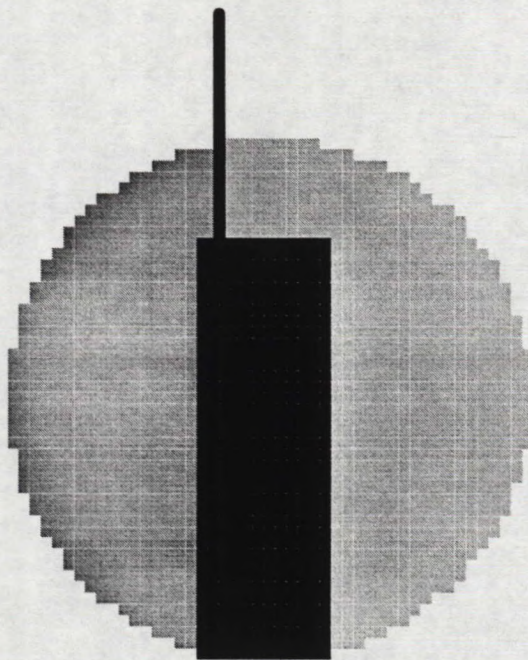
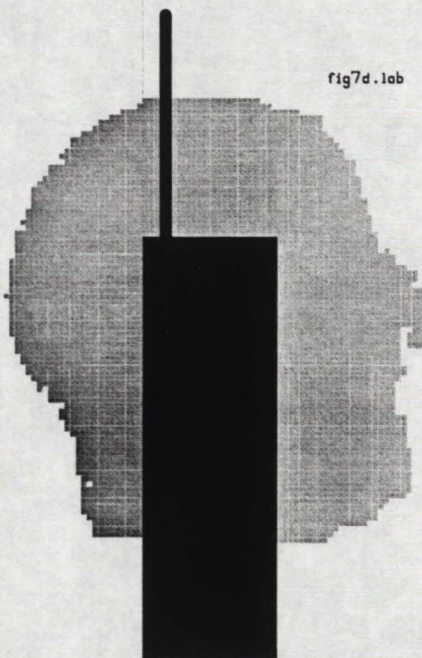


Fig. 7.4 A horizontal or xy plane section at cell #84 through the cell model of the anatomical head.



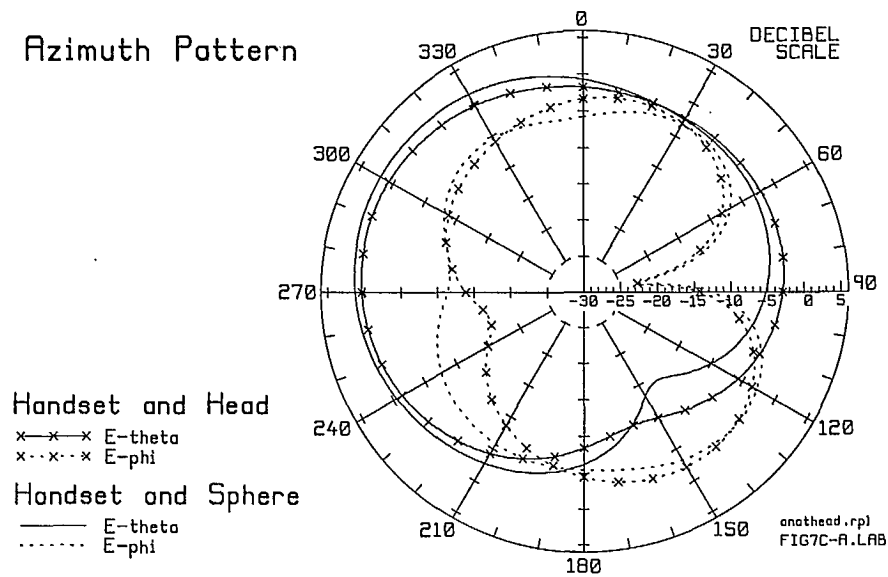
(a) The handset and the sphere head.



(b) The handset and the anatomical head.

Fig. 7.5 The handset and sphere head, and the handset and anatomical head, drawn to the same scale.

Azimuth Pattern



(a) Azimuth pattern.

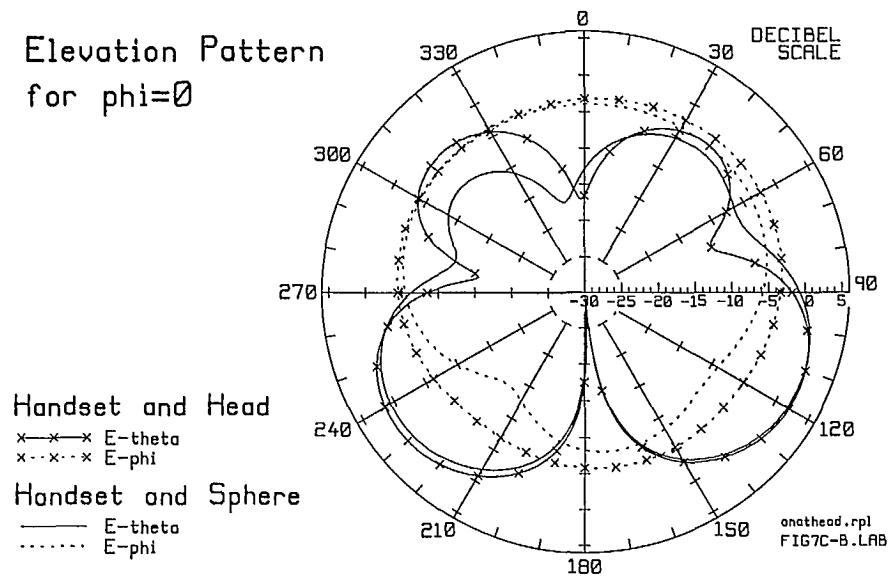
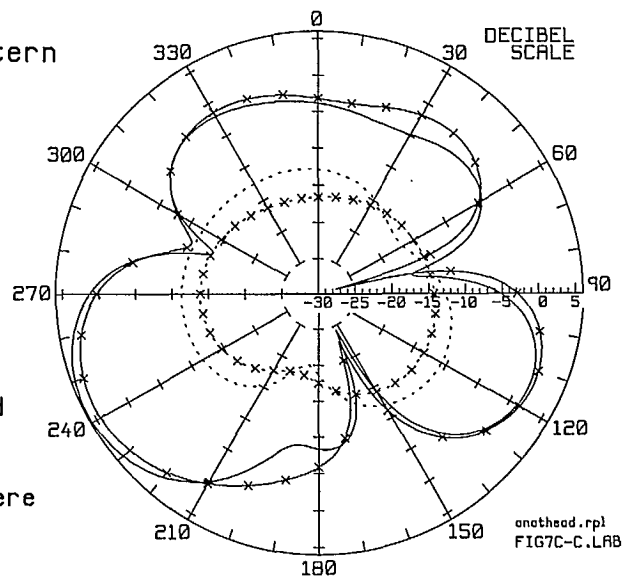
Elevation Pattern
for $\phi=0$ (b) Elevation pattern for $\phi = 0$ degrees.

Fig. 7.6 The radiation patterns of the handset and anatomical head, and of the handset and sphere head.

Elevation Pattern
for $\phi=90$

Handset and Head
 x-x-x E-theta
 x--x--x E-phi
 Handset and Sphere
 — E-theta
 E-phi



(c) Elevation pattern for $\phi = 90$ degrees.

Fig. 7.6 (continued) The radiation patterns of the handset and anatomical head, and of the handset and sphere head.

Chapter 8

The Head Phantom

This report has investigated the radiation patterns of the portable radio handset near simple models of the head such as the box head and the sphere head. Fig. 8.1 shows a realistic head phantom suitable for testing portable radio handsets. The phantom includes a hand to hold the portable radio, not shown in Fig. 8.1. The head phantom will be used in future work to study the radiation patterns of the handset and head, with the handset in various orientations to the head. Also, the near fields of the handset and the phantom head will be measured. The patterns of the handset and phantom head will be calculated with FDTD, and compared with the measurement, as a validation of the FDTD method. Solving the phantom head is a much greater test of the FDTD method than solving the simple head models. For such analysis an accurate cell model of the head phantom is required, and this in turn requires a detailed knowledge of its internal structure. Cross-sectional drawings of the head were not available from the manufacturer. This chapter discusses the derivation of a cell model of the head phantom, suitable for analysis with FDTD.

8.1 The Head Phantom

The head phantom of Fig. 8.1 is a physical model of a head suitable for testing the performance of portable radio handsets. The phantom available for this project[29] includes five tissue types: skin, bone, muscle, eye and brain. The manufacturer provides tabulated information on the permittivity and conductivity of the skin, bone, muscle and eye material. This is reproduced in Appendix 3. The brain cavity in the phantom head is empty and is to be filled with "brain-equivalent liquid" through a hole in the top of the head. The manufacturer provides bottles of such liquid; it can also be mixed from de-ionized water, sugar and salt[21] as was done for the sphere and box heads. In that case the permittivity and conductivity must be measured so that the properties of the brain material are well known.

To construct a cell model for analysis with FDTD we need a "map" of each cross-section of the phantom, identify which regions are skin, bone, and so forth. Such cross-sectional information was not available from the manufacturer, and so had to be sought elsewhere. The medical community uses two techniques to examine the internal structure of the human body, "magnetic resonance imaging" and "computed tomography". Both these methods were tried with the phantom head, as described in the following sections.

8.1.1 MRI Scans

"Magnetic resonance imaging" or MRI uses magnetic fields to excite the atomic nuclei of tissue. The nuclear spin is excited from a low energy state in which it is aligned parallel to the exciting magnetic field, to a higher state in which the spin has a component transverse or opposed to the field. When the spin reverts to the original state a photon is

emitted at a characteristic or resonance frequency. Because different tissues respond in different degrees to the excitation, a cross-sectional map of the body can be assembled from the number of photons received from each area.

A set of MRI scans of the phantom head was made at the Montreal Neurological Institute. These were done in vertical planes oriented from the back of the head to the front, or xz planes in the coordinate system used in this report. Figs. 8.2 and 8.3 are typical MRI scans of the phantom. The MRI scanner was not able to see inside the bone layers. MRI scanning is sensitive to the presence of metals even in tiny amounts. It was suspected that the bone layer contained trace amounts of metal.

Fig. 8.2 shows that the MRI scans show the layers outside the bone clearly, but that the skin and the muscle are not differentiated. The outer surface of the bone layer is clearly distinguished as well. But the internal structure is hardly seen at all.

Fig. 8.3 shows an MRI scan through the eye. We note that the eyeball is not seen at all in the MRI data.

The MRI data includes a complete set of scans at 2 mm intervals. It may be possible to assemble a model defining the outer surface of the skin and the outer surface of the bone layers based on the MRI scans. However, distinguishing the skin from the muscle appears to be impossible. This has not been attempted at this time.

8.1.2 CT Scans

Computed tomography or CT scanning uses a narrowly-collimated beam of X-rays that rotates in a continuous 360 degree motion to image the body in cross-sectional slices. A map of the tissue density is assembled from multiple attenuation readings taken by an array of detectors around the periphery of the body.

A set of CT scans at 2 mm intervals was made at the Royal Victoria Hospital. Figs. 8.4 to 8.7 show typical CT scan of the head phantom. These were done in horizontal or xy planes. The CT scans show the interior structure of the head phantom quite well. The bone layers show up as starkly white regions streaked with dark black bands, which resemble portions of ellipses. The region outside the head is heavily filled in with gray streaks, which appear to radiate outward from the center of the head. These are seen in Fig. 8.5 near the ears, especially on the left side of the head.

The skin/muscle layer is seen clearly in most of the cross-sections. However distinguishing skin from muscle may be a problem. In the neck, Fig. 8.4, the muscle layer around the bone has a more mottled appearance than the skin layer near the surface. In Fig. 8.5 it is not easy to see what areas are skin and which are muscle in the cheeks, nor in the back of the head. The same problem exists in Fig. 8.6. In Fig 8.7, towards the top of the head, the muscle layer is thin and muscle and skin are not clearly distinguished.

Fig. 8.5 shows that the ears are not clearly defined in some of the CT scans, whereas in others, such as Fig. 8.6, the ears are much more clearly seen.

Fig. 8.6 shows a serious deficiency in the CT scans. The phantom has eyeballs which fill the sockets seen in Fig. 8.6, but the CT scan shows no trace of the eyes.

To assemble a cell model for analysis with FDTD, the tissue types in each of the CT scans must be unambiguously identified.

8.1.3 Identifying Tissue Types

Assembling a cell model from the CT scans, possibly using some data from the MRI scans, is a challenging task. Ref. [6] suggests that the gray scale in a typical scan can be subdivided into bands, and each band associated with a particular tissue type. The reference suggests an orderly progression from very white regions for bone, through grayer regions for skin, to a darker gray for muscle, and so forth. This was attempted with the CT scan data. However the results were unsatisfactory. The streaks in the regions outside the head in Fig. 8.5 are dark enough to be confused with the skin layer. The white regions representing the bone are liberally streaked with dark black, causing misidentification of the dark areas as muscle within the bone. It appears that a fully automatic tissue identification based on gray levels alone is not possible. The idea was used in the following as a starting point to distinguish muscle from skin, but it was found that a great deal of manual edit is required in each cross-section. The following section describes a method of identifying tissue types in the CT scans.

8.2 Identifying Tissues in the CT Scan Cross-Sections

To use the CT scan data to derive a cell model of the head suitable for analysis with FDTD, each of the CT scans must be processed to clearly mark each pixel in the scan as free space, or one of the five tissues: skin, muscle, bone, eye or brain. Once the complete set of cross-sections has been processed in this way, then the MKHEAD software of Chapter 7 can be adapted to create a cell model of the phantom for any desired cell size or tilt angle of the head relative to the handset. This section discusses the processing steps used to identify the material types in each CT scan cross-section.

Fig. 8.4 shows a CT scan cross-section of the neck of the phantom. The center is the spine. It is surrounded by a shadowy region of muscle tissue, then an outer layer of skin. The region of bone is mostly white, but has patterns of black within it. The surface of the bone is dark in color compared to the surrounding muscle tissue. The muscle and skin are mainly differentiated, to the viewer's eye, by the texture. The skin is a more solid color than the muscle. There is a large void at the upper right in the cross-section. The top of the scan shows the wooden post that supports the phantom's chin. The data file from which Fig. 8.4 is made uses a gray scale to represent tissue density, with each pixel having a "gray" value on an arbitrary scale, say from 0 for "white" to "1" for black.

An interactive graphics program called EDITMAP was written to aid in identifying areas of bone, muscle, skin and wood in CT scan cross-sections. The first step in using EDITMAP is to convert the CT scan data to a format called "tbb" or "binary table file", which is understood by the EDITMAP program. A utility program called TOTBB reads the "raw" CT scan data and converts it to a "tbb" file for EDITMAP. The gray scale is replaced by a false-color scale, which is designed to roughly differentiate muscle as blue, and skin as green, as shown in Fig. 8.8. The right-hand column in the figure lists the functions offered by EDITMAP, and the following describes how the program is used to identify and mark tissues in a CT scan cross-section.

In EDITMAP the pixels making up the cross-section are classified as either "raw" pixels, which have not been identified by tissue type, or as "bone", "muscle", "skin", "eye", "brain", or "wood". All the pixels in the initial input file, from program TOTBB,

are "raw" pixels, and the object of EDITMAP is to reclassify each pixel as one of the tissue types, or as "wood". EDITMAP permits the user to work on each tissue, one at a time. The "Choose a Material" function is used to select a tissue, and the tissue being edited is named at the top right of the screen. Thus we see "EDIT BONE" in Fig. 8.8.

8.2.1 The Bone Tissue

The first step in processing each cross-section is to identify transitions from free-space to tissues with the "slope filter". This function looks for large changes in saturation from one pixel to the next, and marks such pixels as "bone", the tissue type being edited. Fig. 8.9 shows the pixels that the "slope filter" changes to bone in the cross-section of Fig. 8.8. The transition from the muscle layer to the spine is marked quite well, thus outlining the spine region in "bone" pixels. But this step has the side effect of outlining the surface of the skin with "bone" pixels, as well as the surface of the void and also the surface of the wooden post. This is very easily changed, later in the process.

The central idea in EDITMAP is to outline regions of a given tissue, say "bone", with pixels of that tissue type, and then use the "area fill" function to change all the "raw" pixels within the area to "bone" pixels. Thus the next step is to carefully examine the outline of the spine of Fig. 8.9, and to use the "draw line" function to close any gaps in the outline. Also, regions that are not joined up are joined manually with "draw line" so that the whole region to be filled with "bone" is enclosed. Then "area fill" is used to change all the enclosed "raw" pixels to "bone". The small contours inside the spine in Fig. 8.9 enclose pockets of "raw" pixels that will have to be changed to "bone" individually with "area fill". When most of the pixels in the spine region are "bone", then the "join filter" function can be used to clean up individual "raw" pixels. This function examines each "raw" pixel, and if all its neighbors are "bone", then that pixel is changed to "bone", as well. The result of this step is Fig. 8.10, where the dark blue region in the center is the spine, marked as "bone" pixels.

8.2.2 The Muscle Tissue

The next step is to separate the skin and muscle regions. This is done with the "range filter". The user selects "skin" as the tissue to be edited, and then selects "range filter". This changes "raw" pixels that lie in the gray-scale range from 0.28 to 0.40 to "skin" pixels. These pixels show up as green in Fig. 8.10, distinct from the blue "muscle" pixels. The result is shown in Fig. 8.11, where the pixels marked as "skin" are now shown in yellow. The a thick layer around the surface of the neck is now identified as "skin", but also many regions inside the muscle are marked as "skin" as well, and need to be changed.

The fourth processing step is to clean up the regions of muscle tissue so that all the pixels in these areas are marked as "muscle". The user selects "muscle" with "Choose a Material". "Zoom" is used to enlarge small regions of the map to fill the screen, and then the "Draw a Line" function is used to enclose muscle regions with an unbroken line of red muscle pixels. Then "Area Fill" is used to change "raw" pixels within these regions to muscle. This does not change pixels marked as "skin". The "Revise Area" function is used to modify pixels incorrectly identified as "skin" to

become muscle pixels. This must be done for all the yellow areas in Fig. 8.11. This is a laborious step, and is the bulk of the work needed on each cross-section. In addition, a line of pixels along the void at the upper right was incorrectly marked as "bone" by the slope filter; the "Revise Area" function is used to change these to "muscle". When most groups of pixels within the muscle region have been marked as "muscle", then individual remaining pixels can be converted to "muscle" quickly with the "Join Filter" function. The result is shown in Fig. 8.12. Now the bone and muscle regions have been clearly marked.

8.2.3 The Skin Tissue

Fig. 8.12 shows that the skin region still contains many incorrect pixels, mostly at the surface of the skin but also at the surface of the void. The next processing step is to choose "skin" as the material to be edited and then use the "Revise Area" function to change the "bone" pixels at the surface to "skin". This is quick because the "Revise Area" function is able to follow the contour of pixels all around the surface and change them to "skin" in one operation. Similarly, the line of "bone" pixels at the surface of the void is "revised" to "skin". Small regions of "raw" pixels within the skin region, such as at the bottom center in Fig. 8.12, are changed to "skin" with "Area Fill". The "Join Filter" is useful for changing the great many "raw" pixels just beneath the surface of the neck into "skin" pixels.

Finally, select "wood" as the material and use "Area Fill" to change the "raw" pixels of the post to "wood" pixels. Use "Revise Area" to change the "bone" pixels at the surface of the post to "wood" pixels. If the editing process in the foregoing has been carefully carried out, there will be few "raw" pixels at this stage. Any "raw" pixels are identified and removed with the "Clean Up" function. This searches the entire map for "raw" pixels and changes each to the tissue type of the majority of the neighbors. The result of the editorial process is shown in Fig. 8.13, which should be compared with the input data, Fig. 8.4.

Note that the various functions of the EDITMAP program should be used in the sequence described. For example, using "Clean Up" early in the process destroys the cross-section. If an error is made, then "Undo" removes the last processing step done. It is good practice to exit from EDITMAP and save a backup of the partially-edited cross-section, usually after the marking of the "bone" pixels as in Fig. 8.10. Then if a disastrous error is made in editing skin or muscle pixels, the user can start again with the bone already identified. The EDITMAP program itself does not have a "backup" function. The foregoing did not use the "mild filter" from the function menu. This is similar to the "Join Filter" but is not as effective in identifying and fixing individual "raw" pixels within regions that have been marked as "bone" or "muscle" or "skin".

8.2.4 Discussion

In the foregoing a procedure has been described for identifying the material types in a CT scan such as Fig. 8.4, such that the material type of each pixel is clearly identified, as in Fig. 8.13. Each of the 117 CT scans of the head phantom must be processed with EDITMAP prior to building a cell model for analysis with FDTD. In fact,

the set of 21 neck cross-sections have already been completed. The remaining 95 cross-sections must be simplified.

Identifying material types in some cross-sections will present significant difficulties. In the cross-section near the base of the brain cavity, Fig. 8.5, the ears are very ill defined in the CT scan, and indeed the skin layer on the left side of the head is not clearly seen in the CT scan. There is an apparent "hole" in the skin adjacent to the bone on the right cheek, as well. This may, in fact, be a muscle region. The bone region is filled with dark pixels in this scan. We must speculate as to whether the dark region at the bottom center, within the bone, is the lower or perhaps upper surface of the bone.

Fig. 8.6 shows a CT scan through the eyes. In this scan the ears are quite clearly defined. The regions of bone are also clearly seen and the EDITMAP software should be adequate to identify them. However, the skin on the left side of the head at the back is not clearly seen. It seems that the skin layer gets thin in this cross-section. The brain cavity in Fig. 8.6 is quite well defined.

The most serious deficiency in Fig. 8.6 is the eyes. In fact, the eye tissue is not seen at all in the scan. The sockets in the bone are very clear but are filled with gray with dark bands emanating from the front center, and no eyeballs are evident.

Fig. 8.7 shows a CT scan through the temple region towards the top of the head. In Fig. 8.1, the red muscle is seen clearly through the clear skin coating, and extends well above the eyes to the top of the forehead. But in neither Fig. 8.6 nor Fig. 8.7 is the muscle clearly distinguished from the skin. We can speculate that the light region adjacent to the bone at the left front and at the right front is a muscle region. Lacking further information, these regions would be marked as muscle.

Overall, the CT scans have serious deficiencies as a basis for the cell model. There are no eyes. The distinction between skin and muscle is unclear. The accuracy of the overall model must necessarily suffer from these difficulties.

8.3 Conclusion

To model the head phantom with FDTD requires a full set of cross-sections which clearly identify the tissues, such as that in Fig. 8.13. The "MKHEAD" program of Chapter 7 can be adapted to accept cross-section data derived of this type, and so derive a cell model of a user-specified cell size at a user-specified tilt angle to the handset. Because the CT scan data is much more detailed and complete than the anatomical data set used in Chapter 7, it is expected that only modest amounts of hand-editing will be required to complete a cell model of the phantom derived with MKHEAD.

The CT scan data set presents two serious difficulties which must be overcome before a cell model can be derived. The first is the ambiguity in the muscle and skin in many of the cross-sections. Thus muscle and skin layers in Figs. 8.5, 8.6 and 8.7 are not clearly differentiated. The second obstacle is the lack of eyes. Fig. 8.6 shows no trace of the eyeballs.

It is intended that the hand be included in future studies of the radiation patterns and near fields of the head. The hand was not scanned and so no data concerning its internal structure is available. The hand should be scanned so that it can be included in

the data set and so that a cell model of the hand can be created to include “holding” the handset in future studies.

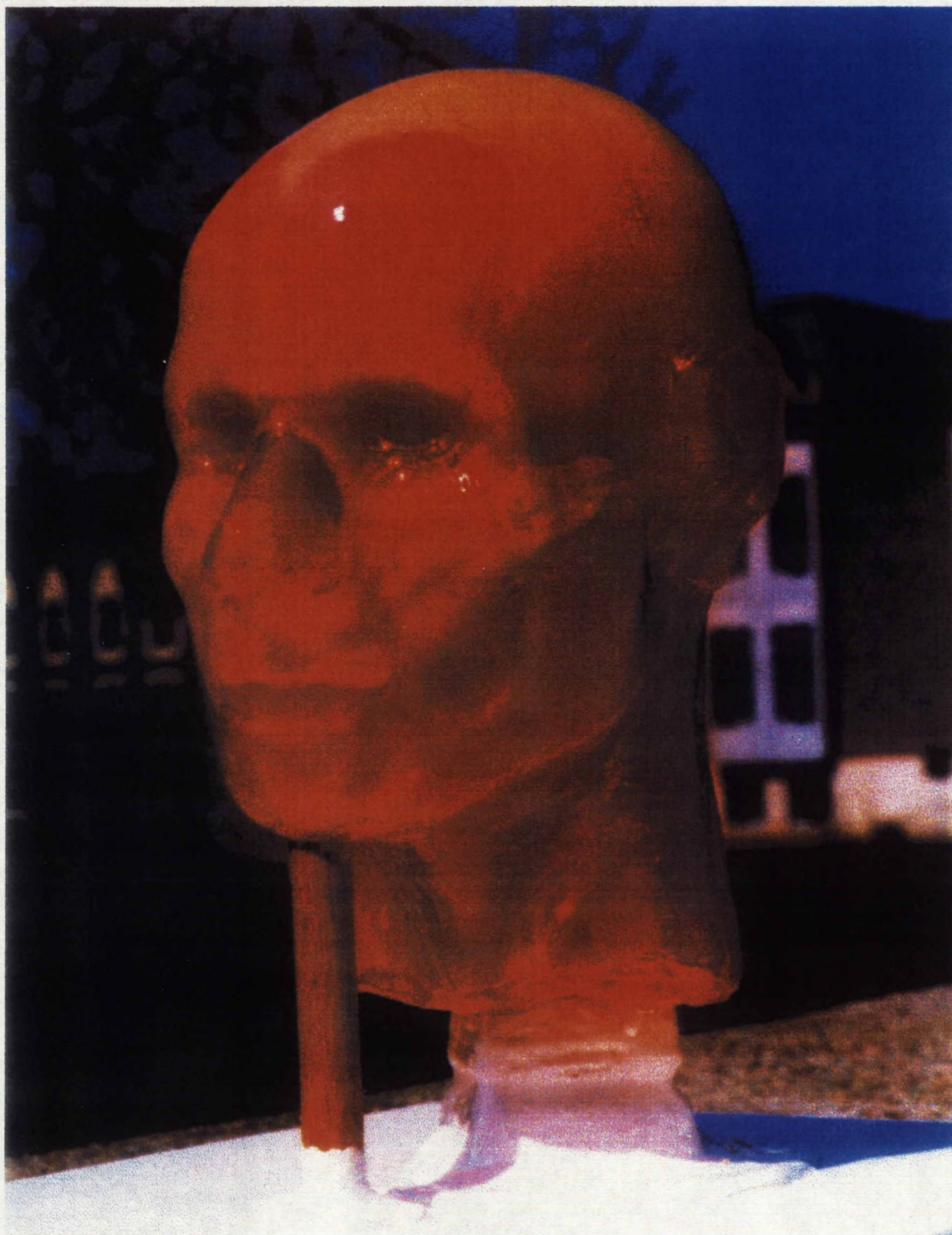


Fig. 8.1 The head phantom.

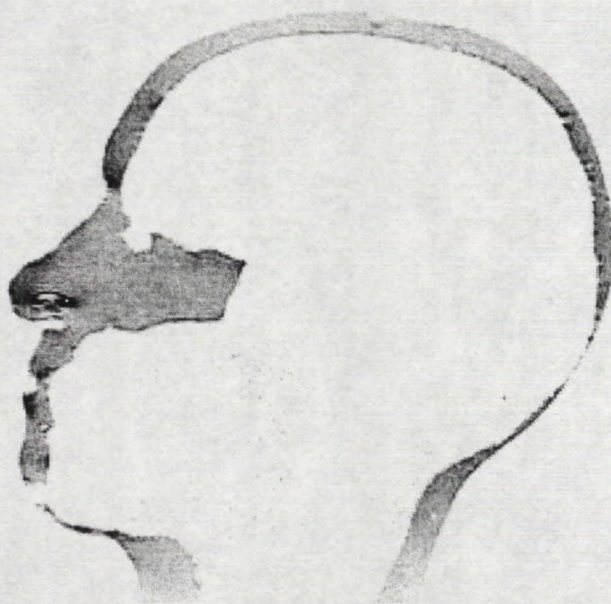


Fig. 8.2 An MRI scan of the head phantom in an xz plane through the center of the head.

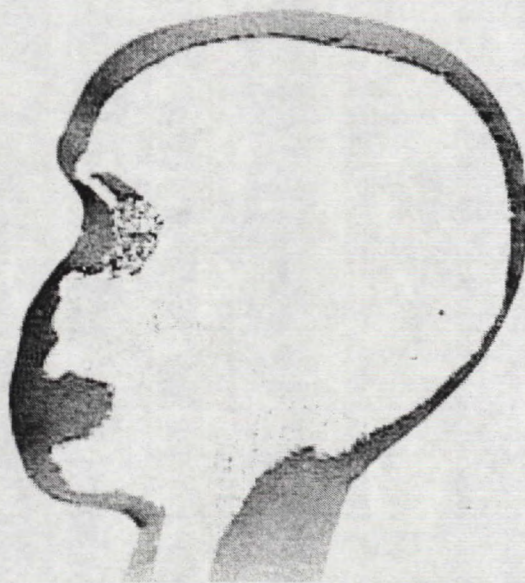


Fig. 8.3 An MRI scan of the head phantom in an xz plane through one eye.

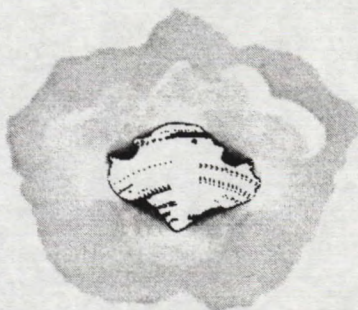


Fig. 8.4 CT scan # 6 of the head phantom, through the neck. The grey circle at the top is the wooden post that supports the phantom's chin.

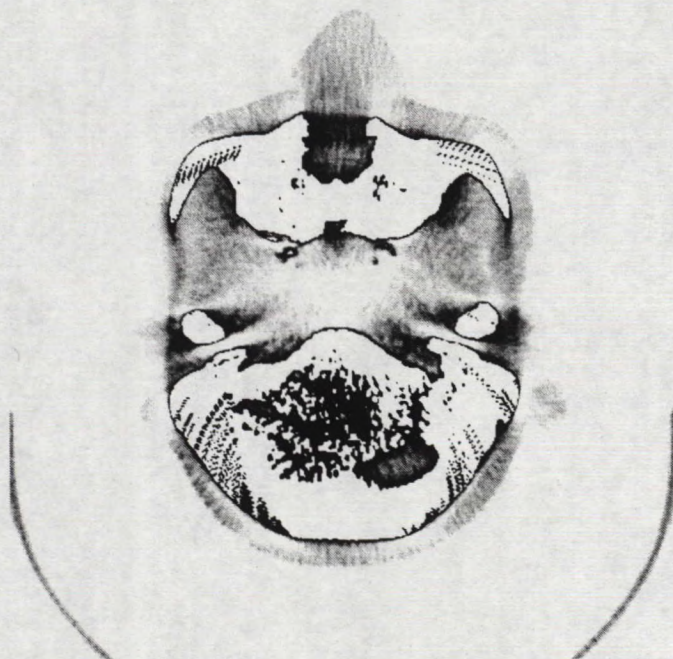


Fig 8.5 CT scan # 57 of the head phantom, near the base of the brain cavity. The grey quarter-circles at the lower left and lower right are the cradle that holds the head in the CT scanning machine.

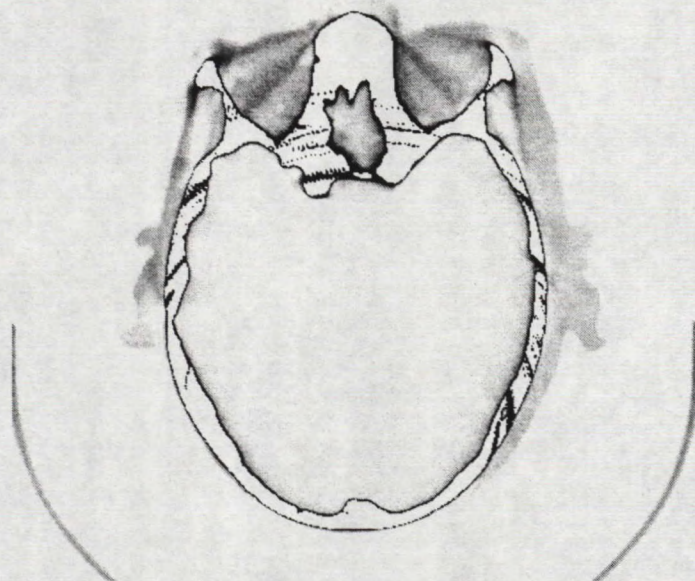


Fig. 8.6 CT scan # 75 of the head phantom, through the eyes.

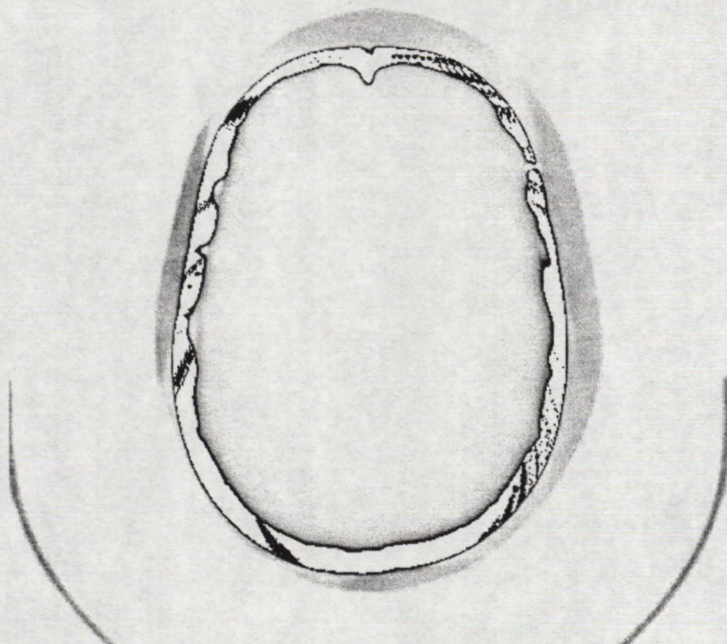


Fig. 8.7 CT scan # 90 of the head phantom, through the forehead.

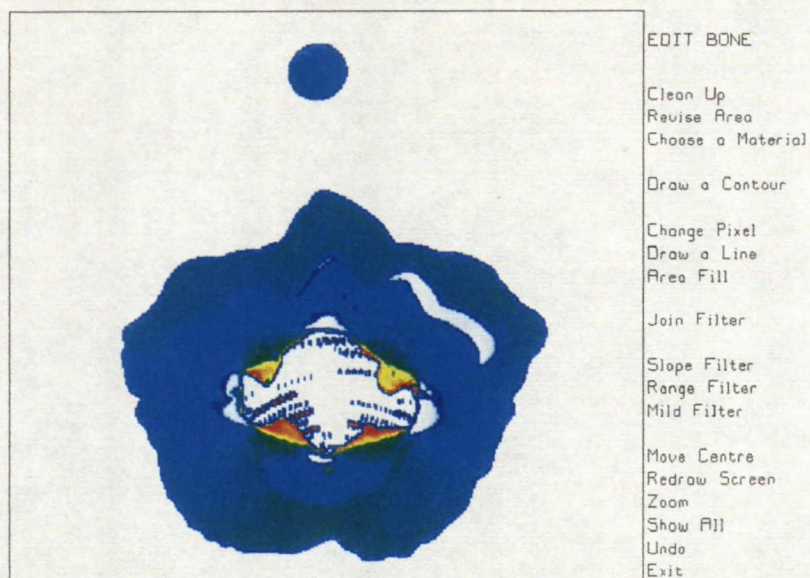


Fig. 8.8 CT scan #6 through the neck, as a "raw" cross-section in the EDITMAP software.

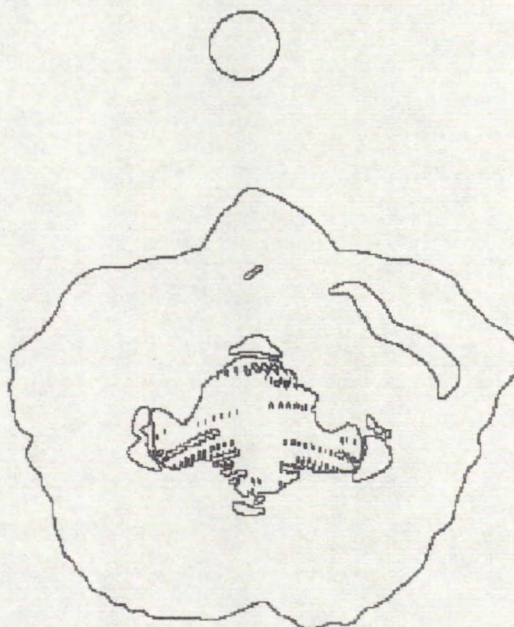


Fig. 8.9 After the first stage of processing with EDITMAP, the surfaces have been marked.

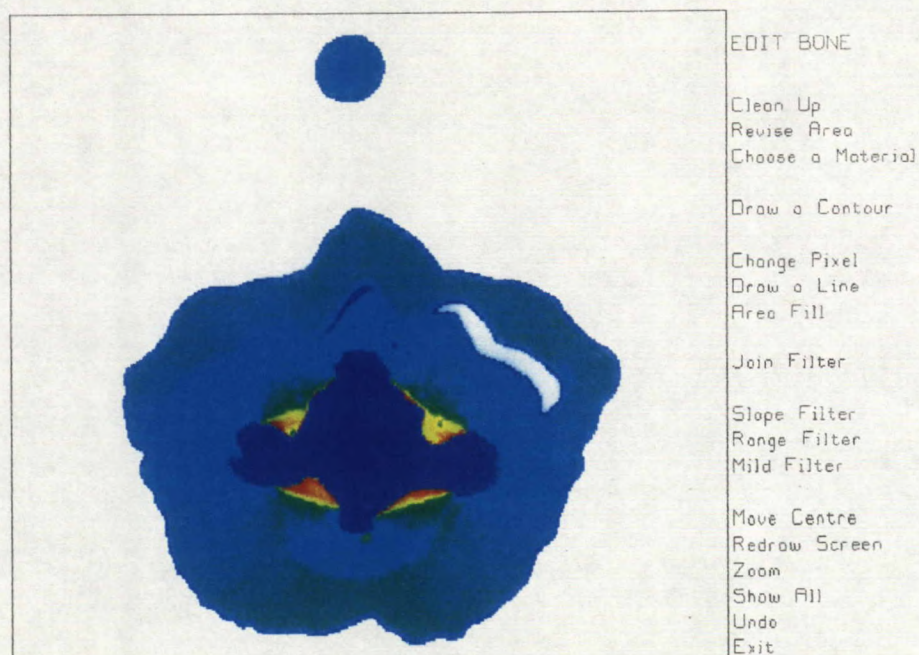


Fig. 8.10 The second stage of processing fills in the spine with "bone" tissue.

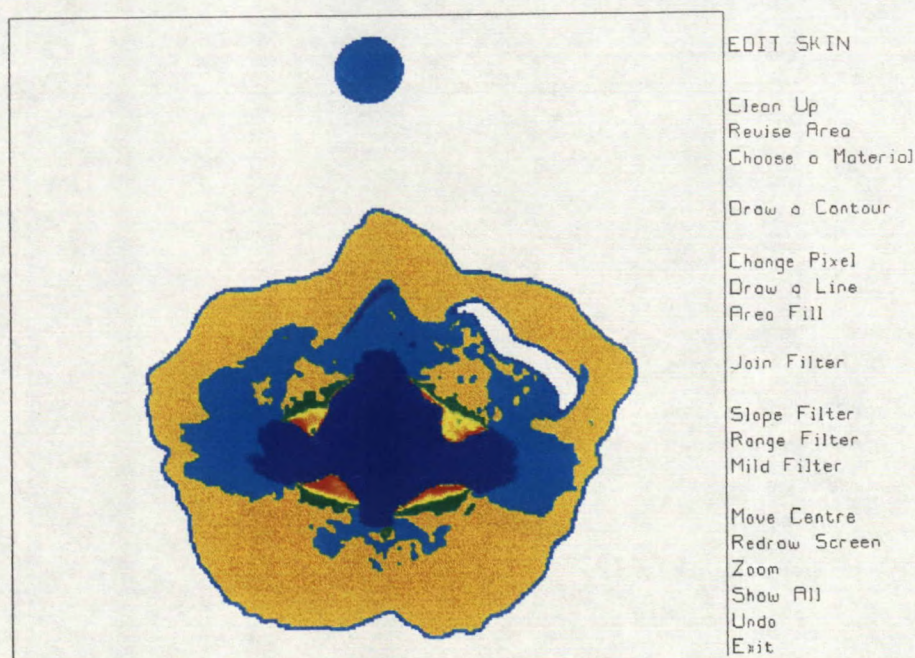


Fig. 8.11 The third stage roughly differentiates "skin" tissue and "muscle" tissue.

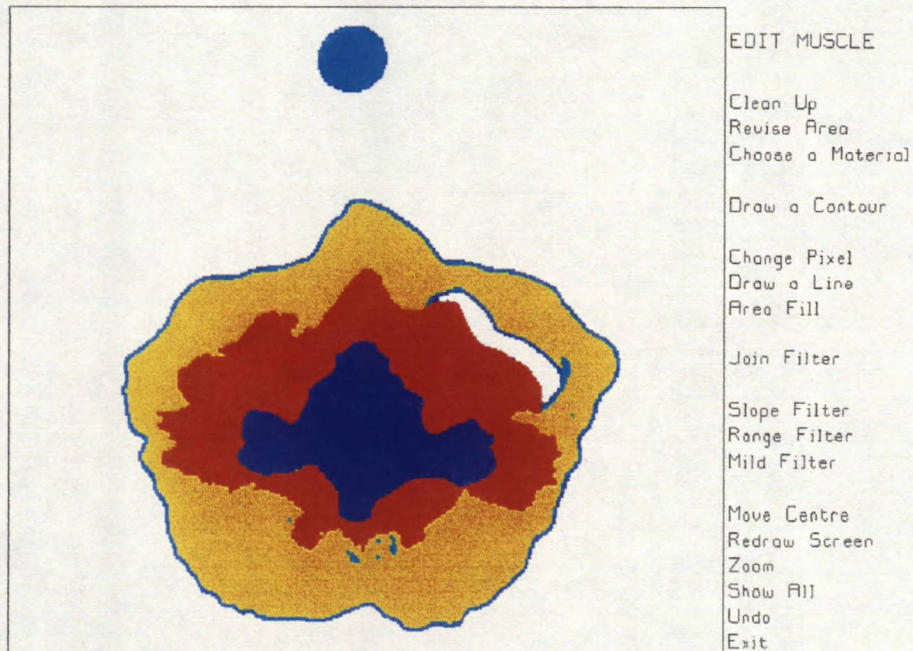


Fig. 8.12 At the fourth stage, “muscle” tissue is identified as lying between bone and skin regions.

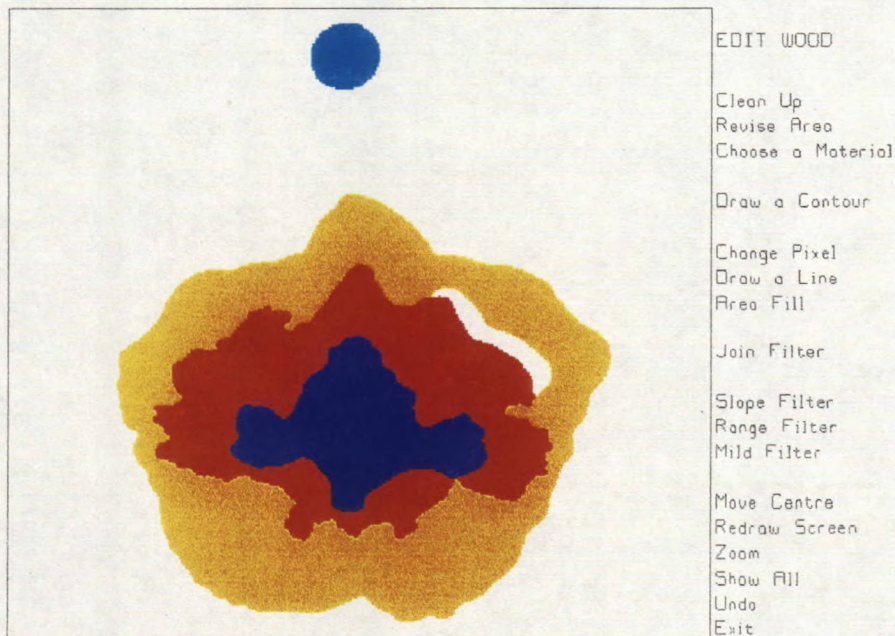


Fig. 8.13 The fifth stage cleans up the “skin” region by changing surface pixels previously marked as “bone” to “skin”. The final stage changes the material of the post to “wood”.

Chapter 9

Conclusions and Recommendations

This chapter summarizes the work presented in this report, and makes recommendations for further work.

9.1 Summary and Conclusions

This project has two principal objectives. The first is to study the fields, both near fields and far fields, of portable radio handsets. The fields are to be found both by measurement and by computation. The fields are to be examined both for the handset in isolation and for the handset operating near a model of the head. The second objective is to validate the computations of the fields using the finite difference time domain method. Various designs of handset are of interest in the long term, and various designs of antenna for each handset.

This report is concerned with the far field radiation patterns of the handset and various head models. The near fields have not been studied in the present work.

9.1.1 Handset and Head Radiation Patterns

The present report advances the first objective by studying the principal plane radiation patterns of the simple portable radio handset that was designed for this study. The radiation patterns of the handset oriented with the antenna vertical are studied, both for the handset in isolation and for the handset near simple representations of the head, namely the box head and the sphere head. The radiation patterns are found both by measurement and by computation. The handset is then tilted 60 degrees to the vertical and its principal plane radiation patterns are computed and examined, in isolation and operating near the sphere head. The patterns are compared with those of the vertical handset.

This report presents an FDTD model of the head based on anatomical cross sections. This "anatomical" head is derived by digitizing the anatomical data, and then determining the material for each cell in the cell model from the nearest point on a digitized cross section. Because the anatomical cross-sections are spaced by approximately 1 cm, and the cell size in the cell model is only 2 mm, the resulting cell model is somewhat rough. Nevertheless, it is used here to compute the radiation patterns of the vertical handset near the head. These are compared with the patterns of the handset near the sphere head and found to be remarkably similar. The process for deriving the anatomical head cell model can also be used to derive a head tilted at 60 degrees to the handset, and hence allows the computation of the radiation patterns of the tilted handset near the head. However, this was not done in the present work.

9.1.2 Validation

The second objective, validation of the computations by comparison with measured data, is the principal contribution of this report. The principal plane patterns of the vertical handset in isolation are found to be in excellent agreement with the measured patterns. The principal plane patterns of the vertical handset operating near the box head are also in excellent agreement with the measured patterns, and indeed the agreement is almost as good as for the handset alone. The computed radiation patterns of the vertical handset operating near the sphere head are compared with measured patterns. The agreement is not quite as good as that for the handset and box head. This may be due to the staircased approximation of the head used in the FDTD computation.

A cell model of an anatomical head or a head phantom is similar in nature to that of the sphere. The curved surfaces of the anatomical head are staircased to the same degree as that of the sphere and the staircasing should introduce similar errors. The agreement of the computed radiation patterns for the handset and sphere head with the measured radiation patterns suggests that computations done with the anatomical head cell model will have good accuracy.

9.1.3 Phantom Head Cell Model

The final contribution of this report is an examination of the problem of creating a cell model of the head phantom. A set of MRI scans of the phantom head are presented and shown to be of limited usefulness. A set of CT scans of the phantom contain much more useful information, but have serious drawbacks. A software tool for identifying tissue types in the CT scan is presented, and used to reduce the raw CT scan data for the neck cross-sections to maps in which regions are clearly identified by tissue type. This is the first step in creating an anatomical head cell model.

9.2 Recommendations for Further Work

This makes recommendations for further work in this project.

In broad terms, the project should move towards more realistic head representations, and should include the hand holding the portable radio. Also, a handset should be designed that is more representative in size and shape of recent cellular telephones. The objective should shift from modeling a simplified handset and head to studying a realistic handset held in a hand near a realistic head.

9.2.1 Modern Handset Design

It is recommended that another handset be designed and built for the measurement phase of the project, that is more like modern cellular telephones in size, shape and geometry. Recent handsets are much smaller than that of Fig. 1.1. Also, handsets are now commonly hinged in the center. Most handsets do not unfold into a straight shape. Instead the mouthpiece unfolds and extends towards the mouth in a rough "L" shape. Some recent handsets use a monopole antenna; others used internal antennas resembling patch antennas.

The new handset should use a monopole for simplicity and should be large enough to use the same 850 MHz oscillator that is part of the present handset. In broader

terms, it may be of interest to investigate handsets with antenna designs other than a simple monopole[6].

The principal plane patterns of the new handset should be measured. The handset should be modeled with FDTD and the patterns compared with the measurements, to establish the computer model. A "bent" handset is more challenging to model with FDTD cells than the simple metal box of the present handset.

The near fields of the handset should be measured. Computations can then be done for comparison with the measurements.

9.2.2 Development of a Cell Model of the Phantom

This report took the initial steps towards developing a cell model of the head phantom. It is recommended that the identification of tissues in the head phantom CT scans be completed as rapidly as possible. The MKHEAD program that was used in this report to derive a cell model of the head in a tilted position from the anatomical cross-section data should be developed to be able to work with the cross-sections derived from CT scans. This software could then be used to derive a cell model of the phantom head at various tilt angles.

The head phantom includes a hand to hold the portable radio. The hand should be CT scanned, and the scans processed to identify tissues so that the cross-sections can be used with MKHEAD. Because we need to rotate the hand cell model in about two axes to position the hand appropriately relative to the handset, the MKHEAD software will have to be improved by adding a second axis of rotation before the hand can be readily added to the cell model.

9.2.3 Development of a Precise Anatomical Head Model

A set of 250 anatomical cross-sections of the head at approximately 1 mm spacing is available from the Visible Human project[45]. These cross-sections should be processed in a similar way to the CT scans, to identify tissue types and prepare an input data set for MKHEAD, so that detailed, precise cell models of the head at various tilt angles can be prepared.

9.2.4 Far Fields of the Handset with the Head

This section makes recommendations for further work dealing with the measurement and computation of the far fields of a portable radio handset, including the effect of the head and hand.

9.2.4.1 Principal Plane Measurements with the Head Phantom

Two phases of measurements with the head phantom are recommended. In the first set, the simple box handset is mounted vertically adjacent to the head phantom, and the principal plane patterns are measured. It would be of interest to compare this set of measurements with the handset and sphere head measurements. Recall that in this report the handset and anatomical head patterns were quite similar to the handset and sphere head patterns.

The hand has a significant effect on the portable radio because it is a thick, lossy dielectric layer covering a large portion of the handset surface. Since the handset carries

substantial currents, the radiated field of these currents can be affected by the dielectric layer, and so the hand can change the portable radio's performance. The hand should be added to the handset and phantom setup, "holding" the handset, and the measurement repeated. This provides an initial assessment of the effect of the hand, for the vertical handset.

A jig is required for holding the head, handset and hand that permits the handset to be mounted in a tilted position, say at 60 degrees to the vertical as used in this report. It would be convenient if the same jig could hold the handset vertical and also tilted. The principal planes of the tilted handset could then be compared with those of the vertical handset, including the effect of the head and hand.

The second phase of measurements would use the new, modern handset. A jig should be made to hold the new handset in the hand phantom, adjacent to the head phantom. The position of the handset and hand in the jig relative to the head should be realistic, with the earpiece near the ear and the mouthpiece adjacent to the mouth. Measurements should be made of the principal plane patterns of the handset, hand and head. The issue of proximity to the ear has been raised. The coupling of the handset fields into the head may be much larger when the handset is touching the ear or pressed tightly against the ear, rather than spaced a short distance away. It may be possible to test by measurement the effect of closeness of the handset to the ear on the radiation patterns.

9.2.4.2 Calibration of the Pattern Measurements

The issue of the calibration of the measured patterns relative to the computed patterns is of considerable importance. In this report, the measured data was scaled or "calibrated" relative to the computed data by finding the RMS field strength summed over the three principal plane patterns using Eqns. 3.2 and 3.3. The RMS field of the measurement was scaled to agree with the RMS field of the computation. The RMS field strength of Eqn. 3.2 is proportional to the radiated power in one radiation pattern. Summing as in Eqn. 3.3 gives a field proportional to the radiated power in the three principal plane patterns. Thus the calibration procedure used here tries to set the radiated power in the measured patterns equal to the radiated power in the computed patterns. Because only the three principal plane patterns are used to estimate the radiated power, the estimate is imprecise and so the best we can claim is that the radiated powers are approximately the same in the measured and computed patterns.

To compare measured and computed radiation patterns on the basis of exactly equal radiated power, we must evaluate the radiated power precisely in each case. A precise measure of the radiated power is obtained by evaluating Eqn. 2.1, which integrates the power density over the full radiation sphere. In the FDTD computation, the set of "conical cut" radiation patterns discussed in Sect. 2.3 are computed and then Eqn. 2.1 is evaluated using numerical integration to obtain an accurate radiated power.

It has proven difficult to measure the conical cut radiation patterns. Ref. [4] presented an initial attempt that was not successful due to the mechanical arrangement used to rotate the handset. It is recommended that a new handset positioner mechanism be developed, permitting an accurate measurement of the field strength over the full set of conical cut radiation patterns. Note that to evaluate radiated power, it is sufficient to

measure two orthogonal components of the “far” field, such as the “horizontal” component E_H and the “vertical” component E_V . Then the power density is found from

$$S(\theta, \phi) = \frac{E_H^2 + E_V^2}{2\eta}$$

and then integrated to find the radiated power, according to

$$P_{rad} = \int_0^{2\pi} \int_0^\pi S(\theta, \phi) \sin \theta d\theta d\phi$$

To evaluate the radiation power it is not necessary to resolve E_H and E_V into spherical components E_θ and E_ϕ . It is sufficient to measure the magnitude of E_H and E_V as the phase is not required for the power density. This simplifies the design of a measurement system aimed at evaluating radiated power, because the phase does not have to be measured, and any two orthogonal field components can be measured, rather than spherical components E_θ and E_ϕ . For comparison of the principal plane patterns with computed data it is convenient if the measured components E_H and E_V correspond to the spherical components E_θ and E_ϕ in the principal planes.

9.2.4.3 Validation of the Computer Models

It is recommended that the computer model of the handset and phantom head be used to compute the radiation patterns for the handset and head configurations used in the measurements. Comparison of the measured and computed radiation patterns provides a validation of the ability of the FDTD method to model a complex, realistic head.

9.2.4.4 Investigation of the Handset and Head Radiation Patterns

Once a good-quality cell model of the head phantom and of an anatomical head is available, a thorough investigation by computation of the radiation patterns of a handset should be attempted. This is probably most useful with a handset model that resembles a modern cell phone, that is, that is considerably smaller than the handset used in this report. The radiation patterns should be graphed as polar contour maps of E_θ and E_ϕ over the radiation sphere. The handset patterns should be documented as a function of the tilt angle to the head, of the vertical position of the handset relative to the head, of the distance from the ear to the handset, and of the position of the hand.

Comparing radiation patterns with the anatomical head with those computed using the phantom head should provide an assessment of the usefulness of the phantom in predicting the radiation patterns of the handset, hence in evaluating handset designs for adequate communication with the base station.

9.2.4.5 Assessment of Adequate Coverage

One major objective of this work is to study the far fields of a portable radio handset. The handset must deliver sufficient field strength for communication with the base station no matter how the user holds it against the head, nor how the user positions the hand, nor the direction in which the user is facing.

For a given position and tilt angle of the handset relative to the head, and a given position of the hand, the field strength can be computed over the full radiation sphere and graphed in the polar contour map format used in Ref. [2]. Such maps can be prepared for various handset tilt angles, positions against the head, and positions of the hand.

In this report, only the principal plane patterns were looked at; in fact for the vertical and for the tilted handset it would be of interest to graph the field over the full radiation sphere. It becomes evident from the principal plane patterns presented in this report that the handset may not provide satisfactory coupling to the base station. At some pattern angles, one polarization can be more than 10 dB below the isotropic level, while the other is comparable to the isotropic level. But at other angles in the patterns both the E_θ and the E_ϕ components are more than 10 dB below the isotropic level. The base station may be able to extract the signal from either a sufficiently strong E_θ or a sufficiently strong E_ϕ . Or, it may receive, say, only right-hand circular polarization. Then if the field components happen to be phased to be principally left-hand circular polarized, the base station may not be able to establish communications. Thus some knowledge of the design of the base station may be needed to establish whether a given set of handset patterns is satisfactory in use.

It might be useful in this project to develop a figure-of-merit for the effectiveness of the radiation patterns for a given handset design, held at a given tilt angle to the head, with a given hand position in communicating with the base station. In aircraft HF antenna design, only field radiated into E_θ is useful, and only field radiated in the angular sector from $\theta = 60$ to $\theta = 120$ degrees is useful, for ground-wave mode communication. Thus the fraction of the total power radiated into E_θ from $\theta = 60$ to $\theta = 120$ is a measure of the effectiveness of a given antenna design. In addition, patterns must be inspected to see if there is any direction in which E_θ is so small compared to the isotropic level that communications in that direction are unsatisfactory.

A similar single-number figure-of-merit of the usefulness of the radiation patterns of a portable radio in a given head and hand setup might be developed for this project. Such a figure-of-merit might be useful in a systems context where the base station designer needs to know the field strength to be expected from handsets, both on the average and in the worst case. This would aid in investigating whether a handset is satisfactory over many positions relative to the head and hand.

9.2.5 Near Field Measurements

This report has been concerned with the far fields of the handset and head. Previous work[3] dealt extensively with comparisons of the computed near fields of the handset and head with measurements. Maps of the vertical component of the electric field were compared for planes of points adjacent to the handset, in front of the head, and on the opposite side of the head from the handset. The presence of a feed cable for the handset led to differences between the measurements and the computations. The probe used in the measurements was not sufficiently small to provide a measure of the electric field at one specific point.

used in the measurements was not sufficiently small to provide a measure of the electric field at one specific point.

A new probe for near field measurement was purchased from Schmid and Partner Engineering AG[23]. This is a three-axis probe that measures the magnitude of three orthogonal components of the electric field with good isolation between the components. The probe uses three small dipole antennas to receive the field, and provides a much truer "point" measurement of the field than the probe used in Ref. [3].

It is recommended that the new probe system be used to measure maps of the near field of the simple handset in isolation. The same maps should be created with the FDTD model of the handset, and a comparison done. This will establish the degree of agreement that can be achieved between measurements and computations of the near field, without the complication of a head model.

It will be necessary to establish whether comparisons should be done of the individual field components measured by the probe, or whether an overall RMS field strength, the square root of the sum of the squares of the three field components, should be the basis for comparison. A software module is required that is able to read the measured data from the three-axis probe measurement and convert it into a suitable form for graphing. A normalization or scaling procedure is needed that is suitable for three-axis probe measurements. These modules will be developed from the near field software described in Refs. [3] and [4].

9.2.5.1 Simple Head Models

The near field of the simple handset near the box model of the head and near the sphere model of the head should be measured with the new probe. The handset and head should be held in a jig that maintains a well-known position of the handset to the head model. This overcomes a difficulty with the near field comparisons in Ref. [3], where the handset position was not precisely known. Also, the electrical parameters of the brain liquid should be measured, so that the FDTD computation can model the head as precisely as possible. Planes of near field points adjacent to the handset, in front of the head, and on the opposite side of the head should be measured as was done in Ref. [3]. This might be extended to behind the head and above the head.

It may be of interest to measure the near fields of the handset tilted relative to the simple head models.

9.2.5.2 With the Head Phantom

The near field of the handset operated with the phantom head should be measured. In the simplest case the handset can be held vertically relative to the head with no hand. This would provide data to establish basic agreement between measurements and computations in the near field.

Measurements should be made of a more realistic configuration, in which the handset is held by the hand model, and is held against the head at a realistic tilt angle. A jig would be necessary to hold the head, handset and hand in a well-known positions relative to one another. Again, measurements in planes adjacent to the handset, in front of the head, on the opposite side of the head, and even perhaps behind the head and above

the head should be done. These configurations should be modeled with FDTD and systematic comparisons carried out.

9.2.5.3 Discussion

It has been suggested[6] that a design for a handset antenna might be developed that inherently has low near fields in the region of space that the head will occupy when the handset is in use. When the head is introduced into the handset near field, since the field in the region of the head was small for the isolated handset, the head couples to the handset much less. Such a handset design may be able to deliver reasonably isotropic patterns, in spite of the low near field in the space occupied by the head.

The near field of antenna designs that claim to have low fields in the region of the head should be investigated. It would be necessary to identify such a design, and to build a measurement model. The near and far fields could then be investigated by the techniques used in this project, both by measurement and by computation.

9.2.6 Computational Issues

The foregoing has identified many work packages for the computational side of the project. These include the creation of a cell model of the head phantom, requiring the development of the MKHEAD software to work with cross-sections derived from CT scans of the head phantom, of the hand. The same software can be used with the "Visible Human" anatomical data. Another is the development of criteria for assessing the coverage of a handset held at a particular angle to the head, and the implementation of the criteria as a software package able to read the radiation patterns over the radiation sphere and provide a measure of their adequacy. A third area is the development of software to interpret the measured data from the three-axis probe.

Not addressed in the foregoing is the need to evaluate the input power to the handset antenna, and hence evaluate the power deposited in the head as the difference between input power and radiated power. One approach to computing input power is to model the feed cable of the monopole[31], to compute a reliable value for the input impedance of the handset antenna, in the presence of the head and hand. This requires adding a sub-system to the FDTD PML code that deals with the antenna feed. Another approach is to enclose the handset in a closed "integration surface" and find the power flow density over the surface. By summing up the power flow through all parts of the surface, the power flow away from the handset can be determined.

Another approach to determining input power is to find the power deposited inside the head and hand, by summing up the power absorbed by each cell in the FDTD model. Then input power is found as the sum of radiated power plus power loss.

All three of these methods should arrive at the same result for the input power. By implementing two or more of the techniques the FDTD code could check for the self-consistency of the results.

9.3 Conclusion

This report has presented the most recent work in a project investigating the near fields and far fields of a portable radio such as a cellular telephone. The project has now extended over five years. The project has developed a software system for computing

near and far fields of handsets and heads of various complexity. The project has developed a reliable measurement system for the principal plane patterns of a handset and head model. A set of preliminary near field measurements has been completed, the shortcomings identified, and the project is ready to carry out a new set of more precise near field investigations.

The project is now poised to investigate much more realistic configurations of handset, head and hand than has been possible up to now. In the upcoming year it is expected that realistic handset, head and hand models will be used to provide reliable computations of the near fields and far fields that are representative of those created when a real person uses a cellular telephone.

References

- [1] S.J. Kubina and C.W. Trueman, "Computational Studies for Prediction of Energy Deposition in Humans Exposed to RF Fields from Cellular Phones", Final Report, Ministry of Industry, Science and Technology, Communications Research Centre, Contract # MIST/CRC 36001-3-3603, Technical Note No. TN-EMC-94-01, Dept. of Electrical and Computer Engineering, Concordia University, March 31, 1994, 57 pages.
- [2] C.W. Trueman and S.J. Kubina, "Characteristics of Electromagnetic Fields Produced by Portable Handheld Transceivers", Final Report prepared for the Communications Research Centre, Ottawa, Contract No. PWGSC/CRC 36001-4-0395/01-ST, Technical Note No. TN-EMC-95-01, Electromagnetic Compatibility Laboratory, Concordia University, March 31, 1995.
- [3] C.W. Trueman, S.J. Kubina and M. Danesh, "Fields of a Portable Radio Handset Near the Human Head", Final Report, Public Works and Government Services Canada, Communications Research Centre, Contract #PWGSC/CRC 67CRC-5-0850/01-ST, Technical Note TN-EMC-96-01, ECE Dept., Concordia University, March 31, 1996, 149 pages.
- [4] C.W. Trueman, S.J. Kubina, D. Gaudine and B. Lorkovic, "A Research Study on Electromagnetic Fields Produced by Portable Transceivers", Final Report, Public Works and Government Services Canada, Communications Research Centre, Contract #PWGSC/CRC U68000-6-0755/001/ST, Technical Note TN-EMC-97-01, ECE Dept., Concordia University, March 31, 1997, 126 pages.
- [5] B. Segal, D. Townsend, K-S Tan, and M.A. Stuchly, "A Workshop on Electromagnetic Compatibility in Health Care and Health Effect of Radio Waves", sponsored by the Canadian Wireless Telecommunications Association, Vancouver, Feb. 26, 1997.
- [6] Y. Rahmat-Samii and M.A. Jensen, "Personal Communications Antennas: Modern Design and Analysis Techniques Including Human Interaction", Short Course presented at the IEEE Antennas and Propagation Society International Symposium, Montreal, Quebec July 18, 1997.
- [7] K.S. Yee, "Numerical Solution of Initial Value Problems Involving Maxwell's Equations in Isotropic Media", IEEE Trans. on Antennas and Propagation, Vol. AP-14, No. 3, pp. 302-307, May, 1966
- [8] K.S. Kunz and R.J. Luebbers, "The Finite-Difference Time-Domain Method for Electromagnetics", CRC Press, 1993.
- [9] A. Taflove, "Computational Electrodynamics, The Finite-Difference Time-Domain Method", Artech House, 1995.
- [10] J.E. Roy, W.R. Lauber and J.M. Bertrand, "Measurements of the Principal Planes Electromagnetic Far-Fields Produced by a Portable Transmitter", Draft Report, Communications Research Centre, Ottawa, November, 1997.
- [11] Z. P. Liao, H.L. Wong, B.P. Yang and Y.F. Yuan "A Transmitting Boundary for Transient Wave Analysis," *Scientia Sinica*, Vol. XXVII, No. 10, p.1062-1076, October, 1984.

- [12] D. Steich, R. Luebbers and K. Kunz, "Absorbing Boundary Condition Convergence Comparisons", IEEE International Symposium on Antennas and Propagation, Ann Arbor, Michigan, June 28-July 2, 1993.
- [13] G.J. Burke, A.J. Poggio, J.C. Logan and J.W. Rockway, "NEC - Numerical Electromagnetics Code for Antennas and Scattering", 1979 IEEE International Symposium on Antennas and Propagation Digest, IEEE Publication No. 79CH1456-3AP, Seattle, Washington, June, 1979.
- [14] G.J. Burke and A.J. Poggio, "Numerical Electromagnetics Code - Method of Moments, Part I: Program Description-Theory", Technical Document 116, Naval Electronic Systems Command(ELEX 3041), July, 1977.
- [15] G.J. Burke and A.J. Poggio, "Numerical Electromagnetics Code - Method of Moments, Part III: User's Guide," Technical Document 116, Naval Electronic Systems Command(ELEX 3041), July, 1977.
- [16] G.J. Burke, "Numerical Electromagnetics Code -NEC-4 Method of Moments Part II: Program Description-Theory", Lawrence Livermore National Laboratory, Document No. UCRL-MA-109338, January, 1992.
- [17] J.P. Berenger, "A Perfectly-Matched Layer for the Absorption of Electromagnetic Waves", Journal of Computational Physics, Vol. 114, pp. 185-200, 1994.
- [18] J. P. Bérenger, "Perfectly Matched Layer for the FDTD Solution of Wave-Structure Interaction Problems", *IEEE Trans. Antennas and Propagation*, Vol. 44, No. 1, January 1996, pp. 110-117.
- [19] J. P. Bérenger, "Improved PML for the FDTD Solution of Wave-Structure Interaction Problems", *IEEE Trans. Antennas and Propagation*, Vol. 45, No. 3, March 1997, pp. 466-473.
- [20] "User's Manual for XFDTD", REMCOM, Inc., Version 2.21e, November, 1994.
- [21] G. Hartsgrrove, A. Kraszewski and A. Surowiec, "Simulated Biological Materials for Electromagnetic Radiation Absorption Studies", *Bioelectromagnetics*, Vol. 8, pp. 29-36, 1987.
- [22] T. Schmid and N. Kuster, "Novel E-Field Probes for Close-Near Field Scanning", pre-publication copy, IEEE Trans. On Vehicular Technology, August, 1995.
- [23] Probe ER3DV4, SN:2201, Schmid and Partner Engineering AG, Oberer Deutweg 59, CH-8400 Winterhur, Switzerland.
- [24] E.C. Burdette, F.L. Cain, and J. Seals, "In Vivo Probe Measurement Technique for Determining Dielectric Properties at VHF Through Microwave Frequencies", IEEE Trans. On Microwave Theory and Techniques, Vol. MTT-28, No. 4, pp. 414-427, April, 1980.
- [25] Hewlett-Packhard Dielectric Probe, part number HP 85070B, with HP 85080A Dielectric Probe Kit, Data Sheet #5952-2381, and HP85071A Material Measurement Software, Data Sheet #5952-2382, published by Hewlett-Packhard, 1993.
- [26] "TX Handset", CRC Drawing Number 96364-01A3.
- [27] M. Vall-Ilossera and C.W. Trueman, "Comparison of the Performance of the PML and the Liao Absorbing Boundary Formulation", Conference Proceedings, 14th Annual Review of Progress of the Applied Computational Electromagnetics Society, pp. 523-530, Monterey, California, March 16-20, 1998.

- [28] C.W. Trueman, S.J. Kubina, J.E. Roy, W.R. Lauber, and M. Vall-Ilossera, "Validation of FDTD-Computed Handset Patterns by Measurement", Conference Proceedings, 14th Annual Review of Progress of the Applied Computational Electromagnetics Society, pp. 93-98, Monterey, California, March 16-20, 1998.
- [29] Head Phantom manufactured by Microwave Consultants Limited, 17B Wooford Road, London E18 2E1, United Kingdom.
- [30] G. Mur, "Absorbing Boundary Condition for the Finite-Difference Approximation of the Time-Domain Electromagnetic Field Equations", IEEE Trans. on Electromagnetic Compatibility, Vol. EMC-23, No. 4, pp. 377-382, November 1981.
- [31] M.A. Jensen, Y. Rahmat-Samii, "E.M. Interaction of Handset Antennas and a Human in Personal Communication", *Proc. IEEE*, Vol. 83, No. 1, pp. 7-17, January, 1995.
- [32] CRC, private communication, drawings PP-01 to PP-17, September, 1997.
- [33] CRC, private communication, measured values for the relative permittivity and conductivity of the brain liquid mixture by Joe Seregelyi, September 11, 1997.
- [34] T. Moreno, "Microwave Transmission Design Data", Artech House, 1989, originally published by McGraw-Hill, 1948.
- [35] C.A. Balanis, "Advanced Engineering Electromagnetics", Wiley, New York, 1989.
- [36] L. Martens, "Electromagnetic Field Calculations for Wireless Telephones", Radio Science Bulletin, No. 217, pp. 9-11, December, 1994.
- [37] V. Hombach, K. Meier, M. Burkhardt, E. Kuhn and N. Kuster, "The Dependence of EM Energy Absorption Upon Human Head Modeling at 900 MHz", IEEE Trans. on Microwave Theory and Techniques, Vol. MTT-44, No. 10, pp. 1865-1873, October, 1996.
- [38] G. Lazzi and O.P. Gandhi, "Realistically Tilted and Truncated Anatomically Based Models of the Human Head for Dosimetry of Mobile Telephones", IEEE Trans. on Electromagnetic Compatibility, Vol. 39, No. 1, pp. 55-61, February, 1997.
- [39] R. Luebbers, F.P. Hunsberger, K.S. Kunz, R.B. Standler and M. Schneider, "A Frequency-Dependent Finite-Difference Time-Domain Formulation for Dispersive Materials", IEEE Trans. on Electromagnetic Compatibility, Vol. 32, No. 3, pp. 222-227, August, 1990.
- [40] D.M. Sullivan, "A Frequency-Dependent FDTD Method for Biological Applications", IEEE Trans. On Microwave Theory and Techniques, Vol. Mtt-40, No. 3, pp. 532-539, March, 1992.
- [41] R. Luebbers and F. Hunsberger, "FDTD for N-th Order Dispersive Media", IEEE Trans. On Antennas and Propagation, Vol. AP-40, No. 11, pp. 1297-1301, November, 1992.
- [42] R. Luebbers, D. Steich and K. Kunz, "FDTD Calculation of Scattering from Frequency-Dependent Materials", IEEE Trans. On Antennas and Propagation, Vol. AP-41, No. 9, pp. 1249-1257, September, 1993.
- [43] A.C. Eycleshymer and D.M. Schoemaker, "A Cross-Sectional Anatomy", D. Appleton and Co., New York, 1911.
- [44] M-C Han and C-W Kim, "Sectional Human Anatomy", Second Edition, Igaku-Shoin, New York, 1989.

[45] “The Visible Human Project”, National Library of Medicine,
http://www.nlm.nih.gov/research/visible/visible_human.html

Appendix 1

Reference [27]: M. Vall-llossera and C.W. Trueman, "Comparison of the Performance of the PML and the Liao Absorbing Boundary Formulation", Conference Proceedings, 14th Annual Review of Progress of the Applied Computational Electromagnetics Society, pp. 523-530, Monterey, California, March 16-20, 1998.

Comparison of the Performance of the PML and the Liao Absorbing Boundary Formulation

Merce Vall-Ilossera
Department of Signal Theory and Communications
Polytechnic University of Catalonia (UPC)
Barcelona
Merce@vitor.upc.es

Christopher W. Trueman
Electromagnetic Compatibility
Laboratory
Concordia University
Montreal
Trueman@ece.concordia.ca

Abstract—The cell space in the finite-difference time-domain method must be truncated with an absorbing boundary. The perfectly-matched layer (PML) formulation for the boundary offers much lower reflection than the Liao formula, but at the cost of much greater memory requirements and much longer execution time at each time step. But because the PML reflects much less and so interacts with the object being modelled much less, a much thinner layer of free space cells can be used to separate the object surfaces from the absorbing boundary. Thus a problem can be solved to a given accuracy with a much smaller cell space using the PML than using the Liao absorbing boundary. This paper examines the tradeoff in memory requirements and execution time of the PML compared to the Liao boundary, for computing the radar cross-section of a metallic rod target and of a dielectric cube.

Introduction

This paper compares radar cross-sections computed using FDTD with measured RCS data for a perfectly-conducting rod and for a high-permittivity, low-loss dielectric cube. The purpose is to compare the performance of the perfectly-matched layer (PML) absorbing boundary condition (ABC) [1,2] with the Liao second-order ABC [3]. The memory requirements for the FDTD cell space and for the absorbing boundary, and the CPU time requirements, are compared on the basis of equally good agreement with the measured RCS.

With the Liao ABC, a layer of free-space cells called the “whitespace” is used to separate the surfaces of the object from the outer boundary of the cell space layer. Using the PML, the whitespace separates the object from the inner surface of the PML, and PML itself has a thickness in cells. The cell space size is determined by the thickness of the whitespace plus the thickness of the PML, as shown in Fig. 1. To obtain good agreement with the measured data, how thick must the whitespace layer be using the Liao ABC? How thick must the PML be? How much whitespace must be used with the PML? The memory requirements to store the field components in Yee’s FDTD [4,5] increase in proportion to the total number of cells, which in turn increases as the cube of the thickness of the whitespace plus the PML layers. The computation time thus increases as the cube of the whitespace thickness. The volume in cells of the PML layer increases in proportion to the area of the outer boundary in cells, which increases as the square of the whitespace size. The memory requirements of the PML thus increase as the square of the whitespace size. Since the PML ABC requires much more computation at each time step for the same space size than does the Liao ABC, it might be thought that a thicker whitespace used with the Liao absorbing boundary is more economical than a thin whitespace terminated with the PML. Indeed, it has been suggested that the Liao boundary be used for day-to-day investigations with FDTD, backed up by using the “expensive” PML to check the accuracy in individual

cases. This paper explores the trade-off between computer memory requirements and running time, comparing the Liao ABC with the PML for the same degree of agreement with measured RCS data.

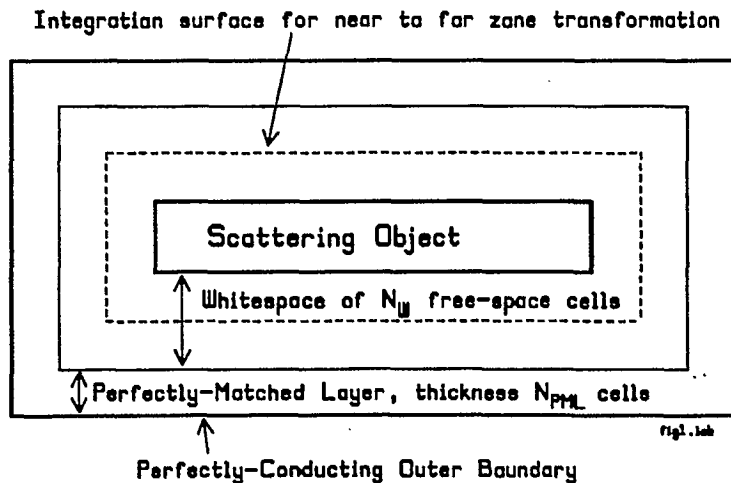


Figure 1 A cross-section of the FDTD cell space showing the scattering object in the center separated from the outer boundary by a layer of free-space cells and the PML absorbing boundary.

The Perfectly-Matched Layer

Fig. 1 shows the FDTD cell space terminated by a PML layer of thickness N_{PML} cells. The outside boundary of the cell-space is perfectly conducting, hence it has a reflection coefficient of unity. A layer of free-space cells separates the surface of the scattering object from the inside surface of the PML. To set up the problem, the user chooses the overall size of the cell space, N_x by N_y by N_z cells, which includes the PML layer, the whitespace, and the scattering object. The user defines the PML layer with the following parameters. The thickness of the PML, N_{PML} cells, is the most important choice. The variation of the conductivity with depth into the PML must be specified as either linear, or geometric, or

parabolic. This paper uses parabolic evolution. The reflection coefficient for normal incidence on the surface of the PML must be specified. In this paper a reflection coefficient of 0.001 has been used.

The time of validity or "cutoff time" of the PML technique is governed [2] by the conductivity of the first layer of PML cells, which is determined by the thickness of the PML, whether geometric or parabolic evolution is chosen, and the reflection coefficient at the surface. Ref. [2] recommends cutoff times at least ten times the time interval over which FDTD is to be run to solve the problem.

The Perfectly-Conducting Rod

The rod target consists of an aluminum parallelepiped of square cross-section, whose length is ten times its cross-sectional size. The plane wave is incident end-on to the rod, with the electric field parallel to one edge of the cross-section. The rod scatters strongly from its front end and from its back end, and as the frequency changes the two scattered fields go in and out of phase, giving rise to the evenly-spaced set of maxima and minima shown in Fig. 2. The RCS was measured as described in reference [6]. The rod was modeled with 10 by 10 by 100 FDTD cells. The rod is excited by a Gaussian pulse plane wave, and the backscattered field as a function of time [7] is computed for 2048 time steps. The field is then Fourier-transformed and divided by the spectrum of the Gaussian pulse to determine the RCS as a function of frequency.

Using the Liao absorbing boundary with a whitespace eight cells thick, the agreement with the measured RCS is very poor. As the whitespace thickness is increased, the agreement gradually improves. With 16 cells of whitespace, the agreement with the measurement is good, as shown in Fig. 2. The maxima marked with the bracket are sensitive to the whitespace thickness and improve dramatically with increased whitespace. The minima also improve with whitespace thickness,

particularly the one marked with the arrow. The maximum at the low end of the frequency spectrum also improves. Increasing the whitespace to 20 cells leads to a small improvement in the agreement, and further increases to little improvement.

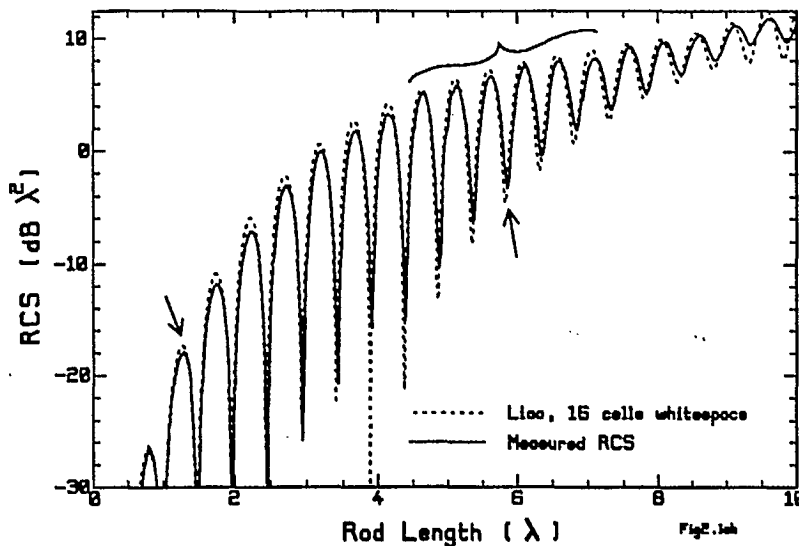


Figure 2 RCS of the rod target with the Liao ABC.

for the FDTD cell space itself, and about 0.9 Mb for the storage associated with the Liao boundary. The agreement with the measurement is quite good. With 20 cells of whitespace, the storage rises to 11 Mb for the cell space and 1.7 Mb associated with the ABC, and the running time increases to 9,505 seconds. The agreement with the measurement is slightly improved over the 16 cell case.

Table 1
Computer Resources Needed to Solve the Rod Scatterer
With the Liao Absorbing Boundary

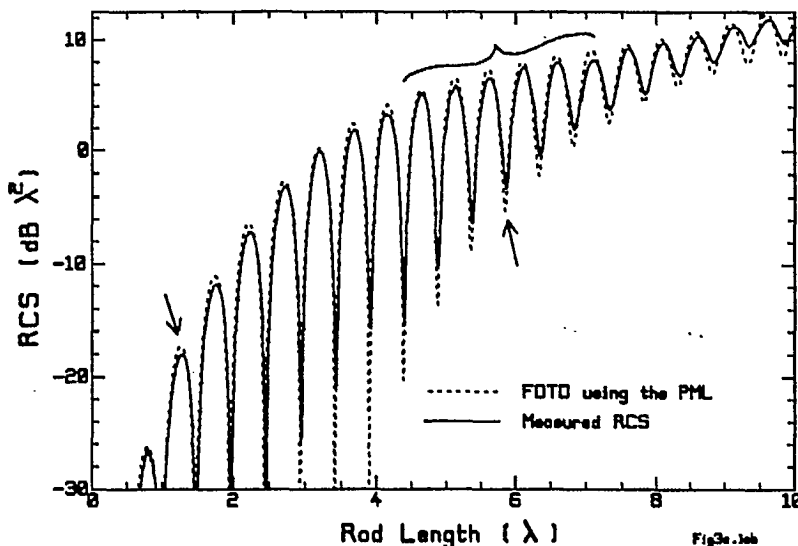
Whitespace	Time	Cell Space Size	Cell Space Storage	Liao ABC Storage
12 cells	4,224 sec	125 x 35 x 35 cells	4,593,750 bytes	643,012 bytes
16	6,541	133 x 43 x 43	7,377,510	854,980
20	9,505	141 x 51 x 51	11,002,230	1,790,404

Using the PML for the PEC Rod

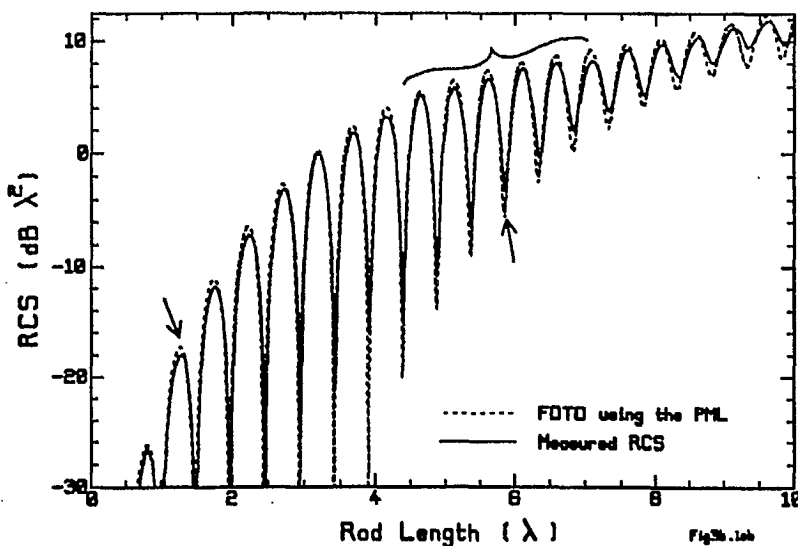
With an extremely thick perfectly-matched layer 10 cells deep, parabolic taper, a surface reflection of 0.001, and 10 cells of whitespace separating the surfaces of the rod from the surfaces of the PML, the agreement with the measured RCS is excellent. The cell space size corresponds to 20 cells of whitespace when the Liao boundary is used, and indeed the agreement with the measurement is about the same as found with Liao and 20 cells of whitespace. However, the PML algorithm is much slower than the Liao method, so the CPU time is much longer. Table 2 summarizes the computer resources needed with the PML. The cell space size is the same for Liao with a 20 cell whitespace and for a 10 cell PML and 10 cells of whitespace, hence the memory requirement for the cell space is the

Table 1 summarizes the computer resources used for the rod problem when the Liao boundary is selected. The FDTD code was run on a 166 MHz Pentium with a 512 kb cache memory and 32 Mb of RAM. The code was compiled with the DEC Fortran-90 compiler [8] and run under Windows-95 to obtain the CPU times reported in this paper. FDTD was the only application running, and the machine had sufficient memory to run the code without paging to disk. Nevertheless, the CPU times from one run to another vary randomly by about 5%, for unknown reasons. For 16 cells of whitespace, the CPU time is 6,541 seconds. The code uses about 7.4 Mb

same. But the storage associated with the PML at 6.1 Mb is much larger than that with Liao at 1.8 Mb. And the running time of 30,326 sec is much longer than Liao's 9505 sec. But a much thinner PML can be used with excellent agreement.



(a) Six cell PML with six cell whitespace.



(b) Four cell PML with four cell whitespace.

Figure 3 RCS of the rod target using the PML.

to 4.6 microseconds, close to the FDTD time interval. But we find little difference between the computed RCS for a 6 cell PML and for a 4 cell PML. But reducing the PML thickness to 2 cells reduces the cutoff time to 0.6 microseconds, and the accuracy of the computed RCS is greatly reduced. With a 4 layer PML and 3 cells of whitespace the computed RCS is little different from Fig. 3(b). This PML formulation requires a total storage of 3.8 Mb and 5,845 seconds to run.

Fig. 3(a) uses a PML 6 layers thick, and 6 cells of whitespace to separate the rod surfaces from the PML. With this formulation, the agreement with the measurement is good, but the storage requirement for the PML drops to 2.3 Mb, and the execution time to 11,842 seconds. Using a whitespace only 4 cells thick, the computed RCS is almost identical, and the storage drops to 1.9 Mb and the execution time to 9130 seconds. This execution time is comparable to the Liao case with 20 cells of whitespace, and the storage associated with PML is almost the same as that with the Liao ABC. But the memory required by the FDTD cell space is 11 Mb in the Liao case and only 3.5 Mb using the PML. This is a huge improvement. Even if we consider a 16 cell whitespace with the Liao boundary to be adequate, the total amount of storage at 8.2 Mb is still much larger than the total of 5.4 Mb for the PML, though the running time of 6541 sec is less than the PML's 9130 sec.

The FDTD program is time-stepped for a total of 3.9 microseconds to solve the rod problem for 2048 time steps. The cutoff time with 4 cells whitespace thickness and a 6 cell PML thickness is 15.6 microseconds, much longer than the FDTD time interval. Decreasing the PML thickness to four cell, Fig. 3(b), reduces the cutoff time

Table 2
Computer Resources for the Rod Scatterer
Using the PML Absorbing Boundary

PML Layers	Whitespace + PML Layers	Time	Cell Space Size	Cell Space Storage	PML ABC Storage
4	8	5,845 sec	117x27x27 cells	2,558,790 bytes	1,173,672 bytes
6	10	9,130	121x31x31	3,488,430	1,900,584
6	12	11,842	125x35x35	4,593,750	2,319,912
10	20	30,327	141x51x51	11,002,230	6,104,232

The Liao ABC with 16 cells of whitespace uses a total storage of 8.2 Mb and a CPU time of 6541 sec. With a 4 cell PML and 4 cells of whitespace, the total storage of 3.8 Mb is 46% less than that used by the Liao formulation, and the running time of 5,845 sec is 89% of that for Liao. Thus by selectively reducing the whitespace thickness and the thickness of the PML layer, we can reduce PML's CPU time and obtain the same degree of agreement with the measurement using much less storage. The PML has a clear advantage.

High-Permittivity, Low-Loss Dielectric Cube

This section compares the computer resources required to calculate the RCS of a dielectric cube resonator with $\epsilon_r = 37.84$, using both Liao and PML ABC. The results are compared with the measured RCS [9]. The side length of the cube is 8.99 mm and the cube was modeled using 15 by 15 by 15 cells to respect the restriction that the FDTD cell size must be smaller than $\lambda/10$. The RCS was measured

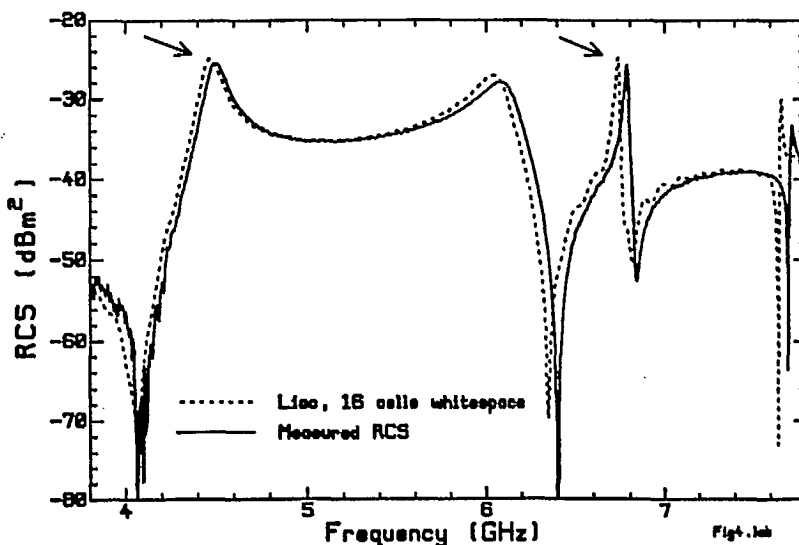


Figure 4 The RCS of the dielectric cube using the Liao ABC.

and computed with a plane wave normally incident on a face of the cube, as a function of the frequency, spanning the cube's first four resonance peaks. The cube is excited with a Gaussian pulse plane wave. FDTD is used to compute the transient far field in the backscatterer direction for 8192 steps. A Prony's series [10] is generated from this FDTD data and is used to extend the time response until it subsides to zero, corresponding to about 131,000 FDTD time steps, with a great saving in computer time. Using the Liao absorbing boundary and an 8 cell whitespace, the agreement with the measured RCS is very, very poor. As the whitespace thickness is increased, the agreement gradually improves, and with 16 cells of whitespace the agreement is quite good, as shown in Fig. 4. As above, using 20 cells of whitespace gets a further small improvement, but more whitespace leads to little change in the RCS.

In Table 3, for 16 cells of whitespace, the FDTD space uses 3.3 Mb of storage, and the Liao boundary, 0.46 Mb, for a total of about 3.8 Mb. The running time is 12,134 sec. If the slightly improved agreement with 20 cells of whitespace is desired, the storage rises to 5.89 Mb and the running time to 18,408 sec.

Table 3
Computer Resources for the Dielectric Cube Scatterer
With the Liao ABC

Whitespace	Time	Cell Space Size	Cell Space Storage	Liao ABC Storage
16 cells	12,114 sec	48 x 48 x 48 cells	3,317,760 bytes	459,268 bytes
20	18,408	56 x 56 x 56	5,268,480	619,012
30	43,187	76 x 76 x 76	13,169,280	1,125,892

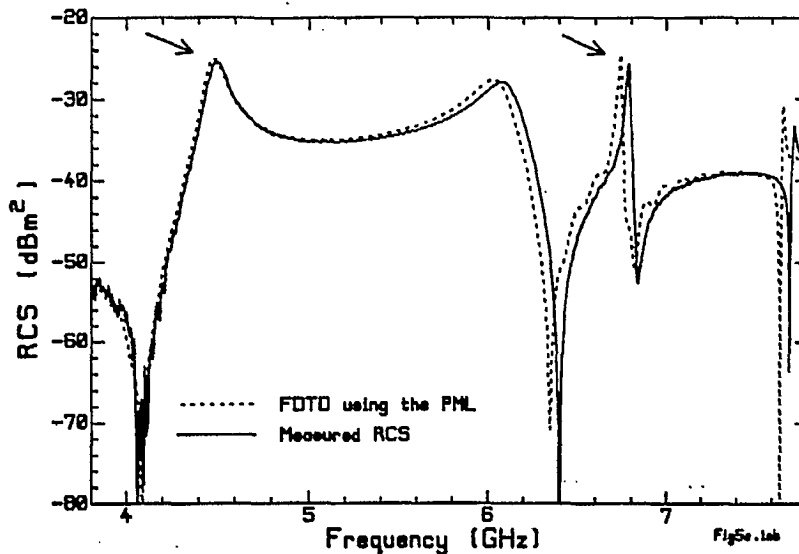
Cube Resonator using the PML

Using a 6 layer PML with 4 layers of whitespace, parabolic progression and a surface reflection of 0.001 obtains the RCS shown in Fig. 5(a). The agreement with the measurement is slightly better than in Fig. 4, especially near the first resonance peak. Thinning the PML to 4 layers still obtains excellent agreement with the measurement, as shown in Fig. 5(b). Note that the computed curve in part (b) is different from that in (a). The second resonance peak is taller than the measured peak in part (a), whereas it is shorter in (b).

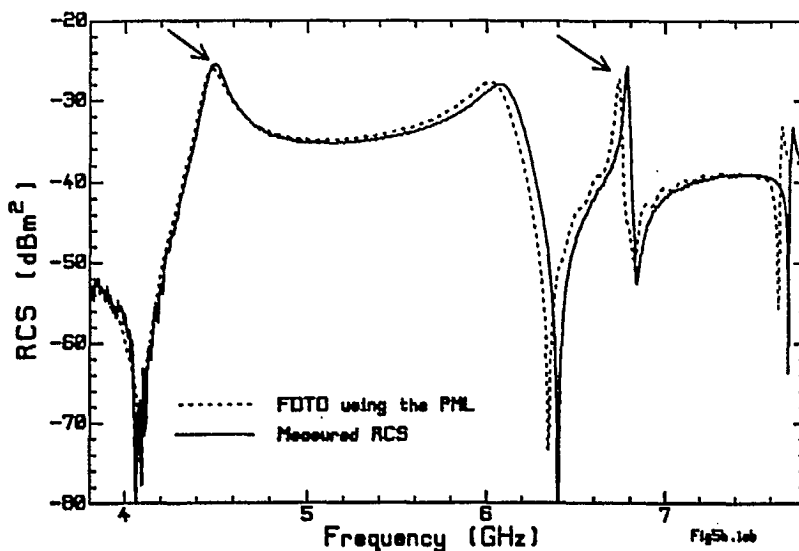
The time interval corresponding to 8,192 steps is 9.43 nanoseconds. The cutoff time for the PML formulation with a six layer PML is 6 ns, suggesting that the PML is thin for the computation of Fig. 5(a). The cutoff time with four layers of PML is only 1 ns, suggesting that in part (b) the layer is very thin. If we increase the thickness of the PML to 8 layers, the cutoff time increases to 14 ns. But the computed RCS is almost identical to that in Fig. 5(a). Hence for this problem, a 6 layer PML is sufficient. The 6 cell PML with 4 cells whitespace uses 2.2 Mb, compared to Liao's 3.8 Mb, a 58% reduction. The running time of 15,366 sec is about 25% longer than Liao's 12,134 sec.

Table 4
Computer Resources for the Dielectric Cube Scatterer
With the PML ABC

PML Layers	Whitespace + PML Layers	Time	Cell Space Size	Cell Space Storage	PML ABC Storage
4	8	9852 sec	32x32x32 cells	983,040 bytes	477,072
6	10	15,366	36x36x36	1,399,680	800,784



(a) Six cell PML with four cell whitespace.



(b) Four cell PML with four cell whitespace.

Figure 5 The RCS of the cube target using the PML.

choose a thicker PML. The results of this paper suggest that a cutoff time 50% larger than the total running time is adequate for good agreement with the measurements.

The results reported in this paper fix the reflection coefficient at 0.001, corresponding to 60 dB. All cases were also solved with a reflection coefficient of 0.01 or 40 dB. The cutoff times are about 50% longer with the larger reflection coefficient. For the rod problem, the agreement of the maxima in the RCS in the bracketed region in Fig. 3 is poorer with the larger reflection coefficient. But for the cube problem, little difference in the results was seen.

Conclusion

This paper has compared the memory requirements and CPU time for solving two scattering problems using the Liao second-order ABC and using the PML. The basis for comparison is equally-good agreement with the measured RCS. For the rod problem the PML used 46% less storage than the Liao formulation, and 89% less CPU time. For the dielectric cube problem, the PML used 58% less storage, but about 25% more CPU time. The PML has the clear advantage.

To use the PML effectively, the user must design an appropriate PML for the problem at hand. This paper has explored the parabolic progression of the PML's constitutive parameters. For very thin PML layers and thin whitespaces the geometric progression might offer better performance [2].

This paper shows good results with a 4 cell whitespace separating the scatterer surfaces from the PML surface. The cutoff time for the PML provides a good guide to the required thickness of the PML layer. Thus the user somewhat arbitrarily chooses a PML thickness and the FDTD code compares the cutoff time with the maximum time requested by the user, equal to the time step multiplied by the total number of steps. If the cutoff time is less than the total time, the code exits on an error, and the user must

The study of the computation of the RCS presented in this paper suggests that for the same degree of agreement with measured data, the perfectly-matched layer is comparable in CPU time and requires much less memory than the Liao absorbing boundary. Thus the PML has a clear advantage over the Liao formulation.

References

1. J.P. Bérenger, "A Perfectly Matched Layer for the Absorption of Electromagnetic Waves," *Journal of Computational Physics*, Vol. 114, No. 2, pp.185-200, Oct. 1994.
2. J. P. Bérenger, "Perfectly Matched Layer for the FDTD Solution of Wave-Structure Interaction Problems," *IEEE Trans. Antennas and Propagation*, Vol. 4, No. 1, pp. 110-117, January 1996.
3. Z. P. Liao, H.L. Wong, B.P. Yang and Y.F. Yuan "A Transmitting Boundary for Transient Wave Analysis," *Scientia Sinica*, Vol. XXVII, No. 10, p.1062-1076, October, 1984.
4. K.S. Yee, "Numerical Solution of Initial Value Problems Involving Maxwell's Equations in Isotropic Media," *IEEE Trans. On Antennas and Propagation*, Vol. AP-14, No. 3, pp. 302-307, May, 1966.
5. K.S. Kunz and R.J. Luebbers, "The Finite-Difference Time-Domain Method for Electromagnetics," CRC Press, 1993.
6. C.L. Larose, S.R. Mishra, and C.W. Trueman, "Measured RCS Polar Contour Maps for Code Validation," *Applied Computational Electromagnetics Society Journal*, Vol. 11, No. 3, pp. 25-43, November, 1996.
7. R. J. Luebbers, K.S. Kunz, M. Schneider and F. Hunsberger, "A Finite-Difference Time-Domain Near-Zone to Far-Zone Transformation," *IEEE Trans. on Antennas and Propagation*, Vol. AP-39, No.4, pp. 429-433, April 1991.
8. DIGITAL Visual Fortran, Digital Equipment Corporation, Maynard, Mass., August 1997.
9. C.W. Trueman, S.J. Kubina, R. J. Luebbers, S.R. Mishra and C.L. Larose, "RCS of High Permittivity Cubes by FDTD and by Measurement," *9th Annual Review of Progress in Applied Computational Electromagnetics*, Naval Postgraduate School, Monterey, California, March 22-26, 1993.
10. M. L. Van Blaricum, R. Mittra, "A Technique for Extracting the Poles and Residues of a System Directly from its Transient Response," *IEEE Trans. on Antennas and Propagation*, Vol. AP-23, No. 6, pp.777-781, November 1975.

Appendix 2

Reference [28]: C.W. Trueman, S.J. Kubina, J.E. Roy, W.R. Lauber, and M. Vall-llossera, "Validation of FDTD-Computed Handset Patterns by Measurement", Conference Proceedings, 14th Annual Review of Progress of the Applied Computational Electromagnetics Society, pp. 93-98, Monterey, California, March 16-20, 1998.

Validation of FDTD-Computed Handset Patterns by Measurement

C. W. Trueman

S.J. Kubina

Electromagnetic

Compatibility Laboratory,

Concordia University,

Montreal

J.E. Roy

W.R. Lauber

Communications Research

Centre,

Ottawa

M. Vall-llossera

Department of Signal Theory

and Communications,

Universitat Politècnica de

Catalunya (UPC),

Barcelona

Abstract-This paper compares the radiation patterns of a portable radio handset at 850 MHz in free space with those of the radio operating near box and sphere models of the head. The patterns are computed with the finite-difference time-domain method, using measured parameters for the liquid representing the brain. The head is found to introduce considerable changes to the radiation patterns, especially for directions where the head lies between the handset and the receiver. The computed radiation patterns are validated in this paper against measured patterns. Excellent agreement is found for the handset alone. The agreement is good for the handset and head models, with some differences in the minima of the radiation patterns, particularly for the sphere head. These may be due to the styrofoam-and-fiberglass-bolts mounting jigs, not included in the FDTD models, or to the cubical cell approximation of the shape of the heads.

Introduction

The finite-difference time-domain method has been used extensively to evaluate the radiation patterns and near fields of a portable radio handset operating near a representation of a human head, for example in Refs. [1] to [4]. The head is a complex three-dimensional structure made up of high-permittivity, lossy dielectric materials and as such is a challenging computational problem. A realistic head phantom is difficult to construct physically and complex to represent in terms of FDTD cells. This paper deals with simplified heads that are easy to build and straightforward to model with FDTD, as a preliminary step to studying a full head phantom. The "box head" is a thin-walled plexiglas box filled with liquid with the electrical parameters of the brain[5]. A simple box has surfaces parallel to planes of FDTD cells and so can be modelled with good accuracy. The "sphere head" is a thin plexiglas spherical shell filled with brain liquid. The sphere head introduces staircasing error into the FDTD model and so we might expect the accuracy of the computations to be poorer. This paper compares the radiation patterns of a handset operating near the box head and near the sphere head with measurements, as a validation of the FDTD computations.

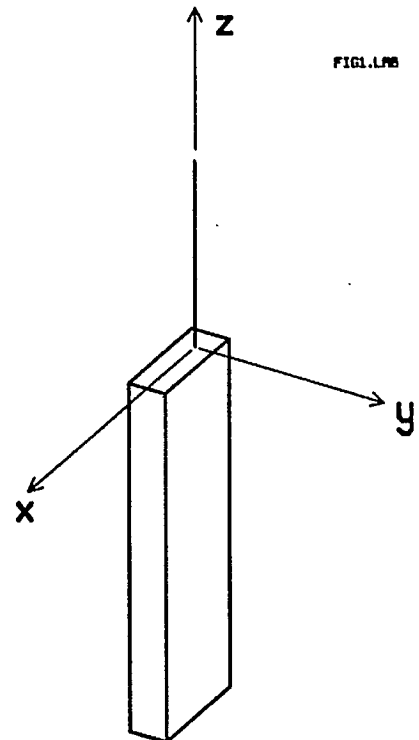


Fig. 1 The portable radio handset in the xyz coordinate system.

Measurement of the Radiation Patterns

The radiation patterns were measured by mounting the handset and head in a jig atop a styrofoam rotator column in a 6x6x6 meter anechoic chamber[6]. The handset contains a battery-operated oscillator at 850 MHz. An open-ended waveguide was mounted on the rotating table near the base of the rotator column to sample the field to provide a reference signal to phase-lock a network analyzer. The horizontal and vertical components of the field were measured by a dual-polarized ridged waveguide horn mounted about 330 cm from the handset. The mounting jig shown in Fig. 2, consisting of styrofoam blocks and fiberglass nuts and bolts, holds the handset in a well-known, reproducible position relative to the head. Fig. 2 shows the jig positioned for rotation in the yz plane in Fig. 1, for measurement of the $\phi = 90$ degree elevation. The elastic bands attached to the nuts in Fig. 2 were removed for the measurement. The patterns were measured in one degree increments.

Considerable care was taken to optimize the quality of the measured data. Unwanted reflections in the anechoic chamber were identified and reduced with absorber. The position of the handset was aligned as accurately as possible using a laser beam as a reference, to reduce alignment error as much as possible. However, the absorber in the chamber is designed for best performance above 1.5 GHz. The relatively short range from the handset to the horns may not be adequate for a true "far field" measurement. These problems will primarily affect the measured patterns in the minima.

Patterns of the Handset

Fig. 1 shows the handset oriented with the broad face of the case parallel to the xz plane, the antenna parallel to the z -axis and adjacent to the $-x$ side of the case. The handset is

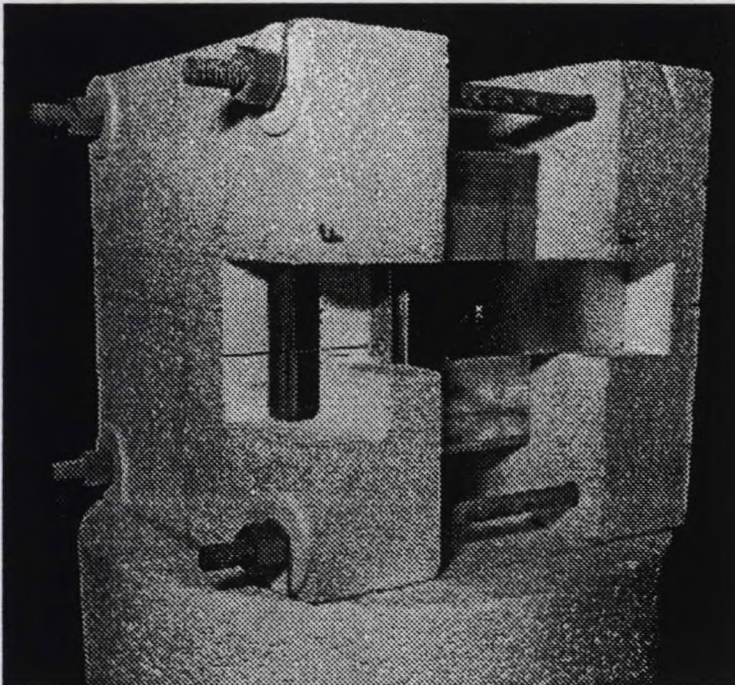
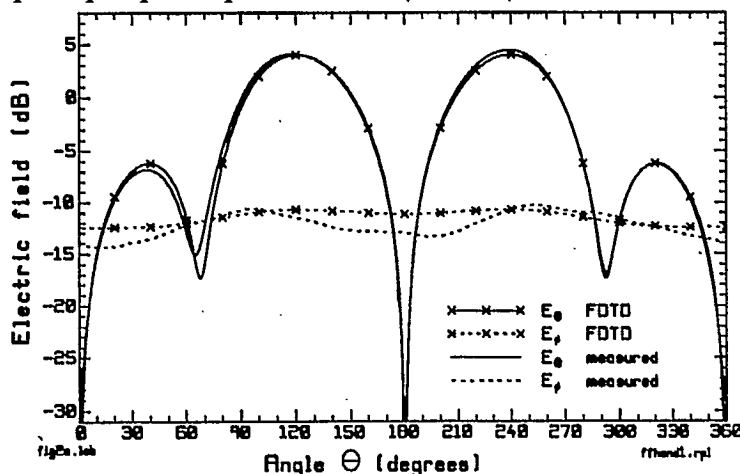


Fig. 2 The handset and box head mounted in the styrofoam jig, positioned on top of the rotator in the anechoic chamber.

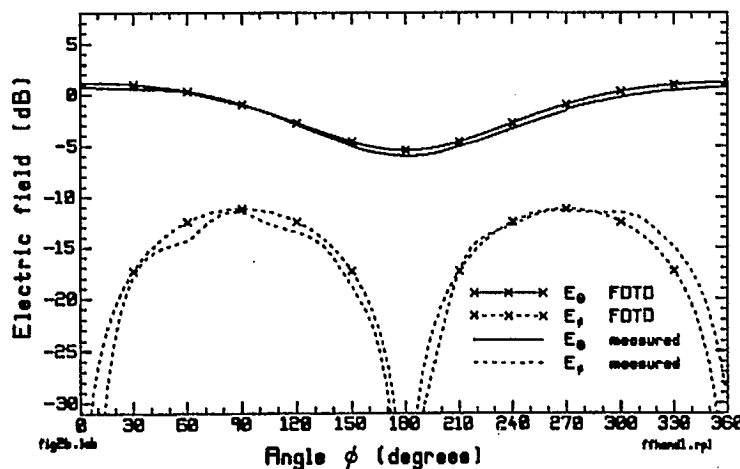
an aluminum box 5.35 by 1.74 by 16.77 cm, with an antenna 8.82 cm in length. These dimensions were chosen so that, using a cell size of 0.441 cm, the handset case is very close to 12 by 4 by 38 cells with a 20 cell antenna. The antenna is positioned 0.87 cm from three edges of the case. The FDTD code uses the perfectly-matched layer[7](PML) absorbing boundary condition. The PML was set to 6 cells in thickness with a surface reflection coefficient of 0.001 and parabolic evolution of the conductivity. The surfaces of the handset and the tip of the antenna were separated from the first layer of the PML by 4 cells of free space or "whitespace". The integration surface for the near-to-far zone transformation was centered within the whitespace. The FDTD computation was run for 2048 time steps with a sinusoidal generator at 850

MHz at the base of the monopole. The computed radiation patterns are true "far field" and do not account for the 330 cm range to the measurement horns. The computed patterns were scaled to have an "isotropic level" field strength[4] of 0 dB.

The radiated power in the measurement is not known, hence the measured patterns need to be scaled for comparison with the computations. The RMS field strength found from the computed principal plane patterns for $\phi = 0$, $\phi = 90$, and $\theta = 90$ was used as a reference level. Then the



(a) Elevation pattern for $\phi = 90$ degrees.



(b) Azimuth pattern.

Fig. 3 The radiation patterns of the handset.

below the computed field.

Fig. 3(b) compares the measured and computed azimuth patterns. The principal polarization is very roughly circular, with quite good agreement between the computation and the measurement, with a difference of about 0.5 dB in the minimum. The cross-polarization is a figure-eight pattern and agrees quite well between the measurement and the computation.

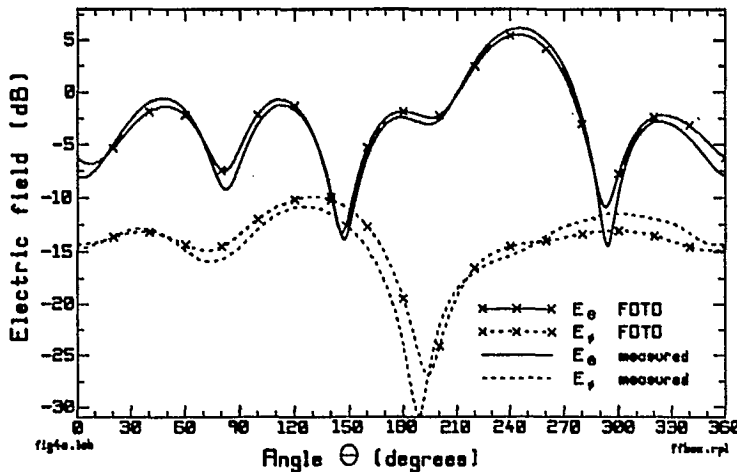
corresponding RMS field strength was found from the measured principal plane patterns, and the measured patterns were scaled to have the same RMS field strength as the computation.

Fig. 3 compares the measured and computed radiation patterns for the handset in free space, in decibels above the isotropic level field strength. In the measurement the handset was held in a simpler styrofoam jig than that in Fig. 2, having no fiberglass nuts and bolts. The computed $\phi = 90$ pattern in Fig. 3(a) is symmetric about the xz plane. It has the main lobe of field strength 4.0 dB directed at $\theta = 121$, that is downward, and a minor lobe of field strength -6.2 dB directed upward at $\theta = 39$ degrees. The measured E_θ polarization agrees very well with the computation, with a difference in the minor lobe near 40 degrees of 0.6 dB and in the major lobe near 240 degrees of 0.4 dB. The differences in the minima are larger. The computed minimum at 68 degrees has level -17.3 dB, whereas the measurement has a minimum at 65 degrees of -15.1 dB. The cross-polarized or E_ϕ field is roughly circular in shape and at a level of about -10.8 dB in the computation. The measured E_ϕ component has maxima at about the same level as the computed field, but has minima about 1.8 to 2.2 dB

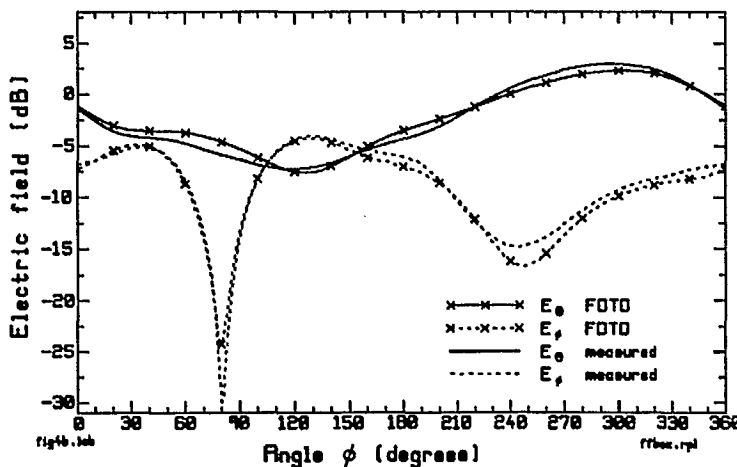
Some differences between the measurement and the computation in Fig. 3 can be attributed to the styrofoam mount for the handset, which was not included in the computation. The agreement in Fig. 3 is about the best that we have been able to achieve between computations and measurements.

The Handset and the Box Head

Fig. 2 shows the handset and the box head, mounted in the support jig. The box head has outside dimensions 17.07 by 13.89 by 21.06 cm and wall thickness 0.5 cm. It is filled with a mixture of de-ionized water, sugar and salt having the electrical parameters of the brain[5] at 850 MHz. The relative permittivity and conductivity were measured to be 40.42 and 1.064 S/m, respectively[8]. The



(a) Elevation pattern for $\phi = 90$ degrees.



(b) Azimuth pattern.

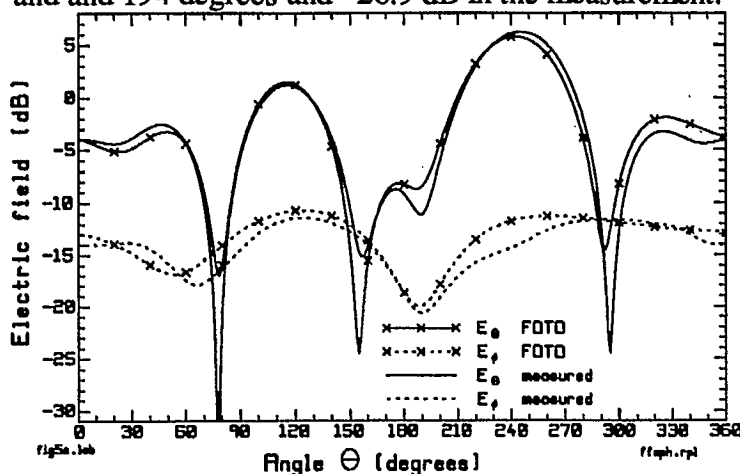
Fig. 4 The radiation patterns of the handset and box head.

245 degrees is seen in both patterns as is the smaller lobe near 325 degrees. The cross-polarized field is about -11 dB for the handset alone, and about -15 dB for the handset and box head.

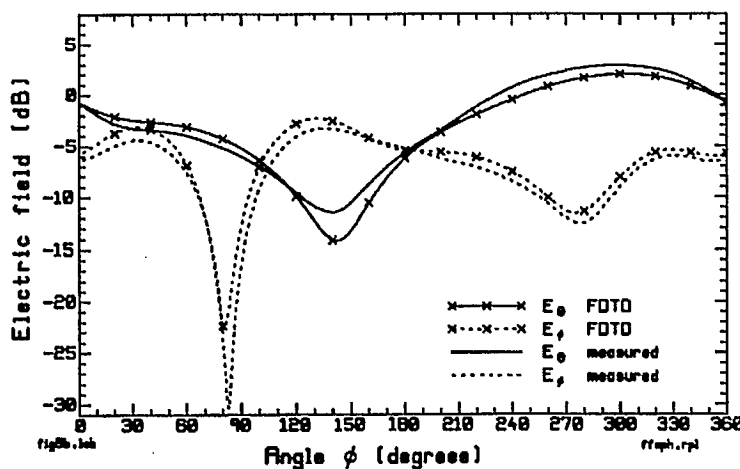
box head is positioned in the coordinates of Fig. 1 on the +y side of the handset, such that if the operator faces in the +x direction, the handset is held in the right hand with the antenna towards the back. The handset is spaced from the box by 0.96 cm. The box is positioned such that if the antenna is on the z-axis, then the back surface of the box is at $x = -5.95$ cm. The bottom of the box aligns with the bottom of the handset. The box is modelled with FDTD cells of size 0.441 cm. This puts the handset case in the FDTD model two cells or 0.882 cm from the box head, and approximates the box dimensions as 17.12 by 14.11 by 21.12 cm. The FDTD code uses the average permittivity and conductivity to update field components that lie in planes that are interfaces between two dielectric materials. The styrofoam blocks and fiberglass nuts and bolts of the positioning jig were not included in the FDTD model.

Fig. 4 shows two principal plane patterns of the handset and box head. The $\phi = 90$ pattern from $\theta = 0$ to 180 degrees has the head between the handset and the observer, and comparing Fig. 3(a) and Fig. 4(a), the head changes the pattern considerably. From $\theta = 180$ degrees to 360 degrees (this corresponds to $\phi = 270$ degrees, $180 < \theta < 0$) the pattern of the handset and box head resembles the pattern of the handset alone. The large lobe near

The agreement between the computation and the measurement in Fig. 4(a) is quite good. The lobe in E_θ in the computation at 50 degrees of -1.4 dB is seen in the measurement at 48 degrees and -0.6 dB. The lobe at 114 degrees and -1.2 dB is reproduced in the measurement at 112 degrees, -0.74 dB. The minimum at 82 degrees of -9.2 dB falls at 81 degrees and -7.5 dB in the measurement. These features are in the part of the pattern where the head is between the handset and the observer. The largest difference in E_θ is at the minimum at 294 degrees and -14.5 dB in the computation, which is seen at 293 degrees, -10.9 dB in the measurement. The cross-polarized field agrees well in shape and level. Again the largest difference is in the minimum at 188 degrees of -30.8 dB in the computation, and at 194 degrees and -26.9 dB in the measurement.



(a) Elevation pattern for $\phi = 90$ degrees.



(b) Azimuth pattern.

Fig. 5 The radiation patterns of the handset and sphere head.

minima in E_θ near 78 and 155 degrees. The measured and computed fields agree quite well except in the minima. The large lobe at 242 degrees and 5.8 dB in the computed field is seen at 246 degrees and

The azimuth pattern is shown in Fig. 4(b). The head causes the azimuth pattern to be less circular and raises the level of the cross-polarized field. The measured and computed patterns again agree quite well, with the largest differences in the minima of the patterns.

The Handset and the Sphere Head

The sphere head is a plexiglas sphere of outside diameter 20.68 cm and wall thickness 0.365 cm. The sphere is filled with the same "brain liquid" mixture used for the box head. The sphere was positioned such that if the base of the antenna is at the origin, the centre of the sphere is at $(x = +1.81, y = 12.14, z = 6.42)$ cm. The curved surface of the sphere is approximated with a staircase of FDTD cells of size 0.441 cm. The model was constructed such that over the whole surface of the sphere the edge of a cell filled with brain liquid never touches the edge of a free-space cell; that is, there is always a plexiglas cell separating the outside from the inside.

Fig. 5(a) shows the elevation pattern for $\phi = 90$ degrees. The pattern is not greatly different from that of the handset and box head. The sphere head changes the pattern from $\theta = 0$ to 180 degrees where the sphere lies between the handset and the observer. The sphere introduces deep

6.2 dB in the measurement. The cross-polarized field is at about the same level for the handset and sphere as it was for the handset and box. The computed and measured patterns agree quite well in both shape and level.

Fig. 5(b) shows the azimuth pattern, which is very similar to that for the box head in Fig. 4(b). The minimum at 143 degrees is deeper for the sphere than for the box. The cross-polarized fields are remarkably similar. The agreement between the computation and the measurement is somewhat better for the box than it is for the sphere. This may be attributable to the staircased approximation of the sphere's curved surface.

Conclusion

This paper has compared measured and computed radiation patterns for a portable radio handset and two simple representations of the head. One objective was to validate the FDTD method for solving lossy, high-permittivity materials such as human tissue. A second objective was to discover the changes in the radiation patterns of a handset when a head is introduced very close to the handset surfaces.

The radiation patterns for the handset alone, Fig. 3, establish the best agreement that we have been able to achieve between the measurement and the computation. The box head is well represented with cubical FDTD cells, with some error in the overall size and relative position of the box to the handset. Fig. 4 for the handset and box head shows agreement that is somewhat poorer than in Fig. 3, but still very good. The sphere's shape is represented approximately by a staircase in the FDTD model. Still, the agreement between the measured and computed data in Fig. 5 is good, with differences in the depth of the minima being the major problem. By including the styrofoam mounting jig with its fiberglass nuts and bolts in the FDTD cell model, somewhat improved agreement may be possible. The limitations of the absorber in the anechoic chamber and the short range from the handset to the measurement horn may account for some of the differences between the measured data and the computation.

References

1. M.A. Jensen, Y. Rahmat-Samii, "E.M. Interaction of Handset Antennas and a Human in Personal Communication", *Proc. IEEE*, Vol. 83, No. 1, pp. 7-17, January, 1995.
2. Q. Balzano, O. Garay and T.J. Manning, "Electromagnetic Energy Exposure of Simulated Users of Portable Cellular Telephones", *IEEE Trans. On Vehicular Technology*, Vol. 44, No. 3, pp. 390-403, August, 1995.
3. J. Toftgard, S.N. Hornsleth, and J. Bach Andersen, "Effects on Portable Antennas of the Presence of a Person", *IEEE Trans. on Antennas and Propagation*, Vol. 41, No. 6, pp. 739-746, June, 1991.
4. C.W. Trueman, S.J. Kubina, D. Gaudine and B. Lorkovic, "A Research Study on Electromagnetic Fields Produced by Portable Transceivers", Technical Note TN-EMC-97-01, ECE Dept., Concordia University, March 31, 1997.
5. G. Hartsgrrove, A. Kraszewski and A. Surowiec, "Simulated Biological Materials for Electromagnetic Radiation Absorption Studies", *Bioelectromagnetics*, Vol. 8, pp. 29-36, 1987.
6. J.E. Roy, W. Lauber, and J. Bertrand, "Measurements of the Electromagnetic Far Field Produced by a Portable Transmitter", Communications Research Centre, Ottawa, September 24, 1997.
7. J. P. Bérenger, "Perfectly Matched Layer for the FDTD Solution of Wave-Structure Interaction Problems", *IEEE Trans. Antennas and Propagation*, Vol. 4, No. 1, pp. 110-117, January 1996.
8. J. Seregelyi, private communication, September 24, 1997.

Appendix 3

Permittivity and Conductivity Data for the Materials Making Up the
Head Phantom [29]

Communications Research Centre Phantom Data

Freq. (Hz)	ϵ'	ϵ''	s	ϵ' SD	ϵ'' SD
Muscle					
7.97E+8	51.821	24.334	1.076	0.199	0.100
8.81E+8	51.729	22.595	1.108	0.201	0.094
9.74E+8	51.559	21.077	1.143	0.207	0.078
1.08E+9	51.389	19.698	1.181	0.203	0.069
1.19E+9	51.271	18.539	1.229	0.205	0.069
1.32E+9	51.152	17.302	1.291	0.206	0.058
1.46E+9	50.960	16.791	1.362	0.205	0.057
1.61E+9	50.782	16.122	1.446	0.207	0.056
1.78E+9	50.623	15.579	1.546	0.208	0.053
1.97E+9	50.407	15.166	1.664	0.210	0.054
2.18E+9	50.187	14.969	1.816	0.215	0.056
2.41E+9	49.908	14.932	2.004	0.214	0.059
2.67E+9	49.540	14.993	2.226	0.201	0.062
2.95E+9	49.108	15.169	2.490	0.195	0.063
Eye					
7.97E+8	69.560	35.366	1.568	1.492	0.883
8.81E+8	69.447	32.850	1.610	1.463	0.818
9.74E+8	69.187	30.620	1.660	1.429	0.732
1.08E+9	68.921	28.593	1.714	1.450	0.667
1.19E+9	68.728	26.921	1.785	1.456	0.621
1.32E+9	68.543	25.537	1.873	1.439	0.566
1.46E+9	68.265	24.343	1.974	1.444	0.516
1.61E+9	67.961	23.367	2.096	1.454	0.499
1.78E+9	67.649	22.553	2.238	1.437	0.487
1.97E+9	67.276	21.928	2.406	1.403	0.465
2.18E+9	66.929	21.566	2.617	1.361	0.440
2.41E+9	66.519	21.401	2.872	1.348	0.417
2.67E+9	66.000	21.356	3.170	1.349	0.398
2.95E+9	65.425	21.472	3.525	1.324	0.396
Skin					
7.97E+8	43.163	15.186	0.673	0.163	0.141
8.81E+8	42.230	15.847	0.777	0.154	0.153
9.74E+8	41.138	16.566	0.898	0.134	0.167
1.08E+9	39.918	17.290	1.037	0.132	0.194
1.19E+9	38.603	17.900	1.187	0.185	0.198
1.32E+9	37.212	18.440	1.352	0.228	0.188
1.46E+9	35.725	18.971	1.539	0.248	0.179
1.61E+9	34.142	19.428	1.743	0.251	0.157
1.78E+9	32.495	19.785	1.963	0.295	0.137
1.97E+9	30.794	20.018	2.196	0.299	0.104
2.18E+9	29.046	20.161	2.447	0.305	0.079
2.41E+9	27.273	20.200	2.711	0.309	0.065
2.67E+9	25.486	20.088	2.982	0.302	0.051
2.95E+9	23.736	19.839	3.257	0.288	0.063

Communications Research Centre Phantom Data

Brain	ϵ'_{NG}	ϵ''	$S_{\alpha\beta}$	ϵ'_{SD}	ϵ''_{SD}
7.97E+8	42.510	15.254	0.676	0.116	0.041
8.81E+8	41.544	15.485	0.759	0.095	0.047
9.74E+8	40.466	15.732	0.853	0.074	0.062
1.08E+9	39.359	15.976	0.953	0.073	0.035
1.19E+9	38.188	16.145	1.071	0.083	0.025
1.32E+9	37.038	16.300	1.195	0.089	0.037
1.46E+9	35.890	16.470	1.336	0.092	0.035
1.61E+9	34.731	16.603	1.489	0.101	0.036
1.78E+9	33.554	16.710	1.658	0.105	0.040
1.97E+9	32.353	16.773	1.840	0.101	0.045
2.18E+9	31.131	16.825	2.042	0.093	0.043
2.41E+9	29.910	16.875	2.265	0.094	0.044
2.67E+9	28.652	16.886	2.506	0.104	0.052
2.95E+9	27.393	16.833	2.763	0.093	0.057
Bone					
7.97E+8	14.915	2.911	0.129	1.478	0.333
8.81E+8	14.766	2.937	0.144	1.386	0.359
9.74E+8	14.505	2.836	0.154	1.290	0.368
1.08E+9	14.177	2.792	0.167	1.259	0.307
1.19E+9	13.953	2.931	0.194	1.293	0.202
1.32E+9	13.860	3.053	0.224	1.138	0.154
1.46E+9	13.697	3.054	0.248	1.238	0.148
1.61E+9	13.556	3.017	0.271	1.289	0.134
1.78E+9	13.412	3.029	0.300	1.257	0.110
1.97E+9	13.224	3.151	0.346	1.262	0.102
2.18E+9	13.007	3.189	0.387	1.307	0.206
2.41E+9	12.771	3.174	0.426	1.295	0.257
2.67E+9	12.582	3.200	0.475	1.266	0.180
2.95E+9	12.401	3.213	0.527	1.247	0.181

CRC Publication Approval and Record Form

This form is to be completed for the approval of all CRC publications and presentations. The level of approval varies with the category of the publication. For details of publication procedures, see the document: Publication Policy and Procedures. For items sponsored by DND, the DREO yellow and green sheets must also be prepared and submitted separately.

Category A: CRC Reports & CRC Technical Notes. **Category B:** Journal & conference papers. **Category C:** Contributions to outside documents such as TTCP, ITU, AGARD, standards, etc. **Category D:** Abstracts **Category E:** Documents with non-CRC employee as main author.

Title: A Research Study on Electromagnetic Fields Produced by Portable Transceivers

Author(s): Dr C.W. Trueman and Dr. S.J. Kubina

Branch and Directorate VPRS/REMC **Document category:** E

Web Address (for CRC Reports & Technical Notes): _____

Details of Publication or Presentation: (e.g. report type & number; name & sponsor of journal; technical body (ex. TTCP), or conference; date & place of publication or presentation; etc.)

Concordia University Contract report TN-EMC-98-01, March 31, 1998

CRC Contract No. PWGSC/CRC U6800-7-0726/001/ST

Security Classification: Unclassified

Releasability: Releasable (☒) Non releasable (☐) Conditionally releasable (☐)

If limitations apply, describe the conditions: _____

Intellectual Property: May require IP protection. Copy sent to DMKT (☐) or Does not require IP protection (☐). Explain: _____

Certifications

All Categories:

Author and date: _____

Manager and date: _____

For Categories A and B:

Reviewer and date: _____

Editor and date: _____

VP and date: _____

For Category D:

VP and date: _____

INDUSTRY CANADA / INDUSTRIE CANADA



208836